PRECISION ENGINEERING CENTER

2001 ANNUAL REPORT
VOLUME XIX
January 2002

Sponsors:

3M Corporation
Burleigh Instruments
Eastman Kodak Company
IBM Corporation
Los Alamos National Laboratory
National Science Foundation
NASA Goddard Space Flight Center
Oak Ridge National Laboratory
Vistakon, Inc.

Faculty:

Thomas Dow, Editor
Greg Buckner
Jeffrey Eischen
Karl Falter
Dieter Griffis
Paul Ro
Phillip Russell
Ronald Scattergood
Albert Shih
David Youden

Graduate Students:

Markus Bauer
Matthew Cerniway
Stuart Clayton
David Gill
Matias Heinrich
David Hood
David Kametz
Bryan Love
Patrick Morrissey
Gang Mou
Nobuhiko Negishi
Witoon Panusittikorn
Jun Qu
Tao Wu

Staff:

Kenneth Garrard
Alexander Sohn
Laura Underhill

TABLE OF CONTENTS

FABRICATION

SUMMARY

The goals of the Precision Engineering Center are: 1) to improve the understanding and capability of precision metrology, actuation, manufacturing and assembly processes; and 2) to train a new generation of engineers and scientists with the background and experience to transfer this new knowledge to industry. Because the problems related to precision engineering originate from a variety of sources, significant progress can only be achieved by applying a multidisciplinary approach; one in which the faculty, students, staff and sponsors work together to identify important research issues and find the optimum solutions. Such an environment has been created and nurtured at the PEC for 20 years; the new technology that has been developed and the 80 graduates attest to the quality of the results.

The 2001 Annual Report summarizes the progress over the past year by the faculty, students and staff in the Precision Engineering Center. During the past year, this group included 10 faculty, 14 graduate students, 2 full-time technical staff members and 1 administrative staff member. Representing two different Departments from the College of Engineering, this diverse group of scientists and engineers provides a wealth of experience to address precision engineering problems. The format of this Annual Report separates the research effort into individual projects, however, this should not obscure the significant interaction that occurs among the faculty, staff and students. Weekly seminars by the students and faculty provide information exchange and feedback as well as practice in technical presentations. Teamwork and group interactions are a hallmark of research at the PEC and this contributes to both the quality of the research as well as the education of the graduates.

The summaries of individual projects that follow are arranged in the same order as the body of the report, that is the four broad categories of 1) metrology, 2) actuation, 3) control and 4) fabrication.

1) METROLOGY

The emphasis of the metrology projects has been to develop new techniques that can be used to characterize surface structure and shape as well as measure important parameters such as tool force.

The Polar Profilometer – Polaris Profilometers for measuring form and roughness have traditionally been based on rectangular coordinates, but such designs have limitations when measuring certain geometries, for example, high aspect-ratio optics whose shape is more polar than rectangular in nature. To meet this need, a polar profilometer has been designed, built and delivered to an affiliate of the Center. This device measures both concave and convex parts ranging from hemispheres to aspheres within a circular measurement field 50 mm in diameter. The resolution is 20 nm with an overall accuracy of 100 nm. Operating procedures have been established for part setup, alignment, reference path specification and measurement. The hardware

platform is a Delta Tau UMAC controller coupled to an IBM PC via USB. This choice offers significant advantages for system integration and represents the future direction of flexible machine controls. A user interface has been written to lead the user through calibration, operation, data acquisition and data evaluation.

Lapping Plate Charging Lapping the air bearing surface of a hard disk head is one of the last steps in the production process. This surface is about 1 mm square and must have a surface finish less than 1 nm and be flat to the order of 10 nm. The goal of this project is to optimize the preparation of the tin lap plate used to produce this surface. The current technique involves creating randomly overlapping circular scratches on the tin surface and then charging the peaks with diamond grit using a rotating flat ceramic ring. The randomness of this texturing process is a suspect in the lack of repeatability in the lapping results. A new surface preparation method has been proposed using a spiral groove on the face of the tin and a new charging technique using a cylindrical roller on the tin surface. An eddy current brake on this roller is also used to measure the interface friction while charging to guarantee a consistent process.

Distortion of Thin Cylinders High-energy physics experiments at Los Alamos National Labs use a thin 100 mm cylindrical shell shrunk fit between two copper electrodes connected to large banks of capacitors. When these capacitors are discharged, large currents flow through these shells and the magnetic fields generated produce tremendous loads that squeezed the diameter of the shells toward zero. The initial shape of these shells is suspected to be a key factor in the efficiency of the experiments. To find an optimal shape such that the shells remain cylindrical as they implode, a computer model has been developed. The goal is to find an initial non-cylindrical shape such that the shell will be cylindrical when it is shrunk onto the copper electrodes.

2) ACTUATION

Real-time control is a necessary technique to improve the precision — accuracy and repeatability — of a fabrication or measurement process. The metrology activities discussed above are intended to develop tools or devices to measure shape, force or properties. Equally important are improved actuators with the ability to create the motion necessary to correct the error.

Design of a Ultrasonic Piezoelectric Motor A new design for an ultrasonic motor has been developed that uses independent, orthogonal, ultrasonic motions of a ceramic tip to move a slideway. The challenge in developing such a piezoelectric motor are 1) the actuator needs to have two different mode shapes at nearly the same frequency and 2) each mode shape must be exclusively excited by one actuator and not by the other. Finite element analysis (FEA) has been used to include all significant features such as the anisotropy of the piezoelectric material, the exact properties and dimensions of the actuators (including any glue joints) when developing each design. The final design is small (30x12x6 mm), operates at 40 KHz, can move the slide at 300 mm/sec and can position it to better than 10 μm (depending on the sensor resolution).

Development of a Piezo Actuator for Cryogenic Environments The Next Generation Space Telescope has a large mirror that must collapse to fit in the cargo bay of the Shuttle Orbiter. Once transported to the cryogenic environment of space (20 to 60 Kelvin), the mirror must be unfolded and the focal point adjusted using many small actuators. These actuators need a stroke of 10 mm, resolution on the order of 10 nm, a design life of 10,000 to 100,000 cycles and must be able to hold their position in a power-off mode. The PEC developed an actuator design for this application built around an 80-pitch screw driven by piezoelectric actuators. The concept involves a fixed nut to support the screw and a driven nut to rotate it. The operation of the motor has been demonstrated from room temperature to cryogenic conditions down to 77 °K.

3) CONTROL

Precision control problems involve both the characterization of the electromechanical system and the selection of hardware and software to implement the control algorithm. As a consequence, studies of each of these aspects are important research topics for the PEC.

Modeling and Control of a Magnetostrictive Tool Servo System Magnetostrictive actuators have the advantage of high strain output and broadband response but have significant hysteresis. Use of these actuators in precision applications requires feedback control and an advanced control scheme to compensate for the errors caused by the hysteresis. A fast tool servo driven by a large magnetostrictive actuator (length = 200 mm with a maximum stroke of 300 μm) is being used to study the application of a non-linear control scheme - sliding mode control - to this type of actuator. The displacement of the actuator as a function of drive voltage has been measured and modeled as a hyperbolic tangent function. A theoretical model of the control system has been created on Matlab and shows the advantages of this advanced control compared to PID control.

Piezoelectric Resonating Structures for Microelectronic Cooling The cooling effect caused by ultrasonic acoustic streaming of the air between two plates is being studied. One plate could be a fixed heat source such as a chip on IC board and the other an ultrasonically vibrating PZT plate designed to increase the convective heat transfer. One of the key issues is the optimal design of the resonator structures. Natural frequencies and amplitudes of vibration predicted by a finite element analysis are used as the criteria to determine the appropriate dimensions of the resonator systems. Different length and width combinations are being investigated with different boundary conditions. The goal is to find an acceptable thickness range that will result in the first-mode resonance being in the ultrasonic range, that is, greater than 30 kHz.

Active Control of Tool Deflection and Chatter using Magnetic Bearing Spindle In a recent project, a technique to compensate for deflection of small milling tools (diameter < 1 mm) has been demonstrated. However, this open loop technique is limited due to uncertainties in part position and tool sharpness. A new project has been initiated to use a magnetic bearing to sense the magnitude of the force components and to automatically correct the position of the tool by

moving the slideway positions or the spindle center. A third axis has been built and installed on the Nanoform DTM which will hold the magnetic spindle. Preliminary experiments designed to measure tool force are being performed using the high-speed air turbine to drive the tool.

4) FABRICATION

High-speed milling, plastic replication and a new technique for diamond turning have been the focus of the fabrication process research over the past year.

Precision Replication of Optics using Injection Molding The fields of optical communication, photonics, and display technologies require the development of high-volume yet high-precision production methods. Injection molded polymer optics fulfill many of the requirements for these parts, but still present challenges. The objective of this research is to investigate the replication of features in precision optics and the co-molding of these optical surfaces onto thermally stable substrates. Statistical experimental design has been used to identify the most important variables responsible for the fidelity of nanomenter-sized feature reproduction. A variety of optical geometries have been produced ranging from a blaze grating to a small Fresnel lens. Experiments using silane to improve the adhesion of plastic lenses to glass substrates are also underway.

Rapid Diamond Milling Turning has been the precision manufacturing method of choice over fly-cutting or milling due to the combination of relatively short machining time and high-quality surface finish from the single crystal diamond tools. However, a major disadvantage of diamond turning is the limited range of materials that can be machined due to tool wear. Previous experiments in Japan, Germany and at the PEC have shown the decrease in wear as a result of vibration the tool. The goal of this project is to uncover the role of the shape, frequency, and amplitude of the tool motion on the cutting process. A new high-speed UltraMill is being assembled that will operate at 10x the frequency of the previous model (5,000 vs 500 Hz).

Biconic Mirror for NASA Challenges in fabrication and testing have historically limited the choice of surfaces for reflective optical instruments to spherical or conic mirrors. However, more degrees of freedom are necessary to meet new performance and packaging requirements. In particular, single-surface astigmatism correction in spectrographs necessitates a toroidal surface, which lacks an axis of rotational symmetry. With support from NASA Goddard Space Flight Center (GSFC), a 94 by 76 mm off-axis, toroidal, biconic mirror has been fabricated using the Variform fast tool servo and the Nanoform 600 diamond turning machine. Issues related to the geometric analysis, decomposition, toolpath generation, controller interfacing, part fixture design, alignment and machining of a pair of these mirrors are discussed.

Laser Scribing For Precision Shape Modification Hard disk heads, called sliders, require careful control of their flatness to keep the flying height as small as possible. While

lapping techniques produce good surface finish, they do not always produce acceptable flatness. A technique has been developed to use a laser to create subtle changes in the shape of the head after lapping. The laser scribing system produces small changes in the curvature by inducing residual stress into the slider. Predicting this curvature as a function of the length and position of the scribe pattern is the objective of this project. A finite element model of the head was created and the shape predicted based on empirical measurements of laser scribed heads. A library of scribing results have been built using this model that allow, through superposition, the shape of complicated scribing patterns to be predicted. Ultimately, the inverse problem needs to be solved, that is finding a scribing pattern to generate a desired change in shape.

1 THE POLAR PROFILOMETER *POLARIS*

Alex Sohn
Ken Garrard
PEC Staff

The project to design and construct the polar profilometer Polaris has been completed. The system has been tested and has exceeded initial expectations in terms of performance. Polaris can measure the profile of any roughly spherically symmetric part that will fit in its 50 mm diameter measurement field to an accuracy of 100 nm. Polaris can measure form error as well as resolve surface features as small as 20 nm. Through the implementation of an intuitive user interface, these measurement capabilities can be exploited with a minimum of setup time and effort.

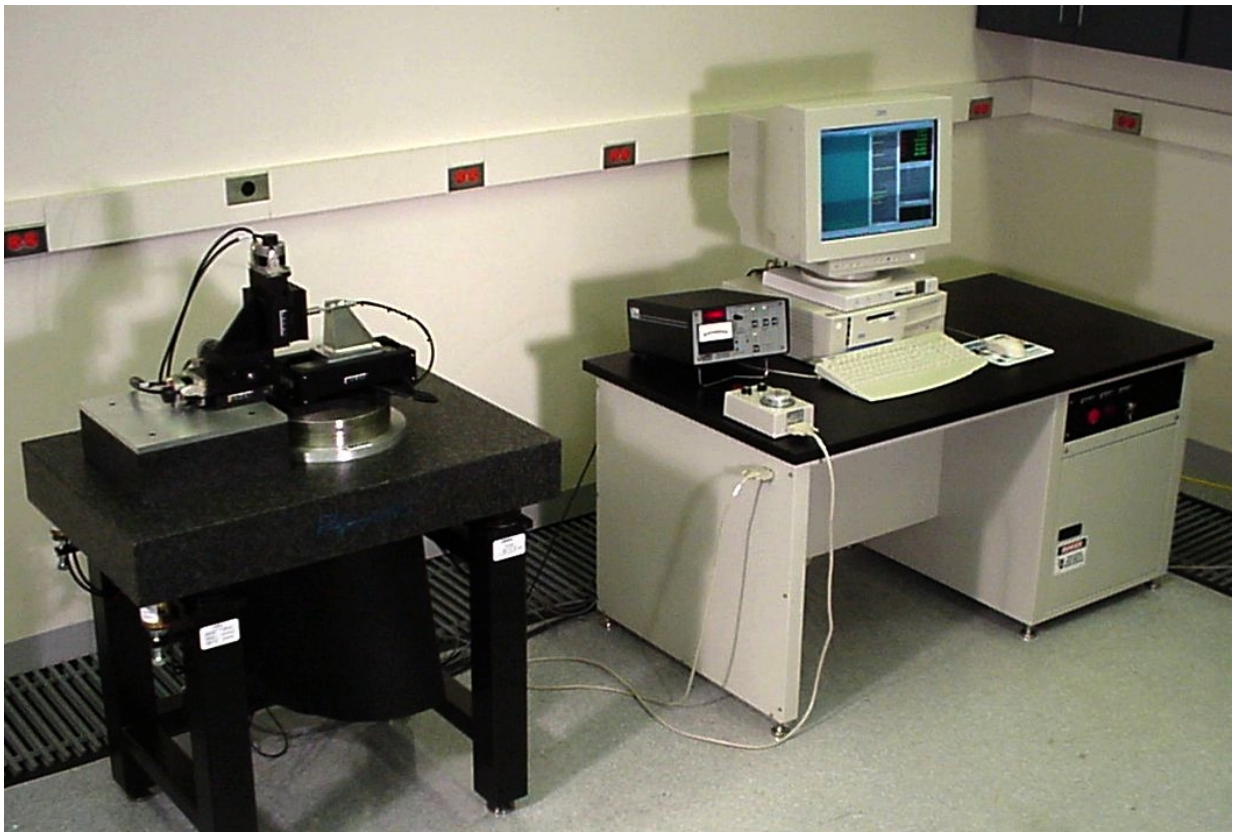

1.1 INTRODUCTION

Profilometers for performing form and roughness measurements have traditionally been based on cartesian geometry. Measuring parts with large aspect ratios presents a significant challenge for commercially available measurement systems. Optical profilometers are slope limited to a few degrees by the ratio of fringe spacing to resolution. Mechanical profilometers are usually limited by the clearance angle of the tip and the non-perpendicular loading direction of the probe – both of which often limit the measurable slopes to less than 45°.

Certain industries, those making high aspect-ratio optics in particular, require the measurement of geometries more polar than cartesian in nature. A polar profilometer, called Polaris, has been designed and built at the PEC to address this need. The device is capable of measuring figure as well as roughness on hemispheres and aspheres both concave and convex within a circular measurement field 50 mm in diameter. This design can be used to measure surfaces to a resolution of 50 nm and an overall accuracy of 500 nm.

1.2 DESIGN

1.2.1 MECHANICAL SYSTEM

As shown in Figure 1, *Polaris* consists of an air-bearing linear slide stacked atop an air bearing rotary table. The linear slide supports an air-bearing LVDT sensor which, while limited in measurement range to 500 μm, has a resolution of up to 2.5 nm. Position feedback on the linear and rotary axes is via encoders with 20 nm and 1μrad resolution, respectively. The axes are actuated by brushless, frameless motors to

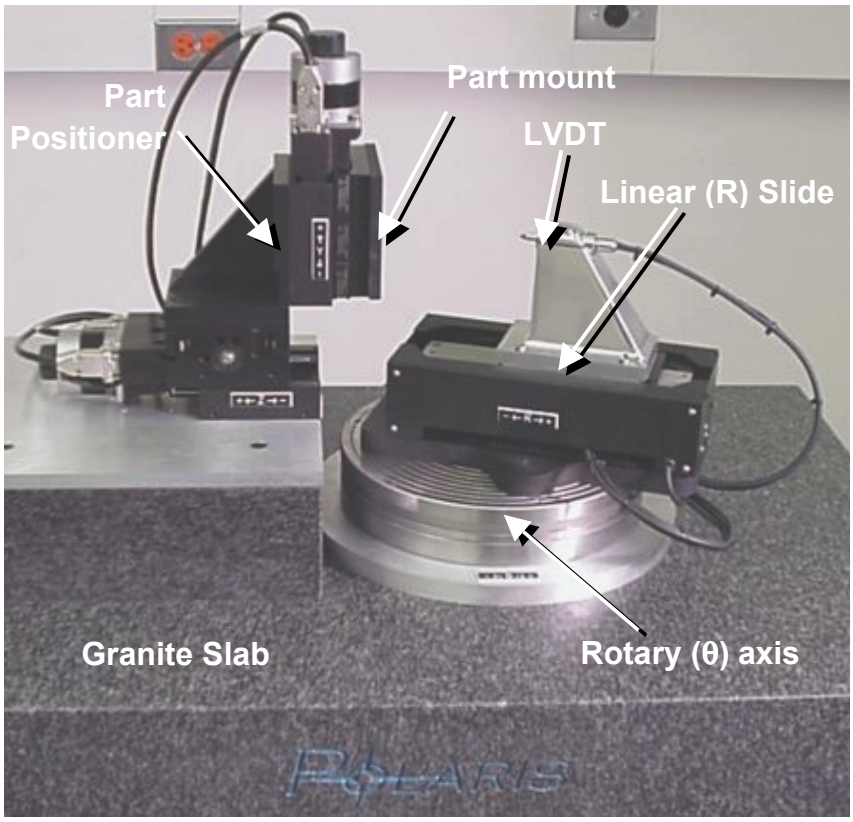

Figure 1. The layout of the measurement unit. The live (R and θ) axes support an air-bearing LVDT. The LVDT is traced across a part (not shown) mounted on the part mount and located for measurement by the part positioner.

prevent disturbances from motor bearings or brushes. A three-axis part positioning stage with vertical part mounting plate is actuated by stepper motors. The purpose of the positioning stage is to locate the part before measurement. The air bearing axes are then used to trace out the nominal surface shape of the part with the LVDT measuring deviations from this nominal path.

1.2.2 Error Budget

To evaluate a precision machine design's ability to meet specifications requires an error budget[1]. Constructing an error budget involves adding the individual errors of the components in an appropriate manner to create the error for the entire system. Roll, pitch, yaw, straightness, and displacement errors in the linear air bearing slide were added to radial, axial, and tilt errors in the rotary air bearing to obtain geometric errors. Thermal errors have also been evaluated by defining a thermal circuit. The following strategy was followed: posed on the specifications of maximum errors of each component, a typical geometric error form was constructed. The shapes of the errors are somewhat subjective, but the maximum amplitudes are those given by the specifications. These geometric errors are then combined in three dimensions for the entire range of motion of the machine to give an estimate of the maximum obtainable errors and their

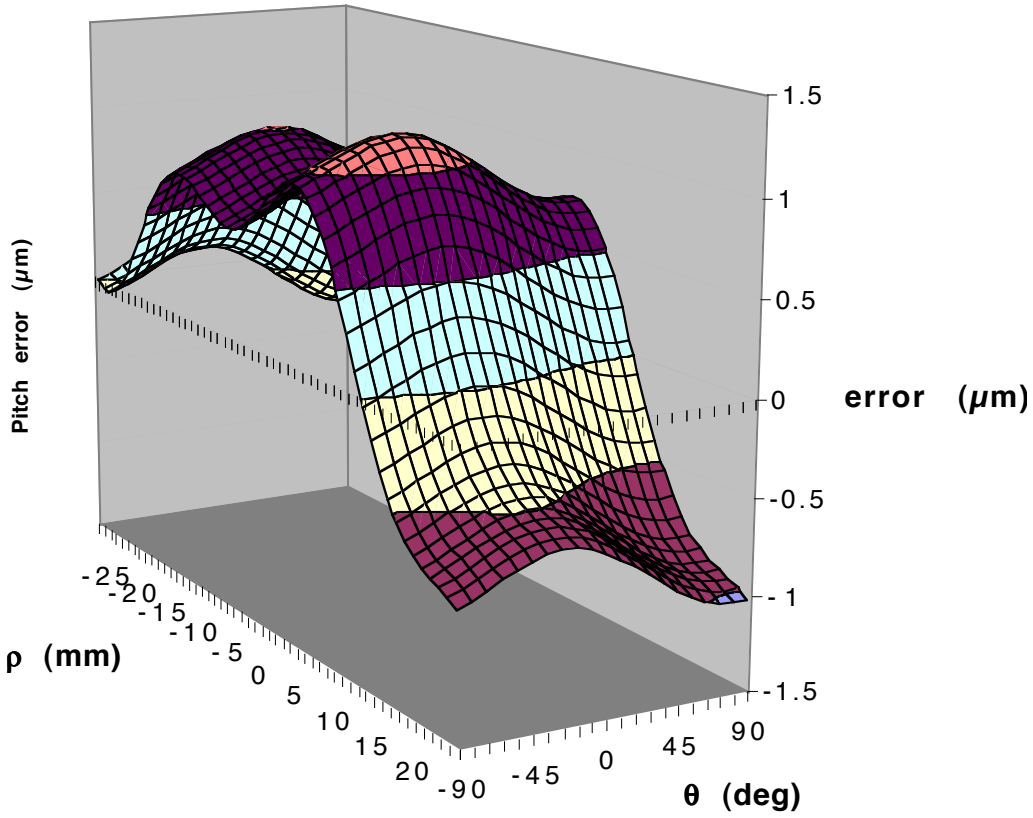

Figure 2. Total Radial Error. This error represents the error in the ρ-direction and is dominated by errors in the linear slide pitch.

directions. Figure 2 shows the total error in the ρ, or radial, direction. The τ or tangential direction and the z or vertical direction were also evaluated, but turned out to contribute substantially less to the total machine error. The graph shows the total error (sum of the errors from all of the sources that influence the position in that direction) as a function of rotary axis position from – 90˚ to + 90˚ and linear axis position from – 25 mm to + 25 mm. The P-P magnitude in the radial direction is approximately 2 μm.

From the geometric error evaluation, it is clear that the errors in the radial direction are excessive. This is, however, less of a problem than it seems since this is a direction of motion and the *R*-axis can be moved to compensate for these errors. All that is required is an error map in the control system that will issue a correction value according to the *R*- and θ- position. Since the prime contributor to the radial direction is the pitch of the linear axis, this error is measured using an electronic level. The results of the pitch measurement are shown in Figure 4.

1.3 COMPENSATION AND CALIBRATION

1.3.1 R-AXIS PITCH

During the design phase of this project, all of the possible geometric errors were calculated from values specified by component manufacturers. The error that was predicted to have the greatest contribution was the pitch of the R-axis, Shown Schematically in Figure 3. Due to an offset of 120 mm from the axis centerline to the LVDT tip and a specified pitch angle of 15 μrad, the pitch could contribute an error as large as 1.8 μm to a measurement (see Figure 2). This error was larger than the target accuracy of 0.5 μm for the entire machine. It must be measured and compensated for in the machine controller.

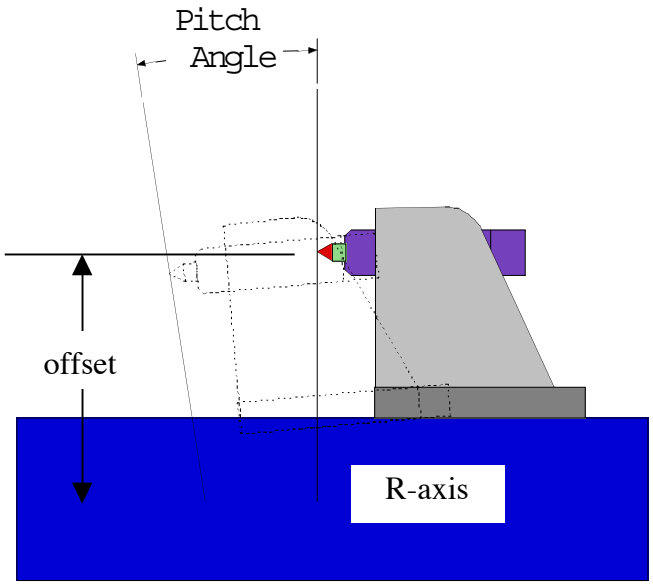

Figure 3 Pitch in the R-axis results in an error at the LVDT tip. The relatively large offset from the slide to the LVDT make this error significant even though the pitch angle is small.

The pitch of the R-axis was measured using an electronic level. The level was placed on the R-axis carriage in place of the LVDT Pedestal and moved through the range of travel of the axis. Since the shifting mass of the level and slideway can cause the air table to shift, data was also collected with the level resting on the machine base. By subtracting the data from the machine base from the data collected on the slideway, the pitch of the R-axis is obtained without shifting of the air table.

Once the data was collected, the R-axis pitch error was plotted as a function of R-axis position shown in Figure 4. The magnitude of the error across the entire travel of the slide is close to 1 μm. This is significantly less than expected from the manufacturers' specificaitons. Because most measurements will use only a small portion of the axis travel, the R-axis pitch error will be less than 0.5 μm. However, the plan is to immune this error in the controller. Compensation will be relatively simple since it is only dependent on R-axis position.

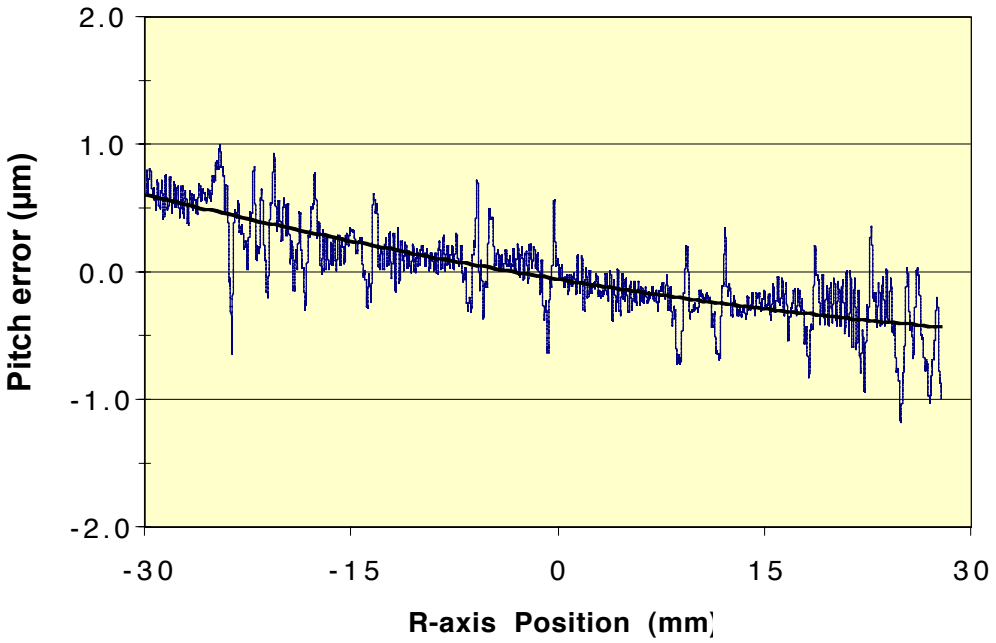

Figure 4 Pitch measurement results over the entire travel of the R-axis of *Polaris*. The pitch error at the probe tip is approximately 1 μm.

1.3.2 LVDT Tip

Probe tips on *Polaris* are interchangeable, though every probe change requires realignment. It is therefore desirable to have a probe tip that can be used for resolving small features as well as measuring form error. To resolve features as small as 1μm, the tip radius must be small in the measurement plane. Out-of plane, however, the radius can be much larger to reduce contact

stresses. A cylindrical contact diamond stylus was therefore chosen as shown in Figure 5. The width is 10 μm and the edge radius is 0.8 μm.

Figure 5 SEM micrograph of the probe tip used on *Polaris*. The view is essentially from the vantage point of a part being probed. The 10 μm long cylindrical contact is oriented vertically in the machine.

1.3.3 LVDT Load

The LVDT probing force can be adjusted in two ways. For coarse adjustments to the probing force, a setscrew at the rear of the LVDT housing is rotated. Fine adjustments are made by adjusting the air pressure to the probe with a precision air regulator. As shown in Figure 6, to measure the force, a flexure of known stiffness is placed into contact with the probe tip after it is adjusted to zero load. As the air pressure is increased, the flexure deflection is measured by the LVDT. Increasing air pressure increases deflection and therefore the probing force proportional to the spring constant of the flexure. This allows the probing force to be adjusted to 0.1 mN (10 mg).

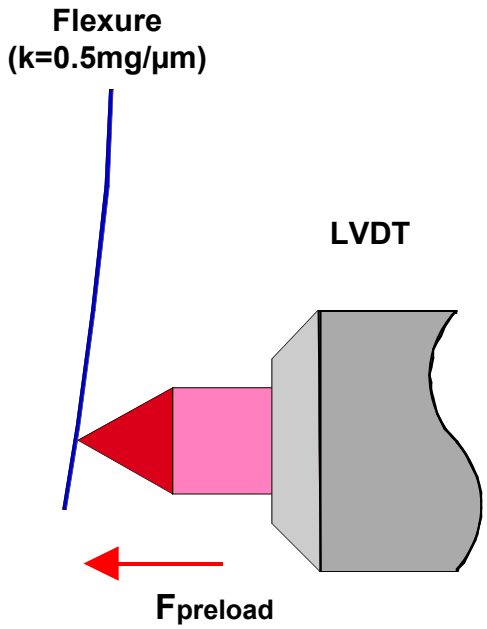

Figure 6 Schematic setup of probe force measurement.

1.3.4 Machine Origin Alignment

Be fore any measurements are made, the origin of the machine's measurement axes (R and θ) must be aligned with the LVDT. The primary criterion for this alignment is that the LVDT output be zero at $\rho = 0$ for all positions of θ. This means that for a probe tip with a radius of r, the LVDT should have a constant output of –r for all positions of θ if the center of the tip is positioned with its center at $\rho = 0$. One means of

achieving this is by placing a flat plate at –r as shown in Figure 7. If the probe is truly centered, the LVDT output will not change as the rotary axis is traversed from –45° to 45°. If, however, there is an offset in either the ρ or τ- directions, the probe output will change in a characteristic way for each direction [1].

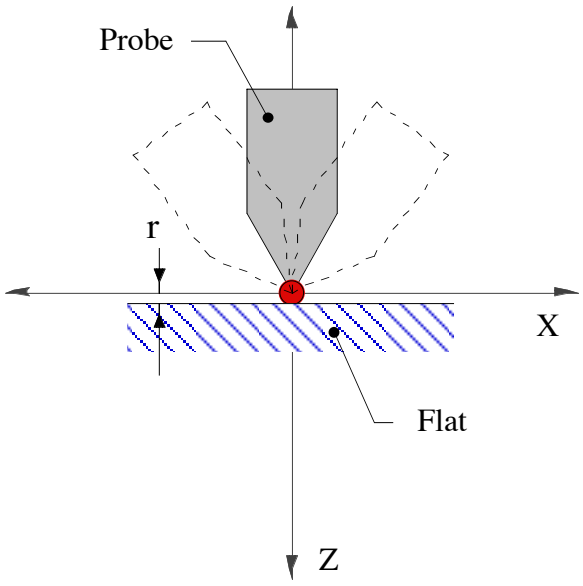

Figure 7. When the probe tip's center is aligned with the machine origin, rotation of the θ-axis will produce no appreciable deflection of the probe.

For an offset of ρ_0 in the ρ-direction, the output of the LVDT will change as a function of the rotary axis position θ:

$$\rho = \rho_0\left(\frac{1}{\cos\theta} - 1\right). \qquad (2)$$

When an origin measurement is made and the ρ-offset is measured, the R-axis zero can be reset to eliminate the offset. In addition to ρ-offsets, there can be an offset in the τ-direction. This offset produces a different response when measured using the flat method. The response of the LVDT is a function of θ that can be written:

$$\rho = \tau_0(\tan\theta). \qquad (3)$$

Once again, this characteristic output can be used to detect and correct the offset – this time in the τ-direction. Since there are no axes of motion in this direction, the linear ® slide will have to be moved slightly to eliminate the offset.

In the actual alignment procedure, the situation will be slightly more complex. A combination of offsets will produce an output of the LVDT according to the sum of Equations (1) and (2)

$$\rho = \rho_0\left(\frac{1}{\cos\theta} - 1\right) + \tau_0(\tan\theta). \qquad (4)$$

Due to the potential range and complexity of the outputs as a function of θ, the data will either have to undergo a curve fit calculation in a plotting package or a set of several measurement iterations will have to be used to minimize the overall error. While the latter technique of measuring, adjusting, then measuring again to see if the error became smaller may not be as elegant as a computerized curve fit, similar operations such as tool centering in single point diamond turning have shown themselves to be more than adequate.

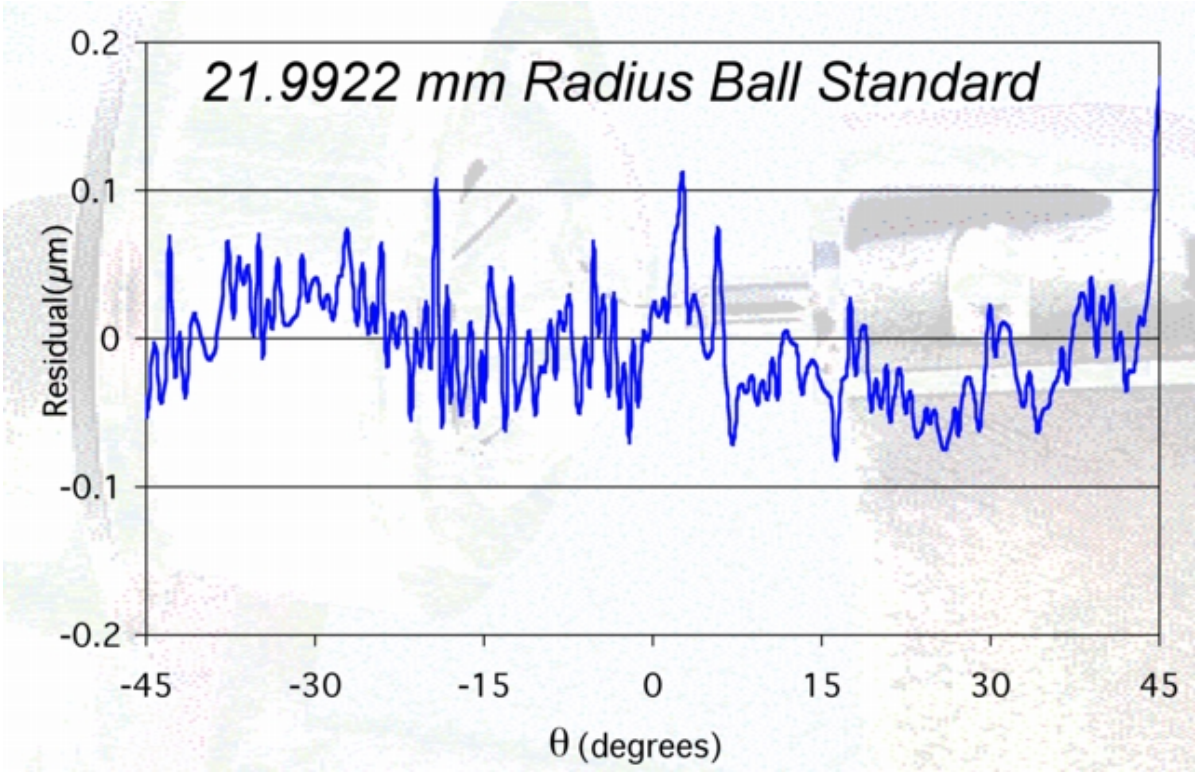

Figure 8. Measurement results obtained from a 21.99220 mm radius calibration sphere. The error indicated is the deviation from the specified radius.

1.3.5 CALIBRATION

Polaris was calibrated using a spherical calibration standard supplied with the PEC's Form Talysurf profilometer. The radius of this spherical standard is specified to be 21.99220 ±25 nm. With the probe centered [1] and the part crowned, the R-axis was moved to +21.99220 mm. At constant R, θ is scanned across the surface of the part while data was collected on all axes. The collected data was combined and a circle fit to the data. The resulting residual plot shown in Figure 8 reveals the shape error. The measurement accuracy over the 90 degree measurement range is ±100nm, well within the specified accuracy of 500 nm.

1.4 MEASUREMENT

Polaris was intended not to measure only spherical surfaces. To test the performance of the system for both form accuracy and the ability to measure small features, a test part was single point diamond turned and measured using the PEC's Zygo GPI XP interferometer, the Center's Form Talysurf profilometer and Polaris. The 12.5 mm copper test part is a spherical surface of nominal 13.3 mm radius superimposed with a binary fresnel zone structure of 314 nm step height. The aperture was limited to F/1.1 since this was the largest reference sphere available on

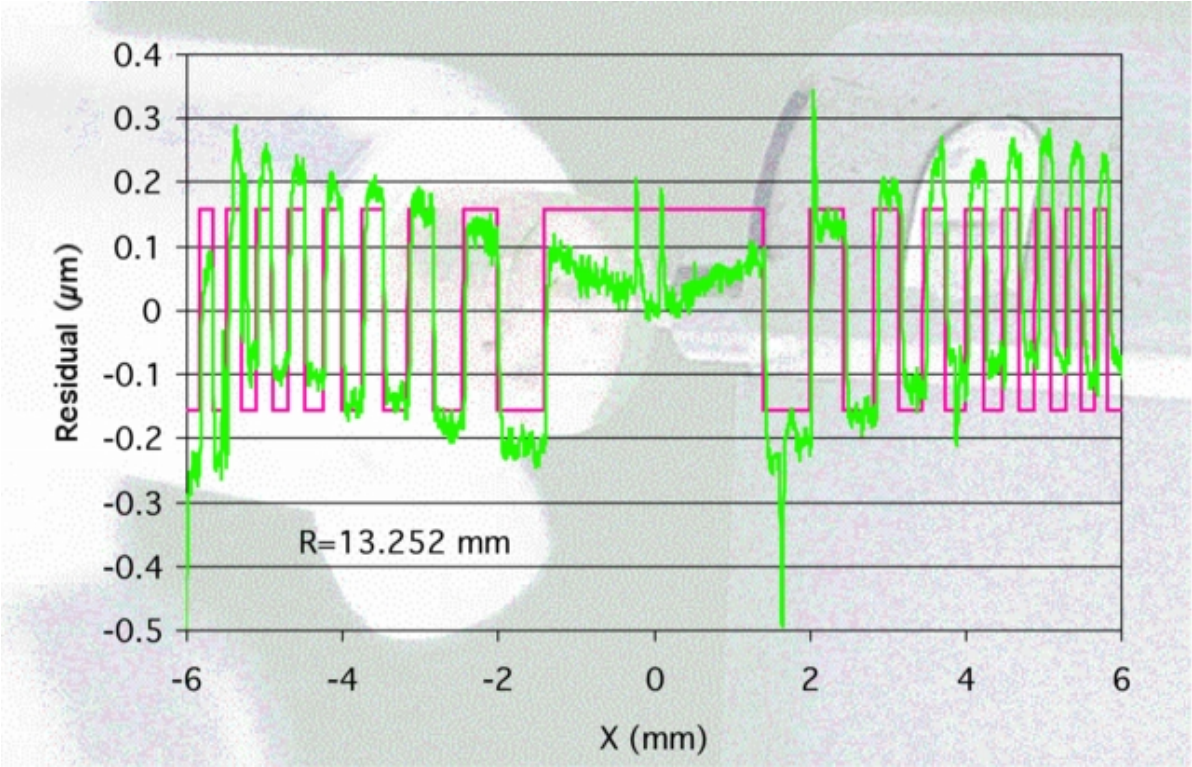

Figure 9. Measurement results showing *Polaris* measurement of binary part. The plot shows the residual data with a radius of 13.252 mm removed superimposed on the ideal profile.

the interferometer. The interferometer was unable to resolve the steps due to the step height ambiguity of one fringe. The interferometer did, however reveal a tool centering error with a magnitude of 200 nm. The interferometer could not be used to accurately measure the absolute radius on the part. The Profilometer measurement of the part showed the absolute radius of the part to be 13.248 mm, 48 μm larger than expected. It also showed the binary features that the interferometer could not resolve. The data agrees with the interferometer on the tool centering error. Polaris showed the absolute radius of the part to be 13.252 mm greater than expected, a fact confirmed by conventional profilometer measurements to within the profilometer's specified radius measurement accuracy. As shown in Figure 9 ,the measured data is closely correlated to the ideal part with a 13.252 mm radius is shown in pink. Polaris also clearly showed the binary zones, their locations and the 200 nm tool centering error. Furthermore, Polaris is capable of this over an angular range of up to 180 degrees.

1.5 CONTROLLER IMPLEMENTATION

The *Polaris* controls consists of a Delta Tau motion controller, hardware emergency stop relay circuitry, a handwheel jog box, a host PC and the firmware and software running on the motion control DSP and the host PC [2].

The Delta Tau UMAC consists of a 3U backplane, an 80 MHz Motorola 56303 DSP card and option cards for a wide variety of I/O interfaces. A single processor system is capable of controlling up to 32 axes with the appropriate option cards. The configuration chosen for *Polaris* includes the Turbo PMAC2-3U CPU card with an additional 512K x 24 data memory buffer. Option cards support up to 4 commutated analog servo axes and 4 pulse-direction stepper motor axes. Home, overtravel, enable and error outputs for all axes are included as well as a handwheel jogger interface. Additional opto-isolated digital I/O (24 bits in, 24 bits out) is available for ancillary logic interfacing (e.g., the emergency stop circuit). A 4 channel 16-bit analog-to-digital converter card was purchased for data acquisition. The LVDT signal will be interfaced to one channel and the others are open, but may be used for machine calibration and geometric error analysis. Communication to the host PC is via a USB communications adapter card. The optional data memory buffer is large enough to contain an entire surface measurement. The standard 128K program memory buffer is also large enough for any anticipated reference surface specification. This greatly simplifies the programming task by eliminating the need for real-time communication between the host PC and the UMAC while a measurement run is active. Periodic update of the axes positions are made via the USB connection; however the response of the host PC is not critical to the successful completion of a measurement. Acquired data is transferred from the UMAC data buffer to the host after the measurement motion program has finished execution.

The host PC is an IBM NetVista (866 MHz PIII) with 128MB RAM, a 20 GB hard drive, a 250 MB ZIP drive and a 19" Triniton monitor. It has no special requirements for interface to the UMAC other than an OHCI compliant USB port and the Windows 2000 Professional operating system. The OHCI (Open Host Controller Interface) is supported by all USB control chipsets except those manufactured by Intel and VIA. Windows 2000 is needed for compatibility of the USB device drivers with the Delta Tau PComm32 software library.

All of the machine hardware is interfaced to the UMAC controller. PLCs monitor the status of the axis overtravel limits, emergency stop status, axis home status and the incremental handwheel jogger. Closed loop control of the R and θ axes is provided by the UMAC's enhanced PID servo firmware. The R axis has a closed loop bandwidth of 50 Hz and and the θ axis has a bandwidth of 25 Hz. Both axes track a desired motion path with less than 10 counts of following error at a reasonable velocity (up to 2°/sec). This allows measurement of a typical part in a few minutes.

1.6 OPERATOR INTERFACE

The user interface software is graphically oriented using the customary metaphors for user control: floating windows, mouse, buttons, both pull-down and pop-up menus, scroll bars, etc.

Although data analysis is not the focus of this project, a 2D plot of both the raw measurement data and a surface error plot over a user determined range with cursors, pan and zoom controls, least squares line fit, slope removal and circular radius fit and are provided. Measurement data files are stored in a simple, tabular text format for easy import into other software packages for further analysis. The operator interface was programmed in C/C++ using the Borland C++ Builder visual development tools. A library containing plotting and instrumentation visual components was purchased from IOComp to aid in developing the data analysis functions.

During testing, it was found that the operator interaction required to successfully measure a part was time consuming. The bulk of this was for probe setup and alignment as well as part alignment (i.e., crowning). The user interface software was designed with the automation of these tasks as a principle objective. Of course, the primary objective is the acquisition of part profile data. The interface software is composed of four windows titled: *User Interface*, *Part Description*, *Measurement Data Analysis* and *Preferences*. Each of these is discussed below.

1.6.1 *User Interface* Window

The *User Interface* window is shown in Figure 10. It is divided into three vertical sections: machine status, measurement and tracking. The tracking section on the left contains a live plot of the probe tip position. During measurement the plot contains a part profile based on the part

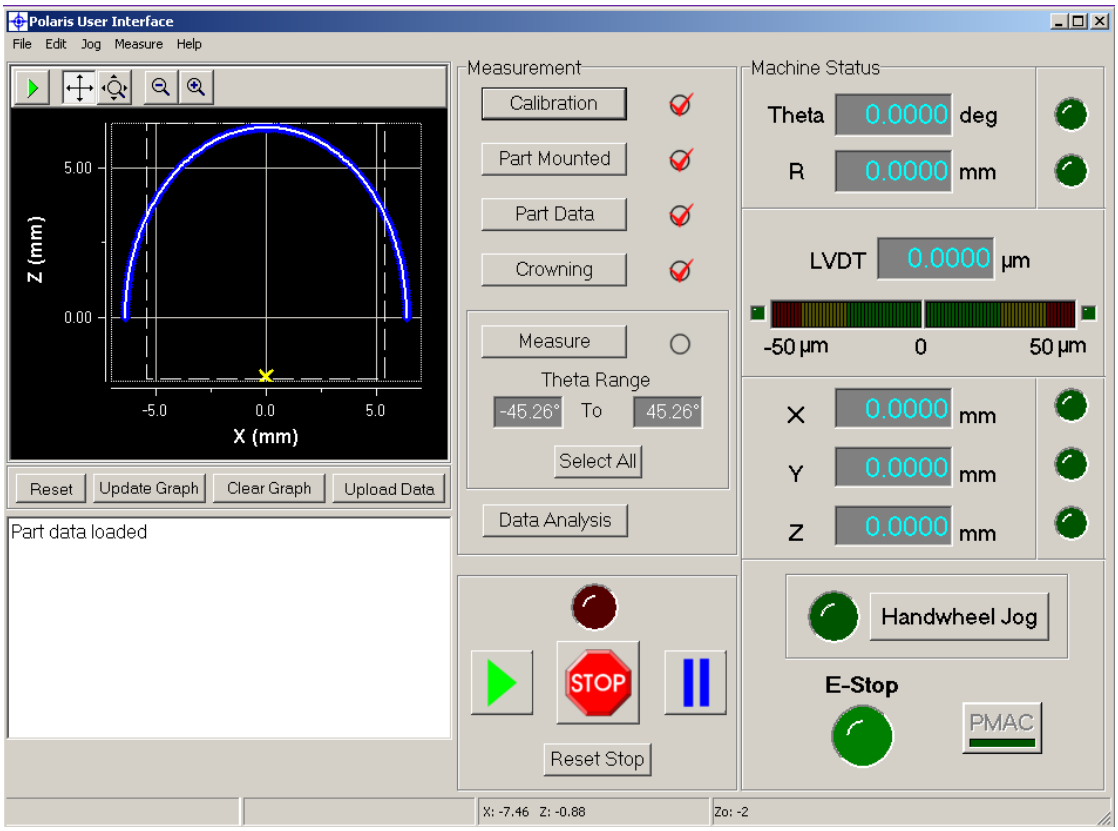

Figure 10. The main *User Interface* window.

geometry as defined by the input part description. When preparing to measure a part, the angular range of measurement can be graphically selected with the mouse from this plot. The lower left panel of the tracking section is reserved for status message display during all phases of machine setup, calibration and part measurement. It is also possible to enable the direct entry of UMAC keyboard commands in this panel. This feature is particularly useful for debugging, but for safety reasons is disabled by default and must be enabled in the *Preferences* window.

Machine Status The machine status section of the window contains real-time updates of all six axis positions including a multi-colored, variable scale slider bar for the LVDT. The slider scale labels change to correspond to the measurement range selected by the operator on the LVDT electronics enclosure. Indicator LEDs for each axis change color as the axis is selected with the handwheel jog box (green), moved into overtravel (red), or is both selected and in overtravel (yellow). An overtravel of the LVDT in the positive direction (i.e., the probe is too far in) is a fatal error when executing a motion program and halts further jogging of the rotary table (either direction), R axis (negative direction) or Z axis (negative direction) until the overtravel is cleared. Negative LVDT overtravel (i.e., the probe is too far out) is a normal condition during part setup and is not fatal during measurement. However, each acquired data point includes a tag field which indicates the selected range and overtravel status of the LVDT. Thus it is possible, although not recommended, to change the LVDT range during a measurement. On the lower right of the machine status section is a button that activates and deactivates the manual handwheel jogger and an indicator for the status of the hardware emergency stop.

Measurement The central section of the *User Interface* window provides buttons that initiate each step of the calibration, part description, crowing and measurement procedures leading to acquisition of profile data. There are also buttons that terminate any axis motion (STOP), pause a measurement (blue vertical bars), resume a paused measurement (green arrow) and acknowledge a stop condition (reset stop). All functions available as buttons in the main user interface window may also be executed from the main pull-down menus.

The measurement process consists of a number of sequential steps, not all of which must be completed for every part. Sub-steps are selected from a right-mouse button pop-up menu associated with each screen button or the main menus. The *calibration* button initiates the axis homing sequence and the calibration procedures that determine the R, τ and θ offsets. Homing only needs to be performed once after each controller power-up. The calibration steps must be performed if the probe tip is changed or disturbed or the machine is environmentally disturbed (e.g., an A/C outage). It is recommended that calibration be performed on a weekly basis or whenever the results of a measurement are suspect. Temporal steps may be skipped by selecting an appropriate action from the pop-up menus. The *part mounted* button acknowledges to the controller that a part has been placed on the 3 axis positioner for measurement and enables further operations. The *crowning* button initiates an automatic procedure that finds the apex of

the part with respect to the LVDT probe by moving the X and Y axes of the part positioner and recording LVDT deflections. This process is automated for both concave and convex parts and requires only that the operator jog the probe in close proximity to the part (a few millimeters).

The *measurement* button initiates the actual measurement of a part. Based on the part description file a motion program is generated, downloaded to the UMAC and executed. The acquired data is automatically uploaded back to the host PC for analysis. Prior to starting a measurement, the operator must define a range of θ axis motion over which the measurement is to be made. This can be done in three ways: by clicking the *select all* button, typing angles into the *from* and *to* boxes, or using the mouse to graphically select the range from the tracking preview plot. The *part data* button brings the *Part Description* window to the foreground and the data analysis button activates the *Measurement Data Analysis* window. They are described below.

1.6.2 *PART DESCRIPTION* WINDOW

The *Part Description* window is show in Figure 11. The path to be followed by the *Polaris* R and θ axes is specified using a subset of the G-codes in rectangular coordinates. Reflection about the X=0 line is automatic so that an existing lathe code file may be used without editing. The restricted set of commands recognized by the G-code interpreter is: G01, G02, G03, X, Z

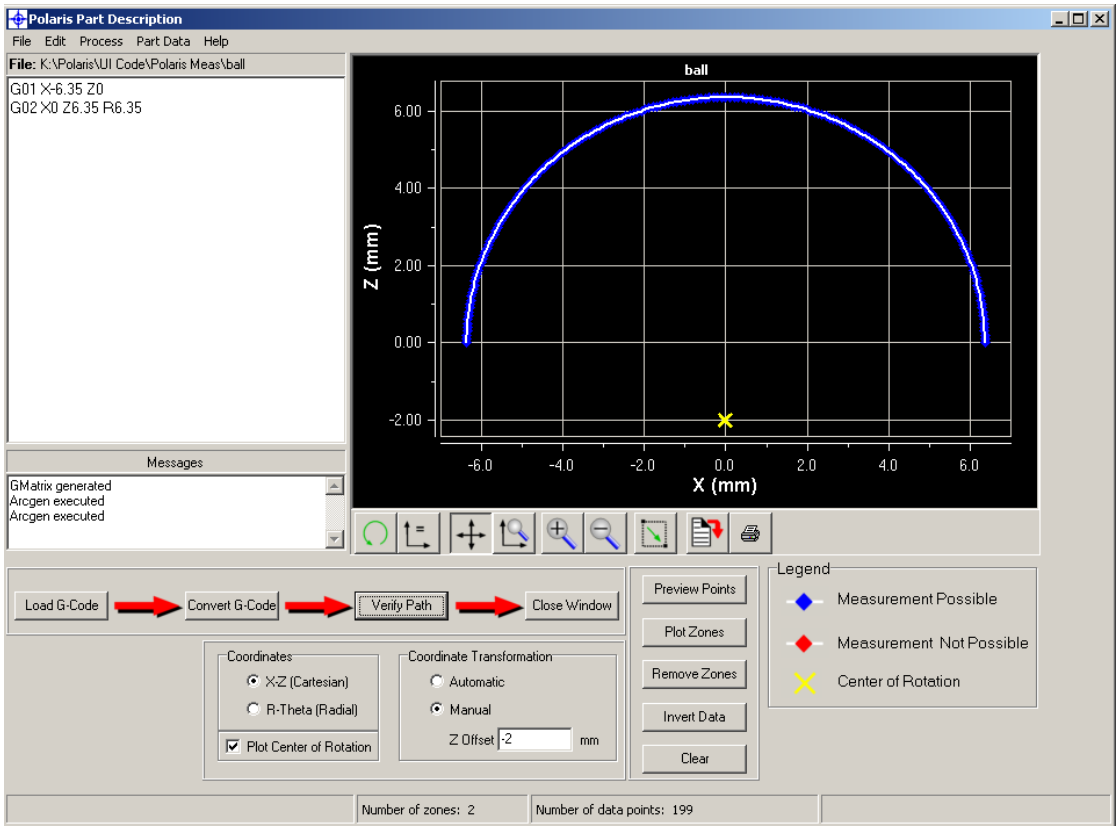

Figure 11. The *Part Description* window.

and R. Other codes are ignored. The interpreter converts the toolpath described by the G-code file into a polar motion program for the UMAC controller. The origin of the XZ part coordinate system may be offset from that of *Polaris* by the user by specifying the Z coordinate of the center of rotation of the θ axis. The software attempts to verify the polar motion path with respect to the angular window of the probe tip and highlights the un-measurable data points in red on the preview plot. Data points in the motion path may also be displayed in a tabular format by selecting the *preview points* button. The plot may optionally contain vertical lines indicating the boundaries between zones (i.e., G-codes) in the input file.

1.6.3 *MEASUREMENT DATA ANALYSIS* WINDOW

The *Measurement Data Analysis* window shown in Figure 12 contains a plot of any user selected region of an acquired data set. It is also possible to plot a previously acquired data set on the same graph for comparison. Two analysis features are provided: least squares line fit and circular arc fit. For both, a residual plot with its own vertical scale is available. The curve fits can be over any number of disjoint or adjacent regions of selected data values. For the linear fit, the plot may be redrawn with the slope removed (i.e., the data set is "leveled"). The circular fit reports the origin and radius of circular curvature of the best-fit arc through the selected data. The data may be viewed and saved in a tabular format. All plots may be printed or copied into

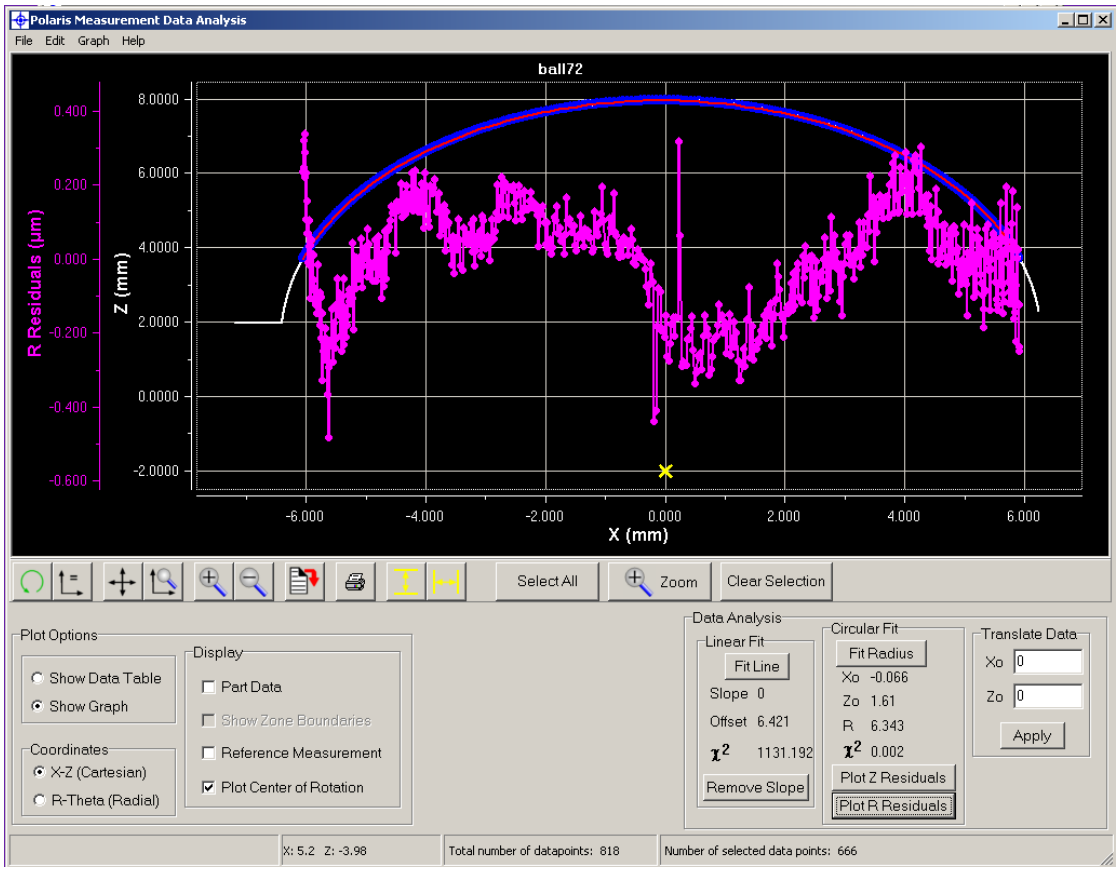

Figure 12. The *Measurement Data Analysis* window.

the clipboard.

1.6.4 *PREFERENCES* WINDOW

The Preferences window contains measurement options, machine calibration values and machine constants needed for proper operation and analysis. The associated data values are saved on the host PC hard drive. The two tabbed panels of this window are shown in Figures 10a and 10b. The probe radius and angle, measurement speed and data gathering period (which defines the amount of data collected) are specified here by the user.

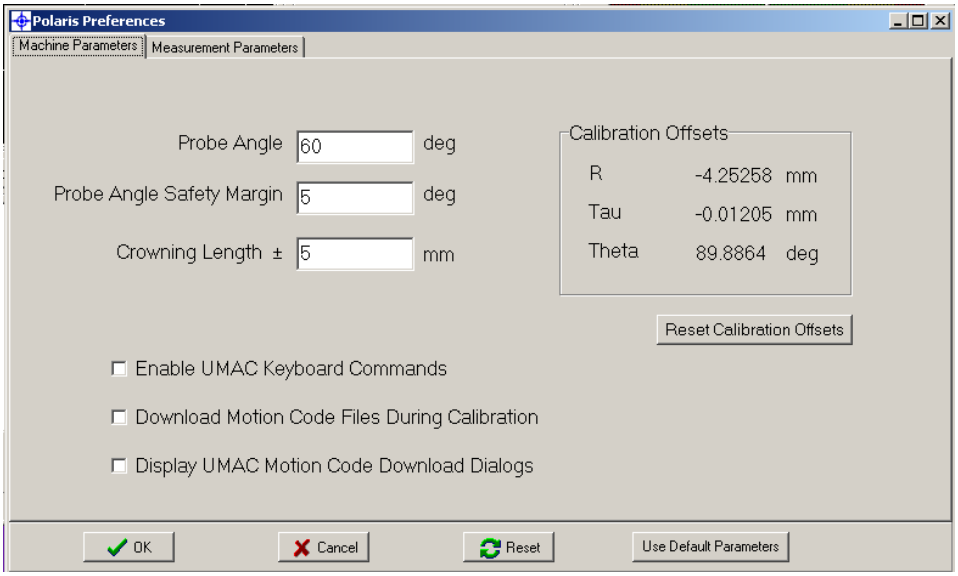

Figure 13. The *Preferences* window – machine parameters.

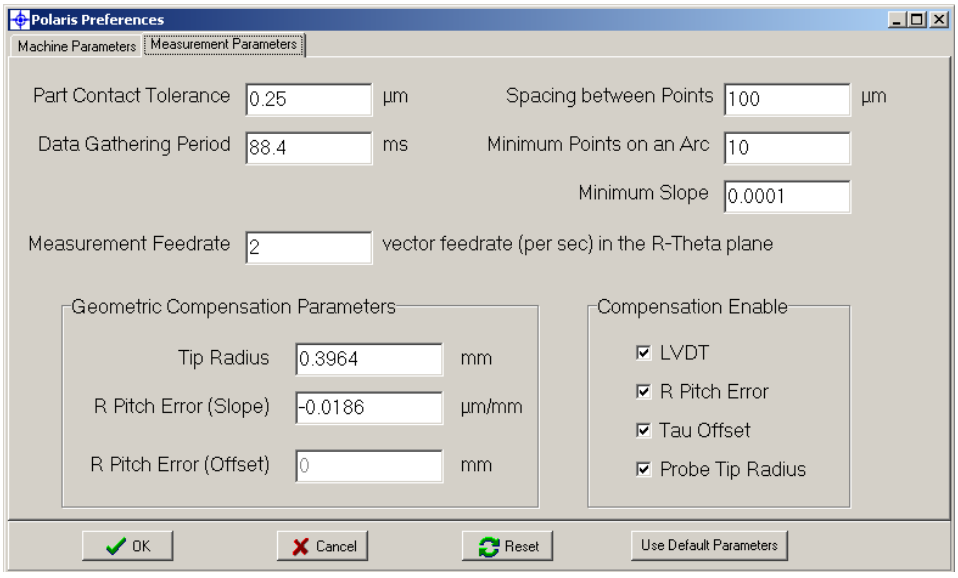

Figure 14. The *Preferences* window – measurement parameters.

1.7 CONCLUSION

This project has culminated in the design and construction of a rotary profilometer that far outperforms the initial specifications. The 20 nm resolution, limited only by the R-axis encoder is better than the design spec by a factor of 5. The 100 nm accuracy is better also by a factor of 5. Furthermore, *Polaris's* completion illustrates the feasibility of a design that can be scaled to meet a large array of aspheric large-aperture measurement needs. Future versions of *Polaris* would include a spherical version with another rotary axis to allow full 3-D surface scanning and versions with increased range and other sensors. Polaris is only the beginning of a new generation of metrology instruments.

REFERENCES

1. Sohn, Alex and Ken Garrard, "Design of the Polar Profilometer *POLARIS*," Precision Engineering Center Annual Report, Vol XVIII, pp 57-67, 2001.
2. Garrard, Ken and Alex Sohn, " *POLARIS* Control and Data Acquisition" Precision Engineering Center Annual Report, Vol XVIII, pp 69-82, 2001.

2 LAPPING PLATE CHARGING

David A. Kametz
Graduate Student
Thomas A. Dow
Professor
Department of Mechanical and Aerospace Engineering
Ronald O. Scattergood
Professor
Department of Materials Science & Engineering

Lapping the air-bearing surface is one of the last steps in the production of hard disk heads. This surface is about 1 mm square and must have a surface finish less than 1 nm and be flat to the order of 10 nm. The head material is a tough ceramic (AlTiC) and the lapping is accomplished with diamonds impregnated into a tin lap surface. The goal of this research is to optimize the preparation of the lap surface to best accomplish the task of lapping the head. Currently, offsetting a loaded rotating steel ring with coarse plated abrasive against the rotating plate creates the textured surface of the lap plate. The resulting pattern of random circular overlapping grooves causes problems with the consistency of the lapping material removal rate. Research has suggested creating a more deterministic and consistent pattern by cutting a continuous spiral groove with a diamond turning machine. The charging of the plate is currently done using a ceramic ring, which is also offset and loaded against the textured plate and rotated. Directional motion, low pressure and relatively large size of the lapping ring cause problems with abrasive waste, large charging time (2+ hours) and poor charging quality. Current research focuses on the use of a roller to impregnate the diamond into the tin surface. Aspects such as smaller contact area, higher contact pressures and freedom to pivot about 3 axes aim to increase charging efficiency by shortening charging time, increasing charging quality and decreasing the amount of abrasive used. A third aspect of the research is the development of methods and equipment to test the lapping performance of the plates during the charging process. No process is currently used and the lapping quality of the plates is often unknown until after it leaves the production area.

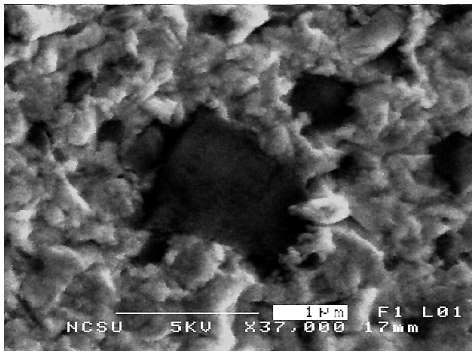

2.1 INTRODUCTION

As the final step in the creation of a hard disk head, the flying surfaces are lapped on a diamond charged tin lap surface. This process gives the head the required geometry and also produces the desired surface finish. The previous process used to create the surface features starts with a newly machined tin lap plate. For examination purposes, the lapping plate contained 28 removable 25 mm diameter plugs in 4 radial positions. This plate is placed in a lapping machine and a steel ring with coarse plated abrasive is loaded against it. The tin and the texturing ring are brought into contact to create a series of circular overlapping grooves. This process leaves a random pattern of grooves and lands over the surface of the plate.

The new process being developed for creating the textured surface uses a diamond turning machine to create a single continuous spiral groove. The pattern can be produced rapidly and the geometry of the features, that is the depth, width and spacing of the grooves, can be changed easily. The grooves also create a uniform geometry over the entire plate, thus making the behavior more consistent. However along with the benefits, this technique brought with it some challenges. One was the deformation of the soft tin surface as the grooves were cut. Depending on the tool geometry, the diamond tool tended to push some of the material out of the groove (rather than cutting it) and as a result, the land surface between grooves was not flat but rather had raised edges. This effect and some ways to avoid it are discussed in this section.

The process of fabricating a lapping plate is being investigated for improvements in speed and head quality. One aspect for improvement is the preparation time of the lap. The time needed to fabricate a plate can sometimes be 2 hours or more. Another improvement being investigated is the reduction the quantity of diamond needed in the charging process. Only a small percentage of the actual diamond in the slurry ends up embedded into the tin plate. A third area concentrates on the predictability of the performance of the lapping plate after fabrication. It is rarely known how the plate will perform before leaving the fabrication area. Understanding the important characteristics in the fabrication of the lapping plate can help determine which steps need improvement for a better end product.

2.2 GROOVE GEOMETRY

A model of the fluid flow [1,2] in the grooves during lapping showed the key parameters to be: 1) depth of groove, 2) width of groove, 3) geometry of groove and 4) width of flat land between grooves. To study the groove geometry produced by different tool shapes, a round nosed cutting tool and a dead sharp cutting tool were each used to groove a plate. A difference in the characteristics of the plate was observed after the use of the two tools, as described next.

2.2.1 DEAD SHARP TOOL

A dead sharp tool and a round nosed tool were used for comparison in creating the grooves in the plate. The dead sharp tool has 2 flat sides 60° apart that meet at a sharp tip (dashed line in Figure 1). The round nosed tool has a 40 µm radius tip with a 60° window (solid line in Figure 1). Due to the difference in tool geometry, a common feature of the groove had to be set. The groove width was selected and set to 50 µm for both tools with no lands. One way to create the grooves is to set the spacing with no lands between them and then do a facing cut to cut off the peaks and create the land. This has the added benefit of guaranteeing a flat land surface. Thus, to see how the tin behaves at the interim stage of this grooving procedure, it was decided to use no lands. This set the depth of the dead sharp tool to 43.3 µm and the round nosed tool to 7.8 µm.

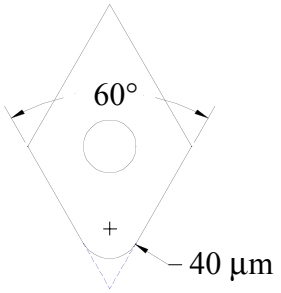

Figure 1: Tool Geometry

Grooving the plate with the dead sharp tool produced an unexpected result; a macroscopic granular appearance was plainly visible to the naked eye. The "grains" had a diameter varying from 0.5 mm to 5.0 mm as shown in the photograph in Figure 2. These features were not apparent when the surface was turned with the round nose tool.

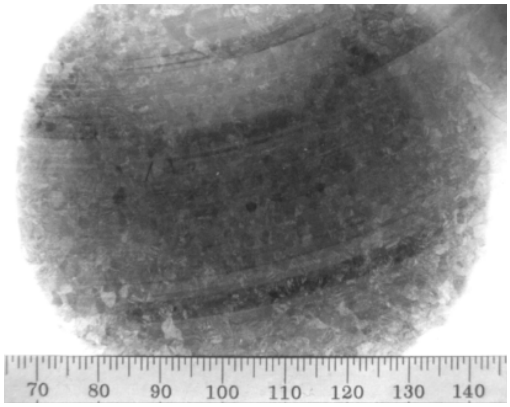

Figure 2: Tin plate surface grooved with dead sharp tool

The appearance of these "grains" caused much speculation as to their origin as well as their effect on the charging and lapping process. Are they really grains? Should they be that big? Why are they visible when the plate is grooved? Why are they only visible when the dead sharp tool is used? To understand the origin of these granular features, SEM micrographs of the individual grains were studied to see why the features were visible. Figure 3 illustrates the edge of one grain and explains why the grain definition exists; and the answer is, the cutting process is different from grain to grain. In the grain on the left, the peaks of the grooves are sharp: on the

right, the peaks have large burrs attached that shade the bottom of the grooves and modify their appearance.

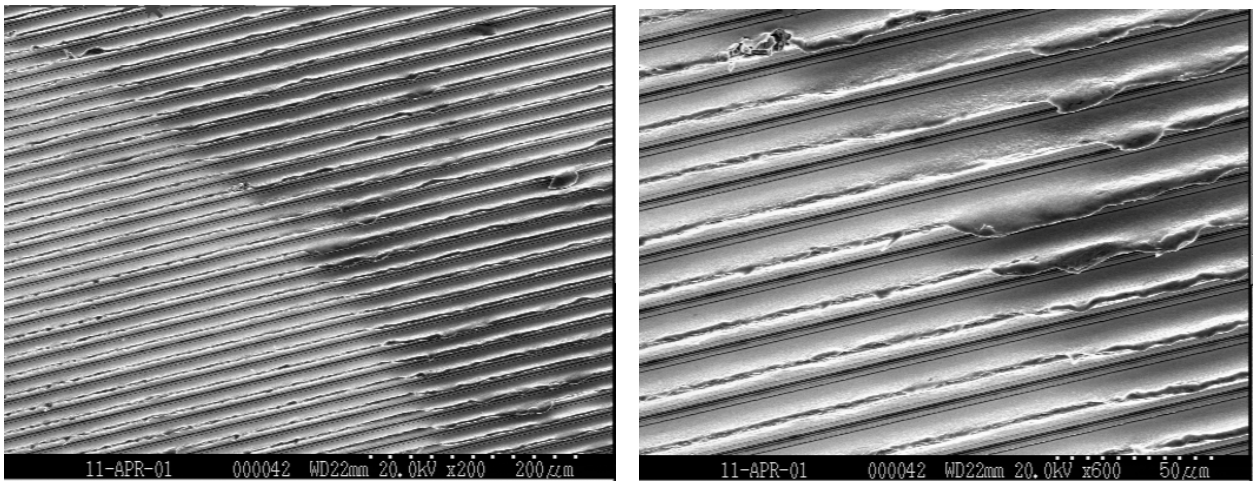

a) Boundary at 200x b) Boundary at 600x

Figure 3: SEM pictures of tin surface features after grooving with dead sharp tool

Metallographic analysis of the rolled tin indicates that the material does, in fact, have large grains on the order of 1-2 mm. In metal grains, there can be a difference in the plastic strain response depending on the orientation of the individual grain. Such a variation could make each grain respond differently to the cutting forces and thereby produce the features seen in Figure 3. The fact that this variation is so pronounced in tin depends on several factors. Tin is a low melting temperature material and the homologous temperature, T/T_{mp}, is 0.59 at room temperature. Consequently, tin will undergo "hot deformation" at room temperature and will be quite soft and ductile. This will enhance burr formation.

In addition, tin is rather unique because it has a tetragonal crystal structure as opposed to the cubic crystal structures of the common metals used for precision machining. It is necessary to have five or more independent slip systems available for unconstrained plastic deformation in a crystal grain. In general, tetragonal crystal structures have significantly fewer slip systems available than do the cubic crystal structures. Although the details are complicated by the fact that the formation of burrs in machining is multi-axial, shearing-fracture process, one can expect that in tin there will be grain orientations where the plastic straining process is constrained by a lack of independent slip systems. This will lead to anisotropy in the burr formation process depending on grain orientation. Slip system constraints are therefore considered to be a contributing factor for the results seen in Figures 2 and 3. In comparison, the burr-formation anisotropy is expected to be less for cubic metals such as copper or aluminum since these have a large number of equivalent slip systems available.

2.2.2 ROUND NOSE TOOL

The visible grainy appearance of the grooved plate was not present when the plate was machined with the round nose tool. Figure 3 shows a comparison the chip geometry for each tool. Two differences are clearly obvious from this figure: first, the depth of cut is much smaller for the round nose tool to produce the same groove width, and second, the round edge of the tool will not match with any edge of the tin crystal structure. The former means that less material must be removed, the forces are smaller and the plowing effect is reduced. The latter creates an averaging effect in a large majority of grains, each grain slipping and shearing roughly the same amount. The net effect is that the burr formation that dominates the appearance when using the dead sharp tool is not a major factor when using the round nosed tool.

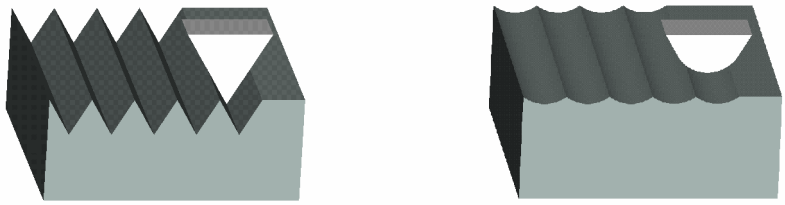

Figure 4. Comparison of the chips produced with dead sharp (left) and a round nosed tool (right)

Since the dead sharp tool exaggerated burr generation, it was decided a round nosed tool would be best for grooving. Another advantage of the round nosed tool is that the grooves can remain shallow and wide, whereas with the dead sharp tool, a deep groove is needed for an equivalent width (44 μm of the dead sharp tool vs. 10 μm with the round nosed tool). This additional depth is unnecessary since it was previously determined [1] that fluid flow effects are roughly equivalent at depths of 10μm or more.

2.2.3 LAND FLATNESS

While exaggerated burr formation is not a major problem when grooving with a round nose tool, the raised edges of the lands were still a problem. The procedure for grooving the plate was to face it with a large nose radius tool (0.5 mm) and then cut the grooves with the 40 μm nose radius tool. Based on the fluid flow model [1], the optimum land to groove ratio was 20-30%. The initial facing tool produced a flat mirror-like surface on the tin. When the round nose tool was used to groove the plate, the tool tended to push up some of the tin next to the groove making the land have raised edges. These edges are reported to affect the charging process, as the lands will not charge as long as these are present. One solution to ridding of these is to do a

shallow pass over the plate on the DTM after the grooving pass and cut the tops of the lands off. Another possibility is to yield the tin during charging by increasing the pressure.

2.3 CHARGING AND PLATE FLATNESS

The charging process used by IBM involves a thick-segmented alumina ring that rides on the surface of the tin lap. The ring has an OD of 175 mm (half that of the plate) and is about 25 mm wide. It is placed in contact with the plate, loaded with 15 kg and a fine diamond slurry dripped onto the plate. As the plate rotates about its center, the alumina ring also rotates and pushes the diamond into the tin surface. The interaction of the tin plate and the alumina ring creates flat plateaus with embedded diamond on the surface. Unfortunately this process can take more than an hour and it consumes a large quantity of diamond slurry compared to that embedded in the plate. It is estimated that less than 1% of the abrasive used in the process gets embedded into the tin plate. For a plate with features generated by the texturing ring, the contact area is on the order of 4% and the average contact pressure is nearly 60 psi. For the grooved plate, the contact area is over 20% and thus the pressure is much lower.

After using the ring to charge the grooved plate with diamond, it was noticed that some areas had a large concentration of diamond and some areas had few, if any diamond. This behavior seemed to be a function of the plate flatness in conjunction with the low charging pressure. To verify this hypothesis, measurements of the figure error of the plate were made at different steps of the fabrication and charging process as shown in Figure 5.

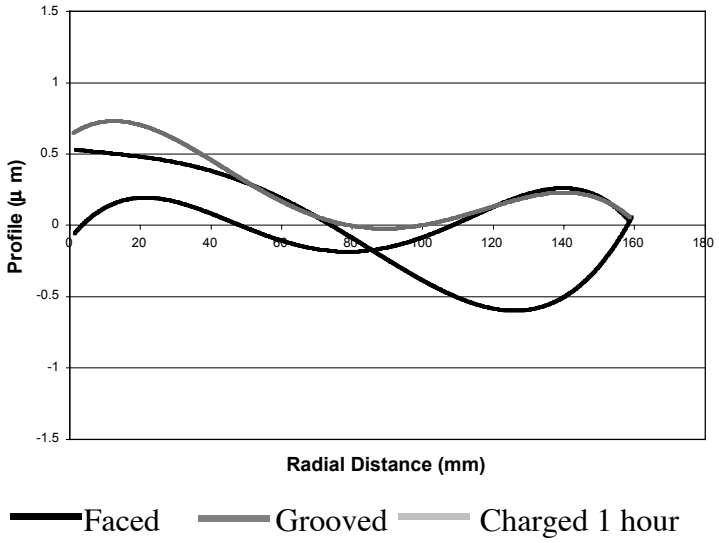

Figure 5. Polynomial fit lines of plate profile of different stages in fabrication

To measure the shape of the plate it was rotated on the diamond turning machine while a capacitance gage was slowly traversed from the outside edge to the center. This was done after each step of the process: facing, grooving and charging. The overall profile of the plate changed throughout the fabrication process, but the peak-to-valley figure error remained the same (≈1 μm) as shown in Figure 5.

The figure error of the plate after grooving is the main focus since this will be the profile of the plate before the charging process begins. Referring to Figure 6, the plate was examined with the SEM at the peak of the profile (radial location of 125 mm), and at the valley of the profile (radial location of 83mm).

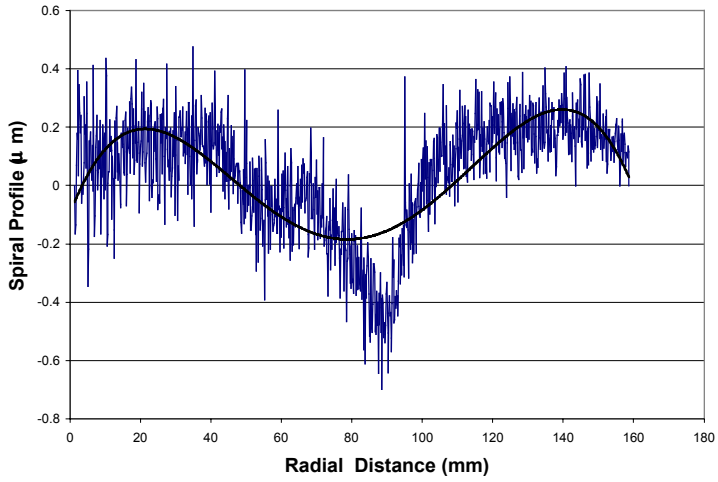

Figure 6. Profile of grooved plate before charging

The SEM examination showed that the area at the peak is fully charged, while the area in the valley shows very little charging. Figure 7 is a comparison of these two regions. This verifies that flatness is a key characteristic in the process of charging if the current charging process is used with the grooved plate. It should be noted that the peak to valley of the profile shown above is roughly 1 μm across 160 mm. While this is an excellent flatness over such a large region, problems still occurred during charging. The large size of the ring combined with the large contact area between the ring and plate produces low contact pressures and inefficient charging of the plate. While pressure can be easily increased, other charging techniques are needed.

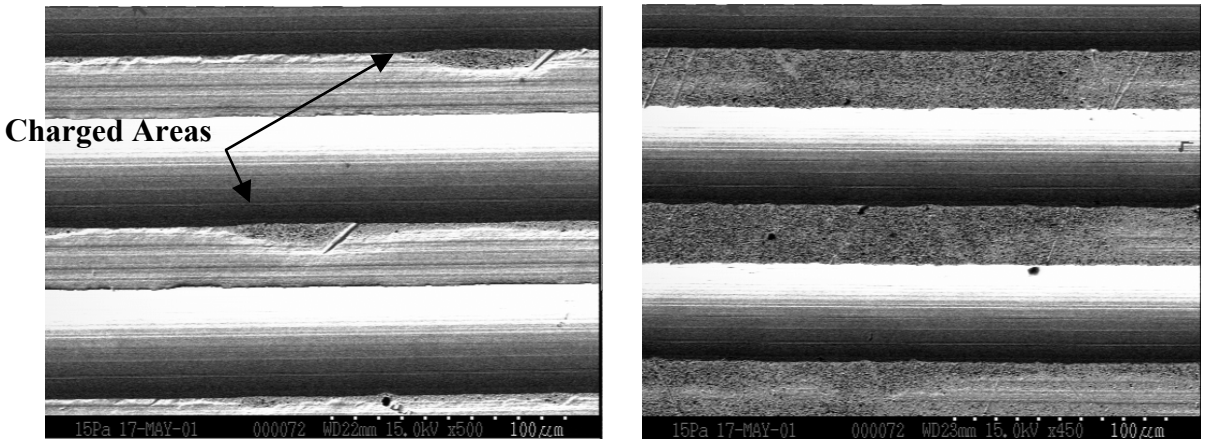

a) Radial Location 83 mm b) Radial Location 125 mm

Figure 7. SEM pictures of tin surface at specified radial locations

2.4 NEW CHARGING MECHANISM

Another way to improve the speed of charging and coverage of diamonds in the lap surface is to change the way the diamond is embedded into the tin. A new design incorporating a cylinder rolling on the plate surface has been constructed and is being studied. This technique is illustrated in Figure 8. A roller is pressed against the grooved tin plate and allowed to roll over the surface. Because the contact is between a cylinder and a flat plane, the pressure will be high, on the order of the yield stress of the tin. This should help to push down any features created at the edges of the grooves and assist in efficiently driving the diamonds into the tin surface.

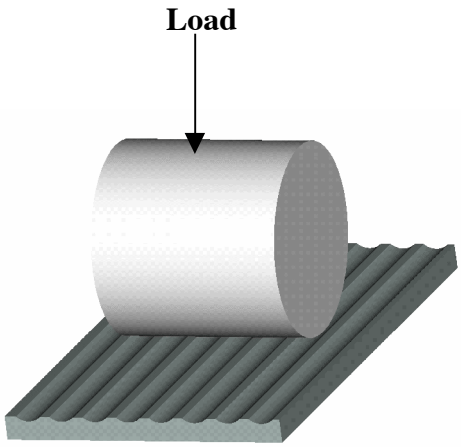

Figure 8. Sketch of the new charging technique using an alumina cylinder to roll the diamond grains into the grooved tin lap

The roller design is intended to solve a number of problems previously encountered.

1) Plate Contact: The rollers being used range from 50 mm (2 in) to 37.5 mm (1.5 in) in diameter and 50 mm to 25 mm in length. The roller is translated radially along the rotating plate until charging is complete using a slide driven by a stepper motor. The contact area is much smaller than the ring and the roller is allowed to pivot along all 3 axes, giving the ability to follow the profile of the plate.

2) Contact Pressure: The contact pressure between the roller and plate is designed to be slightly below the yield strength (35 MPa) of the tin. This makes the tin yield until full contact is formed. The vertical load was calculated using the equation for a cylinder on a flat [3].

$$\sigma = 0.798\sqrt{\frac{P}{K_D C_E}} \tag{1}$$

$$C_E = \frac{1-\nu_1}{E_1} + \frac{1-\nu_2}{E_2} \tag{2}$$

σ is the maximum allowable stress of the tin, P is the vertical load per unit length of the roller, K_D is the diameter of the cylinder, ν_1 is Poisson's ratio of the tin, E_1 is Young's modulus of the tin, ν_2 is Poisson's ratio of the roller material, and E_2 is Young's modulus of roller material. Knowing the length of the roller and the yield stress of the tin, the equations can be solved for P. Multiplying P by the length will give a yield load. It is important to note however, that since the flat is actually a grooved plate with roughly 25% contact area (75% grooves) the calculated load is multiplied by 0.25 to get the actual yield load.

3) Charging Effectiveness: Using a roller that follows the motion of the plate and a larger contact stress should embed more diamond per unit time. Since the previous process used an alumina ring that rotated on one side of the plate, the diamond slurry was forced off the side of the plate by the edge of the ring. This wasted a large amount of diamonds in the slurry since many that were not embedded on the first turn were simply pushed off the plate.

A vertical load of about 178 N (40 lbs) was used for the ring charging process, creating a pressure of 89,632 Pa (13 psi). This is a low pressure considering the yield strength of the tin is 35 MPa (5000 psi). The goal of the roller design is to shorten the charging time and reduce diamond waste. First, the motion of the roller is parallel to the motion of the plate; therefore many diamonds not embedded on the first cycle can be embedded a number of cycles after since the slurry will remain on the plate. Second, the higher pressure of the roller should embed a

higher concentration of diamonds per unit time. With these improvements the charging time of 1 hour currently used can be significantly shortened and diamond waste kept to a minimum.

2.5 ROLLER CHARGING EXPERIMENTS

Two different roller materials have been used in the testing of the new process. The first is an aluminum oxide (alumina, Al_2O_3) roller fabricated by CoorsTek. It is made of AD-998 cast alumina with a measured density of 3.23 $^{g}/_{cc}$. This roller is 50 mm in diameter and length. The second cylinder is made of silicon nitride (Si_3N_4). Keyocera manufactured this roller as a sample. This roller is 38.9 mm in diameter, 31 mm in length and has a density of 3.20 $^{g}/_{cc}$.

2.5.1 COORSTEK ALUMINA ROLLER

The first roller used in the testing process of the new charging mechanism was the 50 mm OD by 50 mm long cast alumina roller. This cylinder mounted onto a steel axle and ground to center with a carbide wheel. Initial tests for the roller were done keeping the roller at one radial position on the plate. This was done to understand how the plate charges with respect to exposure time to the roller. Also, since the plate is 175 mm from center to outside, 3 tests can be done on a single plate using a 50 mm wide roller. The calculated yield load of the tin using a 50 mm wide alumina roller is approximately 17.6 N.

The first test run was done for a total period of 1 hour with a plug removed every 10 minutes of charging. Tests were done with a normal load of 7.78 N, 17.6 N and 27.4 N. These tests showed little charging of the lap plate after 1 hour of charging time for all loads. The lands after charging were also very rough.

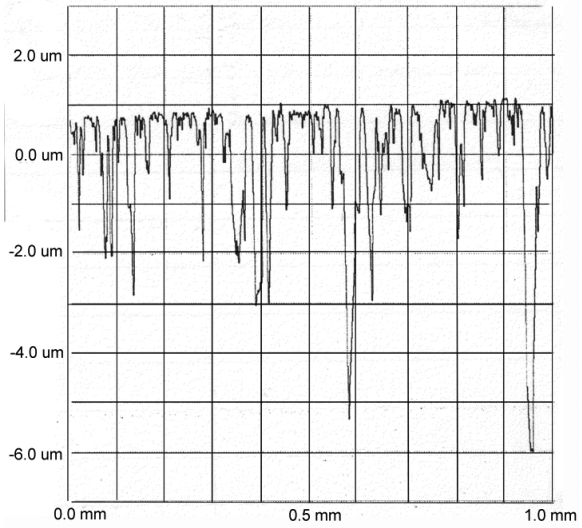

Figure 9. Talysurf profile of CoorsTek alumina roller

The surface profile of the roller was examined using a Talysurf profilometer. The surface of the roller was very rough as illustrated in Figure 9. The P-V was found to be approximately 7.8 μm and the RMS roughness 1.2782 μm. The gaps in the surface ranged from 0.25 μm to 8.0 μm in

depth and about 1 μm to 50 μm in width. With these large gaps, the 0.25 μm diameter diamond may be flowing into these gaps rather than being embedded into the tin surface. Attempts to reduce the surface roughness by polishing were unsuccessful and it was found that the alumina was too porous to be used in this application.

2.5.2 SILICON NITRIDE ROLLER

The second roller used was a sample cylinder made of silicon nitride. This roller is smaller than the alumina roller first used, being 38.9 mm in diameter and 31 mm in length. It was much less porous and had a better surface finish. A 0.5mm long sample profile showed a P-V roughness of 1.65 μm and an RMS roughness of 0.1282 μm. The calculated yield load for this roller is 15.45 N.

The first test run with this roller was done for a period of 1 hour with plugs removed at time intervals of 5, 10, 15, 20, 30, 40, 50 and 60 minutes. The normal loads used were 15.15 N, 17.1 N and 26.9 N.

During charging, darker strips and lighter strips became visible to the eye on the surface of the plate of where the roller was in contact. After further examination, it was determined the darker regions were areas in which there was heavy diamond concentration, and the light regions was where there was little or no diamond concentration. Figure 10 shows a plug examined with the SEM.

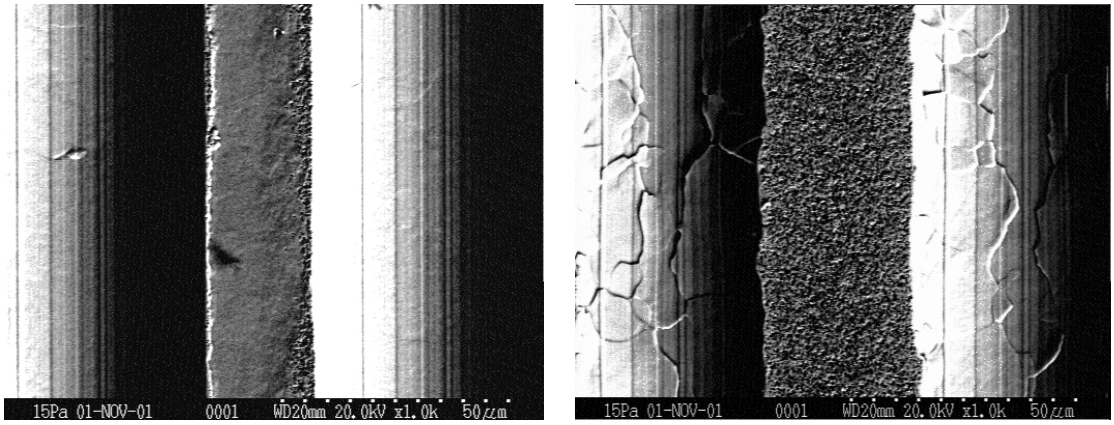

Figure 10. SEM images of light region (left) and dark region (right) after 30 minutes of charging using a silicon nitride roller with a normal load of 15.15 N

The lengthwise flatness of the roller was measured at several locations along the circumference. This profile was then compared with the pattern generated on the plate. Figure 11 shows the overall profile of the roller along side a picture of the charged plate surface. Analyzing the profile and the image, it shows that the tin yielded about 3 μm, causing contact with the roller at the median line as shown in the right image of Figure 11. The P-V of the roller across its entire width was 5.4 μm with the RMS roughness at 0.9763 μm.

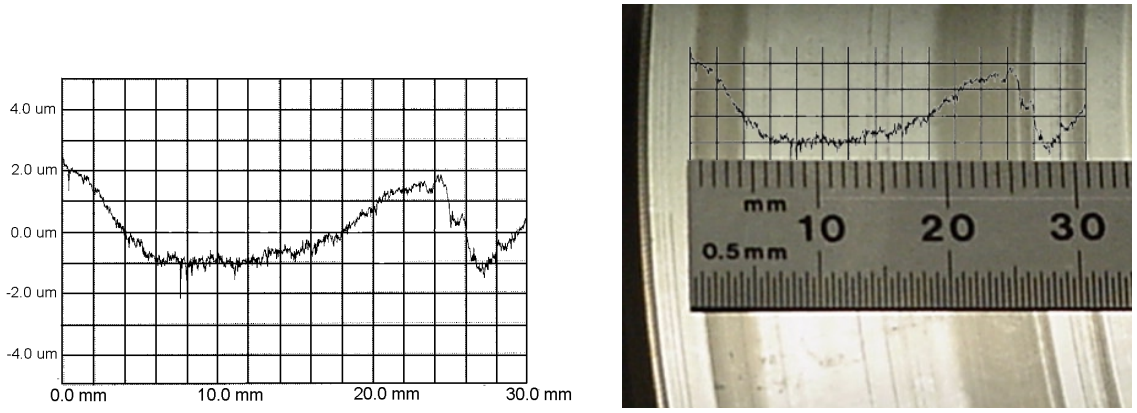

Figure 11. Silicon nitride roller profile (left) and plate appearance after charging (right)

The regions of the roller/tin contact throughout the experiment showed efficient charging performance. The plugs at the light load, 15.15 N, had abrasive covering 23% of the surface after just 10 minutes. This grew to 45% in 30 minutes of charging. This is compared to 20% to 25% attained after 1 hour of charging with the alumina ring in the previous process. The medium load of 17.1 N had about the same results as the lighter load. The heavier load of 26.9 N showed 1% to 5% more concentration per unit time.

Though the roller will be translating in the final process, the roller needs to be as flat as possible to optimize the amount of contact time. An alumina roller is currently being made at Sumitomo Special Metals in Japan. This is the manufacturer of the alumina used in the charging ring currently used by IBM. The roller ordered is 50mm OD by 25 mm long with a flatness specification for a P-V of <1 μm across the width of the cylinder.

2.6 TRIBOMETER DESIGN

One of the objectives of the research is to determine a method of testing the lapping performance of the plates during the charging process. Currently this is not being done, and the quality of the plate is not determined until after it leaves the production area. The goal is to correlate the diamond abrasive concentration of the lapping plate to the material removal rate of the hard disk heads during the lapping process. To do this, a method must be developed to determine the approximate diamond concentration on the plate at any location on the plate at any time.

The concept being tested is that the friction and diamond concentration are directly related. The idea being that as the contact surface changes from tin to diamond abrasive, the friction of the surface changes. To study this concept, a 3-axis load cell was mounted onto an arm that hung over the plate and could be lowered into contact, as shown in Figure 12. Two AlTiC strips were mounted to the load cell parallel to the grooves to contact the rotating plate. The load cell measured the force experienced by the stationary wafer on the moving plate throughout the charging process.

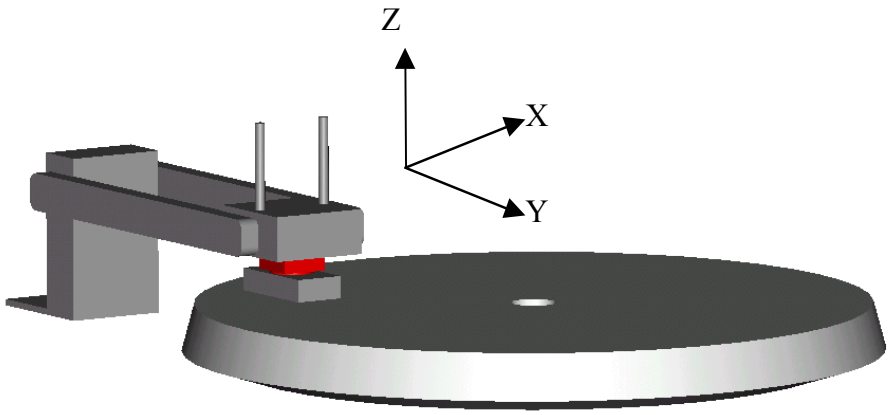

Figure 12. Setup for force measurements with the use of a 3-axis load cell

While charging the plate with the alumina charging ring, the force was measured every 10 minutes for approximately 20 seconds at a sampling rate of 0.1 seconds. The series of values for each time interval were averaged, and the friction coefficient was calculated with the relation shown in equation 3.

$$\mu = \frac{F_y}{N} \tag{3}$$

$\mathbf{F_y}$ is the force measured by the load cell and **N** is the normal load. The outcome was a general increase in friction, with the coefficient of friction value ranging from 0.03 at the beginning to 0.52 after 2 hours of charging. This can be seen in Figure 13.

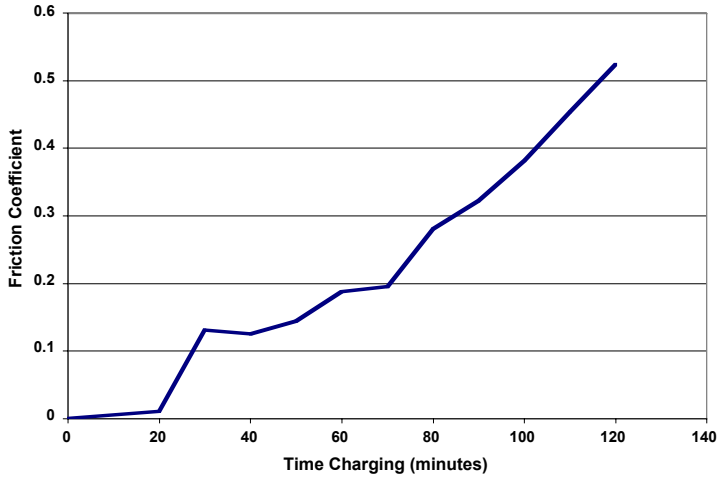

Figure 13. Experimental coefficient of friction values of the charged plate versus time charging

The current design for the tribometer is incorporated in the charging mechanism itself. The roller rotates at a constant velocity at any given radial location due to the friction between the roller and the plate. If a known torque is applied in the opposite direction to its motion, the change in velocity is proportional to the friction between the plate and the roller and that friction can be determined. For a new plate without diamonds, the friction should be low and a small

torque will change the speed significantly. Later in the charging process, the friction will be higher and that same torque will produce a much smaller change in speed.

To track the roller speed, an optical encoder with a resolution of 4096 bits per revolution is attached to the roller axle. This allows enough resolution to track the roller every 0.087 degrees of rotation. An eddy current brake generates the counteracting torque. The use of a magnetic brake helps avoid variances in forces over time experienced with mechanical brakes.

2.6.1 EDDY CURRENT BRAKE

The slowing or "braking" of the roller is done with an eddy current brake. An eddy current brake works by moving a conducting surface through a magnetic field. When a conducting disk is moved through a magnetic field, currents are generated in the conducting material called eddy currents, which generate a field resisting the motion. For the charging mechanism, an electromagnet was constructed and hung off the side of the roller housing. The axle of the roller extends outward onto which a copper disk attaches and rotates with the roller. The copper disc passes through a gap in the electromagnet between the magnetic faces. This design is illustrated in Figure 14.

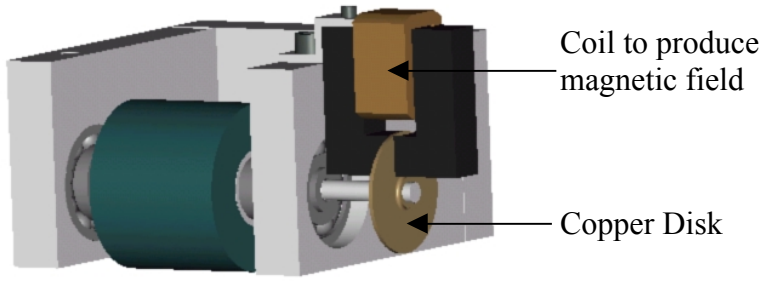

Figure 14. Eddy current brake and roller assembly

An equation for the torque generated by an eddy current brake is shown below [4].

$$T_{Brake} = \frac{1}{\rho} AdB^2 R_D^2 \omega_{Brake} \tag{4}$$

ρ is the resistivity of the copper disk, **A** is the area of the magnetic faces, **d** is the thickness of the copper disk, **B** is the magnetic flux density of the magnetic field, $\mathbf{R_D}$ is the distance from the center of rotation of the copper disc to the center of the magnetic face and **ω** is the angular velocity of the copper disk.

The magnetic flux density of the electromagnet can be found using equation 5, forming the magnetic flux density based on material and geometrical parameters of the electromagnet.

$$B = \frac{\mu N i}{g} \tag{5}$$

μ is the permeability of air, **N** is the number of turns of wire around the magnet core, **I** is the current in the wire and **g** is the width of the gap in the magnet. The magnet constructed has 350 turns of 26 AWG wire rated at 2.25 amps. The gap width of the electromagnet core is 2.0 mm. With a current of 2.0 amps running through the windings, the magnet produces a magnetic flux density of 0.5 Tesla.

The core is 10.0 mm square at the faces, which are centered 10.0 mm above the axis of rotation. The copper disk has a thickness of 1.0 mm and a resistivity of 10.3 (10^{-8}) Ωm. The braking force is a function of the rotary speed (ω) and can be written as

$$T_{Brake} = 1.92\left(10^{-5}\right)\omega \quad \text{[Nm]}$$

To test this brake, a weight was hung on the roller and the acceleration was measured. These tests of the brake performance validated torque shown above. This brake torque was used in calculations to predict the roller behavior during charging. A program was written with inputs of plate rotational velocity, the radial position of the roller on the plate, roller dimensions and normal load. The output was change in roller velocity between a free rolling and a braked roller based the theoretical friction coefficient between the plate and roller.

2.6.2 ENCODER & OUTPUT PROGRAM

A non-contacting rotary optical encoder with a resolution of 4096 bits per revolution is used to track the motion of the roller during the charging procedure. The encoder is connected to a USB-1 Encoder Data Acquisition Device controlled by software run on a PC. The USB-1 features real-time tracking of the encoder and a history buffer with a programmable sample frequency of up to 1 kHz.

While rolling freely, the encoder tracks the roller for a given sample time. This will output a number of bits, B_F, in a certain sample time, T_s. This data will determine the free velocity of the roller during normal motion. The brake can then be engaged and a sample is taken again. Since the roller is now rotating slightly slower than previously, it will output a lower number of bits, B_B, in the same sample period T_s. With this data, the force applied to the roller by the plate can be calculated.

The equation of motion for the system is shown below.

$$T_{PR} = \mu N R\left(1 - \left(\frac{R\omega}{V}\right)\right) = T_{Bearings} + T_{Brake} \tag{6}$$

$\mathbf{T_{PR}}$ is the torque generated by the plate-roller interface, $\boldsymbol{\mu}$ is the coefficient of friction on the plate, **N** is the normal load of the roller, **R** is the radius of the roller, $\boldsymbol{\omega}$ is the angular velocity of the roller, **V** is the velocity of the surface of the roller, $\mathbf{T_{Bearings}}$ is the torque generated by the bearings of the setup and $\mathbf{T_{Brake}}$ is the torque applied by the brake. For a sample time of 1.0 second, a normal load of 10 N, and a plate rotational velocity of 20 RPM, the theoretical counts for the encoder output using the silicon nitride roller are shown in Figure 15. The top graph is for the roller located near the OD of the plate with a speed of 20 RPM. The lower graph is the roller located near the ID.

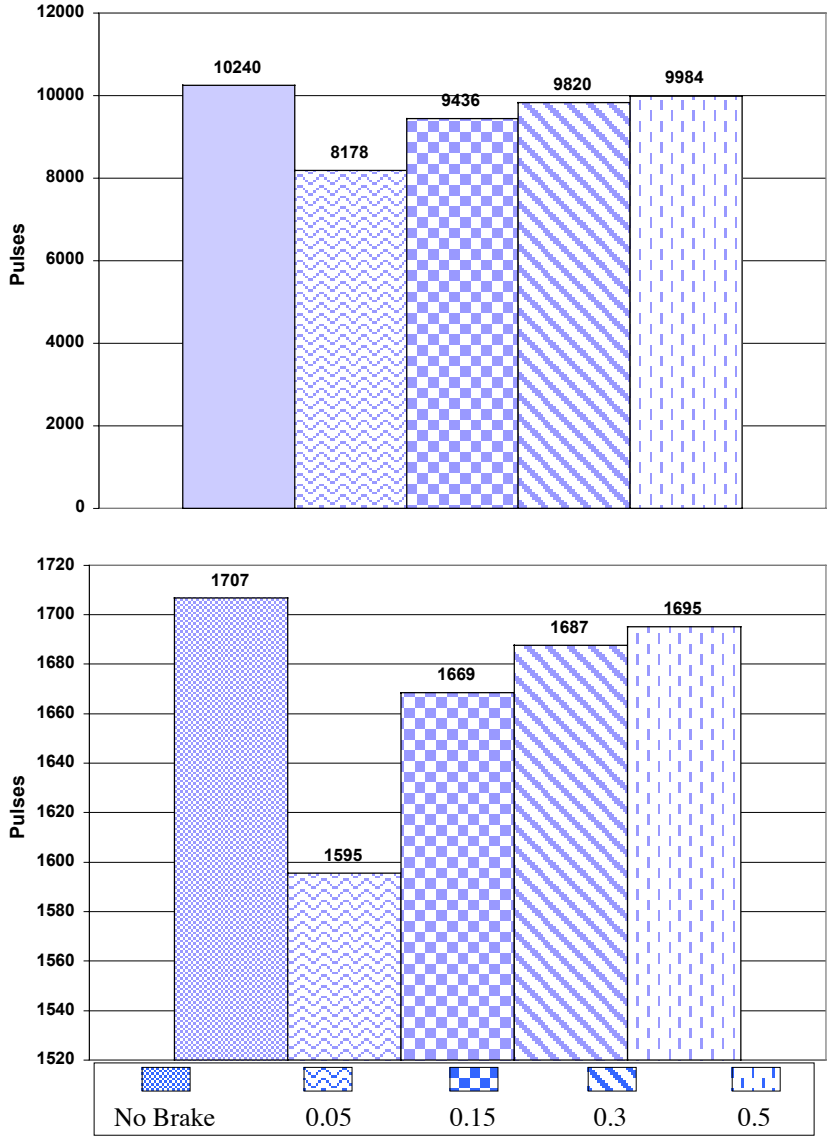

Figure 15. Theoretical output counts for a 1.0 second sample time at a plate radial location of 150 mm (top) and 25 mm (bottom) for varying friction coefficients

The first bar represents the number of counts of a free rolling cylinder; the last 4 are with the brake on and different friction coefficients between the plate and roller. The first of the braked counts is with a friction coefficient of 0.05, the second 0.15, the third 0.30 and the fourth 0.50. Table 1 summarizes the results of Figure 15.

		Brake On / Plate Friction Coefficient							
Radial Position	No Brake	0.05		0.15		0.3		0.5	
(m)	Counts	Counts	Δ	Counts	Δ	Counts	Δ	Counts	Δ
0.025	1707	1595	112	1669	38	1687	20	1695	12
0.07	4779	4201	578	4571	208	4673	106	4714	65
0.15	10240	8178	2062	9436	804	9820	420	9984	256

Table 1. Theoretical counts for various friction coefficients and radial positions

The differences in counts for all values of friction are larger for the larger radial positions. As the roller gets closer to the center of the plate, the velocity decreases as does the encoder counts. For a 1.0 second sample time, the difference between a free rolling cylinder and a braked one may be in the range of noise or uncertainty experienced by the setup. There are a number of ways to overcome this problem. One is to increase the plate rotational velocity. In doing so the roller will have a faster velocity and thus the encoder will output more counts per unit time. Another is to increase the sample time period. The number of output bits is directly proportional to the sample time, thus doubling the sample time will double the counts.

2.7 CONCLUSIONS

The emphasis from the effort this year has been on the charging process of the plate. This began with evaluating the current charging process used and investigating how each parameter affects the end product. One of the conclusions was a realization of how the plate flatness can greatly affect the charging quality.

One possibility to rid of this problem is the use of a smaller roller to charge the plate. A roller would have the ability to better follow the profile of the plate due to its smaller contact length, as well as increasing the pressure due to its smaller contact area. It is hoped that the smaller contact length will increase the overall charging quality while the higher contact pressure will embed more abrasive per unit time, thus reducing the charging time.

The construction and testing of the tribometer hopes to make evaluations of the lapping plate quality during fabrication possible. Future tests involve relating plate surface diamond concentration to the material removal rate. A challenge that must be dealt with during the testing

and calibration of the tribometer is the sensitivity of the output forces due to speed and friction. Forces experienced in the charging process cause small changes in the output, and might be in the range of uncertainty.

REFERENCES

1. Kametz, D.A., Stevens, J. M., T.A. Dow, "Lapping Plate Charging", 2000 Precision Engineering Center Annual Report, pp. 1-24, January 2001.
2. Frene, J., et al. Hydrodynamic Lubrication, Bearings and Thrust Bearings. Paris: Elsevier Science B.V., 1997. 73-78.
3. Roark and Young. *Formulas for Stress and Strain, 5th Edition.* Pp. 516-517. McGraw Hill Inc., 1975.
4. Simeu, E., Georges, D. "Modeling and Control of Eddy Current Brake." System Structure And Control 1995. 1996. Ed. M. Guglielmi. International Federation of Automatic Control. Tarrytown: Elsevier Science Inc., 1996. 109-114.

3 DISTORTION OF THIN CYLINDERS

Patrick D. Morrissey
Graduate Student
Jeffrey W. Eischen
Associate Professor
Department of Mechanical and Aerospace Engineering

Accurately predicting and controlling the shape of thin cylinders (liners) is an integral part of Los Alamos National Laboratory's (LANL) fabrication process that uses such components. These aluminum liners are attached by means of a thermal shrink fit to copper cylindrical components known as glide planes and are used in high-energy pulse power experiments. The primary issues at hand include the following: mechanics of thermal interference fits, physical description of the contact surfaces between the liner and glide planes, joint void description, and material property effects. To investigate these issues, computer generated finite element analysis models have been created and compared to both theoretical and experimental data. A measurement technique has been developed to compare distortions produced in a model interference fit joint to verify the finite element simulation. Verification of the computer generated finite element model with experimental results could provide tremendous aid in accurately predicting the shape, deflection, and stress distribution of such cylindrical elements.

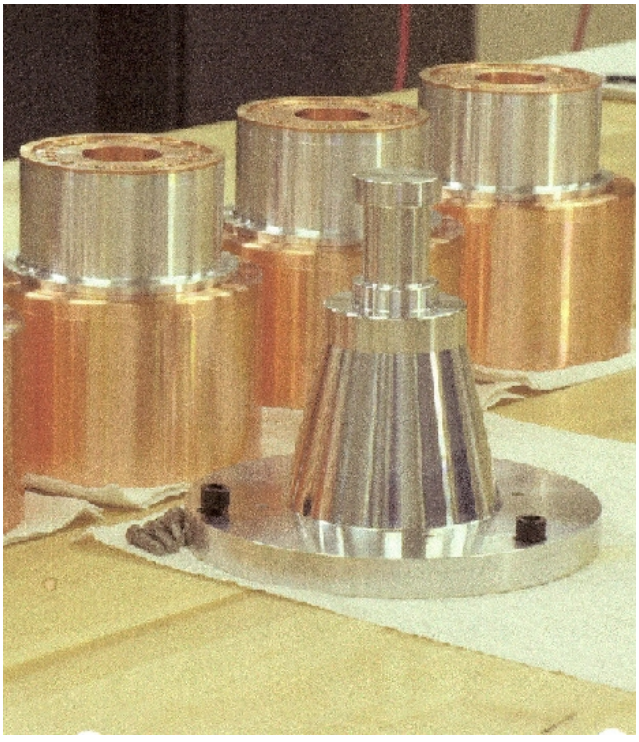

3.1 INTRODUCTION

There is a need to fabricate thin cylindrical components (called liners) for use in high-energy pulse power experiments at Los Alamos National Laboratories. These experiments can potentially incorporate composite liners, that is, liners fabricated from dissimilar materials. Typically the primary material used for the liner is pure 1100 series aluminum. For the experiments needing composite liners, inner cylindrical components can be inserted in these liners either by means of a slight press fit or thermal shrink fit, preferably using the latter of the two to avoid the use of excess external forces that could deform either component. Currently this inner layer is manufactured using copper, but tantalum, stainless steel, or 6061 aluminum may also be utilized.

Copper glide planes are inserted in either end of the cylindrical liner, typically via a thermal shrink fit process. These glide planes serve as a mechanism to transfer tremendous electrical currents to the liner, which leads to a cylindrical implosion of the liner. To optimize the results of these experiments, it is necessary for this cylindrical implosion to occur very uniformly. Therefore, manufacturing dimensionally precise liners with minimal surface flaws is essential. Unfortunately, the shrink fit process naturally results in residual stress and distortion in the liner walls, which need to be compensated. A schematic illustrating the assembly orientation of a single wall liner with glide planes is shown in Figure 1. The nominal diameter of the liner is 100 mm, the height is 55 mm and the wall thickness is approximately 1mm.

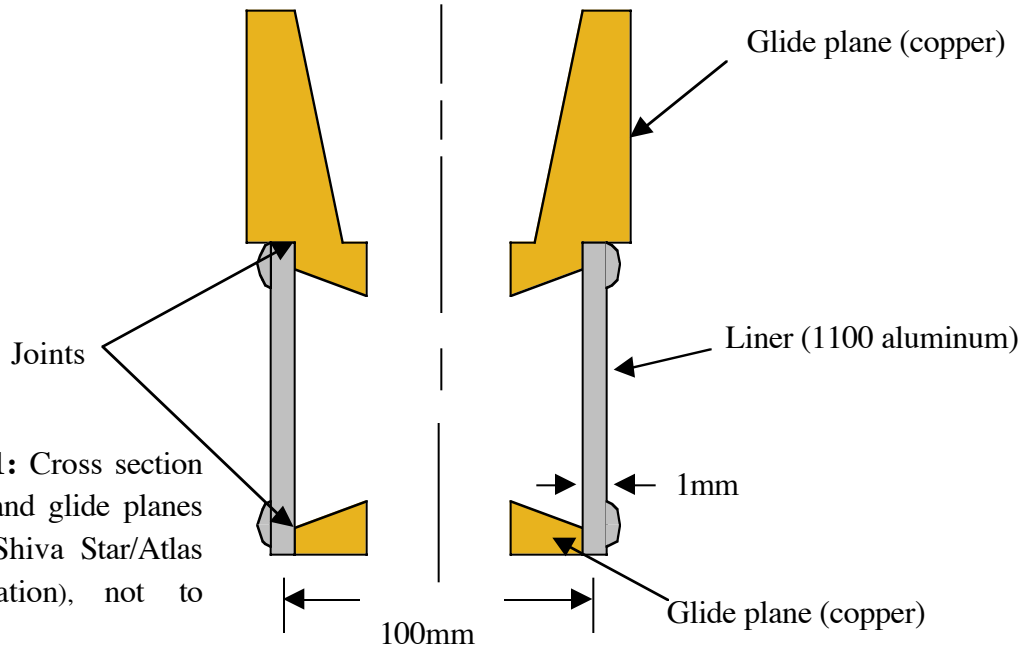

Figure 1: Cross section of liner and glide planes (NTLX Shiva Star/Atlas Configuration), not to scale)

3.2 FINITE ELEMENT MODELING

3.2.1 LANL PROTOTYPE

The stresses and distortions resulting from slipping the glide planes into the liner are impossible to calculate from analytical formulas. These expressions exist only for cylindrical systems in which the interference exists along the entire length of the mating cylinders. In the current problem, only a partial interference exists, since the glide planes only fit into the end portions of the liner. Finite element analysis (FEA) provides an efficient method to calculate the desired quantities for this type of structural configuration. The geometry of this particular shrink fit interface, as well as the geometry of the actual liner itself, is expected to provide results that considerably deviate from those given by standard shrink fit calculations. LS-DYNA, a powerful FEA software package, was used to model the LANL prototype. Figure 2 illustrates the geometry of this axi-symmetric system. The axi-symmetric modeling does ignore some details of the glide planes, such as holes and ports, but this is not expected to impact the results of interest in any significant way.

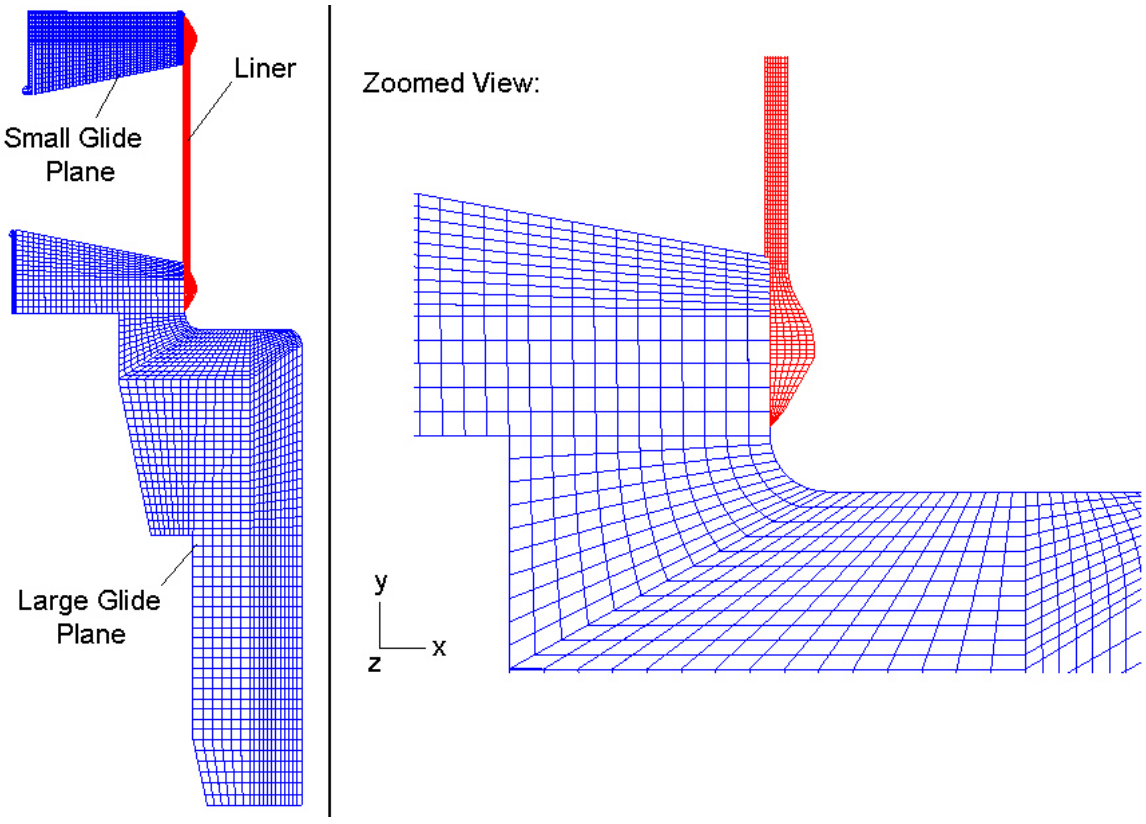

Figure 2: LS-DYNA mesh used for LANL prototype simulation

	COPPER GLIDE PLANES	1100 ALUMINUM LINER
Young's Modulus	1.5954×10^{7} psi	1.0008×10^{7} psi
Poisson's Ratio	0.35	0.33
Thermal Expansion Coeff.	1.7×10^{-5} $(°C)^{-1}$	2.36×10^{-5} $(°C)^{-1}$
Yield Strength	50,000 psi	5,000 psi

Table 1: Material properties used in LS-DYNA simulations

The material properties used for the liner and both glide planes correspond to 1100 aluminum and copper, respectively. These properties are listed in Table 1. Each component is modeled in LS-DYNA as an elastic-plastic material, accounting for any potential yielding. The liner is composed of 1638 elements with 8 elements through the thickness, and the large and small glide planes are composed of approximately 2000 elements each. For this preliminary FEA model in particular, a composite liner is *not* used. A uniform temperature change of -100°C was imposed on the glide planes during simulation. The parts were then slipped together, followed by a return to ambient temperature with "contact modeling" between the parts activated during the transition to equilibrium. The glide planes expanded during this phase, deforming the liner as expected. A displacement vector plot for nodes within the liner is shown in Figure 3(a) and 3(b). The lengths of the arrows indicate magnitude of radial displacement in the liner wall, with the peak deflections occurring at either end of the liner. Note that the vectors are magnified for an enhanced visual representation of the displacement behavior. The displacement decays with distance from the liner ends and actually becomes negative, indicating inward radial movement at the mid-length position of the liner.

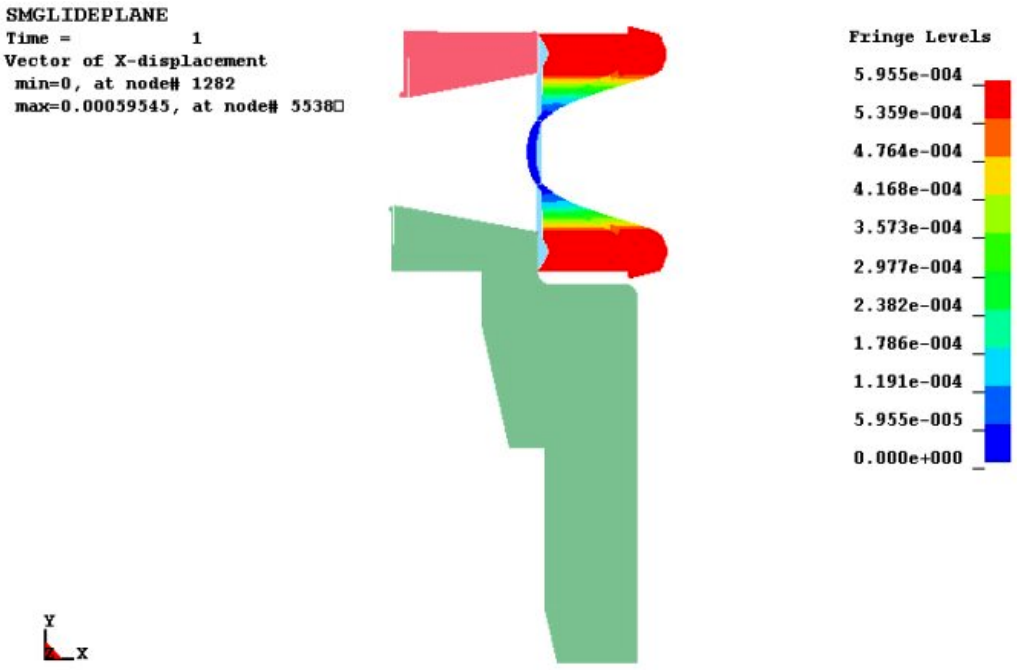

Figure 3: (a) Magnified vector plot of radial displacement along the liner

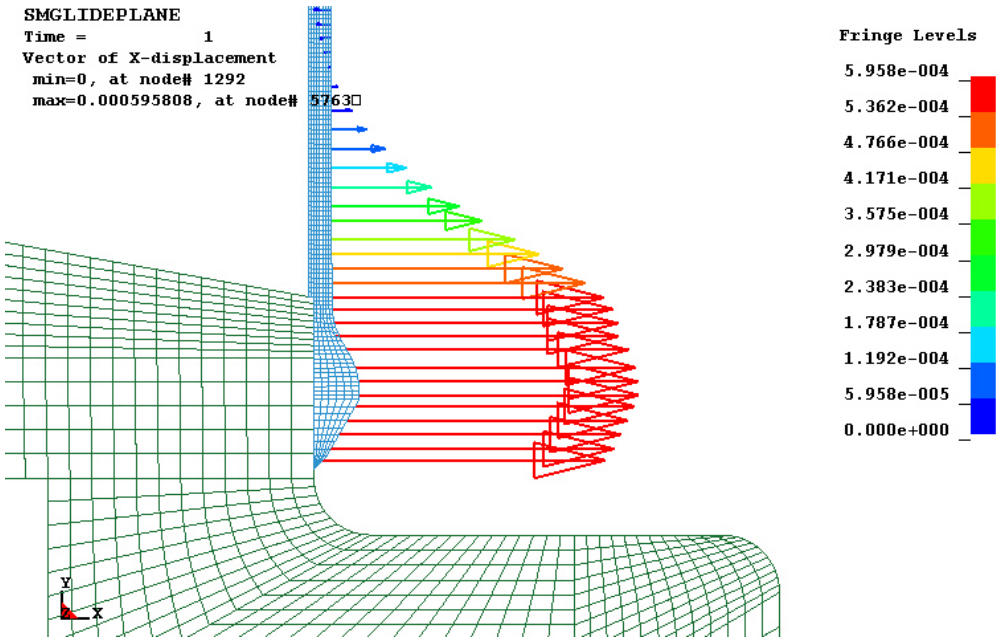

Figure 3: (b) Displacement vector plot of deformed liner

Figure 4 is a graph showing the distribution of radial displacement along the liner wall. The flat sections on the left and right extremities of this graph represent liner displacements in the regions of contact with the large and small glide planes, respectively. Positive values represent liner displacements radially outward, while negative values represent displacements radially inward. Note again that the liner undergoes negative radial displacement in the mid-length position of the liner.

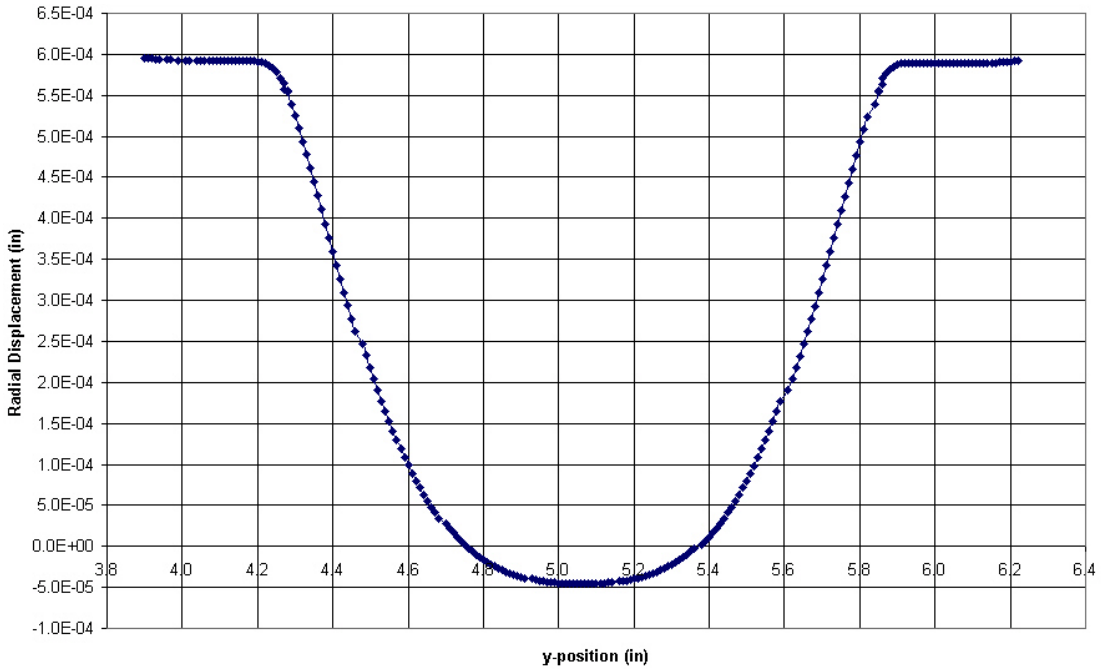

Figure 4: Radial displacement distribution along liner

There is a stress concentration in the liner near the regions in which contact ends with the glide planes, mainly caused by the sharp corner features of the glide planes in these regions. The maximum hoop and radial stress values in the liner are 4180 psi and 508 psi, respectively. Since the yield strength of 1100 aluminum is approximately 5000 psi, yielding and permanent distortion of the liner is not expected.

To improve the cylindrical implosion of the liner, it is surmised that having a uniform, straight walled cylinder *after* the shrink fit process is desirable. Therefore, the deflections caused by the interference, shown in Figure 3 and Figure 4, are potentially problematic. One possible solution is to machine a liner with an ID and OD that vary slightly along the length. This variation represents the negative values of the deflection vectors along the liner, which results in a final shape after assembly that "counteracts" the deflections caused by the interference fit. One such liner was simulated using FEA, and the results are shown in Figure 5 with a comparison to the original liner design. This plot represents the surface profile of the liner wall after the shrink fit assembly has occurred. The top and bottom curves represent the new curved and original liner designs, respectively.

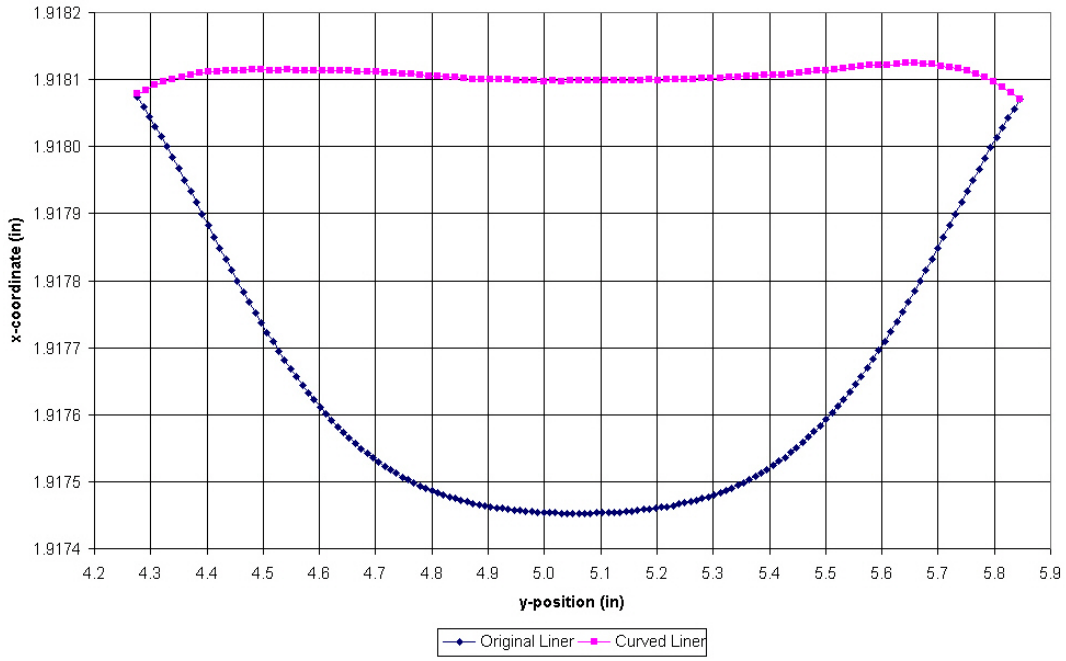

Figure 5: Post-assembly inner radius profile for original and curved liner designs

The new curved liner design improves the overall peak-to-valley deviation of the liner wall from 6.207×10^{-4} inches (15.77µm) to 5.29×10^{-5} inches (1.34µm). Continuing to fine tune the new curved liner design can potentially further improve the flatness of the post-shrink fit liner surface, though this first iteration provides deviation from a perfect flat surface that may be acceptable.

3.3 EXPERIMENTAL RESULTS

3.3.1 TEST SPECIMEN DESIGN

To verify the validity of these LS-DYNA results, an experiment was conducted involving a simple shrink fit test specimen, as illustrated in Figure 6.

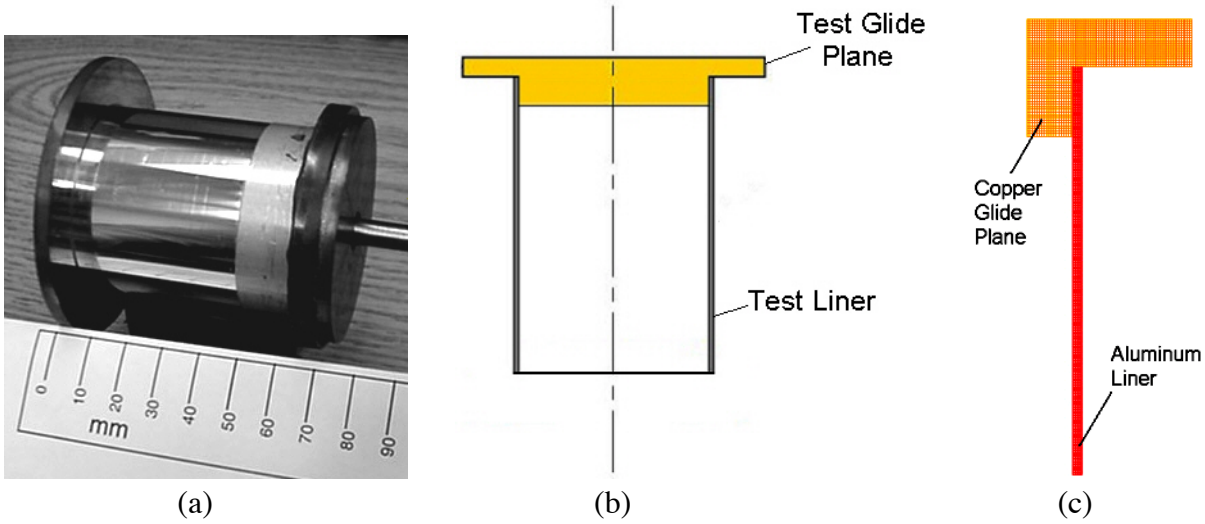

Figure 6: (a) Machined and assembled test specimen, (b) test specimen geometry, and (c) test specimen finite element model

This specimen consisted of a 6061 aluminum liner and a copper glide plane that were machined using the ASG-2500 Diamond Turning Machine. Hoop and radial stress levels were calculated and dimensions were selected to avoid yielding of either part as a result of the shrink fit process. Furthermore, calculations were performed to ensure that sufficient pressure between the two components would be provided to maintain the shrink fit, even with potential temperature changes after assembly. The outer diameter of the glide plane was machined to 48.598 mm, and the inner and outer diameters of the liner were turned to 48.559 mm and 50.544 mm, respectively. These dimensions produced a radial interference δ = 7.6x10^{-4} inches (19.304 μm) along an interface length of 7.366 mm. It is important to note that the overall length of the test liner is approximately 43 mm, much greater than the length over which contact with the test glide plane occurs. This system was assembled by means of a thermal shrink fit, with the glide planes cooled in dry ice to a temperature of approximately 75°C below zero. The parts were then allowed to warm to ambient temperature as they returned to equilibrium. The radial displacement profile of this test liner was compared to finite element results from a model representative of this geometry.

Using LS-DYNA, this test specimen was modeled and the shrink fit assembly was simulated using a similar procedure described for the LANL prototype simulation. Stress calculations for the outer cylinder were performed based on standard cylindrical shrink fit theory using dimensions and material properties identical to those of the test specimen. The calculated results for radial stress, σ_{rr}, and hoop stress, $\sigma_{\theta\theta}$, are shown in Equations (1) and (2) below,

$$\sigma_{rr,liner} = -p = -\frac{\delta}{\left[\frac{R}{E_o}\left(\frac{r_o^2 + R^2}{r_i^2 + R^2} + \upsilon_o\right) + \frac{R}{E_i}\left(\frac{R^2 + r_i^2}{R^2 - r_i^2} - \upsilon_i\right)\right]} = -1.972x10^6\, Pa \qquad (1)$$

$$\sigma_{\theta\theta,liner} = \frac{E\delta}{R} = 5.371x10^7\, Pa \qquad (2)$$

where r_o, E_o, and υ_o are properties of the outer cylinder (liner), r_i, E_i, and υ_i are properties of the inner cylinder (glide plane), δ is the radial interference between the two cylinders, and R is the nominal radius of the outer cylinder. For the region of contact between the two parts, LS-DYNA gave average radial and hoop stress values within the liner of $-1.882x10^6$ Pa (4.5% difference) and $5.339x10^7$ Pa (0.6% difference), respectively. Of course, the other important parameter is liner displacement. A plot describing the radial displacement of the liner's inner wall is shown in Figure 7. The flat region on the left represents the free end of the liner, which is not effected by the thermal shrink fit and therefore yields no displacement. The right end of the graph represents the region of contact between the liner and glide plane, which occurs over the final 0.29 inches of the liner. This interface produces the maximum radial displacement of the liner.

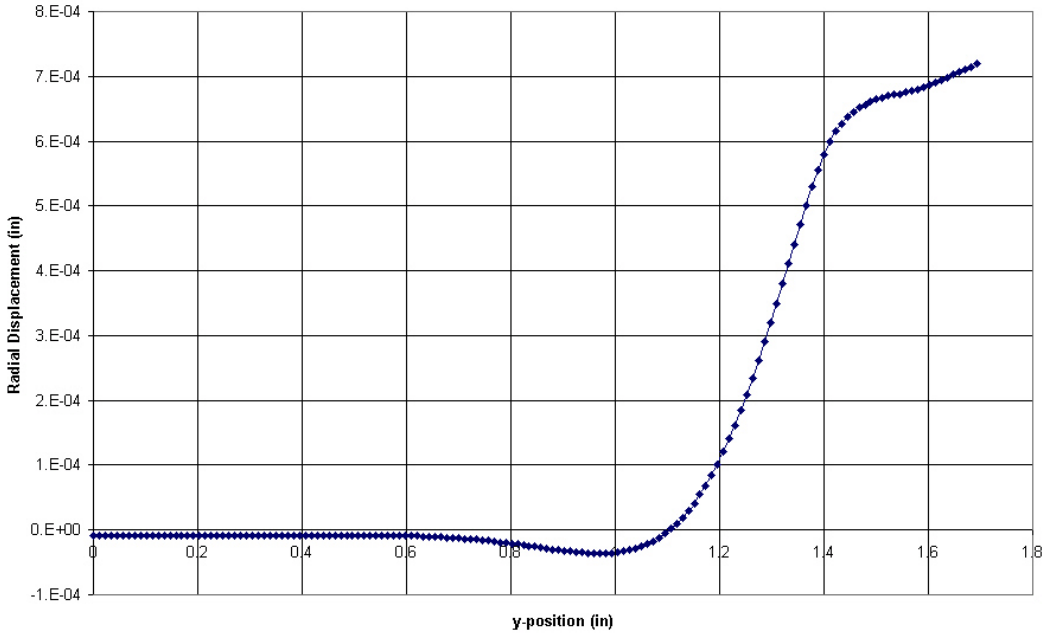

Figure 7: Test specimen liner deflection due to a thermal shrink fit

Note that the maximum radial displacement ($7.3x10^{-4}$ inches, 18.542 µm) in the contact region is slightly less than the radial interference ($7.6x10^{-4}$ inches, 19.304 µm) caused by the difference between the glide plane and liner diameters. This is due the fact that the glide plane is somewhat compressed as a result of the shrink fit, which shrink fit theory does not take into account.

3.3.2 TEST SPECIMEN FABRICATION

It is clear that the LS-DYNA results for the contact region closely follow the results given by shrink fit theory. However, a comparison between LS-DYNA results and experimental results determines how well the simulation tool can be used to predict radial displacement and stress levels in systems such as the LANL prototype. The test specimen glide plane and liner were machined using the ASG-2500 Diamond Turning Machine, and the shape of the test liner's outer surface was determined by measuring along eight lines on the outer surface of the cylinder. These measurements were performed using the Zygo GPI Interferometer. Post-shrink fit measurements of the liner's outer surface were also taken, again using the Zygo GPI Interferometer. The difference in these profiles provides the radial displacement values of the test liner due to the shrink fit interference.

3.3.3 TEST SPECIMEN MEASUREMENTS

The ability to obtain the actual test liner displacement values is dependent upon the completeness of data collection for both before and after shrink fit surface measurements. Figure 8 illustrates the comparison of the LS-DYNA displacement values with actual displacement values determined using the Zygo GPI Interferometer data.

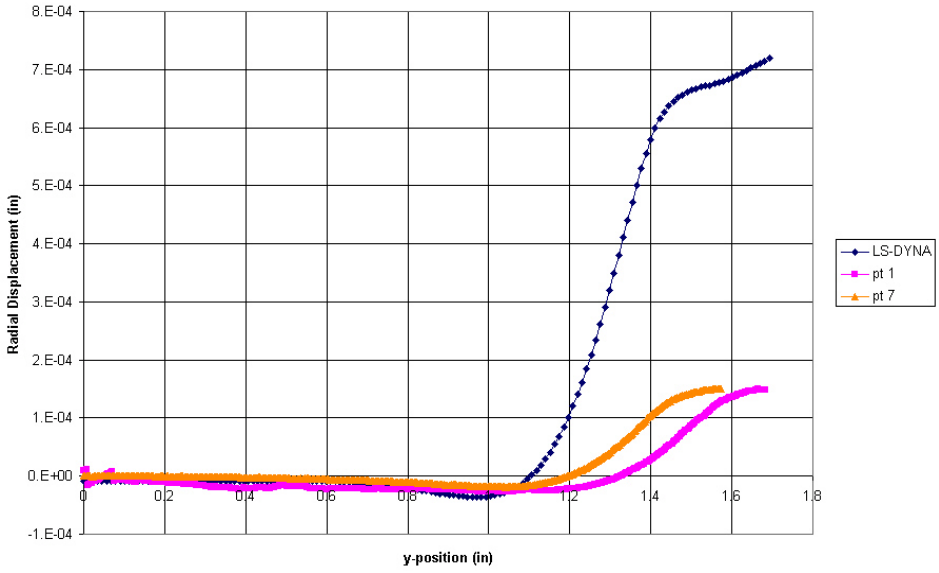

Figure 8: Comparison of LS-DYNA and actual test specimen liner displacement values

Figure 8 shows the actual radial displacement of the liner along two of the eight measurement lines. There is clearly a discrepancy between the liner displacement caused by the glide plane and the displacement predicted by FEA. As mentioned earlier, however, the LS-DYNA displacement values correspond well to the expected values. Therefore, it is concluded that the test liner or test glide plane (or both) components were fabricated with an effective interference much less than the target value of 7.6×10^{-4} inches (19.304 µm). The plots in Figure 8 suggest an actual radial interference of approximately 1.5×10^{-4} inches (3.810 µm). Assuming this is the case (which is reasonable based on the actual deflection data), a simulation model was created using the smaller radial interference of 1.5×10^{-4} inches (3.810 µm). Such a model predicts very similar magnitude and distribution of radial displacement values in comparison to the actual displacement values, as shown in Figure 9. Figure 9 illustrates that the radial displacement values given by the LS-DYNA model lie slightly above the actual values for most points along the y-position of the liner. This particular FEA model did not account for friction effects within the contact region. Furthermore, any inconsistencies in the materials used may have altered the materials' properties to some extent. Such factors are possible causes of the discrepancy between FEA model and actual radial displacement data

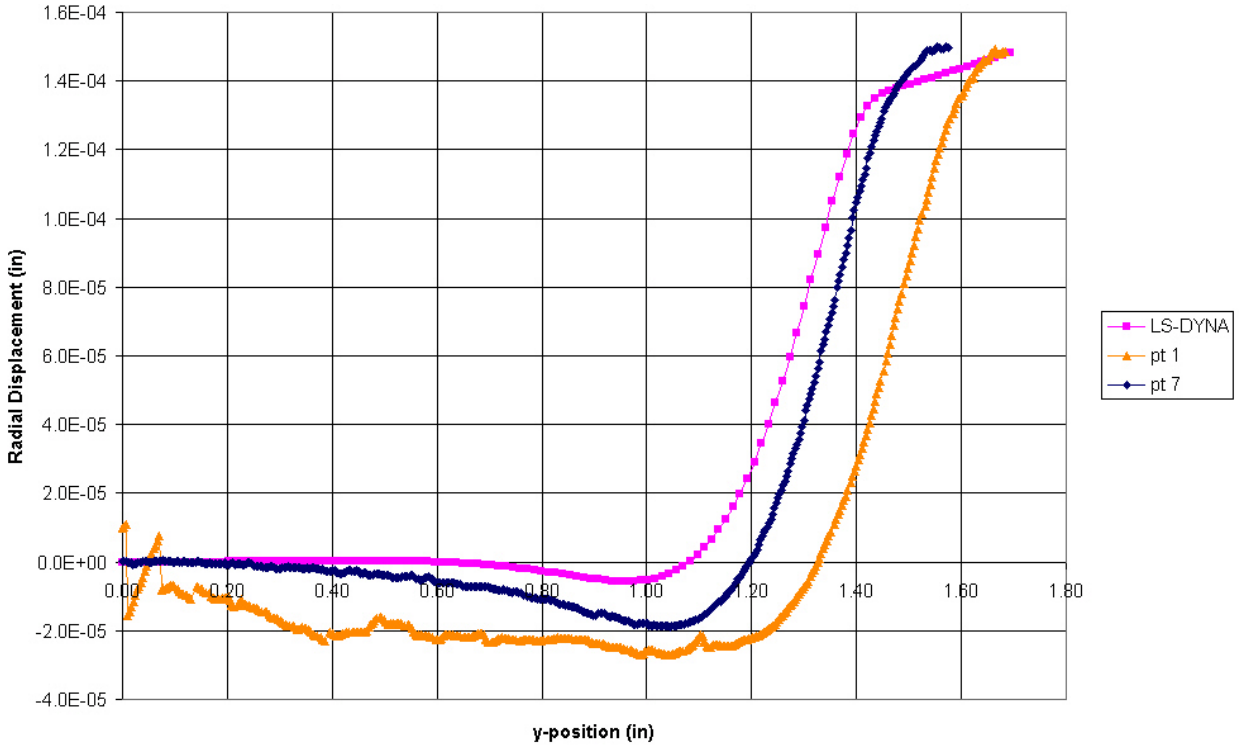

Figure 9: Results of LS-DYNA simulation when modeled with less interference, in comparison to actual test specimen liner displacement values

The Three Dimensional Measurement probe is currently being used to verify the actual dimensions of both the test liner and glide plane. This probe, used in conjunction with the ASG-2500 Diamond Turning Machine, can glide along the surfaces of the test specimen liner and glide plane

to gather coordinate values. This method essentially provides the actual dimensions of the test specimen pieces. Verification of such dimensions will provide further information as to how accurately shrink fit systems can be predicted by finite element analysis using LS-DYNA.

3.4 CONCLUSIONS

The finite element simulation of the actual LANL prototype is a powerful tool when dealing with predictions of liner stresses and radial deflections. Such a simulation shows that the hoop and radial stress levels within the liner do not exceed the yield strength of the 1100 aluminum material, with maximum stress levels occurring near the joints (hoop stress equal to 2.882×10^7Pa). As predicted, the LS-DYNA results also show that the liner does indeed have an abnormal radial deflection distribution when compared to standard shrink fits. The radial deflection values are maximum (15.113 μm) at the joints, and actually become negative at the mid-length region of the liner. The curved liner design, one which "counteracts" the deflection values caused by the thermal shrink fit, helped reduce deflection values considerably. Using such a design decreases the overall peak-to-valley value of the liner's outer surface by a factor of 11.8, from 15.77μm to 1.34μm. Such an improvement should enhance the performance of the LANL prototype.

Verification of the finite element model results can further build confidence when using FEA to predict liner deformations and stress levels. The test liner simulation gives results that correspond well to shrink fit theory in the regions of contact between the two components. The accuracy of the LS-DYNA software is currently being investigated using a comparison to the deflection trend of the fabricated test specimen liner. Although the actual maximum deflection value (3.81 μm) of this liner did not coincide with the simulation's predicted value (19.34 μm), the trend showed striking similarities. It was therefore concluded that the liner and glide plane were machined with such dimensions that produced a smaller effective interference than desired. An altered FEA simulation representing this smaller interference produces a deflection curve that is almost identical to actual values.

4 DESIGN OF A LINEAR HIGH PRECISION ULTRASONIC PIEZOELECTRIC MOTOR

Markus G. Bauer[1]
Graduate Student
Thomas A. Dow
Professor
Department of Mechanical and Aerospace Engineering

A new motor has been designed that uses two independently driven piezoelectric elements, one generating a normal load at the interface and the second generating the tangential force necessary to drive a slideway. The challenges in developing this motor were: 1) the actuator needs to have two different mode shapes at nearly the same frequency and 2) each mode shape must be exclusively excited by one actuator and not by the other. The quality of the operation of the motor directly depends on how well the excitation of both vibrations can be separated. Finite element analysis has been used to model the actuator and predict the dynamic properties of the prototype. The model includes all significant features that have to be considered such as the anisotropy of the piezoelectric material, the exact properties and the dimensions of the actuators (including all joints). Several prototypes were built, and the resulting mode shapes and natural frequencies were measured and compared to the computer models. Open loop testing has shown that the motor generates slideway motion such that the steady state slideway velocity is proportional to the excitation voltage. The motor was also tested in a closed loop control system. Despite saturation of the control input and non-linear dynamics of the motor-slideway system, it was shown that a simple feedback control system using proportional gain or proportional-integrating control algorithms can be used to achieve a stable, responsive positioning system.

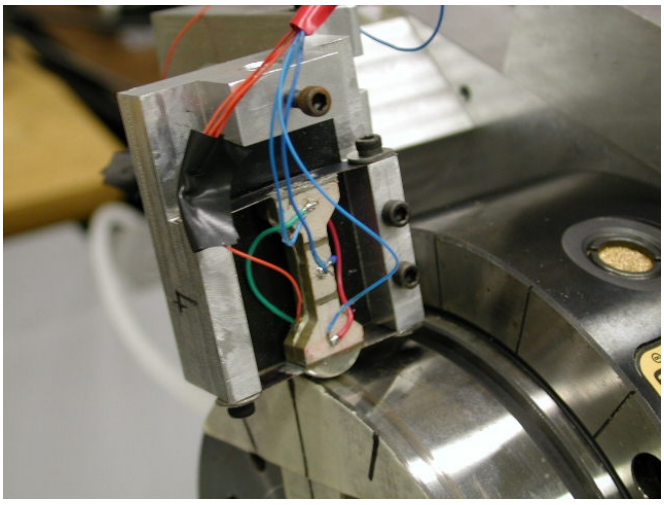

[1] Currently at SCYNEXIS Chemistry & Automation, Inc. in Research Triangle Park, NC

4.1 INTRODUCTION

Ultrasonic piezoelectric motors can be designed to use either traveling waves or standing waves to generate motion. Piezoelectric standing wave motors, the emphasis of this work, use a combination of flexural, torsional or longitudinal vibrations of a piezoelectric actuator. One vibration produces a normal force, while the other vibration generates motion that is perpendicular to the normal force. This combination creates a friction based driving force between one stationary component, the motor, and the object to be moved. The amplitudes of the vibrations and the phase between them are the most important parameters that influence the performance of the motor as illustrated in Figure 1. Variation of the phase alone can be used to control the motor. A phase of 0° between force and motion will not generate slideway motion, 90° results in maximum slideway velocity in one direction and 180° changes the direction of slideway motion.

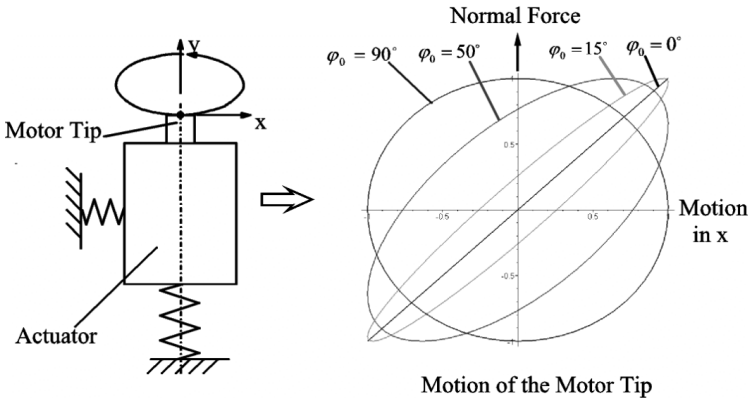

Figure 1. Influence of the phase between normal force and motion

Generally speaking, any structure that can be made to vibrate in orthogonal directions with sufficient magnitude can be used as a motor. A standing-wave motor produced by Nanomotion Ltd. [1] is illustrated in Figure 2. This motor uses the first longitudinal resonance of the piezoelectric material to generate a sinusoidal normal force and the third bending resonance to generate a force in the direction of motion. It is made from a single block of piezoelectric material that is electrically divided into 4 sections. Applying the voltage to different sections changes the direction of motion of the slideway. However, because both vibrations are excited using a single voltage, the phase between force and motion cannot be changed.

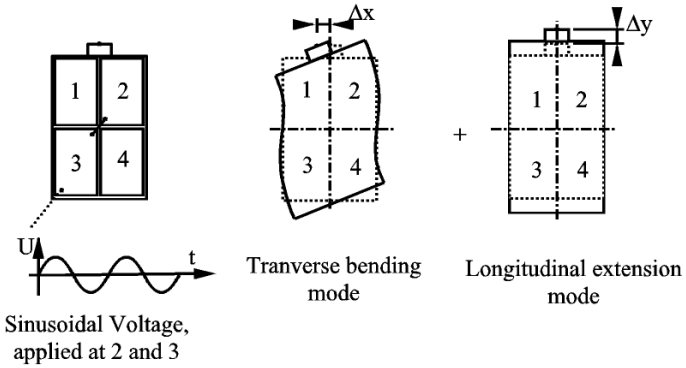

Figure 2. Nanomotion Motor, Mode Shapes [1]

Piezoelectric standing wave motors have the potential to achieve both high velocities (1m/s) and sub-μm resolution in a small, compact and inexpensive package. The operation of these motors is absolutely silent, because the operating frequency is above the audible spectrum, typically around 40kHz. Although commercially available piezoelectric standing wave motors (such as the Nanomotion motor) perform well at high slideway velocities, the inability to independently change the orthogonal vibration amplitudes compromises the fine positioning capability of the motor.

4.2 DESIGN OF NEW ACTUATOR

The objective of this project is to design an actuator that allows normal force and sliding motion to be controlled independently. The normal force can then be kept at an optimal level while the amplitude of the sliding motion and the phase angle between sliding motion and normal force can be used to control slideway direction and speed.

4.2.1 METHODS OF ANALYSIS

To implement the design objective, the motor must have one mode shape that will generate a normal force and one mode shape that generates only sliding motion (and no component of normal force). The resonant frequencies of these two modes must be close enough to each other (~500 Hz) so that a single excitation frequency will amplify the stroke in each direction by the resonance effect.

Analytical models of the actuators were used to approximate the system response. It is necessary to model the motor as a continuous dynamic system to include all natural frequencies. To allow an exact prediction of both natural frequencies and mode shapes, it is necessary to include all details of the design such as any glue joints that exist. As the motors grew in complexity, finite element analysis (FEA) was used to numerically determine all natural frequencies and mode shapes. The results were then analyzed and the dimensions of the system are optimized. This process was repeated until a system was obtained for which the two desired modes are at similar frequencies and have coincident nodes that can be used to attach a support.

4.3 PROTOTYPE DESIGNS

Prototype 1 The principle for the first two prototypes of the standing wave motor was to use two orthogonal actuators, as shown in Figure 3, and to excite each at one longitudinal resonance. Prototype 1, shown on the left, used two orthogonal piezoelectric actuators glued at right angles to a metal block to which the tip was attached. The two masses at the ends were added to adjust the position of the vibration nodes or points of zero amplitude. The location of these nodes is an important aspect of the design because this is where the motor is attached to the frame to support the drive loads.

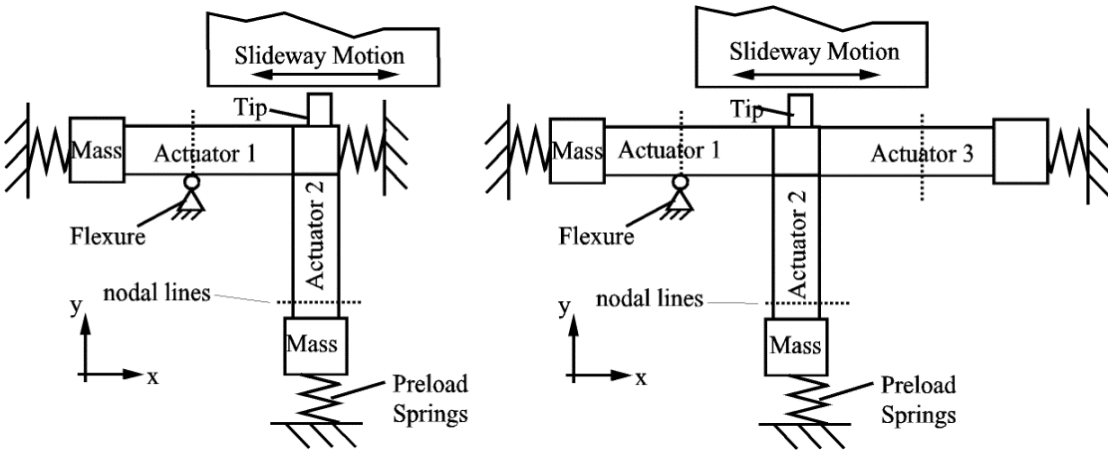

Figure 3. Prototypes 1 at the left and Prototype 2 at the right.

Actuator 1 provides excitation in the direction of slideway motion, and Actuator 2 changes the normal load at the contact point between the ceramic tip on the motor and the slideway drive surface. Motion of the slideway to the right or the left depends on the phase angle between the motion of the drive piezoelectric actuator (Actuator 1) and the loading actuator (Actuator 2). The springs are used to preload the two actuators to keep them in compression and avoid damage to the brittle ceramic.

Experiments showed that when Actuator 2 was excited with +/- 100V at 44.8kHz, the motor produced considerable slideway motion (but only one direction) and a pushing force of 5N. The excitation of actuator 1 does not influence the motor's performance significantly. A change in phase between both excitations changes the magnitude of the pushing force and slideway velocity to some extent, but did not allow a reversal of the direction of motion.

Prototype 2 The T-shaped geometry in Prototype 2 was introduced to create symmetry with respect to the bending motion of Actuator 1 when Actuator 2 is excited. In this design, the tip does not bend and no sliding motion is caused by excitation of Actuator 2. It is not possible to improve the behavior of the other actuator in the same way, because the tip has to be pressed against the slideway. When Actuators 1 and 3 are excited to generate sliding motion, bending motion occurs in Actuator 2. The dimensions of the motor can be chosen such that rotation of the tip is small, but it cannot be eliminated entirely by symmetry (as done for the other direction). Consequently, longitudinal excitation of Actuators 1 and 3 results in bending motion of Actuator 2, which in turn leads to bending in Actuators 1 and 3. Since bending of these is part of the mode that generates the normal force at the tip, the longitudinal excitation of Actuators 1 and 3 also results in a dynamic normal force at the tip. Thus, both modes are still coupled, although the advantage of this prototype is that the effect of one mode on the other is much smaller than in Prototype 1.

Experiments showed that a dynamic normal force of +/- 30N can be generated with a voltage of +/-100V applied at Actuator 2. Unlike Prototype 1, the excitation of Actuator 2 generates predominantly a dynamic normal force at the tip (the thrust force is very small). A maximum slideway velocity was measured to be 0.5m/s, when both actuators were simultaneously excited. The slideway velocity is about 15 to 20% higher in one direction than in the other, due to the coupling of both modes.

The major disadvantage of this Prototypes 1 and 2 is that the natural frequency of the mode that generates the thrust force can be different from the natural frequency that generates the normal force. This difference must be on the order of 500 Hz for the motor to function properly and it is virtually impossible to fabricate the motor such that both resonances are at the same frequency. Therefore, it must be possible to modify the length or width of one actuator or change the attached mass to fine-tune the frequencies. This could not be done, because all alterations of these designs influenced both mode shapes and resonant frequencies to about the same extent. If, for example, the length of one actuator is reduced, each individual resonance increases, but the difference between these values does not change significantly.

Prototype 3 Prototype 3, illustrated in Figure 4, was designed to eliminate the coupling between different mode shapes. The shape is basically the T-shaped Prototype 2 without the bottom part of the T. This design also changed the loading of the glue joints from tension to shear. It consists of two piezoelectric plates with a thin brass electrode between them. The electric field is applied between one of the electrodes on the outer surface (1) or (2) and the brass electrode in the center. Applying a sinusoidal voltage at the outer electrodes (1) extends and contracts the upper half of the actuator and thus excites the bending mode. An electric field that extends across the actuator will excite the longitudinal mode of vibration. This is done by applying voltage to the inner electrodes (2). Prototype 3 uses the fifth bending mode to generate a dynamic normal force and the 2nd longitudinal mode to generate sliding motion in a very similar manner to Prototype 2. Because these two modes are orthogonal, it is virtually impossible to have any interaction between them.

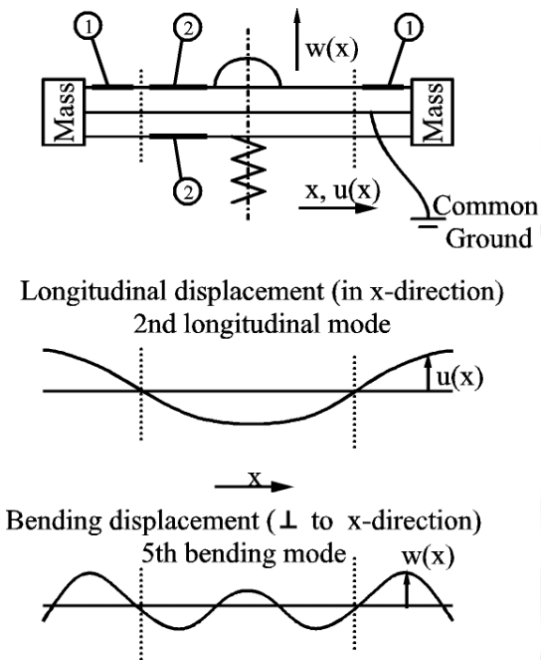

Figure 4: Prototype 3

Initial measurements of the frequency spectrum for the forces at the tip indicated that the resonances for the normal force and for the thrust force differ by about 2 kHz. This difference

was reduced by carefully adjusting the mass at the ends of the motor. However, this design was not capable of generating slide motion because the maximum dynamic normal force of ±4N was not sufficient to overcome the static frictional forces induced by the slideway preload.

4.4 FINAL MOTOR DESIGN

The final design of the ultrasonic motor is as shown in Figure 5. This design is similar to Prototype 3 but the orientation of the actuator is perpendicular rather than parallel to the slideway. This configuration is more efficient because it uses vibration modes of the lowest possible order and the longitudinal mode is used to generate the dynamic normal force. The result is an actuator that allows separate excitation of the first longitudinal mode of vibration and the second bending resonance. Exciting electrodes 2 and 5 with a sinusoidal excitation voltage excites only the longitudinal vibration mode. This allows the adjustment of the dynamic normal force at the tip such that the normal force alternates between almost no compression and twice the preload. The bending vibration is effectively excited with a sinusoidal voltage at electrodes 1 and 4 and with the inverse of this voltage at electrodes 3 and 6.

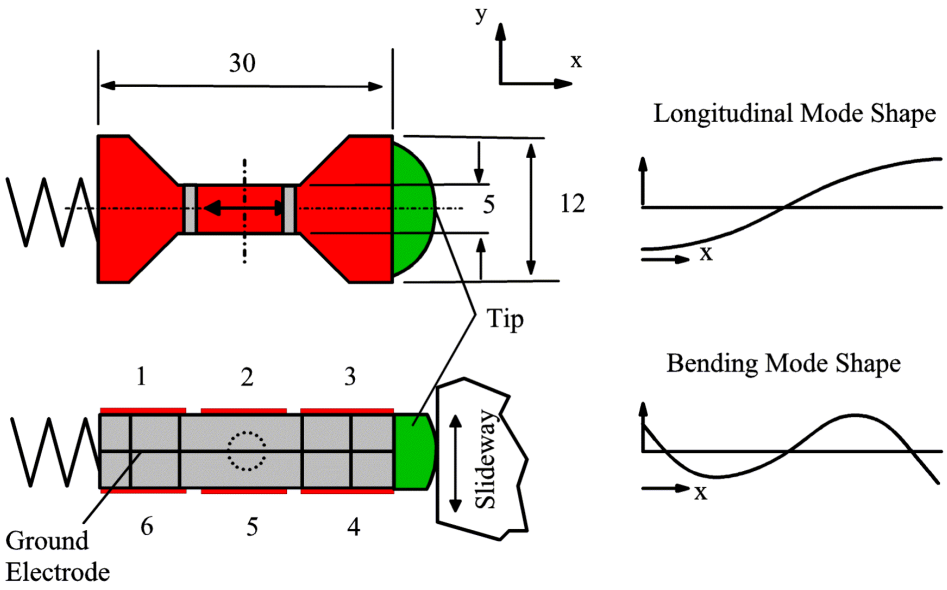

Figure 5. Final Actuator Design and Operating Modes

Variation of the bending excitation or the phase between bending and longitudinal excitation can be used to control the slideway velocity. In either case, the problems associated with the slip-stick effect at slow slideway velocities are eliminated, because once per cycle the normal load goes to zero and even a small thrust force will initiate sliding between motor tip and slideway. The most efficient motor operation can be achieved when the phase is close to 90° and variation in the amplitude of the bending vibration is used to set the slideway velocity.

4.5 MOTOR PERFORMANCE

The final motor design was studied extensively in both the open and closed loop modes of operation. It satisfied the objectives of the project to independently control the two modes of motion: one in the normal direction and the other along the motion direction of the slideway.

4.5.1 OPEN LOOP PERFORMANCE

Figure 6 shows series of measurements of the slideway velocity when a constant bending excitation is applied to an initially motionless slideway. In this experiment, an air bearing spindle is used as the slideway. Its inertia is equivalent to a linear slideway with a mass of 2.28 kg. When the excitation voltage is applied, the slideway accelerates until a steady state velocity is reached. The steady state slideway velocity is linearly proportional to the bending excitation. This becomes apparent when the steady-state slideway velocity from the measurement in Figure 6 on the left is plotted as a function of the excitation voltage as done in Figure 6 on the right. It should be noted that the initial acceleration is virtually independent of the excitation amplitude. Instead, it depends on the preload, the accelerated mass, the coefficient of friction, and the phase.

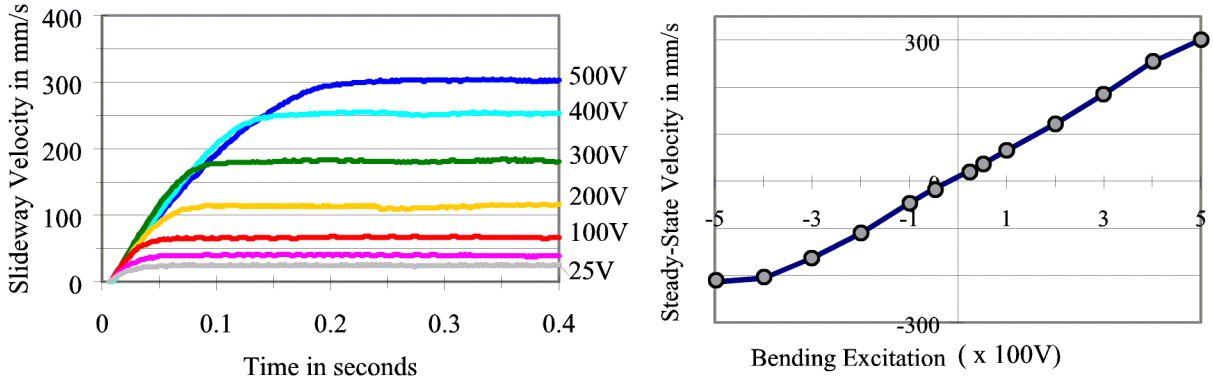

Figure 6. Slideway Velocity for Constant Bending Excitation

The measurements show that unlike most conventional standing wave motors, any excitation of the bending amplitude or thrust force results in slideway motion. The smallest obtainable constant slideway velocity is essentially limited by the noise and the linearity of the electric components that generate and amplify the sinusoidal excitation voltage.

4.5.2 CLOSED LOOP POSITION CONTROL

To evaluate the ability of the motor to position the slideway, it has to be tested in a closed loop control system. A block diagram of this system is shown in Figure 7. The computer-motor interface transforms the control parameter into the signals that are able to drive the motor. The

two voltages that oscillate at the motor frequency of 40kHz are modulated such that the control parameter is proportional to either the phase angle between both motor vibrations or to the amplitude of the signal that excites the thrust force. A sampling rate of 500Hz was chosen. Three power amplifiers are used to achieve a maximum output voltage of +/- 500V at the actuator. The slideway position, the goal of the control effort, is measured using an incremental encoder with a resolution of 11.08μm and compared to the commanded position. The error is the difference between commanded and measured slideway position, which is the basis for the control algorithm to compute the appropriate motor control value.

It seems practical to use a single transfer function that represents the behavior the computer-motor interface, the power amplifiers and the motor-slideway system. This transfer function $G_m(s)$ describes the slideway position (x) as a function of the control parameter (bending amplitude). The use of another control parameter requires a different transfer function. As sketched in Figure 6, excitation of the motor primarily leads to the slideway velocity. In the effort to relate the slideway position, the goal of the control effort, to the actuator excitation, the slideway position is proportional to the integral of the actuator excitation. Even if a proportional gain controller is used, any position error results in an actuator excitation (which is proportional to the error). Because the motor generates slideway motion until the error is zero, the steady state error is zero for an ideal implementation of this principle. In this respect, the ultrasonic standing wave motor has the same characteristic as electromagnetic motors.

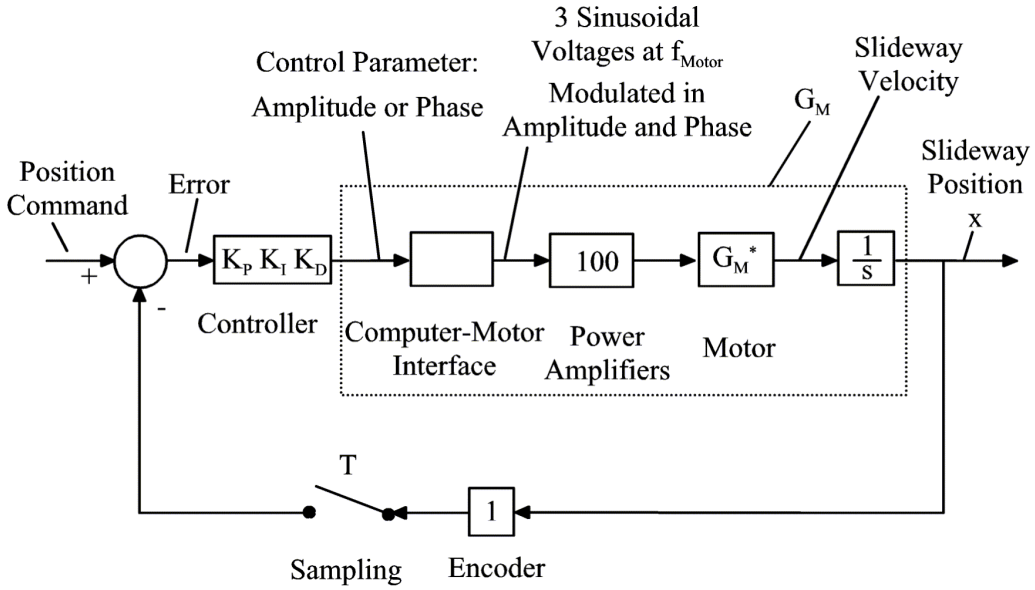

Figure 7. Block Diagram for Motor-Slideway System

Transfer Function To characterize the behavior of the ultrasonic motor, it may be useful to determine the transfer function of the motor G_m. This transfer function is a function of the excitation voltage and the system response such as position, velocity and acceleration. A

simplified equation of motion was developed from the open-loop measurements as shown in Figure 6 can be expressed as:

$$\ddot{x} \cdot U^* + \dot{x} \cdot K_1 = K_2 \cdot U \tag{1}$$

where $U=U^*$ excitation voltage

x coordinate of slideway motion (in mm)

The constants $K_1=10V/s$ and $K_2=600mm/s^2$ were determined by matching initial acceleration and steady-state velocity to the open loop measurements that are presented in Figure 6. They depend on slideway mass (2.28kg), friction (μ=0.2), preload (10N), phase (=90°), the specific performance of each individual actuator and the longitudinal actuator vibration (± 10N) at a frequency of 40kHz. Note that this equation is made under the assumption that an excitation of the bending vibration is used to control the slideway motion.

To directly derive the transfer function G_m from the equation of motion (4.2), the system's response ($\ddot{x}, \dot{x}$ *and* x) must be expressed as a function of the input variable U. The term $\ddot{x} \cdot U^*$ makes the equation nonlinear. The equation can be linearized by replacing U^* in equation (1) with a constant voltage. In order to achieve a fast response the motor needs to run at maximum speed for as long as possible. As the bending excitation is limited to 4.5 V (into the power amplifier or 450V at the motor), large changes in position saturate the motor excitation, which introduces another nonlinearity to the system.

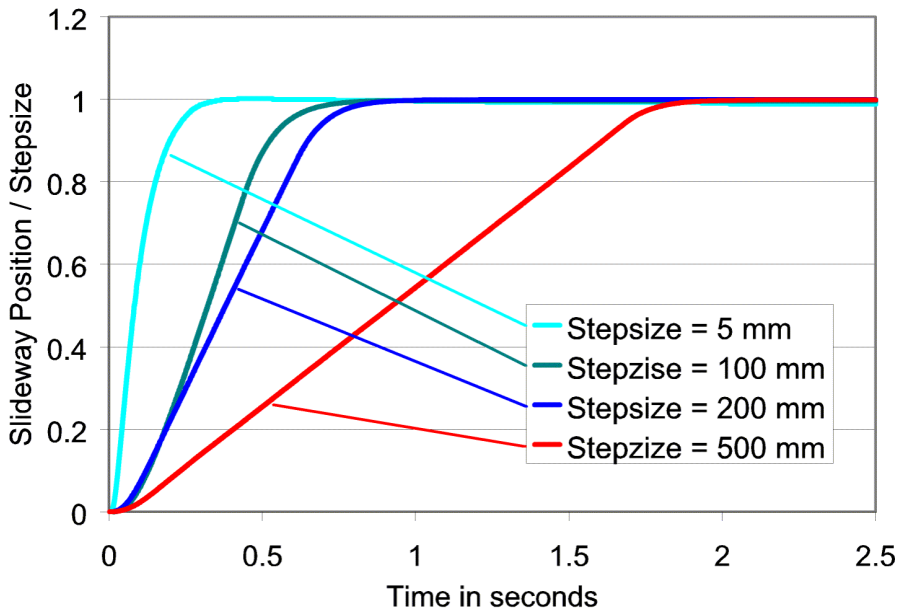

Figure 8. System Response to a Step Input using P-Feedback Control (K_p=0.15)
Preload ca. 10N, Slideway Mass = 2.3kg

Closed Loop System Response Figure 8 shows the response of the system to step inputs of different magnitude. The controller uses only proportional gain which was empirically adjusted to a value of K_p=0.15, which results in the fastest response time without overshoot. The average slideway velocity for the 500mm step input is 260mm/s, only slightly below the maximum open loop motor velocity of 300mm/s. Smaller gains result in slower response times and larger gains lead to overshoot. Despite the non-linear properties that were mentioned above, measurements show proportional gain algorithm leads to a stable, responsive positioning system.

Steady State Errors As a very basic assessment of the motor-slideway behavior, is can be said that the input variable (bending excitation) leads to slideway velocity. Slideway position, which is the integral of velocity, is the goal of the control effort. Without using additional control algorithms, the steady state error of such systems in closed loop configuration is zero, provided the system is stable:

$$\frac{X(s)}{C(s)} = G_{CL}(s) = \frac{K_p\ G_m(s)}{1 + G_m(s)} \tag{2}$$

Assume the motor transfer function (linearized for 500V excitation, based on the model) has the form:

$$G_M(s) = 60 \cdot \frac{2}{s^2 + 2 \cdot s} \tag{3}$$

The error is : $$E(s) = X(s) - C(s) = C(s) \cdot (1 - G_{CL}(s)) \tag{4}$$

The steady state value is given by applying the final Value Theorem [2]:

$$e_{steady-state} = \lim_{s \to o} s \cdot E(s) = \lim_{s \to o} s \cdot C(s) \cdot (1 - G_{CL}(s)) = \lim_{s \to o} C(s) \cdot s \cdot \left(1 - \frac{120K_p}{s \cdot (s+2) + 120K_p}\right) \tag{5}$$

For a step input, C(s)=1/s,the (theoretical) steady state error is zero.

$$e_{steady-state} = \lim_{s \to o} s \cdot \frac{1}{s} \cdot \left(1 - \frac{120K_p}{s \cdot (s+2) + 120K_p}\right) = 0 \tag{6}$$

However, for a ramp input, $C(s) = \frac{K_c}{s^2}$,the steady state error is:

$$e_{steady-state} = \lim_{s \to o} s \cdot \frac{K_c}{s^2} \cdot \left(1 - \frac{120K_p}{s \cdot (s+2) + 120K_p}\right) = \lim_{s \to o} K_c \cdot \left(\frac{s+2}{s \cdot (s+2) + 120K_p}\right) = \frac{K_c}{60K_p} \tag{7}$$

For an ideal implementation of the system characterized by the (theoretical) transfer function G_m, Equation (6) states that the steady state position error for step inputs is zero. The relationship in Equation (7) shows that the (theoretical) steady state error for a ramp input (into the same

system) is proportional to the slope of the ramp (comparable to the feedrate) and inversely proportional to the gain K_p. Practically speaking, if the motor has to follow a trajectory or if a external disturbance has the characteristic of a ramp input, a steady state following error will exist. This behavior is not unique to ultrasonic motors. For example, electromagnetic DC servo motor show essentially the same behavior; however the mechanism by which the error is introduced into the system is different.

The effect of a ramp error on the system explains the existence of a small steady state position error (up to 500μm) that was observed during the experiments. Compared to the step size for the measurements shown in Figure 8, an error of 500μm is too small to be distinguished in the graph. It was observed during the experiments, that the size of the steady state position error depends in part on the gain K_p but mainly on the amount of velocity that is generated by the longitudinal actuator vibration. Misalignment of the motor can create a slow slideway motion (up to about 3mm/s), which is independent of the motor control input. However, when integral control is added, it is possible to achieve zero steady-state position error while maintaining the systems response that was achieved using P-control as shown in Figure 8.

4.6 CONCLUSION

This research shows that it is possible to design ultrasonic standing wave motors whose slideway velocity is linearly proportional to the excitation voltage. This is possible by designing an actuator that allows independent excitation of two orthogonal vibration modes at the same frequency. The quality of the operation of the motor depends on the separation of these vibrations. Coupling between longitudinal and bending vibration causes uncontrolled slideway motion, which is responsible for a small steady-state position error that cannot be eliminated using a proportional gain feedback controller. Despite saturation of the control input and nonlinearities in dynamics of the motor-slideway system, it was shown that a simple feedback control system is stable and suitable for controlling the slideway position. A Proportional-Integral controller can be used to achieve a steady-state error within one encoder increment while maintaining the overall performance shown for the Proportional Gain controller.

With overall dimensions of about 35x30x6mm, and a mass of 13g, the final prototype comes in a small and light package that can be used to accelerate any slideway, rotational or linear, to a velocity of 500mm/s with a maximum force of 5N. In addition, the motor is insensitive to changes in the frictional properties and changes in the surface. At this point, the maximum force is limited by the physical strength of the actuator; however, multiple motors can be used to produce larger forces. The motor generates a constant slideway velocity over a range from 1mm/s and 500mm/s, and that speed is linearly proportional to the control input.

REFERENCES

1. US Patent #5616980, April 1, 1997
2. G.Franklin, J. Powell, A.Emami-Naeini, "*Feedback Control of Dynamic Systems"*, 3rd edition, Addison-Wesley 1995

5 DEVELOPMENT OF A MINIATURE ACTUATOR FOR CRYOGENIC APPLICATIONS

Matias D. Heinrich[1]
Graduate Student
Thomas A. Dow
Professor
Department of Mechanical Engineering

The Next Generation Space Telescope is designed to utilize a large optical mirror that must collapse to fit in the cargo bay of the Shuttle Orbiter. Once transported to the cryogenic environment of space (20 to 60 K), the mirror must be unfolded and the focal point adjusted using many small actuators. These actuators need a stroke of 10 mm, resolution on the order of 10 nm and a design life of 10,000 to 100,000 cycles. The actuator design must also hold position in a power-off mode. The number of actuators is undecided but is expected to be in the range of 100 to 2,500. Conventional low voltage piezoelectric materials offer a low cost and low power consumption solution but stroke at cryogenic temperatures is significantly reduced. The prototype is based on a precision 80 pitch screw that has inherent power-off holding for axial loads. Displacement is accomplished by rotating the screw relative to a fixed nut using piezoelectric actuators for clamping and rotation. Several designs where built and operated successfully at room temperature and the final design was also tested at liquid nitrogen temperatures (77 K). This design had a displacement of 7.7 nm/cycle with 0.2 N load and 5 nm/cycle at 0.5 N load operating at 2 Hz cycles. A small cold testing chamber was built with the prototype submerged in liquid nitrogen. Running the prototype under these conditions showed displacement of 0.5 nm/cycle.

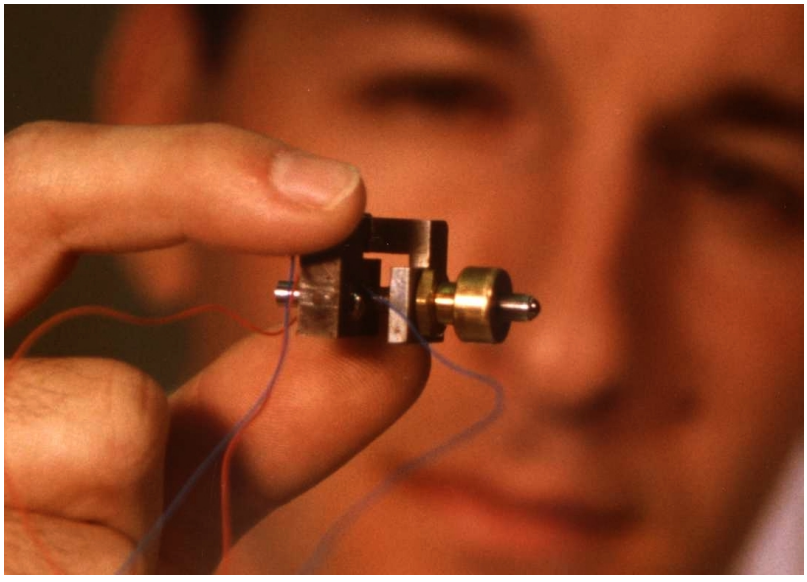

[1] Currently at Vistakon, Inc in Jacksonville, FL

5.1 INTRODUCTION

A goal of the Next Generation Space Telescope (NGST) is to detect object 400 times fainter than what is detectable from other infrared, ground-based, telescope systems such as the Keck Observatory or the Gemini Project. The proposed design includes a mirror 8 meters in diameter (vs. 1.4 m on the Hubble Space Telescope). NGST will be transported using the space shuttle orbiter or other Evolved Expendable Launch Vehicles (i.e. Titan and Atlas rockets). However, the cargo bay capacities cannot accommodate either the size or weight of a single piece 8 meter mirror. The solution is to build the primary mirror from an adjustable, reflective surface. Tentative designs include a flexible, thick-film like plate or several smaller mirrors, each with a fixed reflective surface shape that can be adjusted independently from other sections. In either case, the primary mirror shape will have to be adjusted using many smaller actuators. For the thick-film plate, a matrix of these actuators will push against the non-reflective side of the plate.

These actuators are one of the major challenges of the NGST project and a number of requirements and goals have been set. The requirements are the specifications that are needed for the design to be effective and the goals are the specifications that would aid in the final design, assembly and testing but are not absolutely critical. The key requirements of interest in this design are: resolution less than 20 nm, a range larger than 6 mm and the capability to hold the setting in a power-off condition. Since the intended environment for the device is space, it must operate under cryogenic conditions.

Linear motors utilizing piezoelectric actuators seem obvious solutions with products such as Burleigh's Inchworm or the New Focus Picomotor. However, piezo ceramics show extremely diminished strain in cryogenic temperatures (approximately one-sixth of that at room temperature). Recently, TRS Ceramics from State College, Pennsylvania, has developed a single crystal piezoelectric material. This material is capable of producing strains in cryogenic environments similar to those of conventional piezoelectric ceramics at room temperature. However, it is much less rigid than the conventional materials limiting its application to these applications.

Other challenges must also be addressed in these designs including size, weight and power off set-and-hold. One way to address the power off set-and-hold is to build the device such that a fine pitch screw is rotated inside a fixed nut to produce axial displacement. Because of the small pitch angle of the threads, axial load is not enough to overcome rotational friction thereby producing no motion.

5.2 DESIGN OF PIEZOELECTRIC MOTORS

Traditionally, there are two types of precision piezoelectric motors: the first is an Inertia Clamp design that relies on the mass, acceleration and applied forces (including variations between static and dynamic friction) of the system. The second is an Active Clamp design that relies more heavily on static friction and clearance between actuators and displacing components.

5.2.1 INERTIA CLAMP DESIGN

Conventional piezoelectric ceramics are often used for precision motion control such as in the New Focus Picomotor [3] seen in Figure 1. This device depends on the difference between the static and dynamic coefficient of friction at the screw/nut interface to convert the small displacement of the piezoelectric crystal to a useful rotation of the screw. A slightly elongated nut can be distorted with a piezoelectric actuator (PZT). The rapid expansion coupled with the inertia of the screw will force the threads on each side of the nut to slide in opposite directions. When the piezo is slowly retracted, the friction in the threads provides the torque to turn the screw in a stationary nut (not shown) and thus extend the end of the screw.

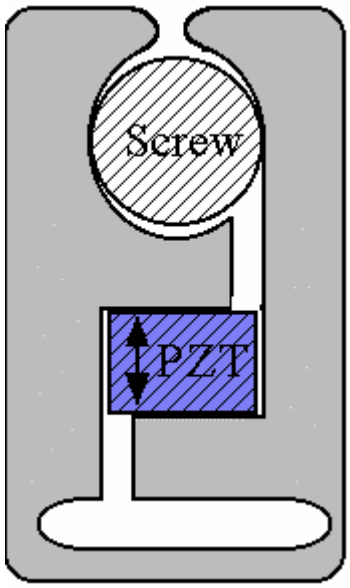

Figure 1. New Focus Picomotor

This is a relatively inexpensive device (~$400) but the current design is not acceptable for the cryogenic environment. First, the difference between the static and dynamic friction coefficients needed for the operation of the Picomotor may not be the same in space environment as at room temperature. Second, the strain available from the standard polycrystalline materials is severely reduced at low temperatures.

Another inertia clamping system was developed by Steward Observatory at the University of Arizona (see Figure 2). This design also utilizes a fine pitch screw but instead of piezoelectric actuation, it uses electromagnets to produce an impulse force. The impulse force accelerates the nut suspended by three flexures. The friction force between the nut and screw accelerates the screw but at the same time the nut is slowing down as it winds up the flexures. When the nut and screw reach the same velocity, the friction between the two is a maximum and the flexures slow down and stop the nut and screw. The energy stored in the flexures then unwinds the nut and returns it to the nominal position returning the screw with it. Since the screw slipped relative to the nut in the first part of the stroke, but not during the return part, the screw undergoes net rotational displacement and thus an axial displacement as well.

To model this system, a finite difference program was created that estimated the forces, displacements and directions of each component during one cycle. Variables such as the geometry of the screw and nut (diameter, mass), velocity of the mass when it hits the nut and properties of the flexures (thickness, length and width) were varied and the final displacement of the screw was calculated. This model was used to study the sensitivity of the system to operating conditions (such as friction) and the dimensions of each component.

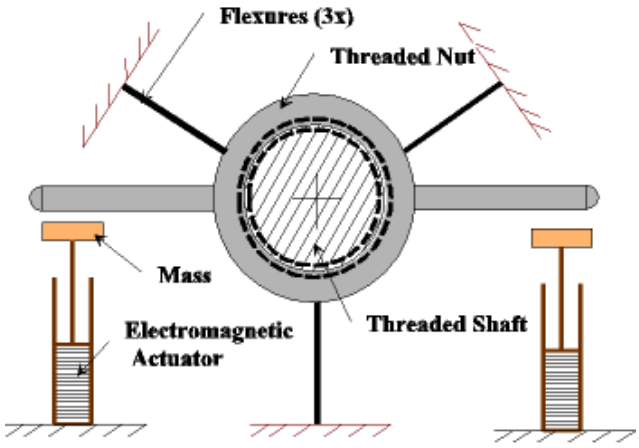

Figure 2. Steward Observatory Design

A major concern is magnitude and velocity dependence of the friction in a space environment and how much that will affect resolution and displacement. Smooth surfaces in a vacuum, such as space, tend to stick together and create very large friction coefficients. The friction will also produce a hysteresis effect when these motors switch directions. This hysteresis is due to the deforming nut (Picomotor) and flexures (Steward Observatory) not returning to the nominal position after every cycle.

5.2.2 ACTIVE CLAMP DESIGN

An active clamp design differs from an inertia clamp in that it relies on static friction to cause motion and clearance (or very little contact) for retraction. Burleigh's Inchworm [2] is a commercial example of such a design. These types of actuators rely on a clamping-displacing-unclamping-retracting cycle on a slideway or bar. The PEC has created an active clamping design based around a fine pitch screw similar to those mentioned above. The actuator, designated the "Cryoworm", uses one piezoelectric actuator for clamping a screw and a second actuator to cause rotation. The design of the clamping nut is shown in Figure 3. It was built around a slightly modified #8-80 screw where the threads were machined off on a portion. This portion allows the nut to clamp the screw on a smooth surface eliminating damage to threads and reducing wear of the alumina tip. Another threaded nut, which is attached to ground, converts the rotational motion

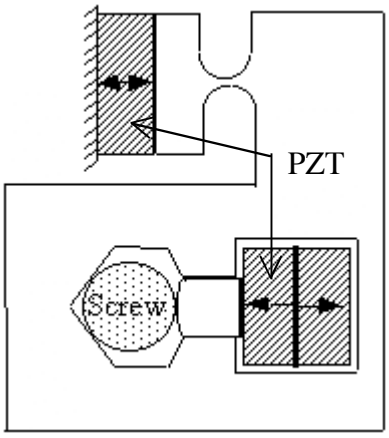

Figure 3: Clamping Nut of Cryoworm

into axial motion.

Two square waves, 90° out of phase, are used to drive the clamp and rotation actuators. Figure 4 shows 3 cycles of the clamp/rotation process. The process starts with the rotational actuator, which is energized at about 8 seconds in Figure 4. A large step in the displacement of the end of the screw accompanies this actuation step because the screw is pushed radially in the stationary nut and the screw tends to move axially due to the shape of the threads. The clamp actuator is then actuated (at 10 sec) to attach the screw to the clamping nut. This action also moves the screw in the nut and produces a step. The next step is to de-energize the rotational actuator (at 14 sec) which results in a drop in the displacement by removing the side load on the screw. Finally, the clamp force is removed from the screw at 16 sec and the new position of the end of the screw is reached. For the three cycles shown in Figure 4, the average motion for each step is 3.6 nm.

There are a number of design issues that need to be addressed. A large preload on the end of the screw will reduce the step deflection discussed above by keeping the screw centered in the nut.

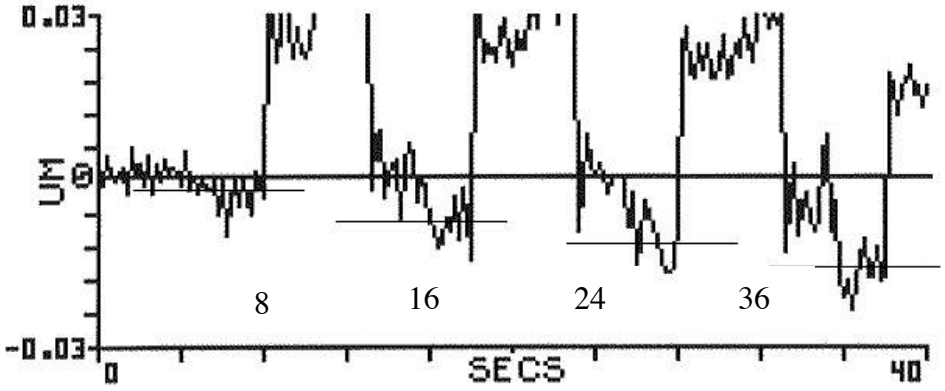

Figure 4: Capacitance Gage Measurement of Three

The stiffness of the flexure both axially and rotationally plays an important role on the operation of the motor. If it is too stiff in bending, it will induce a lateral load on the screw but no rotation. If the axial stiffness is too low, it will waste the small stroke of the piezoelectric stack without causing rotation. A possible solution is to redesign the clamping nut with two symmetrical rotational PZT's on either side of the screw. With this configuration, the forces created by the two bending flexures are cancelled out thereby transferring only a moment.

5.3 DESCRIPTION OF THE FINAL DESIGN

The Mark 3.1 is the result of a series of active-clamp prototypes designed for the NGST system. This design is an improvement of that described above that integrates the front endplate, columns and standoffs into a single component call the "integrated front endplate". This steel component allows the rotational nut and actuators to be directly mounted to the rigid endplate rather then to the more compliant components (the column and standoff of the 3.0 design). Without the need for screws to hold the columns to the end plate, the structure is shorter (25%) reducing the distance between the clamping brass nuts and end plates. This increases the stiffness of the structure in the axial direction, which also improves the clamping effect. Additionally, the integrated front endplate eliminates parts, reduces cost and is easier to assemble. A sketch of the design is shown in Figure 5.

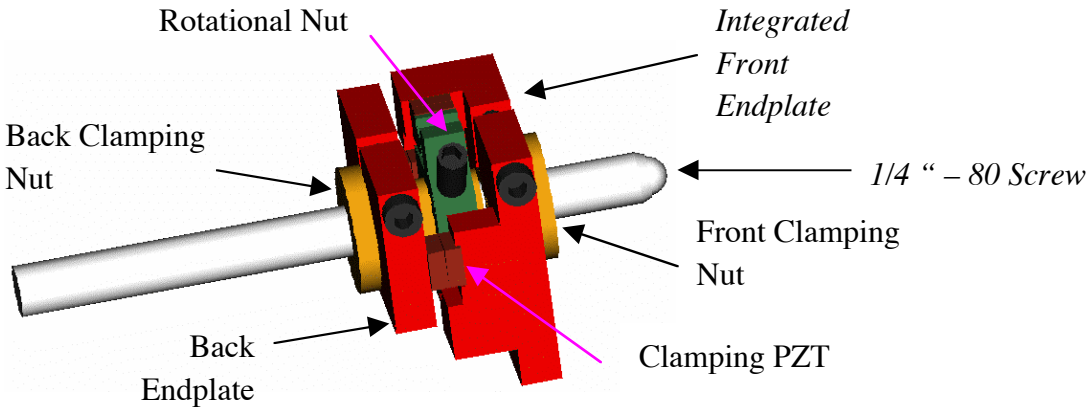

Figure 5. Overall view of the actuator prototype

5.4 ACTUATOR OPERATION

Operation of the actuator involves four steps:

1) the rotational nut is forced to rotate around the center of the screw by a pair of piezoelectric actuators and it carries the screw along with it;
2) the clamping actuators push the front and rear clamping nuts apart increasing the friction needed to rotate the screw;
3) the rotational nut is deactivated and it rotates back to its initial position but without the screw; and
4) the clamping actuators are released.

Each step of the actuator can be viewed in the axial motion of the screw as observed in Figure 6. The first step (rotating the screw) is seen as a small upward sloping motion displacement (1). The next step (2) is to clamp the screw which sends it away from the load as a sharp downward

motion of about 1μm. This is caused by the clamping actuators pushing the clamping brass nuts apart and increasing the axial load on the front clamping brass nut. The screw/nut interface at the front clamping brass nut is supporting the axial load F. When the clamping actuators are energized, the force on the front nut is increased, and as a result, the nut is pushed away from the load.

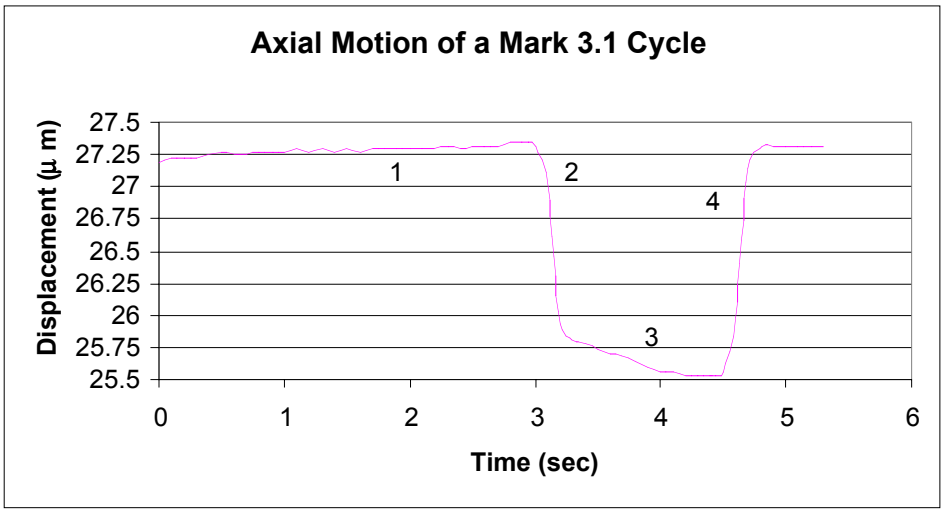

Figure 6. Axial motion of Mark 3.1 for one Cycle

The third step (3) in the displacement motion of Figure 6 is a result of de-energizing the rotational actuators to move the rotational nut its nominal position. Because the screw is clamped, there should be no axial motion of the screw. However, some motion is evident in Figure 6, which has two possible sources. The first is creep of the clamping actuators; that is, rapid displacement for the majority of their stroke (from step 2) followed by slow creep for the remainder. The continuing downward slope from segment 2 to segment 3 of the cycle could be attributed to creep. Another possible source of motion is radial forces on the screw generated when the rotational nut and modified brass rotate back to their nominal position. If the two tensile forces used to generate the moment and rotate the screw are not equal, then the rotational nut will tend to pull the screw radially. Radial forces on the screw create relative motion between the screw and the clamping brass nuts and move the screw. However, this is unlikely because the clamping brass nuts are firmly locked with the screw during this stage of the cycle. Whatever the source, the prototype displaces a small amount during the de-rotation of the screw. The final step (4) in the motion is a large positive jump in displacement upon relieving the clamp load. The positive jump has approximately the same magnitude as the negative jump seen from steps 2 and 3.

5.4.1 Room Temperature Performance

When a series of steps such as illustrated in Figure 6 are strung together, the motion of the actuator can be determined. Figure 7 shows the axial displacement of the Mark 3.1 design for a

series of actuation cycles. An ADE 3940 capacitance gage is used to measure the displacement of the screw, which in this case has an axial load of 0.2 N. The figure shows displacement of the actuator from 60 nm to 300 nm in 31 cycles or 7.7 nm per cycle. The motion of the screw shows evenly displacing steps.

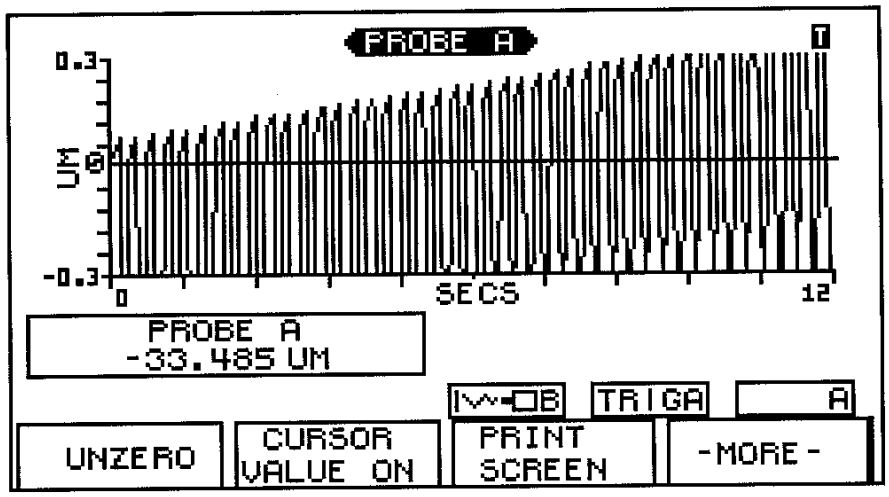

Figure 7. Axial Displacement of Mark 3.1 (0.2 N Preload)

A second test is shown in Figure 8 with a higher preload (0.5 N) on the screw. The added load creates additional friction at the interface between the screw and the front clamping nut that leads to slippage when the rotational actuators are energized to rotate the screw. Consequently, a reduction in displacement is noticed with an average step size of 5 nm/cycle measured from Figure 4.

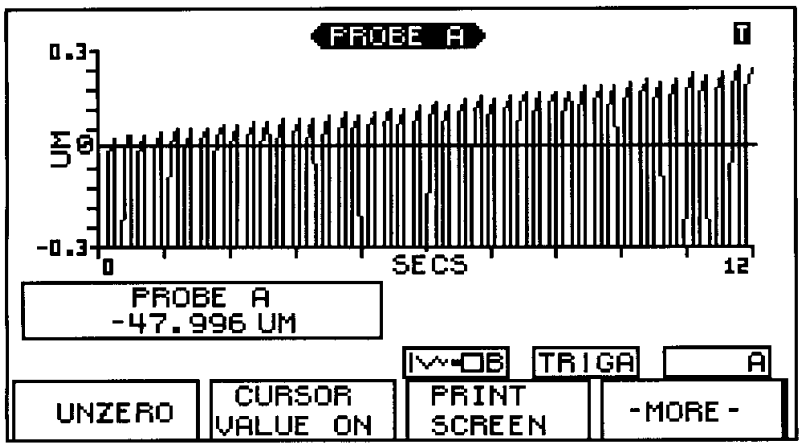

Figure 8. Axial Displacement (0.5 N Preload)

5.4.2 CRYOGENIC PERFORMANCE

To measure the performance of the actuator under cold conditions, the prototype was mounted on a piece of aluminum that rested in a plastic dish filled with liquid nitrogen as shown in Figure

9. The aluminum served as a thermal conductor to extract heat from the prototype to the liquid nitrogen. The dish and the prototype where placed inside of a chamber (150 mm x 150 mm x 100 mm) made from 19 mm R4 closed cell styrofoam. One hole was bored to allow the screw to project outside of the box and another hole to carry wiring as well as a tube transporting nitrogen gas into the chamber. The nitrogen gas was used to purge the chamber for 10 minutes prior to adding the liquid nitrogen to eliminate any water vapor that could condense and freeze on the prototype. A 25 mm diameter hole was cut into the top cover to allow liquid nitrogen to be poured in and minimizing ambient air from entering the chamber during the filling. The parallel loading device was insulated from the screw of the prototype by placing a 6 mm thick piece of red oak on the end of the parallel loading plate. To minimize the Hertzian contact between the bearing ball and the loading device, a small piece of spring steel (1 mm thick) was glued on the other face of the red oak. The parallel loading device was mounted externally on a 19 mm thick piece of solid pine. The pine has a low thermal expansion coefficient to reduce thermal effects when nitrogen vapor pours through the screw hole, around the screw of the prototype and onto the wood.

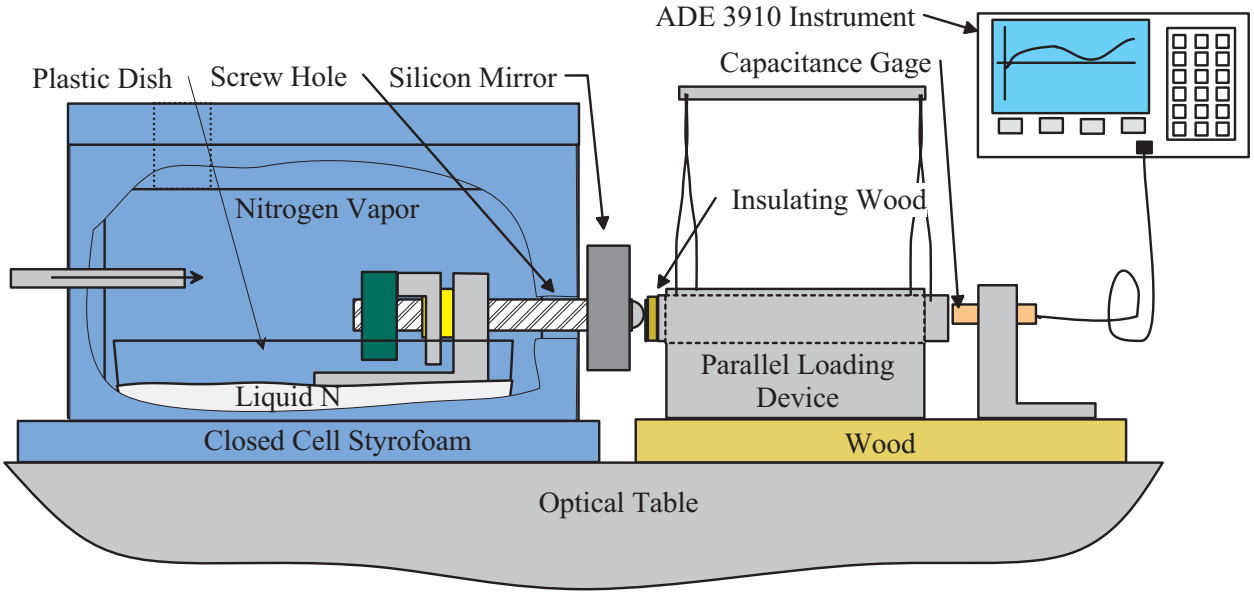

Figure 9. Cryogenic Testing Apparatus

To measure displacement, a small silicon mirror was attached to the portion of the screw exposed to the ambient air. A laser beam was pointed at the mirror and the reflected light was aimed at a large flat wall located 3.53 m from the center of the screw. As the prototype is powered and begins to displace, the rotation of the screw is tracked by the reflected image on the wall. The setup gives the advantage of magnifying the rotation of the screw such that a one degree rotation of the screw will cause a two degree sweep of the laser beam. Knowing the distance from the wall to the center of the screw and measuring the change in position of the laser beam on the

wall, the angular rotation of the screw can be easily calculated. Also, the axial displacement is calculated knowing the pitch of the screw.

Cryogenic Testing Procedure The test procedure began by marking the laser beam on the wall. A stopwatch was started when the compressed nitrogen was started. After 10 minutes, the one inch hole in the lid was uncovered and two cups of liquid nitrogen where poured into the chamber. Every five minutes, a half-cup of liquid nitrogen was added into the chamber. Forty minutes into the experiment, the prototype was started by sending the clamping and rotation signals from controller with a frequency of 1 Hz. The reflected laser beam disappeared due to the condensation and frost buildup on the silicon mirror so the actual minute-by-minute displacement could not be tracked. After 5 minutes, the actuator was stopped having undergone 300 cycles. The apparatus was then left undisturbed allowing everything to warm up to room temperature. As the ice melted off the silicon mirror and the water evaporated, the laser beam reappeared and a final reading was taken when the apparatus reached equilibrium with the room temperature; approximately 3 hours was needed for the entire experiment.

Performance at Cryogenic Temperatures To verify the design of the experiment, three experiments where preformed. The first was done at room temperature. The displacement of the laser beam was tracked on a minute by minute basis. The displacement was 28 mm/min at a distance of 3.53 m from the actuator. Based on the laser path and the pitch frequency of the threads (317.5 μm/rotation), the displacement was 6.7 nm/cycle; that is it reproduced the results discussed in Figures 7 and 8.

The second experiment was performed using cryogenic conditions but the minute-by-minute data could not be captured due to mirror icing; only the start and finish points where noted. The distance between the start and finish point of the laser beam was measured to be 23 mm over an operating period of 5 minutes. This is equivalent to 0.5 nm/cycle. This change seems reasonable due to the expected reduction of the PZT amplitude with temperature.

A third experiment was run to verify that the measured displacement of the actuator during cryogenic testing was true displacement rather then thermal drift. This experiment was identical to that of the second experiment but in this case the prototype was never operated. There was some drift in the setup and the distance between the start and finish point of the laser beam was 3 mm. However, this displacement is much smaller then the 23 mm displacement of the second experiment described above and thus could be ignored.

5.5 CONCLUSIONS

A piezoelectric cryogenic motor has been developed to meet the actuator requirements of the Next Generation Space Telescope. The design objectives for an actuator have been met as follows:

1) **Position resolution requirement 20 nm with a goal of 10 nm. -** The piezoelectric actuator testing has shown that in a cryogenic environment (~80 K) the actuator can take step sizes less then 1 nm/cycle and at room temperature this value is on the order of 10 nm/cycle.
2) **Stroke of the design must be at least 6 mm with a goal of 10 mm** - The actuator is built around a threaded screw and therefore the stroke of the design is governed by the length of the screw minus the length of the chassis. For the Mark 3.1 prototype, the screw length is 65 mm with a chassis length of just under 25 mm. The effective stroke of the design is thus 40 mm, four times greater then the 10 mm requirement.
3) **Operating temperature range of 20-60 Kelvin with a goal of 20-300 Kelvin** - The structure was designed to match the thermal expansion of critical components; e.g. the brass nut on the steel screw and the axial strain of the screw versus the surrounding structure. The same actuator setup (such as preload on nuts) could be used during both the room temperature and cryogenic testing. While no liquid helium facility was available to test the design at 20 K, the design was tested at 77 K and steps as small as 0.5 nm were measured.
4) **Capable of holding a load in place with no power supplied to the actuator** - This is a major requirement of the motor and allows for a satellite telescope to have large quantities of the motor but not require power to hold position. The design of an actuator around a precision high pitch screw using a threaded nut attached to ground allows for built-in power off holding capability.

REFERENCES

1. Brown, R.A. Hubble Space Telescope Web Site. "HST Second Decade," http://sso.stsci.edu/second_decade/
2. Fasick, J.C., "Development of a Nanometer Resolution Constant Velocity Piezotranslator", MS These, N.C. State University, 1998.
3. New Focus.com web site. "MRA and Rotating Shafts" . http://www.newfocus.com/Online_Catalog/6/145/1106/body.html

6 MODELING AND CONTROL OF A MAGNETOSTRICTIVE TOOL SERVO SYSTEM

Witoon Panusittikorn
Graduate Student
Paul I. Ro
Professor
Department of Mechanical and Aerospace Engineering

In spite of high mechanical strain output with a broadband response, a magnetostrictive actuator contains significant hysteresis and is highly nonlinear at moderate to high drives. Full utilization of these actuators requires a feedback loop as well as an advanced control scheme in response to various inputs. The dynamic strokes were measured using an optical sensor. The nonlinear control input was computed based on the elongation errors and the magnetization model investigated by Smith et al. An analytical model for the nonlinear control approach, sliding mode control, was developed. A relaxed Lyapunov stability condition in sliding control scheme was introduced to achieve a simple implementation. The results of simulation supported the validity of the purposed approach. Sliding controller yielded much better tracking performance over PID and open loop control.

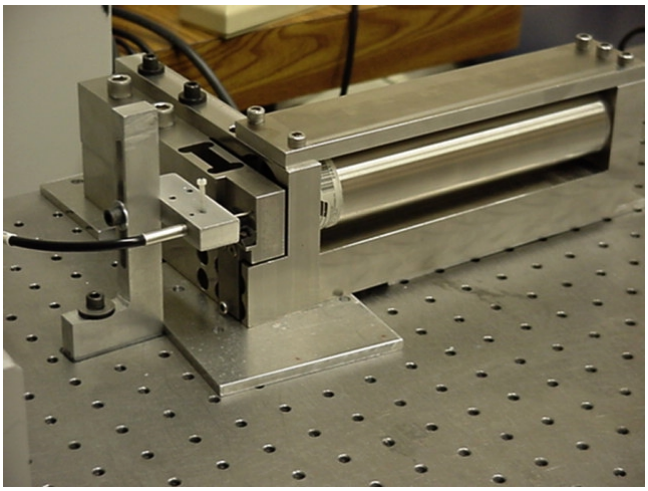

6.1 INTRODUCTION

This paper addresses the modeling and development of the nonlinear control methodology for a magnetostrictive system. As an application of smart materials, magnetostrictive transducers can generate high mechanical strain with a broadband response, and provide accurate positioning. Even though these properties characterize a good tool servo application in precision machining, full utilization of these actuators generally requires an advanced controller as well as accurate model of the transducer dynamics in response to various inputs.

At moderate to high drives, the output from a magnetostrictive actuator contains significant hysteresis and, in effect, is highly nonlinear. The control of this nonlinear tool servo system is a challenging issue.

6.1.1 SMART MATERIALS

Smart materials are substances that have a property to change their shape when they are subjected to a specific type of energy input. For examples, shape memory alloys change their length when heat is applied. Piezoelectric ceramics react when exposed in an electric field. Magnetostrictive materials such as Terfenol-D (Terbium, Fe, the Naval Ordnance Laboratory, and Dysprosium) produce strain in an electro-magnetic field. Also, these materials can release a particular type of energy when they are deformed by an external force.

Magnetostriction Properties

The magnetostriction effect was discovered by 19th century English physicist James Joule [8]. In the presence of a magnetic field, the rotation of small magnetic domains in the materials causes internal strains. These strains result in an elongation in the direction of the magnetic field. When the field is increased, more domains rotate until magnetic saturation is achieved. Since these magnetostrictive forces are molecular in origin, the mechanical response is very fast.

6.1.2 MAGNETOSTRICTIVE TRANSDUCERS

The design of these transducers is to put a rod of Terfenol-D into a metal tube, surrounded by a series of electromagnetic induction coils. The coils generate a moving magnetic field that travels wavelike down the successive winding along the tube. The traveling magnetic field causes each cross section of Terfenol-D to stretch and, then contract when the field is removed, producing a stroke and force output. The amplitude of motion is proportional to the magnetic field provided by the coil system.

The transducers are used in many applications: both civilian and military. The military application is to use smart materials to fine-tune the shape of the airfoil cross section of an aircraft wing in flight, reduce aerodynamic drag, and improve maneuverability. For civilian applications, the transducers are extensively employed for paper production, medical dispensing, automotive accessories such as sunroofs and automotive brake systems.

6.1.3 MAGNETIC HYSTERESIS

When a magnetostrictive material is subjected to a magnetic field, the domains inside the material crystal rotate, resulting in changes of its shape. If the crystal is perfect, the material can expand and contract without loosing energy. However, the crystal usually contains inclusions or pinning sites, which impede the rotation of the domains. The relationship between the applied magnetic field and the induced magnetization displays significant hysteresis and saturation effects at high drive levels as shown in Figure 1. The dashed line represents the anhysteretic (hysteresis-free) magnetization while the solid line portrays the hysteretic magnetization. When the applied magnetic field increases, both magnetizations evolve until they reach the saturation.

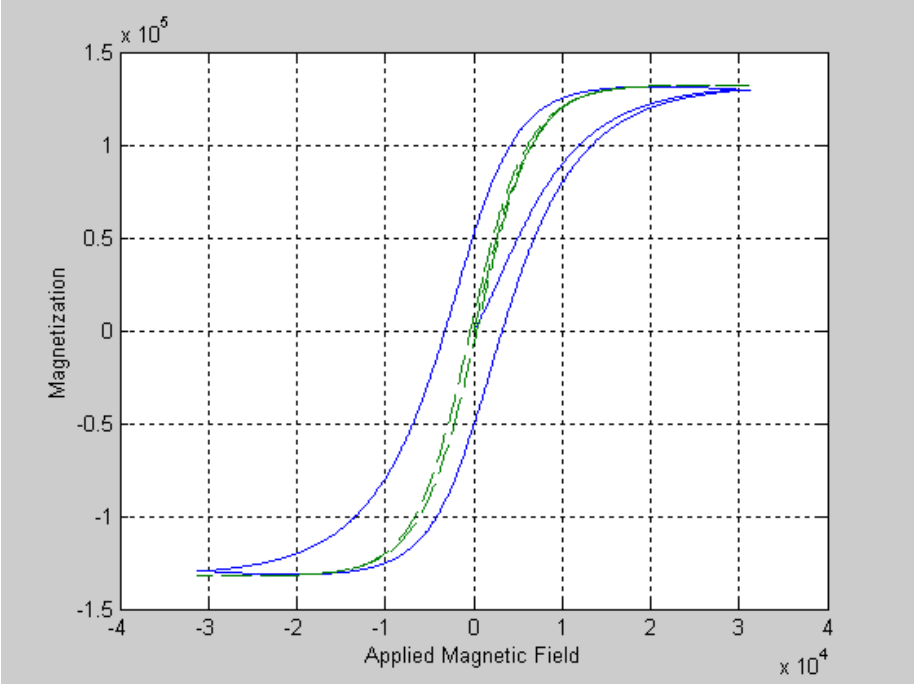

Figure 1: Hysteresis in the Relationship between Applied Magnetic Field and Magnetization

6.2 DETAILS OF THE PROJECT

6.2.1 EXPERIMENTAL APPARATUS

With an optical sensor, the dynamic strokes (displacements) of the actuator can be measured under various voltage inputs at different frequencies and amplitudes. When the dynamics of the actuator is acquired, a DSP board, which integrates A/D and D/A converters, is needed to generate control signal input to the actuator. The control input follows the nonlinear control algorithm in order to deal with the hysteresis and nonlinearities issues.

Based on the feedback signal from measurement, a PID and nonlinear control approach, sliding mode control are developed. A signal is generated through the D/A channel from the DSP board and directed to the actuator. This makes this system a closed loop control system.

Figure 2 shows the layout of a closed-loop magnetostrictive transducer. An optical probe is attached near by the tip of the actuator measuring the dynamic displacements. The data is, then, acquired by using a DSP board, which incorporates with a personal computer. The control input is computed based on the displacement errors and the nonlinear control scheme. The voltage input is given back to the transducer to compensate for the hysteresis and nonlinearities, which cause the inherent displacement errors.

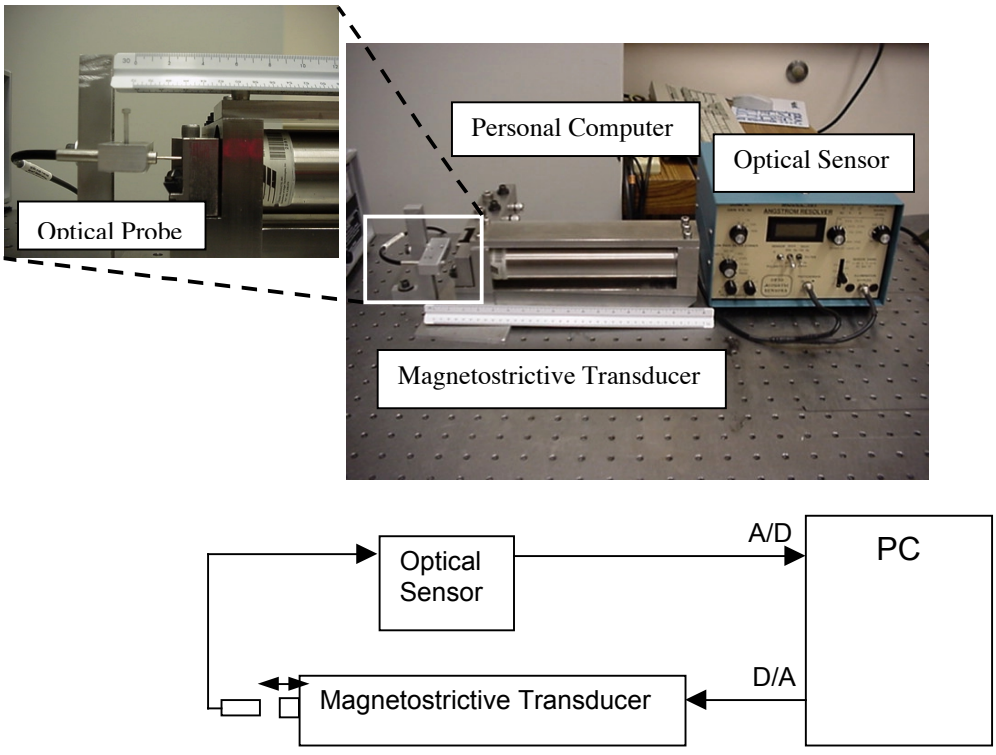

Figure 2: Closed Loop Magnetostrictive Transducer

As a robust control scheme, sliding mode control can offer many good properties, such as insensitivity to parameter variations or uncertainties, external disturbance rejection, and fast dynamic response. In order to obtain better tracking performance and robustness, a sliding mode control algorithm for this magnetostrictive actuator is simulated and tested.

The results from a sliding mode controller will be compared with the results from the open-loop control and PID control, and conclusions will be drawn on the effectiveness of the sliding mode for the control of the magnetostrictive actuator.

6.2.2 MAGNETOSTRICTIVE ACTUATOR MODEL

The magnetization model used to characterize the transducer dynamics is described by Calkins, Smith, and Flatau (1997). The magnetization component of this model is based on the Jiles-Atherton mean field theory for ferromagnetic materials [1-4]. The theory is based on the energy losses due to domain wall intersections with inclusion or pinning sites within the material. For a material, which is free from inclusions, the domain wall movement can be reversible which leads to anhysterestic (hysteresis free) behavior. However, materials such as Terfenol-D contain second phase materials, which impede domain wall movement [5]. At low field levels, domain wall translation about the pinning sites is reversible, resulting in a reversible magnetization. At moderate to high drive levels, domain walls oppose remote pinning sites causing an irreversible magnetization. It is this component which incorporates the energy loss and hysteresis in the materials. Figure 3 shows the data flow in the magnetization model of a magnetostrictive core when the current is given as an input.

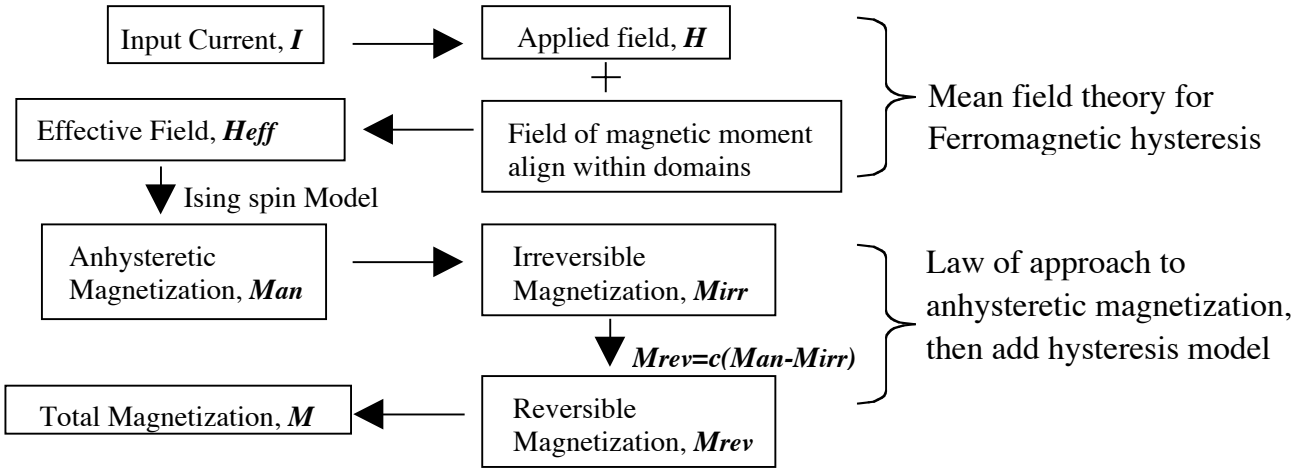

Figure 3: Flow Chart of a Computational Magnetization for a Magnetostrictive Core

The equations of the magnetization model are listed as following:

Equation (1) and (2) show the relationship between input voltage and magnetic field of the coil.

$$\sum V = V_s - IR = V_l \tag{1}$$

where

$$V_l = \frac{d\lambda}{dt} = \frac{d(N\phi)}{dt} = \frac{d(NBA)}{dt} = \mu NA\frac{dH(t)}{dt} \tag{2}$$

Effective field is a combination of the applied field and stress interaction as expressed in Equation (3).

$$H_{eff}(t) = H(t) + \alpha M(t) \tag{3}$$

Using the Ising spin model, Anhysteresis magnetization can be described as

$$M_{an}(t) = M_s\left[\tanh(\frac{H_{eff}(t)}{a})\right] \tag{4}$$

Then, the hysteresis is added to anhysteresis magnetization by computing irreversible and reversible magnetization in Equation (5) to (8).

$$\frac{dM_{irr}}{dt} = n\frac{dI(t)}{dt}\frac{M_{an}(t) - M_{irr}(t)}{k\delta - \alpha(M_{an} - M_{irr})} \tag{5}$$

$$H(t) = nI(t) \tag{6}$$

$$M_{rev}(t) = c\left(M_{an}(t) - M_{irr}(t)\right) \tag{7}$$

$$M(t) = M_{rev}(t) + M_{irr}(t) \tag{8}$$

The strains generated by the magnetostrictive core are given by bulk magnetostriction in Equation (9). It implies that a magnetostrictive transducer produces only positive strains for every magnetization.

$$\lambda(t) = \frac{3}{2}\frac{\lambda_s}{M_s^2}M^2(t) \tag{9}$$

where

V_s Input voltage

R Resistance of the induction coil

V_l Voltage across the induction coil

N, n Number of coil turns and number of turns per unit length

Φ	Magnetic flux
B	Magnetic flux density
A	Cross section area
μ	Permeability of the air closed by the magnetostrictive rod
H	Magnetic field
H_{eff}	Effective magnetization
M	Magnetization
M_{an}	Anhysteresis magnetization
M_{rev}	Reversible magnetization
M_{irr}	Irreversible magnetization
M_s	Saturation magnetization
λ_s	Saturation magnetostriction
λ	Magnetostriction
δ	+1 when $dH > 0$ and -1 when $dH < 0$
α	Magnetic and stress interaction
a, c, k	Constants, which characterize the hysteresis shape

According to the model described above, the computational hysteresis responding to various input voltages is shown in Figure 4. At a moderate drive level of 4 volts, the profile indicates a significant hysteresis, whereas the outline is fairly linear at a low drive level of 1 volt.

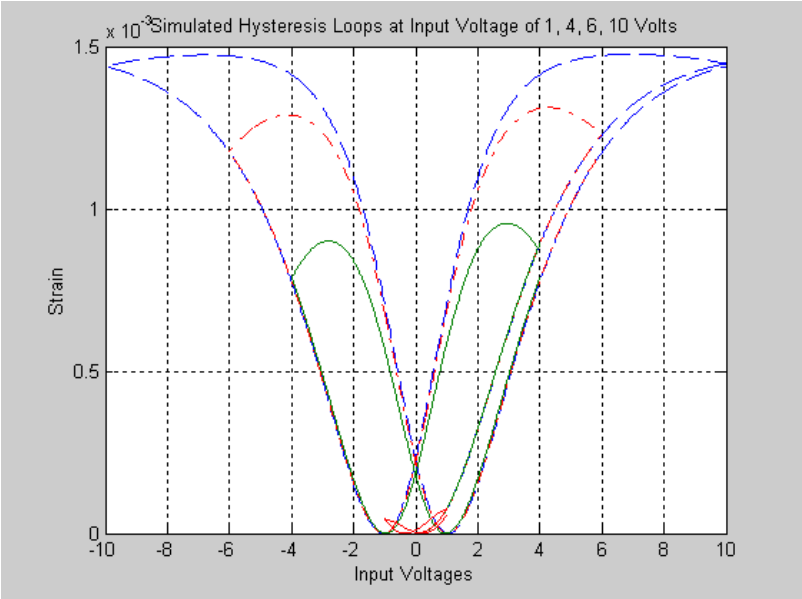

Figure 4: Simulated Hysteresis at Various Input Voltages

6.2.3 SLIDING MODE CONTROL

The modeling inaccuracies can have strong adverse effects on a control system. The model imprecision may come from unknown system dynamics, or intentionally simplifying a representation of the system dynamics. Sliding mode control is a simple approach to a robust control designed to handle with these problems. The typical structure of a robust controller is composed of a nominal part, and additional terms to deal with model uncertainties.

Intuitively, sliding mode control is based on the concept that it is easier to control 1st order system than general nth order systems [6]. Accordingly, a simplification is introduced, which allows nth order to be replaced by 1st order problems. Sliding controller design provides a systematic approach to the problem of maintaining stability and consistent performance in the face of modeling imprecision. Sliding control has been successfully applied to robot manipulators, underwater vehicles, automotive transmissions and engines, high performance electric motors, and power systems.

For a simplified model representation, anhysteretic magnetization is used as a nominal model of a sliding controller and the hysteresis gap is, then, left over as an imprecise model. According to the magnetostrictive model, the elongation (or displacement Y) is the product of magnetostriction and the length l of magnetostrictive rod. Therefore, the nominal displacement is

$$\hat{Y} = \frac{3}{2}\frac{\lambda_s}{M_s^2} M_{an}^2 \times l = \frac{3}{2}\frac{\lambda_s l}{M_s^2}\left(M_s \tanh(\frac{H}{a}) \right)^2 \tag{10}$$

The magnetic field H is proportional to the input voltage V_s, which is an equivalent control input $\hat{U}$ of sliding controller. The nominal displacement $\hat{Y}$, in terms of positive constants k_m and a_m, becomes

$$\hat{Y} = k_m \tanh^2\left(a_m \hat{U}\right) \tag{11}$$

Due to the model simplification, the nominal displacement $\hat{Y}$ does not include some unmodeled dynamics, such as hysteresis gap. The actual displacement Y is

$$Y = \hat{Y} + \Delta Y = k_m \tanh^2\left(a_m (\hat{U} \mp \Delta U_{gap})\right) \tag{12}$$

Define an error e to be

$$e = Y_d - Y \tag{13}$$

while Y_d is a desired displacement.

In order to achieve a good tracking performance, sliding surface S is defined as a combination of proportional and integral terms of the displacement error.

$$S = \Lambda e + \int e dt \tag{14}$$

Once the trajectory reaches the sliding surface $S = 0$. Then, the equivalent control $\hat{U}$ can be drawn from the dynamics $\dot{S} = 0$ as

$$\dot{S} = \Lambda \dot{e} + e = \Lambda \dot{e} + (Y_d - \hat{Y}) = 0 \tag{15}$$

$$\Lambda \dot{e} + Y_d = k_m \tanh^2 (a_m \hat{U}) \tag{16}$$

$$\hat{U} = \frac{1}{a_m} \tanh^{-1} \sqrt{\left| \frac{\Lambda \dot{e} + Y_d}{k_m} \right|} \tag{17}$$

Observably, the actual displacement Y in Equation (12) has the sign of ΔU_{gap} corresponding with the direction of the displacement trajectory. The increasing displacement, for example, lets ΔU_{gap} be negative. However, this sign change is in the opposite direction to the sign change of sliding surface S. Accordingly, the actual displacement Y is obtained as

$$Y = k_m \tanh^2 \left(a_m (\hat{U} - \Delta U_{gap} \operatorname{sgn}(S)) \right) \tag{18}$$

The Lyapunov stability criterion is used to derive a sliding condition such that the sliding surface $S = 0$ can be reached within a finite time. The sliding condition is obtained as

$$S\dot{S} \le -\eta |S| \tag{19}$$

where $\eta \ge 0$.
By including the parameter uncertainties, the sliding condition is

$$S\dot{S} = S(\Lambda \dot{e} + Y_d - Y) = S\left(\Lambda \dot{e} + Y_d - k_m \tanh^2 \left(a_m \left(U - \Delta U_{gap} \operatorname{sgn}(S) \right) \right)\right) \le -\eta |S| \tag{20}$$

From Equation (18), the condition, then, becomes

$$S\left(k_m \tanh^2 (a_m \hat{U}) - k_m \tanh^2 \left(a_m \left((\hat{U} + \Delta U) - \Delta U_{gap} \operatorname{sgn}(S) \right) \right)\right) \le -\eta |S| . \tag{21}$$

Separating the sliding surface into its magnitude component and sign results in

$$S = |S| \times \mathrm{sgn}(S)$$

$$|S|\,\mathrm{sgn}(S) \times k_m \left(\tanh^2(a_m \hat{U}) - \tanh^2\left(a_m\left((\hat{U} + \Delta U) - \Delta U_{gap}\,\mathrm{sgn}(S)\right)\right)\right) \le -\eta |S| \tag{22}$$

In order to satisfy sliding condition in the presence of uncertain dynamics of *Y*, a discontinuous term is added to the nominal control input. Then, the sliding control input is

$$U = \hat{U} + \Delta U = \hat{U} + k\,\mathrm{sgn}(S)$$

For a positive *S*, Equation (22) is re-expressed as

$$\tanh^2(a_m \hat{U}) - \tanh^2\left(a_m \hat{U} + a_m(k - \Delta U_{gap})\right) \le -\frac{\eta}{k_m}$$

or

$$\tanh^2(a_m \hat{U}) + \frac{\eta}{k_m} \le \tanh^2\left(a_m \hat{U} + a_m(k - \Delta U_{gap})\right)$$

Since the range of hyperbolic tangent is from zero to one, and the magnitude of the displacement k_m is very small i.e. 250e-6 m, the constant η must be very small. For simplification, the stability condition parameter $\eta = 0$, then the switching gains is simply

$$k \ge \Delta U_{gap} \tag{23}$$

For a negative *S*,

$$-\tanh^2(a_m \hat{U}) + \tanh^2\left(a_m \hat{U} - a_m(k - \Delta U_{gap})\right) \le -\frac{\eta}{k_m}$$

$$\tanh^2\left(a_m \hat{U} - a_m(k - \Delta U_{gap})\right) \le \tanh^2(a_m \hat{U}) - \frac{\eta}{k_m}$$

With the same reason as the case of positive *S*, the stability condition parameter $\eta = 0$, then

$$k \ge \Delta U_{gap}$$

Even though the outcome is quite a simple form, one question remains on how to obtain the magnitude of hysteresis gap ΔU_{gap}. The gap is not known in advance, nor constant for every magnitude of the control inputs. To this end, an approximation is needed.

Figure 5 shows the relationship between dY, dU, and slope, λ, of the hysteresis loop. The displacement difference dY represents the magnitude of errors, which corresponds to | *S* |, while

dU is meant to the hysteresis gap ΔU_{gap}. The slope of hysteresis loops is obtained by averaging the slopes in the simulated hysteresis model. Then, the switching gain k is

$$\boldsymbol{k} \geq \frac{|\boldsymbol{S}|}{\lambda} \tag{24}$$

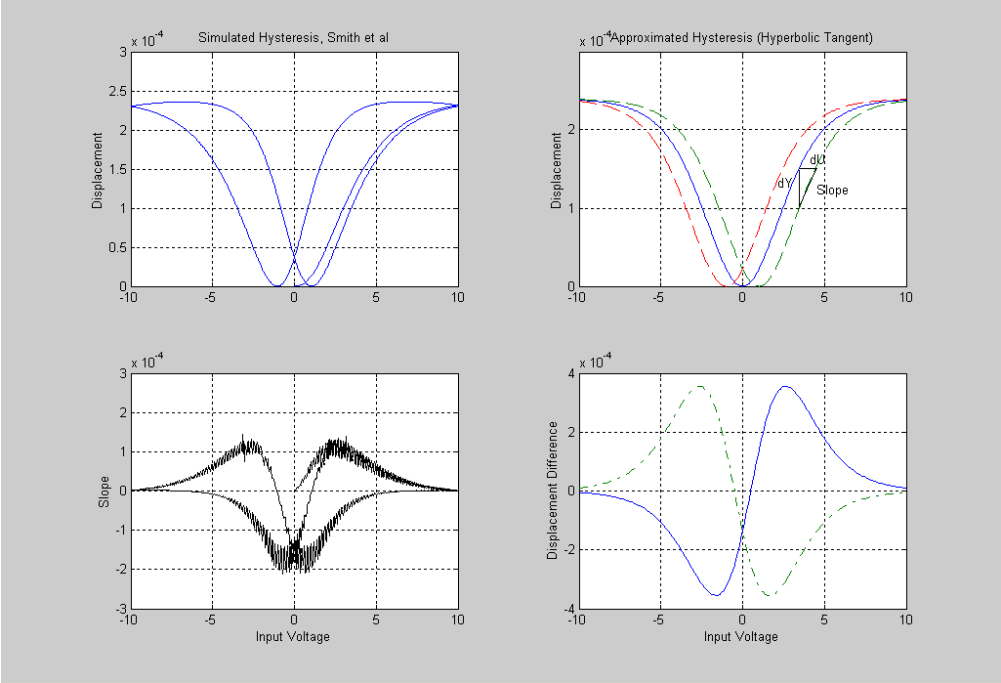

Figure 5: Approximation Approach to Determine a Hysteresis Gap ΔU_{gap}

Because the stroke of a magnetostrictive transducer is small (displacement = 250 μm), the displacement errors are, in turn, extremely small. It is reasonable to relax a stability condition to

$$S\dot{S} \leq \delta|S| \tag{25}$$

where δ is a positive number close to zero. Let U_m define a nominal control input as

$$k_m \tanh^2(a_m U_m) = Y_d \tag{26}$$

and the control input U as

$$U = U_m + \Delta U = U_m + k\,\mathrm{sgn}(S) \tag{27}$$

The criterion is, then

$$|S|\text{sgn}(S)\times(\Lambda\dot{e}+Y_d-Y)\le\delta|S|$$

$$\text{sgn}(\boldsymbol{S})\times\left(\Lambda\dot{\boldsymbol{e}}+\boldsymbol{k}_m\tanh^2(\boldsymbol{a}_m\boldsymbol{U}_m)-\boldsymbol{k}_m\tanh^2\left(\boldsymbol{a}_m(\boldsymbol{U}_m+\boldsymbol{k}\,\text{sgn}(\boldsymbol{S})-\frac{|\boldsymbol{S}|}{\lambda}\text{sgn}(\boldsymbol{S})\right)\right)\le\delta \quad (28)$$

For a positive S,

$$\frac{\Lambda\dot{e}}{k_m}+\tanh^2(a_mU_m)\le\tanh^2\left(a_m(U_m+k-\frac{|S|}{\lambda})\right)+\frac{\delta}{k_m} \quad (29)$$

The square of hyperbolic tangent terms has a range from 0 to 1, and k_m, δ are close to zero. The magnitude of velocity term $\dot{e}$ can be small if the actuator does not have an initial displacement error. When δ and $\dot{e}$ are negligible, the switching gain k that satisfies the condition is also determined as

$$\boldsymbol{k}\ge\frac{|\boldsymbol{S}|}{\lambda}$$

The result is the same for the case of a negative S. Using this relaxed stability criterion, the implementation of control inputs is much simpler. The velocity term $\dot{e}$ is not required while the switching gain k still remains in the simple form. The simulation of this magnetostrictive transducer model with the new stability criterion will be shown in the next section.

6.2.4 SIMULATION OF MAGNETOSTRICTIVE TRANSDUCER

The magnetostrictive transducer model is simulated with SIMULINK toolbox in MATLAB. The open-loop control and two feedback control schemes: PID and Sliding Mode Control are compared in terms of performance. The control input with the relaxation in the stability criterion is employed in Sliding Control scheme. The resulting figures will be illustrated to support the validity.

According to the magnetostrictive transducer model by Smith *et al* [5], the relationship between input voltages, anhysteretic magnetization, irreversible magnetization, and reversible magnetization can be depicted in Figure 6. For a given input voltage V_s, the corresponding magnetic field H of the coil is computed. Then, anhysteretic, irreversible, reversible, and total magnetization are determined by mean field theory for ferromagnetic hysteresis and the law of approach. The resulting strain, in turn, is obtained by the computation in strain subsystem block.

The diagram of the closed loop control scheme in Figure 7 shows that the output is fed back to compare with the desired displacement. Then, the corresponding errors are computed and relayed to the controller. A sliding controller, for example, generates the control input U, in terms of the desired displacement and the errors, to the transducer block.

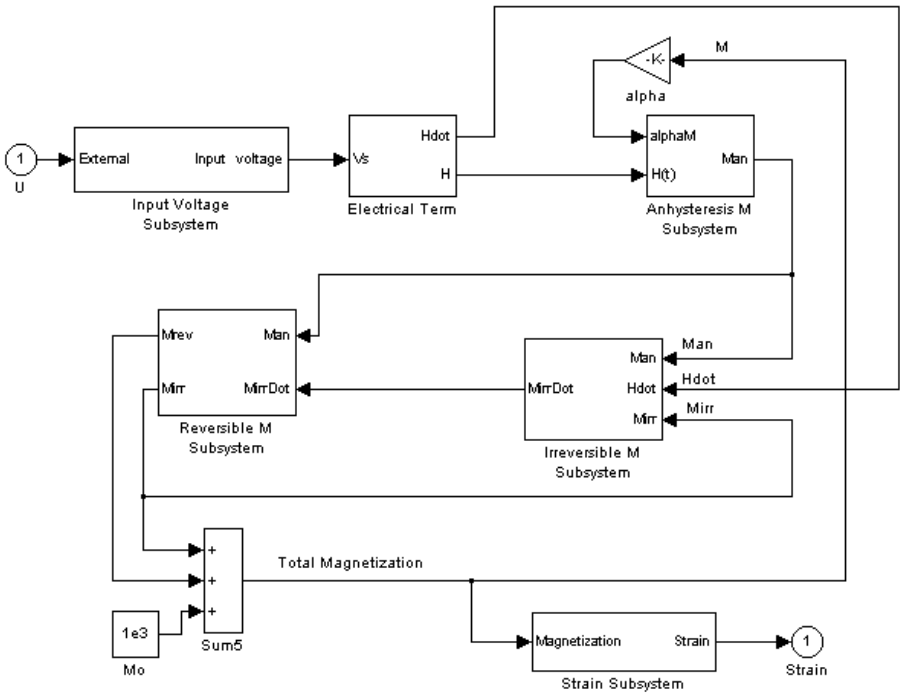

Figure 6: Magnetostrictive Transducer Model

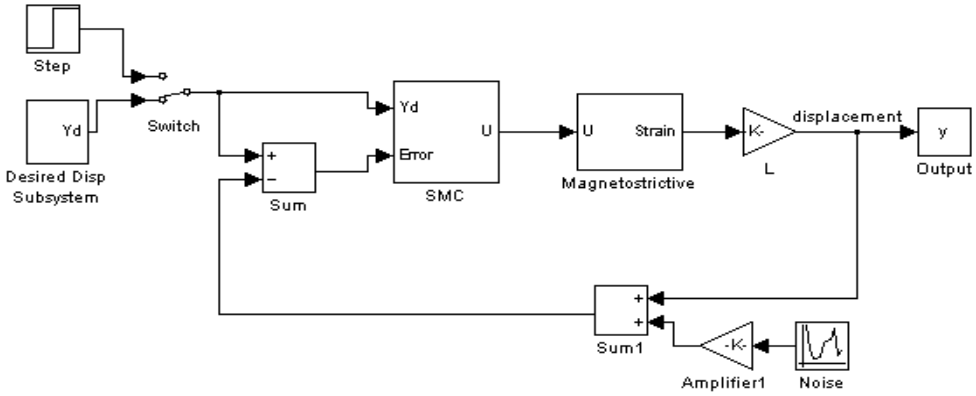

Figure 7: Closed Loop Control Diagram (Sliding Controller)

To compare the tracking performance between an open loop, PID, and sliding mode control, an absolute value of sinusoid with the frequency of 25 Hz is given as a desired displacement. The results are shown in Figure 8.

Small figures on the first row show trajectories of the desired displacement (solid line) and results of various control schemes (dashed line). The resulting trajectory of the open loop contains a phase lag and incorrect magnitude. The outcomes of both closed loop controllers, on the other hand, are approximately on top of the desired displacement.

On the second row, the figures are the focuses at the peaks of the displacement path. The significant error of the open loop is depicted. The PID controller, also, shows a slight off-track. An error spike of the sliding control scheme appears in which the desired trajectory changes the direction. The sliding controller, however, keeps right on top of the desired path.

The figures on the last row show the resulting errors. Because of the phase lag, the open loop shows the displacement error about 40%. The small off-track path of the PID controller yields the error about 1.5% around the peak of the desired path. Due to the nearly perfect tracking performance, the sliding controller brings in even smaller error. In fact, it is less than 0.1%.

Basically, an input voltage of the open-loop scheme is linearly proportional to the magnitude of a given desired displacement. It is not designed to compensate for nonlinear characteristics such as hyteresis, or saturation. As a result, the open loop controller produces large errors. And it is clear that the performance of sliding control is much better than PID control. The tracking trajectory of sliding controller is nearly perfect except at the peak of the sinusoid.

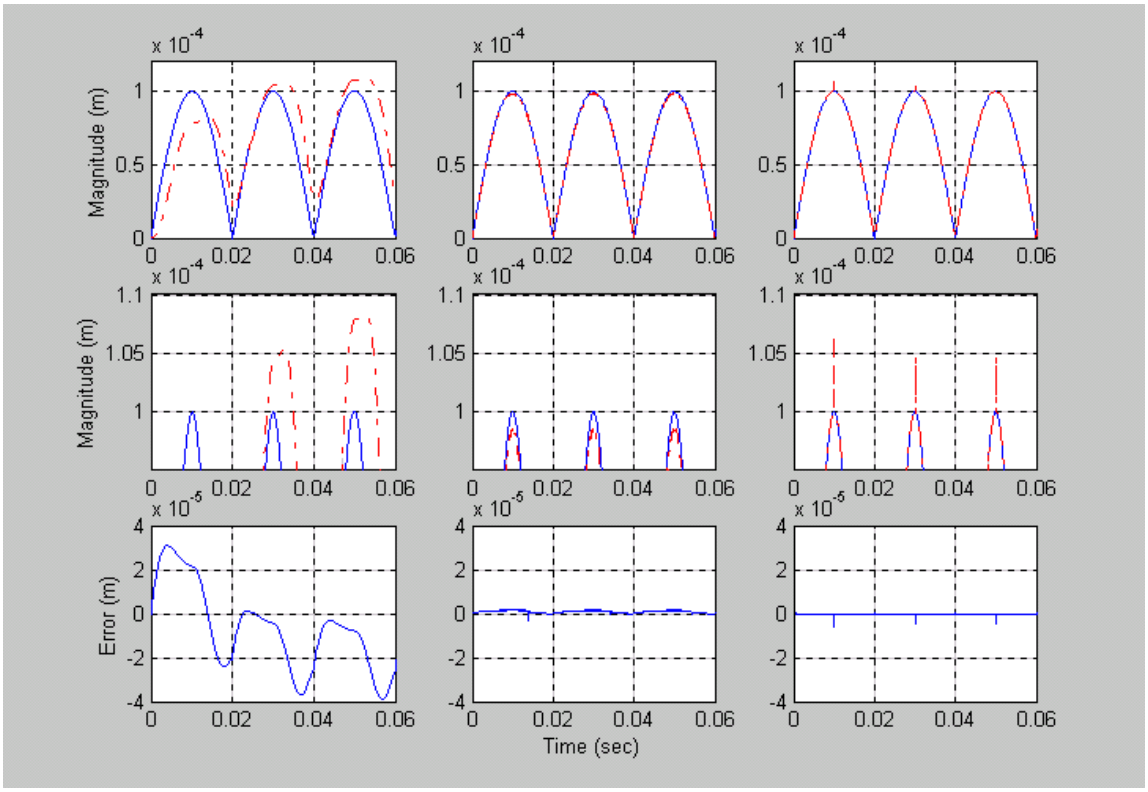

Figure 8: Resulting Output of Open Loop, PID, and Sliding Control

To support the validity of a relaxed stability criterion in sliding control, Figure 9 illustrates the evolution of the stability criterion $S\dot{S}$. If the criterion is less than or equal to zero, the sliding control yields a stable closed loop system. The close look of the stability criterion indicates that the variation is extremely close to zero. Accordingly, it is certain that the purposed control scheme satisfies Lyapunov stability criterion.

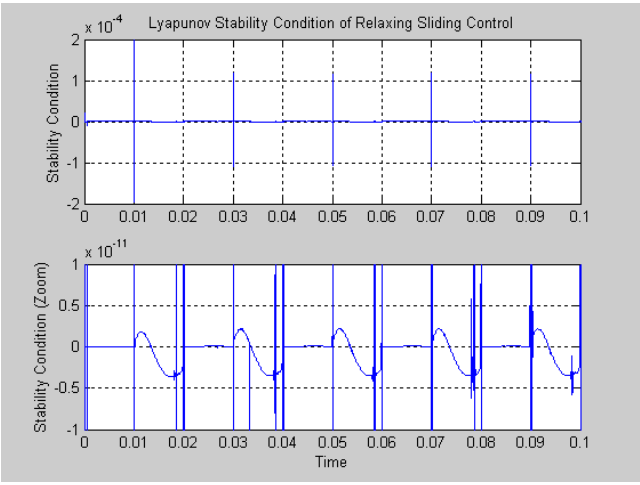

Figure 9: Lyapunov Stability Condition of Relaxing Sliding Control

6.3 CONCLUSION

To fully understand how to control a magnetostrictive transducer at high drive levels, the magnetostrictive phenomenon and mathematical models for a magnetostrictive transducer has been studied. The magnetization model investigated by Smith *et al* [5] used a mean field theory for a ferromagnetic hysteresis and the law of approach to determine the anhysteretic magnetization and, then, add hysteresis to the model. Bulk magnetization relation transforms the hysteretic magnetization to strain. The relation between an input voltage and output strain is highly nonlinear.

A nonlinear control approach, sliding mode control, is analyzed to deal with uncertainties in the system model such as hysteresis or saturation, external disturbances, or unmodeled dynamics. A relaxation in stability condition is introduced to achieve a simple implementation of this control scheme. The results of simulation support the validity of the purposed approach. Sliding controller yields better tracking performance over PID and open loop control.

REFERENCES

1. Calkins, F.T., R.C. Smith, and A.B. Flatau, "An energy based hysteresis model for magnetostrictive transducers," ICASE Report 97-60, IEEE Transactions on Magnetics, 1997.
2. Jiles, D.C., "Introduction to Magnetism and Magnetic Materials," Chapman and Hall, 1991.
3. Jiles, D.C., and D.L. Atherton, "Theory of ferromagnetic hysteresis," Journal of Magnetism and Magnetic Materials, 61, pp. 48-60, 1986.
4. Jiles, D.C., J.B. Thoelke, and M.K. Devine, "Numerical determination of hysteresis parameters for the modeling of magnetic properties using the theory of ferromagnetic hysteresis," IEEE transactions on Magnetics, 28(1), pp. 27-35, 1992.
5. Smith, R.C., "A Nonlinear Optimal Control Method for Magnetostrictive Actuators," Journal of Intelligent Material System and Structures, 9, pp. 468-486, 1998.
6. Slotine, J.J, and W. Li, "Applied Nonlinear Control," Prentice Hall, 1991.
7. Smith, R.C., C. Bouton, and R. Zrostlik, "Partial and Full Inverse Compensation for Hysteresis in Smart Material Systems," Proceedings of the American Control Conference, pp. 2750-2754, 2000.
8. Ashley, S., "Magnetostrictive actuators," Mechanical Engineering, 1998.

7 PIEZOELECTRIC RESONATING STRUCTURES FOR MICROELECTRONIC COOLING

Tao Wu
Graduate Student
Paul I. Ro
Professor
Mechanical and Aerospace Engineering

The design of piezoelectric resonating structures was investigated for generating acoustic streaming which may be used for cooling microelectronic components. The vibration characteristics of different piezoelectric structures were simulated by the finite element method and validated with analytical approaches. Considering the product of resonance frequency and dynamic tip deflection as a performance merit, the effects of length and location of the actuators as well as the boundary conditions were analyzed for four different piezoelectric resonator designs. Results show that there exist the optimal length and location of actuators in the resonating structures. Boundary condition is an important factor in actuator design as well.

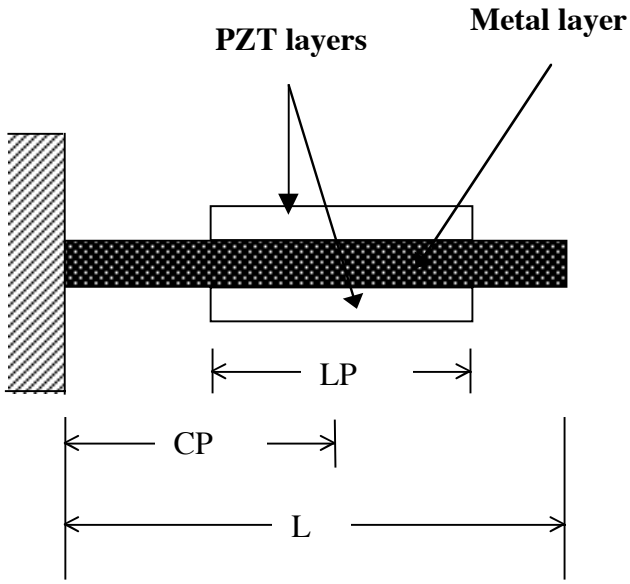

7.1 INTRODUCTION

The feasibility of an air stream created by acoustic streaming from an ultrasonic flexural wave (UFW) as a cooling mechanism for large-scale system has been experimentally verified [1]. This makes it possible to use the UFW generated on a small piezoelectric resonator as a miniature fan for microelectronic systems.

Due to the direct and inverse piezoelectric effects, the use of piezoelectric materials as an actuator has been studied extensively in many fields. Piezoelectric actuators were used for actuating and controlling the vibrations of structural members in the smart structures as demonstrated by the very early experiments of Luis and Crawly [2]. There are two major approaches to structural actuation. One uses piezoelectric actuators that cover the entire structure, and the other approach is to use discrete piezoelectric actuators that occupy a relatively small area of structures. There are some design issues related to these two approaches that are discussed in this section.

In designing resonating structures for cooling effects, a figure of merit needs to be applied to evaluate the vibration performance of the piezoelectric actuators. In this study, the product of resonance frequency and corresponding vibration amplitude was used. To date, there have been many reports on the analytical equations regarding the fundamental resonance frequency and static tip deflection for simple piezoelectric systems [3-8]. However, few papers mentioned the analytical expressions for the whole set of resonance frequencies and dynamic vibration amplitudes. Also, it is generally impossible to derive the theoretical expressions for complex resonating structures. Finite element analysis (FEA) is an alternative tool to perform both static and dynamic analyses for any complex system. In this section, the vibration characteristics of different piezoelectric designs are simulated using a commercial FEA software package ANSYS5.6. These characteristics are then evaluated and compared by using the figure of merit for different designs.

7.2 THEORY: PIEZOELECTRIC FEA FORMULATION

Piezoelectricity is a coupled field effect. In piezoelectric material, stress and strain are coupled to electric field and polarization. Coupled-field elements are needed to perform piezoelectric analyses which contain all the necessary nodal degrees of freedom and include electrical-structural coupling in the element matrices[9]. The piezoelectric finite element formulation is briefly described as follows.

The constitutive behavior of a piezoelectric material within the linear range has the form:

$$\sigma_{ij} = D_{ijkl}\varepsilon_{kl} - e_{mij}E_m \quad (1)$$

$$q_i = e_{ijk}\varepsilon_{jk} + \mu_{ij}E_j \quad (2)$$

where, σ_{ij} is stress tensor, q_i is electric flux density vector. ε_{ij} and E_i are strain tensor and electric field vector, respectively. D_{ijkl} is the elastic stiffness tensor (evaluated at constant electric field), μ_{ij} is the dielectric tensor (evaluated at constant mechanical field), and e_{ijk} piezoelectric stress coefficient tensor.

For a piezoelectric finite element, the displacements and electrical potentials within the element domain can be approximated by establishing element shape functions and nodal solution variables:

$$u = N_u^n u^n \quad (3)$$

$$\varphi = N_\varphi^n \varphi^n \quad (4)$$

where u^n and φ^n are nodal displacement and nodal electrical potential, respectively. N_u^n and N_φ^n are displacement shape functions and electrical potential shape functions, respectively.

The strains and electrical fields can be obtained as:

$$\varepsilon = B_u^n u^n \quad (5)$$

$$E = -B_\varphi^n \varphi^n \quad (6)$$

where B_u^n and B_φ^n are the spatial derivatives of the element shape functions, N_u^n and N_φ^n, respectively.

With the application of variational principles on the mechanical equilibrium equation and the electrical flux conservation equation, in conjunction with Eqs. (1)-(6), the piezoelectric finite element system of equations can be expressed as:

$$[M_{uu}]\{\ddot{u}\} + [C]\{\dot{u}\} + [K_{uu}]\{u\} + [K_{\varphi u}]\{\varphi\} = \{F\} \quad (7)$$

$$[K_{\varphi u}]\{u\} + [K_{\phi\phi}]\{\varphi\} = \{Q\} \quad (8)$$

where, $[M_{uu}]$ and $[K_{uu}]$ are the mass and displacement stiffness matrices, $[K_{\varphi u}]$ is the piezoelectric coupling matrix, $[K_{\varphi\varphi}]$ is dielectric stiffness matrix, {F} and {Q} are respectively the mechanical force vector and the external applied electrical charge vector acting on piezoelectric element.

7.3 NUMERICAL SIMULATION METHOD

Three analysis methods which are static analysis, modal analysis and harmonic analysis were performed in the numerical simulation by the finite element software package ANSYS[10]. Static analysis calculates the effects of steady loading conditions on the piezoelectric structures. Modal analysis is used to obtain the solution of the motion equation of a deformable system. In the simulation, reduced method was used to perform the modal analysis. The reduced method uses the HBI algorithm (Householder-Bisection-Inverse iteration) to calculate the eigenvalues

and eigenvectors. It is relatively fast because it works with a small subset of degrees of freedom called a master DOF. Using the master DOF leads to an exact stiffness matrix but an approximate mass matrix. The accuracy of the results depends on how well the mass matrix is approximated, which in turn depends on the number and location of the master DOF. In this simulation, the master DOF was chosen to be in the direction of beam vibration. To predict the dynamic behavior of the structure, full-method harmonic analysis was employed. The full-method harmonic analysis uses the full system matrices to calculate the harmonic response, where the matrices may be symmetric or asymmetric [10]. To take advantage of the ultrasonic noise-free features, the desired operation frequency range was set to be greater than 20kHz in the simulation.

Bimorph is one of the most useful piezoelectric structures. Bimorph usually consists of two thin piezoelectric layers bonded together, which produces curvature when one ceramic layer expands while the other layer contracts. A center shim is usually laminated between the two piezoelectric layers to increase mechanical strength and stiffness, but it also tends to reduce motion. To simulate the bimorph, the piezoelectric actuator patches were constructed using 3-D Coupled-Field Solid Elements SOLID5 and the middle brass shim was modeled by SOLID45. The element edge length on surface boundaries of 0.4mm, 0.3mm, 0.2mm and 0.1mm were tested. Little variation in the parameters of interest, i.e., resonance frequencies and dynamic displacements, was observed between the two smallest grid spacings, so the final meshing edge length was 0.2mm to guarantee reasonable accuracy and speed. The fixed-free boundary condition was applied by constraining the nodal displacements in x, y and z directions at one end of the beam. To simulate the electrode surfaces of the bimorph actuator, the same level of nodal electrical potential was prescribed at the nodes on the surfaces[9].

7.4 PIEZOELECTRIC RESONATING STRUCTURE DESIGN

In resonating structure dynamics, there are two primary parameters in the actuator structure design, i.e., natural frequency w and harmonic tip deflection A. The product of these two parameters can be used to evaluate the acoustic streaming velocity and the cooling effect by PZT vibration. The characteristic surface velocity can be written as:

$$v = wA \tag{9}$$

In this section, v is figure of merit to evaluate the resonating model performance.

For the simulation, two-layer brass reinforced piezoelectric elements from Piezo Systems Inc. were used. The thickness of the brass shim is 0.127mm and the thickness for each of two ceramic sheets is 0.191mm (bonding layer negligible), which brings the total thickness of the piezoelectric element to 0.508mm. The properties of the PZT ceramics and brass are listed in Table 1.

Table 1 Material Properties

Materials	d_{31}	Young's Modulus (N/m^2)	Density (kg/m^3)	Poisson's ratio
PZT ceramic	190×10^{-12}	6.6×10^{10}	7800	0.31
Brass		11×10^{10}	8800	0.35

In modal analysis, the reduced analysis method was used and master degree of freedom was defined to be in the direction that beam vibrates. The same level of nodal electrical potential was prescribed at the nodes on the surfaces. 10 modes were extracted and expanded, among which the first mode of vibration in the ultrasonic range was selected. In harmonic analysis, the electric field of 200 volts per mm was applied on both ceramics in such a way that one ceramic layer contracts while the other one expands.

Four different piezoelectric models (see Table 2) were simulated as follows: (i) Model 1, where the length of PZT is the same as that of metal shim (Figure 1); (ii) Model 2, which considers fixed locations but different lengths of the actuators (Figure 1); (iii) Model 3, in contrast to Model 2, has the actuators with fixed lengths while different locations (Figure 1); and (iv) Model 4, which implies indented actuators (Figure 2).

Table 2 Bimorph Models

Bimorph Models	L	LP	CP
Model 1	6mm, 8mm, 10mm	LP = L	CP = L/2
Model 2	8mm	$1mm \le LP \le 7mm$	4.5mm
Model 3	8mm	4mm	$2mm \le CP \le 6mm$
Model 4	l_1 = 12mm, l_2 = 10mm	N/A	N/A

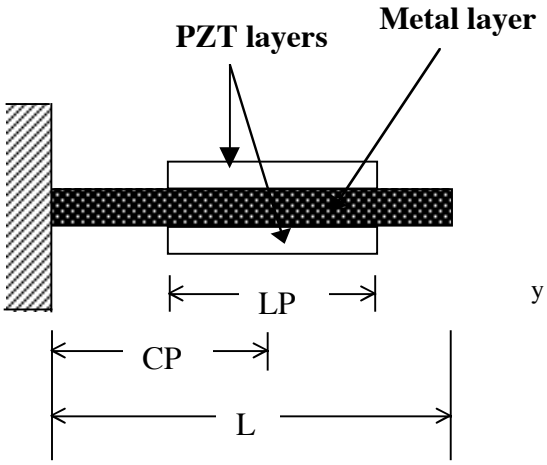

Figure 1 Schematic of PZT actuator model

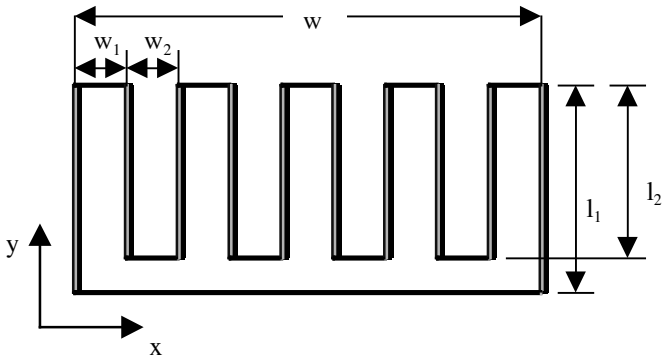

Figure 2 Indented shape actuator model

7.4.1 MODEL 1 – EQUAL SHIM AND PZT LENGTH

Generally speaking, the effect of width of the beam on vibration characteristics can be neglected when it is much smaller than the length. In the applications of microelectronic systems, the dimensions of the piezoelectric actuator should be very small, say, less than 10mm. So, in this analysis, the width of the actuator is fixed at 2mm, while three different lengths of the single actuator are chosen for comparison; 10mm, 8mm and 6mm.

Table 3 Resonance Frequencies for Model 1

Length of Actuator	1st Resonance Frequency	2nd Resonance Frequency	3rd Resonance Frequency
10mm	2503	15532	43029
8mm	3921.2	24196	66600
6mm	6994.2	42639	115810

By performing modal analyses, the first three vibration resonance frequencies for three actuators were calculated and are given in Table 3. Clearly, with an increase of the bimorph length, the resonance frequencies decrease. To operate in the ultrasonic range, the third mode shape for L = 10mm and second for L = 8mm and 6mm actuators were selected. The corresponding mode shapes are given in Figure 3. It can be seen from the figure that the maximum amplitudes occur both at the beam tips.

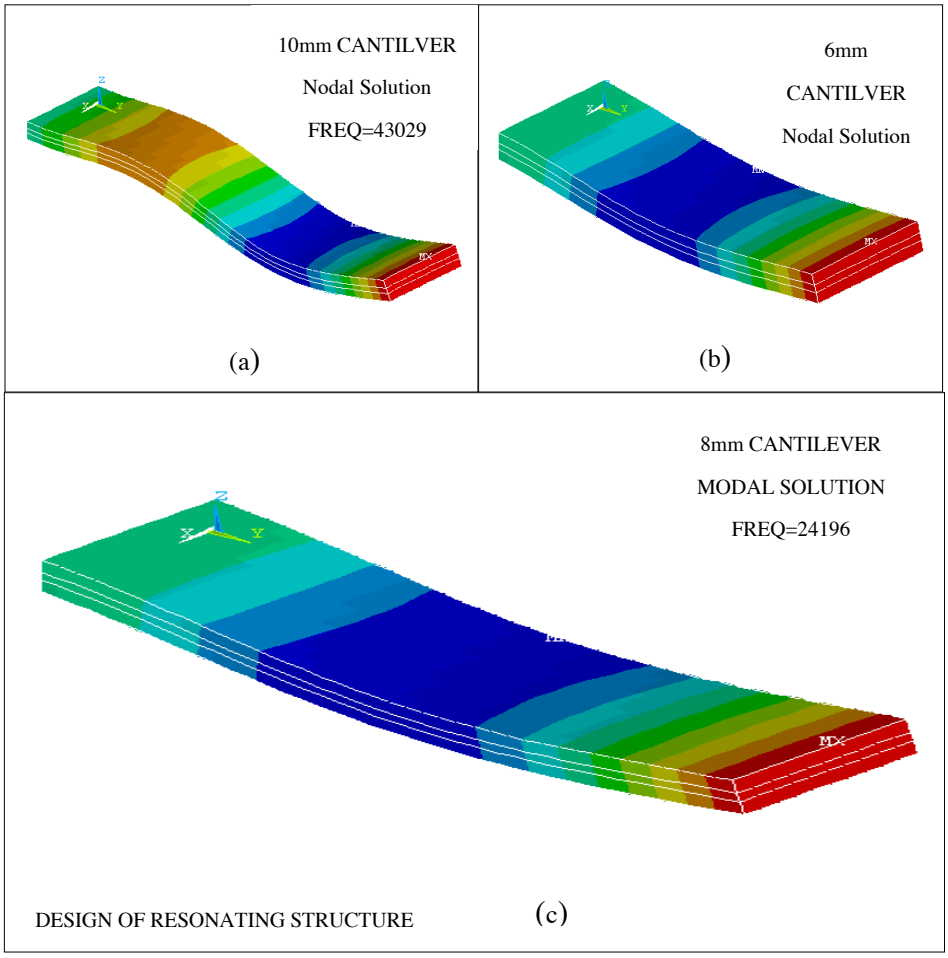

Figure 3 Mode shapes for Model 1 (a) The third mode shape for 10mm by 2mm bimorph (b) The second mode shape for 6mm by 2mm bimorph (c) The second mode shape for 8mm by 2mm bimorph

The vibration amplitude can be determined by harmonic analyses. Figure 4 shows the harmonic analysis results on the vibration amplitudes of beam tip *vs*. ultrasonic frequencies for three different length actuators. The first ultrasonic resonance frequency and tip amplitude as well as the figure of merit are listed for comparison in Table 4.

Table 4 Comparison of Performance Merits for Model 1

Length of actuator	First Ultrasonic Resonance Frequency (HZ)	Tip Amplitude (μM)	Figure of Merit
10mm	41032	4.544	1.1715
8mm	23015	11.714	1.6939
6mm	40704	6.524	1.6685

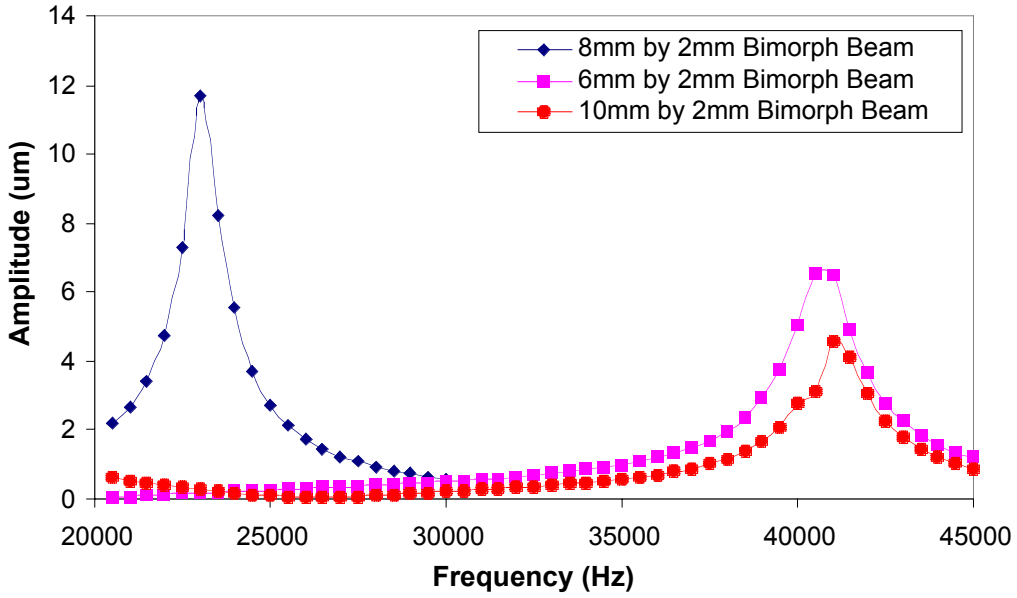

Figure 4 Harmonic analysis results for three size bimorphs in Model 1

As given in table 4, L = 8mm actuator has the largest figure of merit among these three structures, which indicates that the 8mm piezoelectric actuator is the best among three choices. Compared to the L = 8mm case whose first ultrasonic resonance frequency is the second mode shape, the 10mm actuator shows a much smaller amplitude in its third mode. Even though the 10mm bimorph's third resonance frequency is larger than 8mm bimorph's second resonance frequency, the 8mm bimorph has the larger figure of merit. Also due to the fact that the vibration amplitude is larger for the longer beam in the same mode shape, the 8mm long bimorph exhibits a higher figure of merit than the 6mm one.

7.4.2 MODEL 2 – FIXED LOCATION ATUATOR WITH DIFFERENT LENGTH

In Model 2, the length of PZT is different from that of the beam. This means that the piezoelectric actuator covers only a part of the metal beam. Keeping the beam length (*L*) and center location of PZT on beam (*CP*) fixed at *L = 8mm, CP = 4.5mm*, the effects of PZT lengths on the actuator's performance were investigated. The figure of merit is plotted as a function of the length of the actuator *LP* in Fig. 5. For the fixed value of *CP*, the range of *LP* is restricted. As the actuator length begins to increase from 1mm, i.e., the length ratio of actuator to beam is 0.125, both the third mode of the resonating structure (the first ultrasonic resonance frequency) and the corresponding tip amplitudes increase, which result in the constant increase of figure of merit in this range. However, when the actuator length is larger than 4.7mm (the length ratio of 0.588), both the amplitude and frequency decrease and hence the figure of merit decreases with the length ratio. Therefore, the optimal solution is found when $LP / L = 0.588$.

The vector plot of the amplitudes at frequency 63900Hz (3rd resonance frequency for $LP/L = 0.588$) is given in Figure 6(a). The maximum amplitude occurs at the free end of the beam. A blow-up of the amplitude of the part of the beam covered by the actuator can be obtained in Fig. 6(b). One observation can be made that when $LP/L = 0.588$, the two edges of the actuators on the beam correspond to points of approximately opposite curvatures, which agrees with the conclusions in Ref. [11]. So to obtain the optimal figure of merit, the actuator should be placed between two points of opposite curvatures when the location of actuator is fixed.

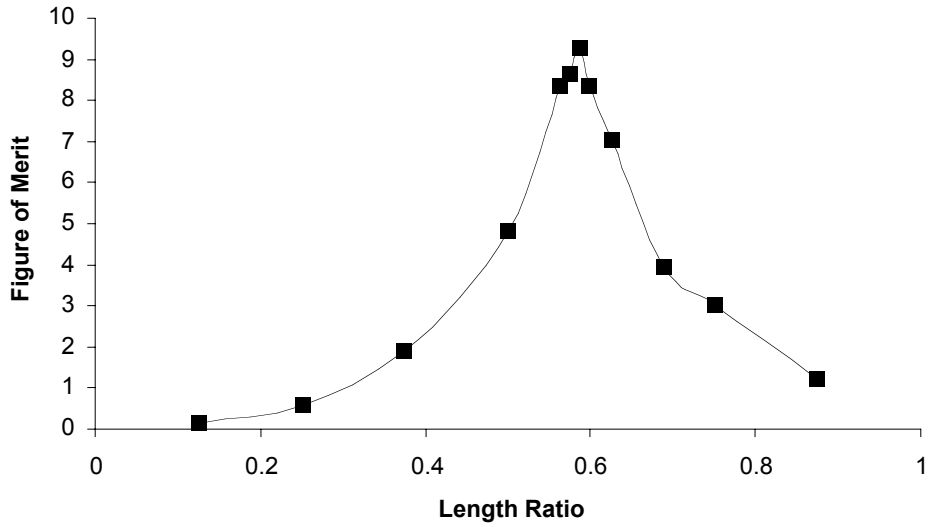

Figure 5 The performance merit vs. length ratio of actuator to beam (LP/L) in Model 2

7.4.3 MODEL 3 – FIXED LENGTH ACTUATOR WITH DIFFERENT LOCATION

In Model 3, keeping the beam length and actuator length fixed at *L = 8mm and LP = 4mm*, the performance merit as a function of the center location of PZT on the beam is shown in Figure 7. Similar to Model 2, the range of *CP* is restricted for the fixed value of *LP*. As seen in Figure 7, there are two peak values of figure of merit when CP is in the range of [2mm, 6mm]. The optimal solution can be found when $CP/L = 0.6$. The vector

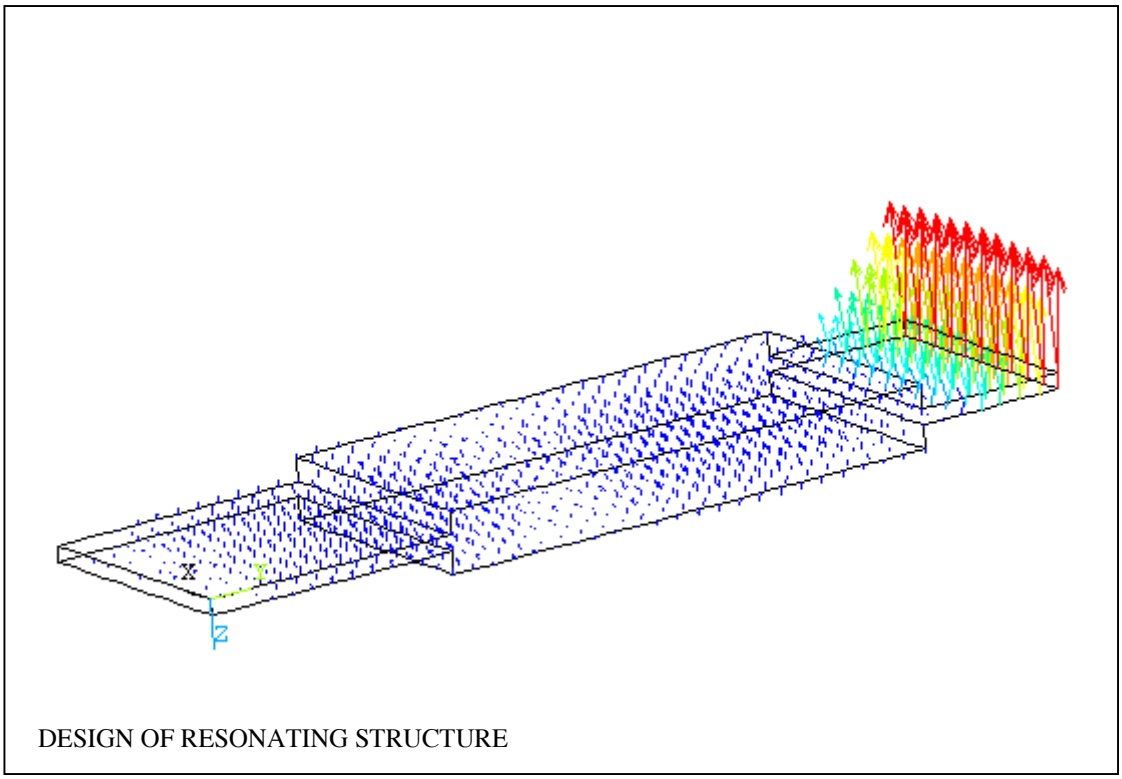

(a)

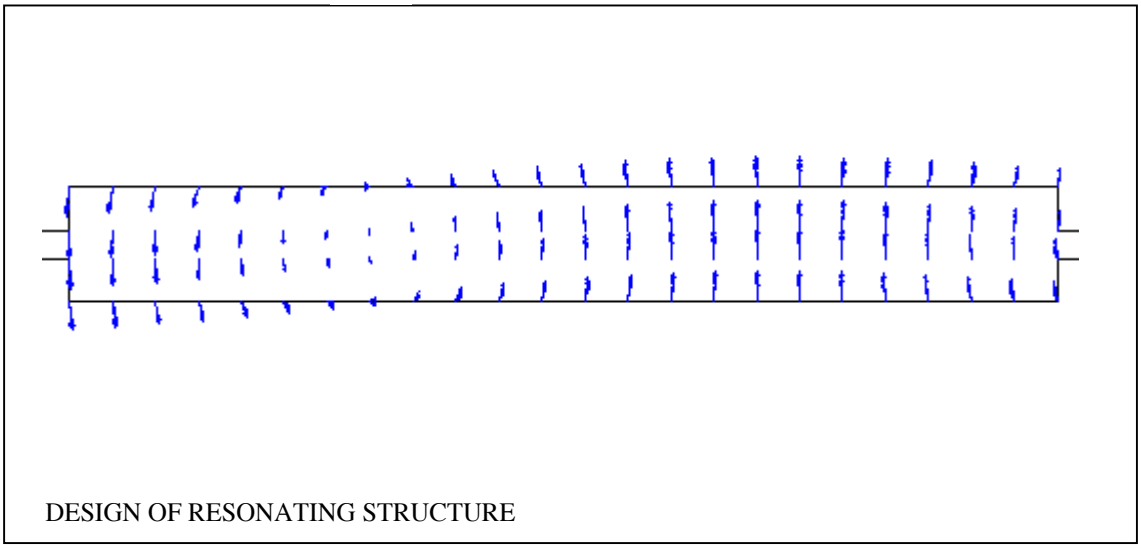

(b)

Figure 6 Vector plot of amplitudes at frequency 63900Hz in model 2 at optimal ratio $LP/L = 0.588$ for: (a) entire vibration structure; and (b) the part of beam covered by the actuator

plot of the amplitude at frequency 65900 (3rd resonance frequency for $CP/L = 0.6$) is given in Figure 8(a). From the blow-up of the amplitude of the part of the beam covered by the actuator (Fig. 8(b)), it is shown that when $CP/L = 0.6$, the two edges of the actuators on the beam corresponding to points of approximately equal curvatures, which again, agrees with the conclusions in Ref. [11]. Therefore, when the length of actuator is fixed, the actuator should be placed between two points of equal curvatures in order that the optimal performance merit can be obtained.

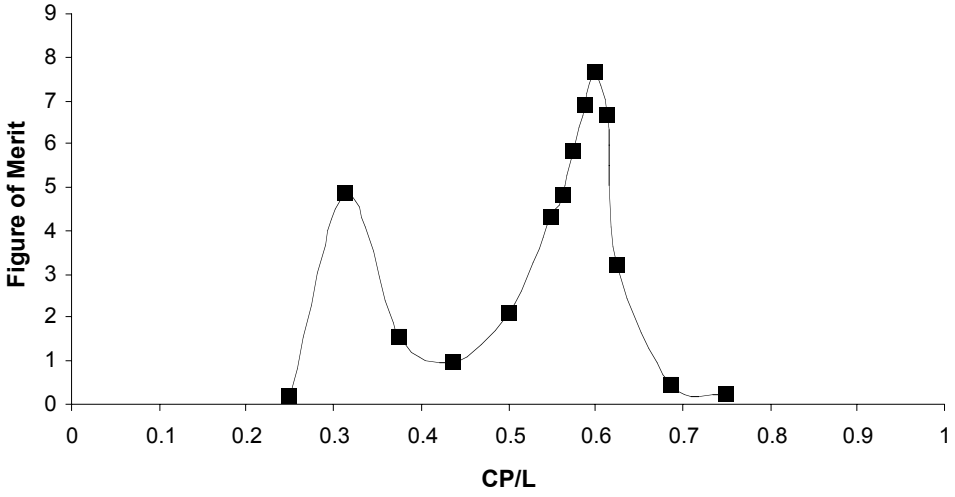

Figure 7 The performance merit vs. ratio of actuator center location to the beam length (CP/L) in Model 3

7.4.4 MODEL 4 – SERRATED SHAPE MODELS WITH DIFFERENT BOUNDARY CONDITIONS

In model 4, a 24mm by 12mm bimorph has been designed into the serrated shape (see Fig. 2). The dimensions of different parts are: $l_1 = 12mm$, $l_2 = 10mm$, $w_1 = 2mm$ $w_2 = 3.5mm$ and $w = 24mm$. The thickness of the bimorph is 0.508mm. This piezoelectric actuator can be regarded as a composite structure made up of several 10mm by 2mm bimorphs. Two different boundary conditions were applied and compared in the simulation:

(1) Type I boundary condition was to fix the structure at surface $x = 0$.

(2) Type II boundary condition was to fix the structure at three surfaces: $x = 0$, $y = 0$ and $y = w$.

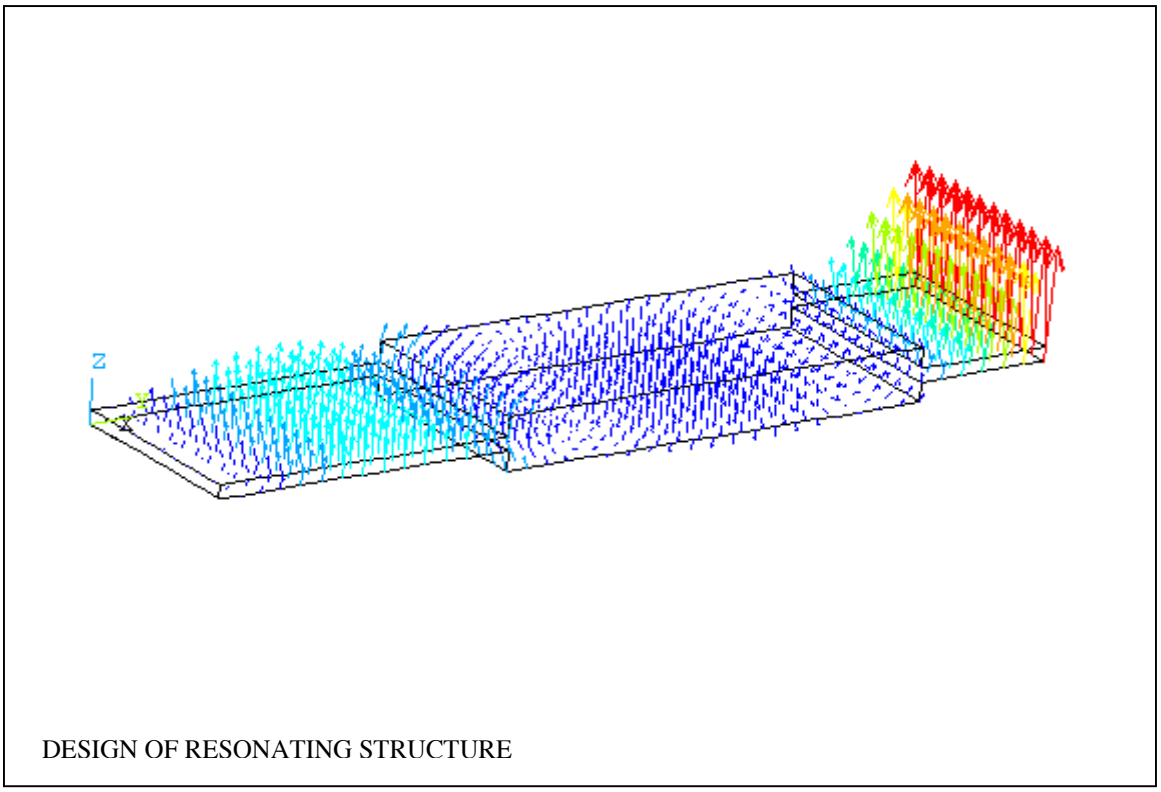

(a)

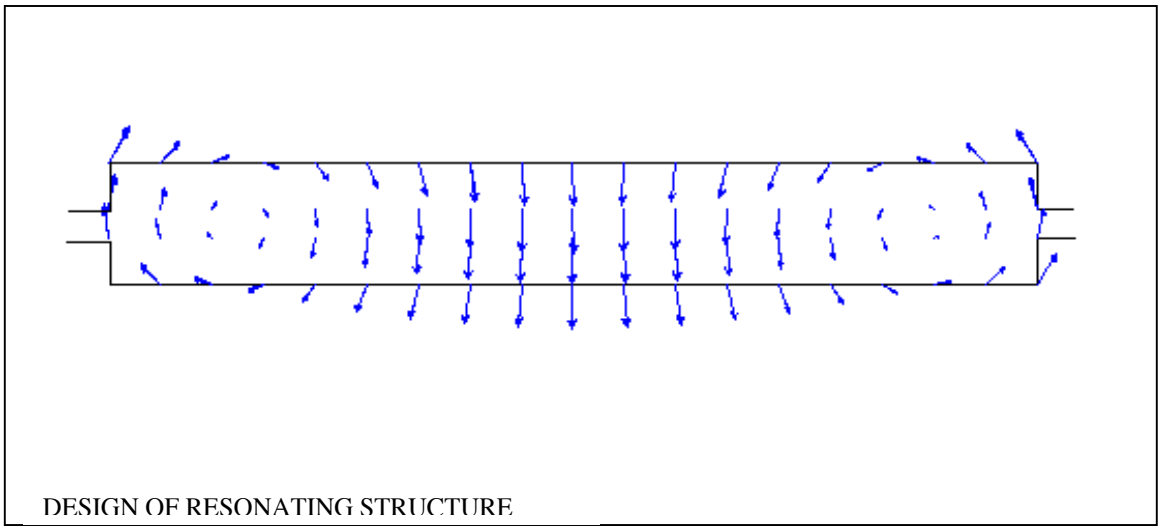

(b)

Figure 8 Vector plot of amplitudes at frequency 65900Hz at optimal ratio $CP/L = 0.6$ in Model 3 for:(a) entire vibrating structure; and (b) the part of beam covered by the actuator

The amplitudes versus the ultrasonic frequencies for these two types of boundary condition are obtained using harmonic analyses and shown in Figure 9. The peak value of amplitude under Type II boundary condition is larger than that under Type I boundary condition, indicating that different boundary conditions also affect the performances of the vibrating structures.

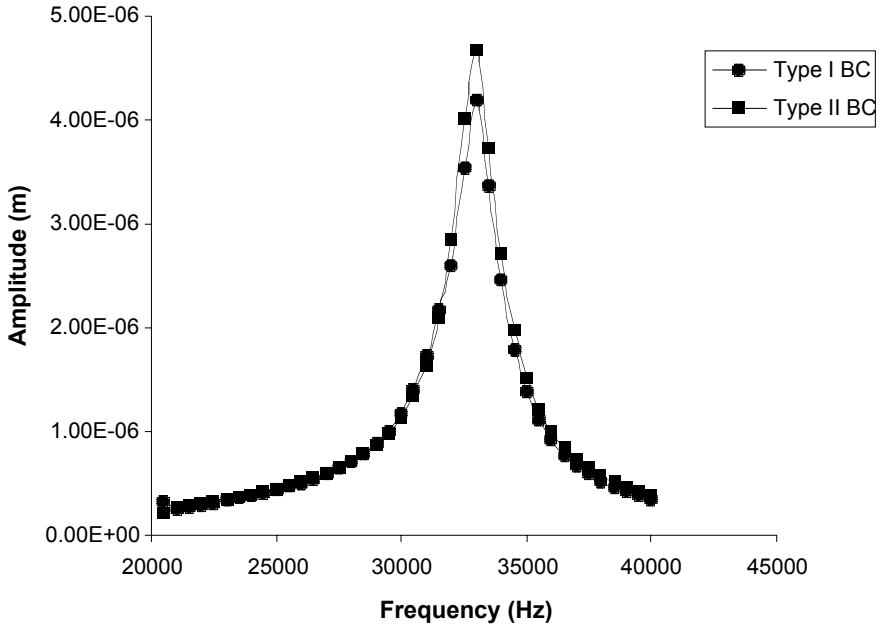

Figure 9 Harmonic analysis results for two different types of boundary conditions in Model 4

7.5 CONCLUSIONS

Four different piezoelectric resonating models were investigated using FEA software ANSYS. First, the results of the piezoelectric finite element simulation was validated with analytical approaches. Good agreements instill confidence that the present computer simulation method is sufficiently accurate to analyze more complex piezoelectric structures. One performance merit was proposed to evaluate the vibration characteristics of different actuator models. By simulation, the effects of actuator length, location of actuator as well as boundary conditions were analyzed for these piezoelectric models. It is shown that, for the piezoelectric model with actuator covering the entire structure, the 8mm long actuator structure performs better than the 10mm and 6mm lengths. For the models using discrete piezoelectric actuators that occupy a relatively small area of structures, the analysis shows that to obtain the optimal performance merit, the actuator should be placed between two points of opposite curvatures when the location of actuator is fixed. In the case of fixed actuator length, the actuator should be set between two

points of equal curvatures. Boundary conditions of the serrated shape structure also have measurable influence on the performance of the vibrating structures.

REFERENCES

1. Ro, P.I. and Loh, B.G., "Feasibility of using flexural waves as a cooling mechanism", *IEEE Transactions on Industrial Electronics*, 48(1): 143-149, February, 2001
2. Crawly, E.F. and Luis, D.J., "Use of piezoelectric actuator as elements of intelligent structures", *AIAA J.*, 25: 1373-1385, 1987
3. Smits, J.G., Dalke, S.I. and Cooney, T.K., "The constituent equations of piezoelectric bimorphs," *Sensors and Actuators A*, 28(1): 41-61, 1991
4. Bailey, T. and Hubbard, J.E., "Distributed piezoelectric-polymer active vibration control of a cantilever beam", *Journal of Guidance, Control, and Dynamics*, 8(5):605-611, 1985
5. Crawly, E.F. and Anderson, E.H., "Detailed models of piezoelectric actuation of beams", *J. of Intelligent Material Systems and Structures*, 1:4-25, 1990
6. Crawly, E.F. and Lazarus, K.B., "Induced strain actuation of isotropic and anisotropic plates", *AIAA Journal*, 19(6): 944-951, 1989
7. Lee, C.K., "Theory of laminated piezoelectric plates for the design of distributed sensors/actuators, Part I: Governing equations and reciprocal relationships", *Journal of Acoustical Society of America*, 87(3):1144-1158, 1990
8. Pai, P.F., Nayfen, A.H. and Oh, K., "A nonlinear theory of laminated piezoelectric plates", AIAA Paper No. 92-2407, *Proceedings of the 33rd SDM Conference*, Dallas, TX, 577-585, 1992
9. Lin, M.W. and Abatan, A.O., "Application of commercial finite element codes for the analysis of induced strain-actuated structures," *Journal of intelligent material systems and structures*, 5: 869-875, 1994
10. Moaveni, S., "Finite element analysis: theory and application with ANSYS", Upper Saddle River, NJ: Prentice Hall, 1999
11. Barboni, R., Mannini, A., Fantini, E. and Gaudenzi, P., "Optimal placement of PZT actuators fir the control of beam dynamics", *Smart Materials and Structures*, 9:110-120, 2000

8 ACTIVE CONTROL OF TOOL DEFLECTION AND CHATTER DURING PRECISION MILLING OPERATIONS USING MAGNETIC BEARING SPINDLES

Stuart H Clayton
David W Hood
Graduate Students
Thomas A Dow
Gregory D Buckner
Advisors

Department of Mechanical and Aerospace Engineering

The primary objective of the proposed research is to increase the quality and productivity of precision milling operations through the development and demonstration of advanced control algorithms for magnetic bearing spindles. These real-time algorithms will correct for tool deflections caused by cutting forces and reduce surface defects and tool damage caused by regenerative chatter. The magnetic bearing spindle will be mounted to a vertical axis on the Nanoform 600 diamond turning machine. The vertical axis designed and implemented at the PEC includes an air-bearing slideway, Kollmorgen ServoDisc™ motor, Heidenhain linear incremental encoder, pressurized air cylinder and a Norgren precision regulator for counterbalancing, and a Delta Tau Programmable Multi-Axis Controller (PMAC) based control card. These features give the vertical axis a linear displacement resolution of 10 nanometers that is needed to accurately measure and compensate cutting forces for the smoothest, most accurate surface finishes for milling, diamond turning, or grinding.

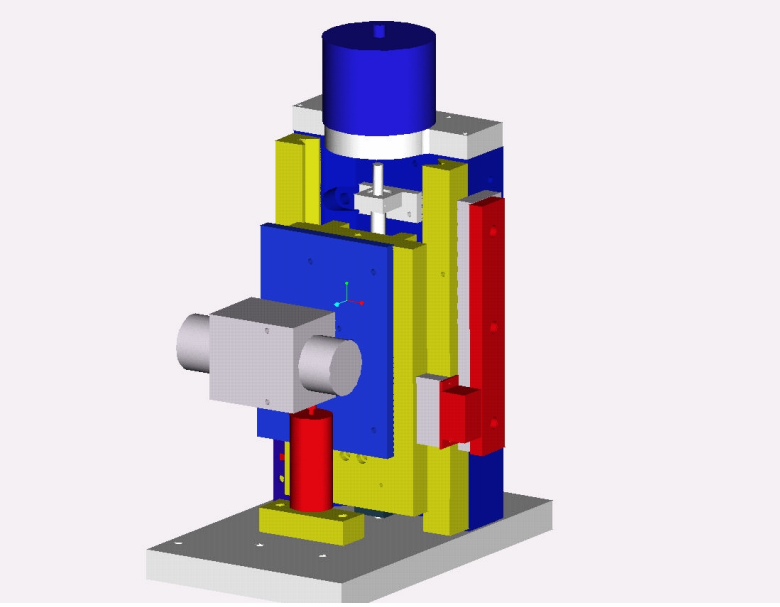

8.1 INTRODUCTION

A three-year research program was recently funded by the National Science Foundation to develop path compensation and chatter control algorithms for high-speed, precision milling operations using miniature milling tools (diameter<1mm). Magnetic bearing spindle will make this research possible by enabling the application of high-bandwidth control forces to the rotating spindle. While other researchers have used actuators that contact the rotating tool [1], radial magnetic bearings provide a non-contacting means of applying these control forces. Spindle displacement sensors will be used to determine the magnitude and direction of tool cutting forces. The required bandwidth for path compensation is expected to be low due to the tool force vector changing slowly relative to tool rotation. Chatter, however, is a high-frequency phenomenon (tool and structural natural frequencies of 5-20 kHz) that will require high-bandwidth control strategies. Chatter compensation will explore real-time vibration cancellation and active damping strategies. In all cases, the performance of these algorithms will be demonstrated through simulations and experimental evaluations.

The initial task of this project involved the construction and implementation of a third axis for the Nanoform 600, which is currently equipped with two planar axes of travel. One axis is along the spindle axis (z), and the other is perpendicular to the z axis (x). This new axis will move vertically on the Nanoform and allow the diamond turning machine to act as an ultraprecision milling machine.

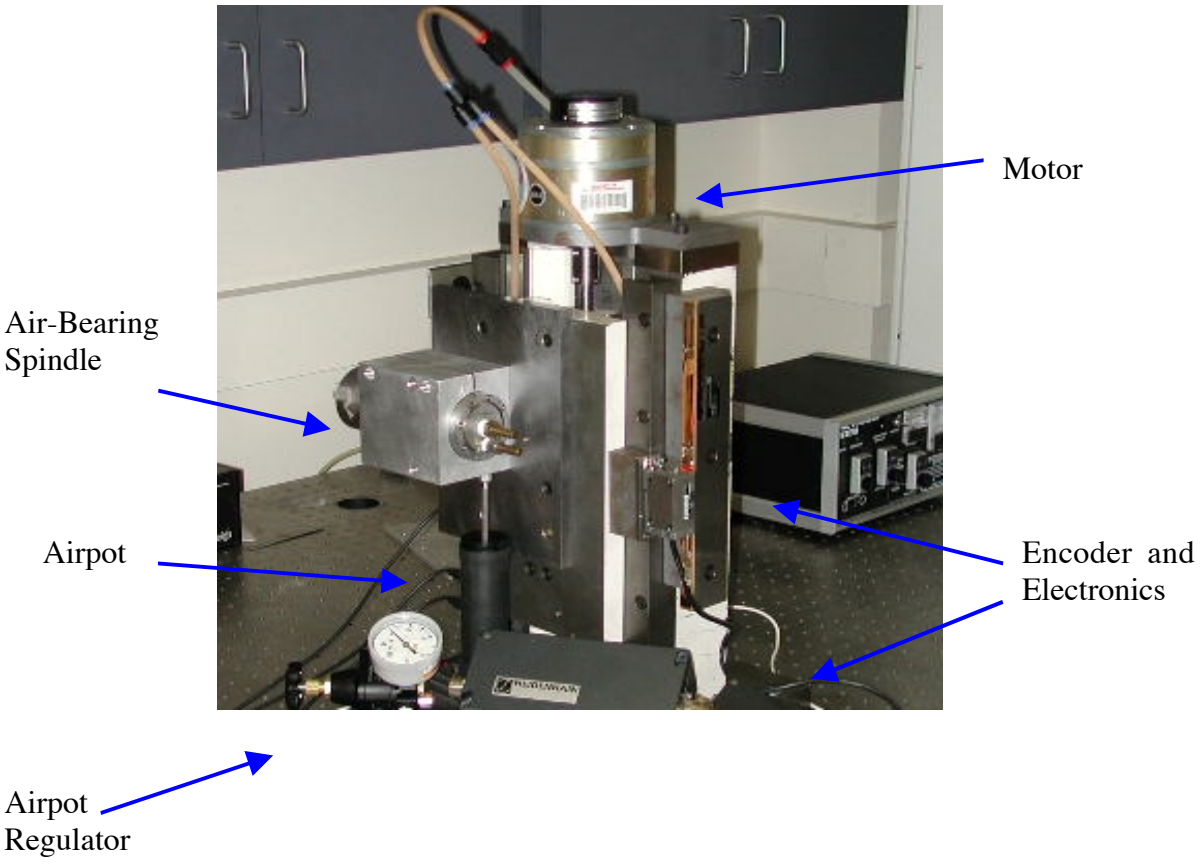

Figure 1. Picture of Y-axis for Nanoform 600 Assembled

8.2 MECHANICAL SYSTEM

8.2.1 LINEAR SLIDEWAY

The linear slideway used for the vertical axis is an air-bearing design by Dave Youden, previously of Rank Pneumo. This air-bearing slideway, shown in Figure 1, operates under a constant air pressure of 0.41 MPa. Each vee has a set of orifices on the upper and lower side for air flow. This diamond-shaped attachment was designed with a 25 µm step that is about 125 mm long. Each of these surfaces were lightly stoned and cleaned to remove any possible corrosion. The vee rails were also stoned and cleaned to provide the cleanest surface possible for smooth travel. Once the vee surfaces were cleaned properly, the slide was carefully aligned using a pair of Federal gages. The slide was assembled with an 8 µm air gap, measured normal to the vee surfaces.

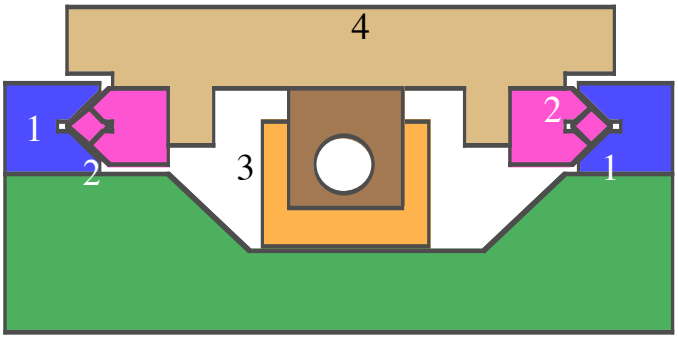

Figure 2. The air bearing slideway, shown in cross section, is constrained by double vees (1) nested in matching vee rails (2). The ball screw (3) moves the stage (4) with respect to the slide base (5) via a coupling (6).

The lead screw was attached to a Kollmorgen servo disc motor via a flex coupling. A thrust bearing assembly that consisted of double angular contact ball bearings was also introduced to control the loading issue when the slide was turned vertically. The bearing must control loads of about 45 kg with the magnetic bearing spindle. The slide has a maximum travel of about 150 mm; however, with the integration of 2 photoelectric limit switches and the counterbalance design, a total travel of about 85 mm was obtained. This 85-mm range should be sufficient considering the small vertical displacements required from diamond turning and grinding.

8.2.2 SLIDEWAY STIFFNESS

The mechanical design of the slideway is crucial to the overall surface finish from turning and grinding. The slideway needs to be as stiff as possible to minimize machining accuracies**.** There are three different sources of concern in the slideway system - the mounting brackets, the air bearing, and the ball screw/nut. To test the stiffness of the system in various directions and determine the stiffness, several deflection measurements were made with forces applied to various portions of the slideway as shown in Figure 3. The results of the measurements are shown in Table 1. Each displacement was measured with a Federal Gage electronic indicator while the force was applied with a Chattilon force gage.

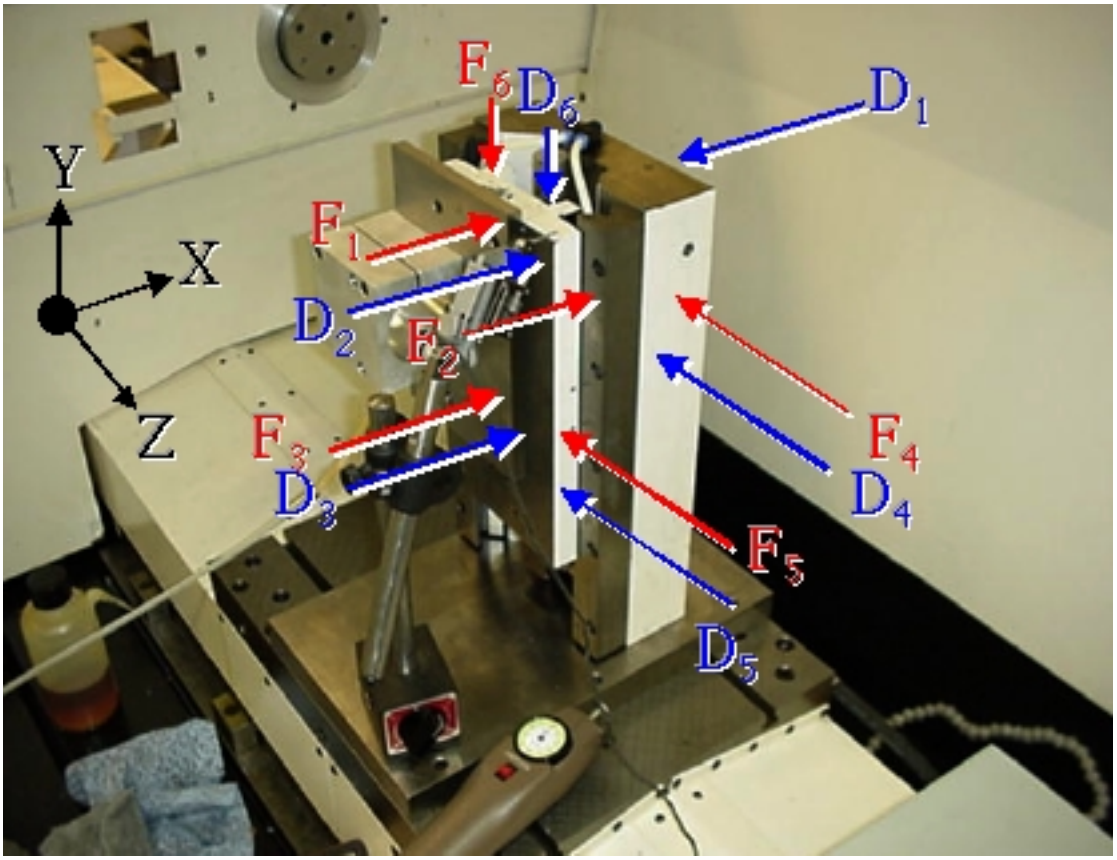

Figure 3. Position of Applied Force, F_X and Measured Displacement, D_X.

The direction and location of load points and deflection measurement points are shown in columns; that is F_1D_1 refers to a load applied at F_1 with the deflection resulting from that applied force measured at D_1. Based on the results in Table 1, the lead screw direction is the least stiff and the screw starting backdriving at about 145 N. The air bearing itself was found to be rigid as expected with nearly all the deflection occurring in the structure. Overall, the upper limit of stiffness is about 12×10^6 N/m (67,000 lb/in) in the x- and z- directions when the structure and the air bearing are included.

	Force applied at F_X, Deflection measured at D_X in µm							
Applied Force [N]	F_1,D_1	F_2,D_1	F_1,D_2	F_2,D_2	F_3,D_3	F_4,D_4	F_5,D_5	F_6,D_6
50	6	6	5	7	4	6	7	8
100	12	13	12	11	8	8	12	22
150	19	20	17	18	12	11	16	*
Stiffness [N/µm]	8.15	7.95	8.77	8.31	12.30	11.49	8.30	5.50
Compliance [µm/N]	0.12	0.13	0.11	0.12	0.08	0.09	0.12	0.18

Table 1. Stiffness Values of Y-axis

8.2.3 COUNTERBALANCE DEVICE

The vertical orientation of the y-axis introduces some general problems due to gravity creating a moment on the lead screw from the result of a hanging mass. The vertical axis was designed as a spindle mount for miniature milling tools for use with air and magnetic bearing spindles. From the weight of the spindles and other mounting plates and brackets, the lead screw and the motor could be placed under a considerable amount of stress. In order to have the vertical axis operate as smoothly and accurately as possible, a counteracting device was needed. This counterbalance was needed to counteract the total mass that was offset from the center of travel (the lead screw). The motor and amplifier must provide more work to raise the slide than it would to lower the slide due to gravitational effects. Based on the weight of the small high-speed milling spindle and the proper mounting plates, the components were found to have a mass of approximately 20 kg. The center of gravity of the moving slide and its components was found to be located on the slide itself, since the air spindle weighs considerable less than the slide.

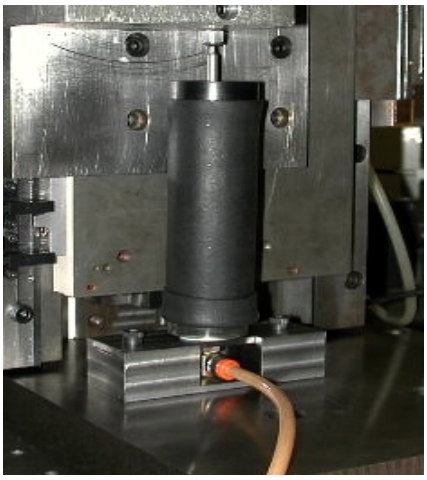

Figure 3. Pressurized cylinder as counterbalance.

Two counterbalancing devices were considered and researched for this application. One was a counterweight system involving pulleys, cables, and an equivalent mass and the other was a counterbalance that used pressurized air as shown in Figure 3. The pressurized air cylinder was chosen after weighing the pros and cons of each option. The pressurized cylinder manufactured by Airpot Corporation operates from 0-0.69 MPa with a piston diameter of 32.5 mm. This implies that the Airpot can counterbalance up to 573 N at 0.69 MPa. The cylinder has a stroke of 100 mm and the piston rod has a universal ball joint on each end to assure proper operation under slight misalignment. The cylinder is made of glass and the piston is fabricated from graphite to provide the least amount of friction possible. A pressure difference of only 345 Pa is needed to activate movement to the piston of the Airpot. To complement the air cylinder, a Norgren precision regulator model 11-018 was selected. This is a high-pressure precision regulator that operates from 0.021-1.03 MPa. For this regulator, a 552 Pa pressure change is necessary for engagement. The pressurized cylinder also contributes no added inertia and with the purchase of a precision regulator, the system costs under $200. The current counterbalance design will be used for both the air spindle and the magnetic bearing spindle, which is much heavier.

8.3 DRIVE SYSTEM

8.3.1 MOTOR

Kollmorgen manufactures the motor used for the motion of the slide. It is a ServoDisc™ motor employing flat disc armature technology. The armature is iron-less with a very low inertia that delivers high acceleration and zero cogging. All this is incorporated into an exceptionally compact package as seen below. This motor also features a large torsional stiffness for precision control of speed and acceleration. The operating characteristics of the ServoDisc™ motor are found in Table 2. These characteristics make this motor very favorable for precision applications. The high peak torque, low cogging torque, and small moment of inertia are very beneficial. This allows the motor to make precise movements moving the slide to a resolution in the nanometer range (dependent on the feedback sensor parameters). The torque curve for the motor is shown in Figure 5.

Figure 4. ServoDisc™ motor

Peak Torque	650 N-cm
Rated Speed	3000 RPM
Rated Power Output	187 Watts
Cogging Torque	60 N-cm
Rated Terminal Voltage	34 Volts
Rated Continuous Current	7.79 Amps
Moment of Inertia	0.395 kg-cm^2
Peak Acceleration	164.5 kRad/s^2
Mechanical Time Constant	3.66 ms
Electrical Time Constant	<0.15 ms

Table 2. Parameters of Y-Axis Motor

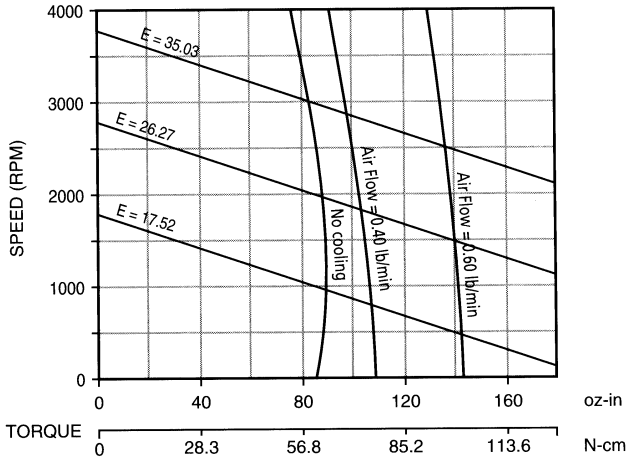

Figure 5. Torque vs. speed curve for ServoDisc™ motor

For operation, the maximum motor speed is on the order of 10 revolutions per minute. Therefore, the concern is with low speed torque of the motor. As seen in the figure above, as the air flow around the motor increases, the shaft operating torque increases as well. In the plot, E is the terminal voltage to the motor. As the terminal voltage to the motor increases for a given shaft torque, the operating speed of the motor increases as well. In this application, there is no outside cooling; therefore, the permissible operating torque for 10 RPM is 60 N-cm. This motor is well suited for this application.

8.3.2 FEEDBACK DEVICE

To control the position of the slide, a high-resolution feedback device is required. For this application, a Heidenhain LIP 101 model incremental encoder was selected. The LIP 101 is a linear, exposed encoder compatible with linear motors. An exposed encoder has advantages over a sealed encoder such as higher accuracies and no friction since it is non-contacting. This feedback device consists of 2 components, a reader and a grated encoder. The reader is mounted to the movable slide, while the encoder is mounted to the base to provide a rigid support. The reader was installed as the moving unit to reduce the amount of moving mass and to provide the greatest possible rigidity in the measuring direction.

Figure 6. Heidenhain LIP 100 Series Exposed Incremental Encoder

The LIP 101 encoder has an 8 μm grating, which allows a resolution up to 10 nanometers. To compliment the LIP 101 encoder, Heidenhain EXE 660 electronics, which is the interpolation and digitizing electrical equipment, was also needed. The purpose of the EXE 660 is to read a sinusoidal input from the encoder, amplify and interpolate the signal, and digitize the signal. The output of the EXE 660 is connected to a control device, such as a PMAC-based control card.

With the current settings of the EXE 660, the sinusoidal signal is interpolated 100-fold at a signal cycle of 4 μm to produce a resolution of 10 nm. Therefore, each count read by the encoder is equivalent to a linear displacement of 10 nm.

With the combination of the LIP 101 and the EXE 660, the slide could (if desired) reach traversing speeds of about 70 m/min at an acceleration of about 20 m/s^2. These limitations ensure the PEC that the slow, steady movement of the Nanoform axes will be monitored precisely. Also, the LIP 101 has a natural frequency on the order of or above 2 Khz, which is on the order of 20 times higher than the first natural frequency of the machine axes that are on the order of 100 Hz. The natural frequency of the slide was found from using the stiffness and the movable mass of prior sections.

8.3.3 LIMIT SWITCHES

Three limit switches are incorporated giving a lower limit, upper limit, and a home position between the two outer limits. The upper limit is placed in a position that stops the movement of the slide before contacting the motor mount. The lower limit is placed in a position that stops movement before the slide constrains the counterbalance. The limit switches are micro-sized photoelectric sensors featuring a pulse modulated light source and are manufactured by Aromat. The input voltage to the sensors is 5-24V. They each consume 80 mA of current.

The limit switches were placed on the same side as the spindle, since the encoder was mounted on the other side of the slide. It would be ideal to place the limit switches on the other side of the slide due to cutting fluid, debris, etc. but this was not feasible due to the encoder being mounted there. However, the limit switches are fairly robust and small debris will not effect their operation. Figure 7 is a picture of the limit switches actually mounted on the slide. As seen in the figure, there are three switches on the slide and a corresponding elbow bracket that when blocking the path between the switch causes a trigger in the PMAC card. In figure 7, the switch on the right is for the lower limit, the switch on the left is for the upper limit, and the switch in the middle is the homing switch.

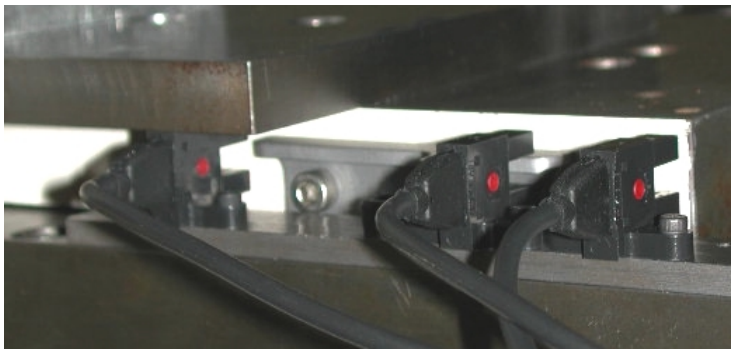

Figure 7. Limit Switches Mounted on Slide

The limit switches chosen are normally light on, meaning they give a low output when nothing is blocking the light path. When obstructed however, the output of these limit switches goes high and signals the PMAC controller to stop movement of the slide. The reason for this convention is safety. If it would happen that one of the limit switches would fail, then the PMAC controller would see a high input and would also stop motion of the slide. The PMAC control demands normally low input from the limit switch and the limit triggers when the input from the switch

goes high. Also with a normally closed switch, greater noise rejection is incorporated when compared with normally open switches. The limit switches are set up to trigger on a rising edge. Therefore, when the PMAC controller senses a rising edge of input voltage from a limit switch, the slide has reached a limit and all motion is stopped. This trigger condition is set by the I-variable IX25 on the PMAC card.

8.4 ACTIVE CONTROL SYSTEM

8.4.1 PMAC

The controller for the slide is manufactured by Delta Tau. This controller is a high-performance servo motion controller capable of commanding 4 axis of motion simultaneously. It incorporates a 56k Digital Signal Processor from Motorola with 4 output digital-to-analog (DAC) converters. It also features 4 full encoder channels with over-travel limit, home, and amplifier fault/enable flags. The controller is installed on the bus interface of a host computer and pulls all power from the computer including power for the limit switches as well as the encoder. It can also be setup to use external power for the limit switches and encoder. This involves changing jumpers on the PMAC card and bringing in the outside power on pin 59 and 60 on the JMACH connector. Typically, outside power can come from the servo amplifier or another commercial amplifier. Using an outside power supply allows for optical isolation of the digital computation circuitry from the analog output circuitry on the PMAC card.

For motion programs, the user has available "S-curve" acceleration and deceleration. These rates of acceleration and deceleration along with the maximum velocities, jogging rates, etc. are set with the appropriate I-variables in the PMAC library. PMAC control also allows for cubic trajectory calculations, linear interpolation, circular interpolation, spline, and other complicated motion that diamond turning might require.

Along with multi-axis control, the PMAC allows built in PID control of each axis for motion programs. This PID control is setup and tuned in the PEWIN program that interfaces the PMAC card with the operating system and user interface. Various control parameters are available to fine-tune the slide for various motion commands and movements. To tune the motor, PMAC has an auto-tune feature that suggests appropriate PID control variables based on motor parameters, slide parameters, and encoder feedback from a series of step functions. However, for particular applications, these numbers are not always optimal and need minor modifications.

Currently, the control parameters are being studied to improve the performance of the slide. It is believed that there is some stiction in the slide causing a resistance to motion and appropriate PID values have not been found at this time.

8.4.2 MAGNETIC SPINDLE

Future research involves a magnetic spindle made by Koyo of Japan that will be incorporated to the third axis of the Nanoform diamond turning machine. This spindle operates up to 100,000 RPM and provides 6 HP. The tooling system consists of a precision collet with a capability of

up to 3/8" maximum tool diameter. The specifications of the spindle are given in Table 3 and the schematic is located in Figure 8.

Rotational Speed	100,000 RPM
Peak Power	4.5 kW
Continuous Power	3.0 kW
Max. Axial Load	350 N
Max. Radial Load	100~150 N
Static Axial Stiffness	45 N/μm
Static Radial Stiffness	40 N/μm

Table 3. Parameters of Magnetic Bearing Spindle

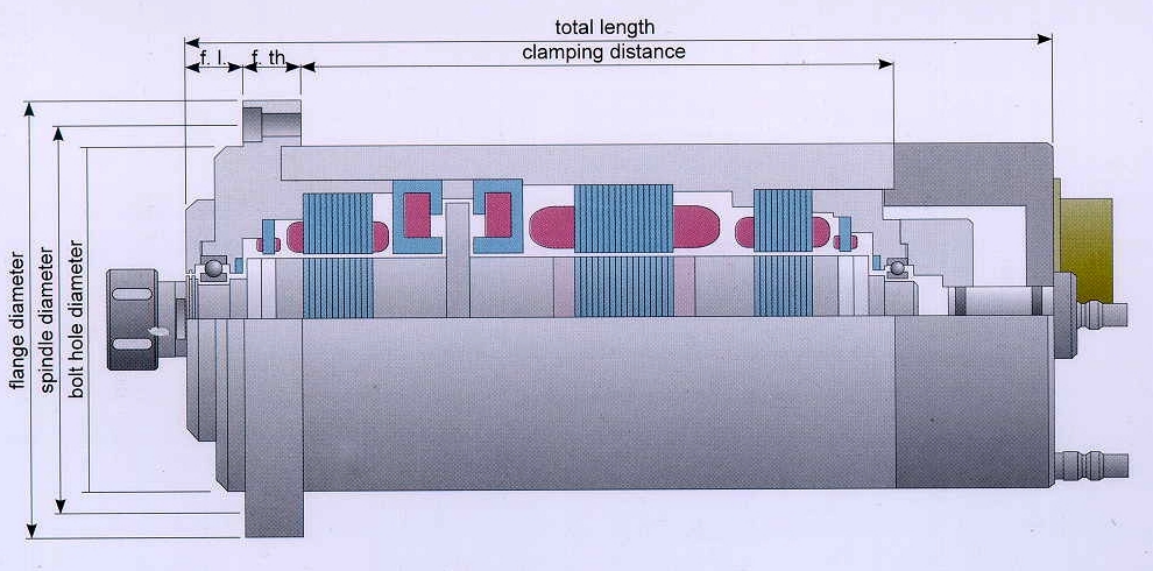

Figure 8. Magnetic Bearing Spindle

8.5 FUTURE RESEARCH

The y-axis plays an important role in the future research of this NSF-sponsored project. The magnetic bearing spindle will be attached to the y-axis, and its position is certainly critical during precision milling operations. Arcona and Miller's previous work [2,3] at the PEC on tool force modeling will be used to automate tool path compensation for tool deflection. Also, the dynamic modeling of magnetic bearing spindles is being research extensively with the aid of an active magnetic bearing textbook [4]. With the combination of the y-axis implementation, tool force

calculations, and magnetic bearing modeling, active tool compensations should improve the surfaces of machined materials.

8.6 CONCLUSIONS

The y-axis air-bearing slide has been assembled and is currently being tested and tuned prior to being added to the Nanoform 600. The slide now has a counterbalance, feedback system with 10 nanometer resolution, limit switches for over-travel protection and a programmable multi-axis control card (PMAC). There are, however, some issues of concern that need to be addressed in the near future. One area of concern is the interference of chips and cutting oil during operation. The Heidenhain encoder will need to be covered to prevent any incorrect encoder readings. Once these issues have been resolved, the next step would be to interconnect the y-axis with the other Nanoform axes control. Cutting experiments using small, high-speed milling tools will then be conducted. The results of these tests will be compared to previous experiments conducted by Miller [3]. The magnetic bearing spindle is expected in July and it will be mounted on the y-axis to replace the air bearing spindle.

REFERENCES

1. Yang, M.Y. and Choi, J.G., A Tool Deflection Compensation System for End Milling Accuracy Improvement, Transactions of the ASME, Vol 120,222-229, (1998).
2. Arcona, C. Tool force, chip formation and surface finish in diamond turning. Ph.D. Dissertation, North Carolina State University, (1996).
3. Miller, E. Deflection prediction and error correction of high seed miniature milling tools. MS. Dissertation, North Carolina State University, (2000).
4. Schweitzer, G., Bleuler H. and Traxler, A. Active Magnetic Bearings. VDF, 1994.

9 PRECISION REPLICATION OF MESO AND MICRO OPTICS THROUGH INJECTION MOLDING

David D. Gill
Graduate Student
Thomas A. Dow
Professor
Mechanical and Aerospace Engineering

The objective of this research is to extend the limits of current optical production techniques for complex, thermally-stable, ultraprecise optical components produced in large volume. Injection molding of polymer is a high volume process that has promise in the replication of meso and micro optical features, but the process is not well understood on this scale. Additionally, polymer has great advantages in its ability to be formed into complex and intricate shapes, but the high coefficient of thermal expansion and hygroscopic nature have prevented the widespread use of polymer for precision optics. This research addresses these challenges on two fronts. The first is through an increased understanding of the injection molding process for the replication of micro optics. Precision molds have been produced with optical features of varying size, shape, step height, and aspect ratio. These features include a spherical lens, fresnel lens, blaze diffraction grating, and wedding cake feature These features have pitch as small as 10μm and step heights as small as 1.25μm.

The second challenge, the thermal instability of polymer lenses, is being addressed through research into co-molding these optics onto thermally stable substrates, that is, the injection molding of optics directly onto the surface of the substrate. Challenges include the surface chemistry, modification of properties at the polymer-substrate interface, and the handling, positioning, and mold design factors for using a brittle substrate material in the high-pressure, high-temperature environment of the injection mold.

9.1 INTRODUCTION

Integrated circuit manufacturers are increasing the speed of their computer processors at an impressive rate that is pushing the bandwidth limits of bus communications in their current form. New methods of board-to-board and chip-to-chip communication must be developed in the near future to relieve the bandwidth limitations. Optical communication pathways have been suggested and researched, but many obstacles still prevent the use of this method of data exchange. The cost of producing optics is foremost among these barriers. New methods of production must be developed so that high quality optics can be produced in high volumes. Injection molding offers high volume production, but before implementation of this process in micro and meso optics molding, more must be understood regarding the molding process. Additionally, for polymer optics to be used in the varied environments that computers encounter, a means of limiting thermally induced optical changes must be developed.

9.2 INJECTION MOLDING: PROCESS FACTORS AND REPLICATION FIDELITY

The injection molding process has been in use for many years, but still remains a mixture of art and science. This is especially true for the production of very small parts. This is due to the large surface area per volume of the part as well as the relative scale of the part features to the polymer molecules that may consist of coils as long as several micrometers [1]. Additionally, though some meso-scale optic molding is currently done in industry, there is a lack of publicly-held knowledge of the optic replication process as it is usually a core competence of the companies involved [2]. The lack of public knowledge has limited the growth of the field. Injection molding is not typically classified as a precision process due to the effects of the significant pressure and temperature changes necessary for the process. However, with an increased understanding and control of the injection molding process, as it pertains to meso and micro optics, comes greater precision and fidelity in replication.

9.2.1 INJECTION MOLDING FACTORS AND THE MOLDING PROCESS

Of primary importance to the development of an understanding of the injection molding process is an understanding of the process factors (variables) and their effects on the replication fidelity of the optics. The factors of injection molding can be found through a brief description of the molding process that consists of 4 steps described below and illustrated in Figure 1.

1. Metering – During the metering step, the polymer pellets from the hopper feed into the screw. The screw rotates slowly while slowly translating backwards away from the mold. The screw threads, which fit tightly against the inside diameter of the barrel, move the polymer pellets toward the shot area. In the plasticating section of the screw, the root

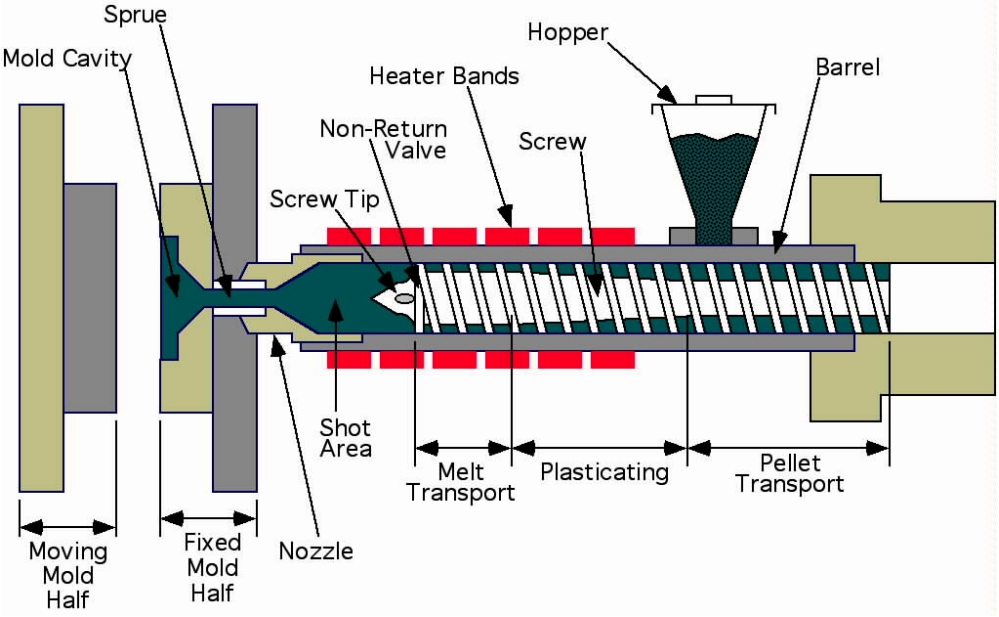

Figure 1 Injection Molding Machine Components

diameter of the screw increases causing the polymer to shear against the walls of the barrel. This shearing action causes the polymer to melt and the screw threads mix this melt thoroughly while transporting it forward to the shot collection area. Once enough molten polymer has been collected in the shot area, metering is complete, and the screw stops rotating. The molding factors of the metering stage are the *polymer temperature* (maintained by electric resistive heating bands on the outside of the barrel) and the *screw rotation speed* which affects the shear rate and thus the viscosity of the polymer.

2. Injection – During the injection step, the mold is closed, bringing the moving half of the mold into contact with the fixed mold half and then applying significant force to overcome the high pressure that occurs in the mold cavity, keeping the mold halves in contact. The screw is then translated toward the mold at high speed and high pressure. This translation forces the non-return valve at the tip of the screw to close and prevents the molten polymer from flowing backward along the screw. The polymer is injected through the sprue and into the mold cavity. The factors of the injection stage are the *injection pressure* and the speed or rate at which the polymer is injected, commonly called the *injection speed*.
3. Holding – The polymer in the mold cavity begins to cool, especially near the mold walls which are temperature controlled. As this cooling occurs, the polymer shrinks away from the mold wall. However, if pressure is maintained on the screw, the cooling polymer is forced back against the mold wall and dimensional accuracy is maintained though additional stress is locked into the part. The molding factors of the holding stage are the *hold pressure* and the *hold time*, the amount of time for which the hold pressure is maintained. After some

time, the polymer in the sprue will solidify causing the application of hold pressure past this time to be useless.

4. Cooling – During the cooling stage, the polymer part continues to cool within the closed mold until a point that it can be ejected from the mold without deformation. The molding factors of the cooling stage are the *cooling* time, the amount of time that the polymer is allowed to cool, and the *mold temperature* as controlled by the water flowing through internal passages in the mold plates.

The final molding factor is the *mold position.* The features in the mold used in this experiment are positioned on a circular insert that can be rotated in the mold. This causes the polymer to flow across the features in a different order depending on the rotation angle of the insert.

9.2.2 APPARATUS

To address the research goals, a series of experiments has been performed on a laboratory-scale Nissei hydraulic injection molding machine at the PEC. This machine has a 6.2cm^3 shot volume and a 14mm screw that allows very thin optics to be produced in a single cavity mold while still staying within common design practices regarding the ratio of shot volume to screw volume. The available mold clamping force is 69 KN with a maximum injection pressure of 175 MPa. The machine has an integrated mold heating and cooling system that employs water as the heat transfer medium. The parts replicated to date have been single and double cavity parts approximately 1800mm^2 in area with thickness below 350μm.

A mold system was designed and built to fit the Nissei machine. This system is shown in Figure 2. The moving and fixed steel mold bases were designed to have minimal deflection under the loading conditions experienced by the mold members. The mold plates mount to the mold bases and contain internal passages through which the temperature control medium flows. The aluminum mold inserts mount to the mold plates. These mold inserts are diamond turned with a flat on the moving side and a cavity on the fixed side. The fixed side aluminum insert also holds the copper insert that contains the optical mold features. The moving mold base surrounds the part ejection system that consists of a hydraulic cylinder, ejector plate, ejector sleeve, and ejector pin. The cylinder moves the ejector plate that holds the head of the ejector pin. The pin slides in the ejector sleeve. As is seen in Figure 3, a small space, called the sprue puller, is left at the end of the ejector sleeve. During injection, this cavity fills with polymer. When the mold opens, the friction between the walls of the ejector sleeve and the sprue puller helps to pull the part out of the cavity and to stay with the moving side of the mold. Once open, the ejector pin forces the sprue puller out of the ejector sleeve and the part falls down the parts chute.

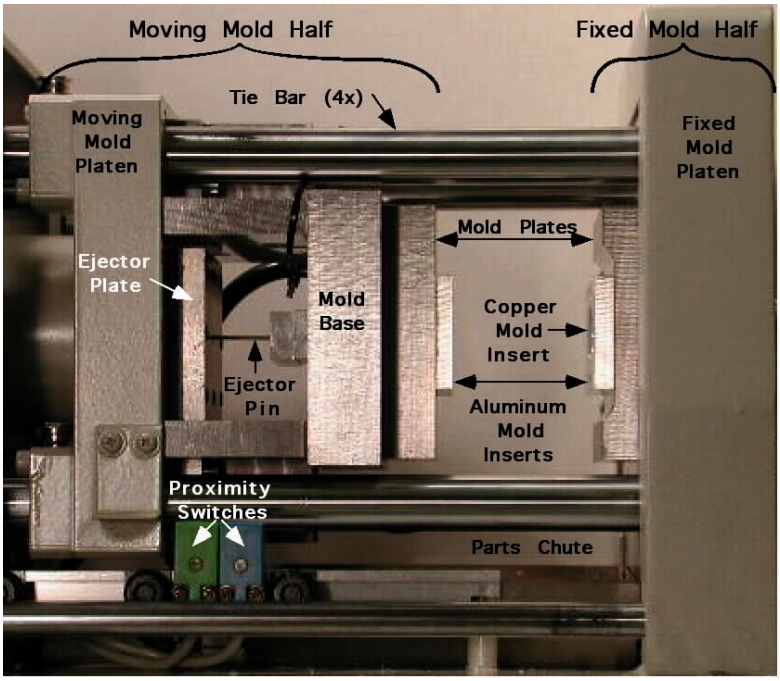

Figure 2 Mold System Used in Replication Experiments

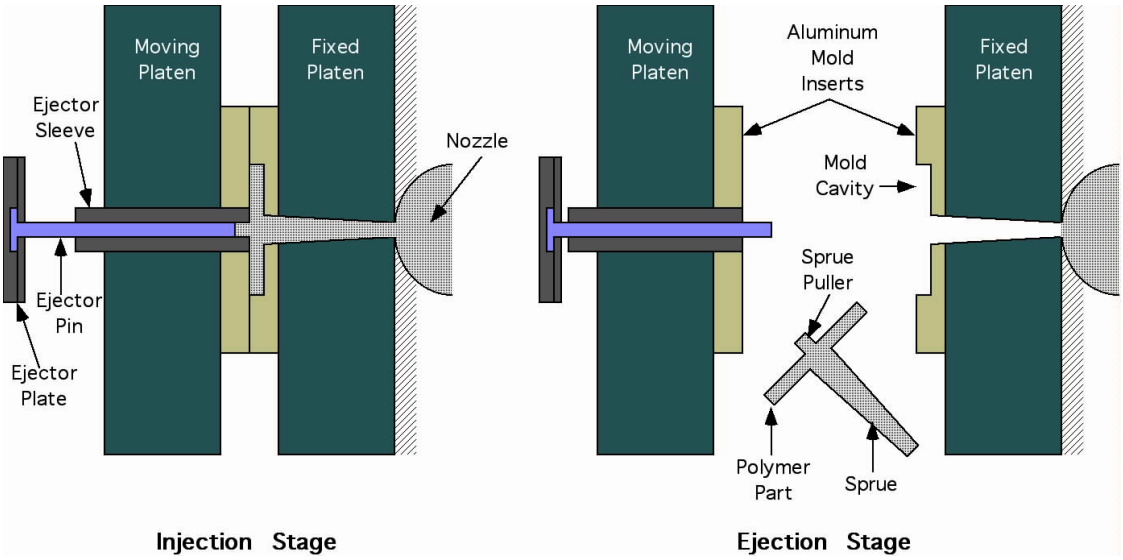

Figure 3 Cross-Sectional View of Mold and Ejection System

9.2.3 Optical Features in Injection Molding

The optical features used in this research are representative of the features that might be required for optical communications in computers. The features were diamond turned or diamond scribed in small-grain copper and are shown in Figure 4. The spherical lens and spherical Fresnel lens contain large radius arcs. The Fresnel combines these arcs with sharp steps of 160µm height.

The blaze grating provides sharp steps of only 1.2µm step height for comparison. The wedding cake feature has large steps and provides different feature depth to feature width aspect ratios. This set of features gives a range of depth from 600nm to 600µm and aspect ratios from 0.026 to 0.4.

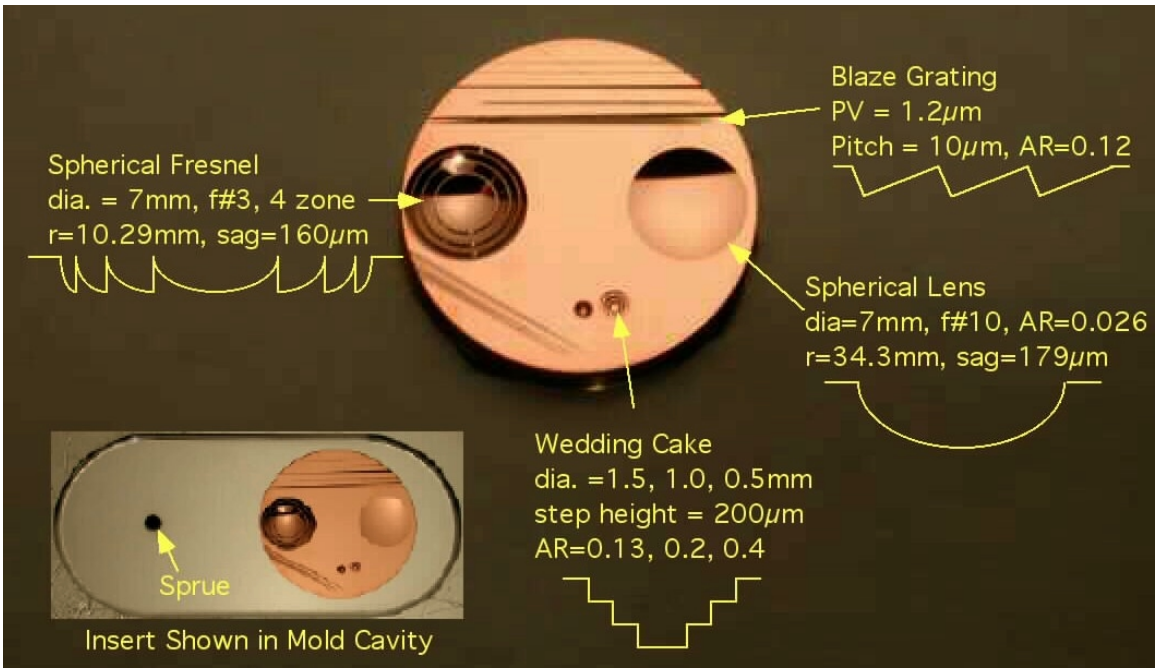

Figure 4 Mold Insert Showing Optical Features and Dimensions

The features were designed to be measured using stylus profilometry, interferometry, scanning probe microscopy, and optical transmission tests. The copper mold insert was fitted into a diamond turned aluminum mold cavity as shown in the lower left hand corner of Figure 4 and mounted in the injection molding machine. Because this insert was circular, it was possible to mount the insert in the mold cavity with the mold features located at different positions with respect to the polymer flow as it entered through the sprue and proceeded to fill the mold cavity.

9.2.4 Design of Experiment

Experiments were conducted with the molds described above to investigate the response of replicated optical features to different molding variables. The nine variables or factors listed above in the molding process description were chosen for this study due to their importance in general-purpose injection molding. A reduced-factorial, screening design of experiment was developed for the nine factors and initial high and low values were determined for each factor using Atohaas Plexiglas VLD poly(methyl methacrylate) (PMMA).

The high and low factor values for the first eight factors were determined as the minimum and maximum values at which the optical features could be replicated with reasonable fidelity; that is, the features must be measurable to show any correlation between molding factors and the replicated surface. To determine the low values of the factors, all factors were initially set to low values and then individual factors were lowered in a stepwise manner until the part was no longer acceptable. This factor was left at the lowest acceptable value and the process was repeated with the next factor. The high values were determined by the limits of the molding machine except for the polymer temperature and the cooling and hold times. The high value for polymer temperature was determined by the onset of material degradation and the cooling and hold time high values were set at the longest acceptable time for a production environment. The ninth factor was feature position which incremented the rotatable copper mold insert through 360 degrees in 90 degree intervals. The factors and their high and low values are given in Table 1.

Table 1 High and Low Factor Values for Design of Experiment

Factor	***Low***	***High***
Polymer Temperature	470°F	523°F
Mold Temperature	120°F	176°F
Injection Pressure	88 MPa	175 MPa
Injection Speed	5.85 cm^3/s	13 cm^3/s
Cooling Time	0 s	10 s
Hold Time	0.35 s	1.89 s
Hold Pressure	70 MPa	175 MPa
Screw Rotation	20 rpm	205 rpm
Mold Position	0°, 90°, 180°, 270°	

A specific set of factors with each set to one extreme or the other is called a treatment. Using these maximum and minimum values, a design of experiment was developed that reduced the number of treatments from 1024 (testing each factor at both of its values against every other condition in the table) to 32 by making the following assumptions: 1) the factors do not interact and 2) the effects of the factors vary linearly between the high and low factor value given in the table. Through statistical analysis of the chosen 32 treatments, it was shown that two variables in the test were not constrained by the first assumption and could interact without compromising the test results. Injection speed and injection pressure were chosen as the variables most likely to interact. In the experiment, each treatment consisted of the production of more than 100 parts to allow the process to reach equilibrium with each part's cycle time between 3 and 15 seconds. Five of the final 25 parts were collected for each treatment and 3 of those 5 were measured, the extra 2 parts being backups in case of handling damage. The measured parts were then compared to measurements of the mold features to reveal the correlation between injection molding process factors and feature replication fidelity.

9.3 RESULTS AND DISCUSSION

Through the measurement of replicated features, an understanding of the response of the replicated surfaces has been found as have the replication abilities of injection molding.

9.3.1 MEASUREMENT OF THE REPLICATED OPTICAL FEATURES

Each replicated PMMA feature was compared to the matching feature in the mold; however, the method of quantifying that measurement is different for each feature type. The form of the spherical and fresnel lenses was tested using a phase measuring interferometer. Measurements of these lenses included astigmatism, coma, spherical aberration, and the residual PV and RMS after removing a best-fit sphere from the measurement data. The step heights of the wedding cake and blaze grating features were measured using a stylus profilometer and white-light interferometer respectively. Figure 5 shows an interferometer measurement of a spherical lens feature in the mold and as replicated PMMA. The measurement reveals that the PV residual error after a best fit sphere has been removed is 10 times greater for the replicated lens than the mold. This was true for all of the measurements on the spherical lens and Fresnel lens, so the error in the mold was neglected in the design of experiment for these two features.

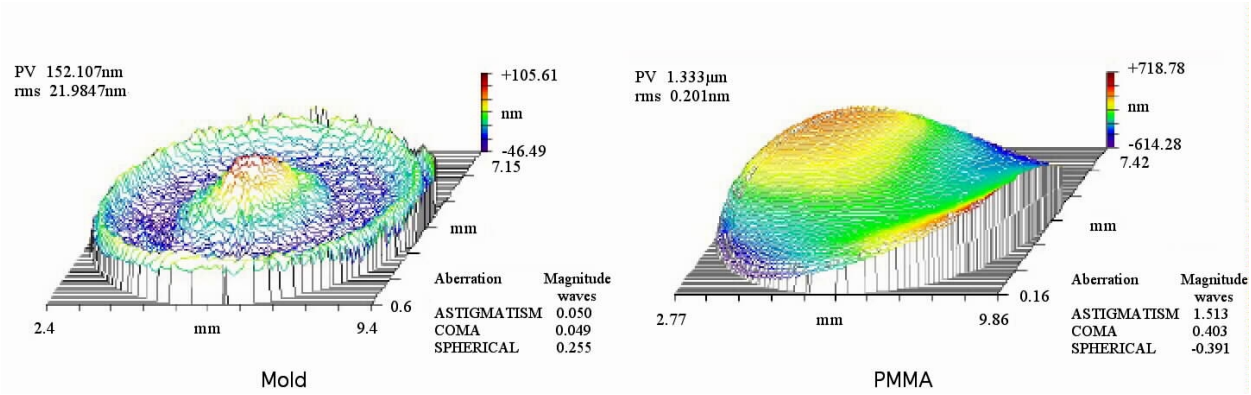

Figure 5 Oblique Interferometer Image Showing Error in Mold and Replicated PMMA for 7mm Diameter Spherical Lens

Each replication error value used in the analysis of the design of experiment consisted of an average of several parts. The optical aberrations of the spherical lens and Fresnel lens were measured and averaged for 3 lenses for each factor treatment. The blaze step height error was measured for 5 steps on each of the 3 parts produced for the factor treatment, and these 15 values were averaged. The 3 step errors of the wedding cake feature were averaged for the 3 lenses produced for the treatment as well. This averaging helped to de-emphasize values with extreme results.

9.3.2 FACTORS AND THEIR EFFECTS

Through the partial-factorial screening design of experiment, it was possible to determine which molding factors yielded significant replication responses. The most accessible results of the design of experiment are through an F test that signifies confidence in the correlation between the effect and the molding factor change from low to high value. The residual of this F test is called the "p" value, which shows the correlation to be significant if the value falls in the range of 0%<p<5% (0.0<p<0.05). To clarify, if a test showed that p=0.0001, the probability of the change in feature measurement happening due to chance instead of due to the change in factor values is 1 in 10,000. The p values were determined by analyzing the data using JMP statistics software from SAS. Each factor-measurement combination was analyzed and a graph produced as shown in Figure 6. The graph shows the response of blaze error to the factor mold temperature. The dots at mold temperature values of -1.0 and 1.0 are the measured blaze grating errors (% in this case) corresponding to the low and high mold temperature values respectively. The dashed horizontal line shows the average of all of the data, while the angled solid line connects the mean of the blaze error data at low mold temperature to the mean of the blaze error data at high mold temperature. The curved, dashed lines represent the 95% confidence values from the F test. Graphically, if the curved lines cross the horizontal average line, there is high confidence that the change in the average error measurement from the low mold temperature to the high mold temperature is due to the change in the factor value. The graph also displays the p value.

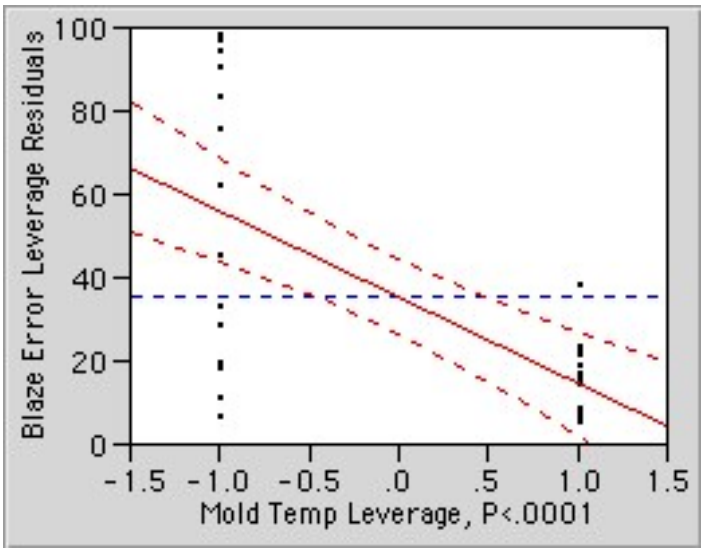

Figure 6 JMP Graph Showing the Response of Blaze Error to Mold Temperature

A convenient means of showing the results of the experiment is to graph the value 1/p, where any bar with a height greater than 20 (1/0.05) shows a significant correlation. Such a graph is presented in Figure 7. The column representing the response of blaze error to mold temperature

has been shortened to 1/p=500 for ease of viewing, but the actual value for this combination is 1/p>10,000. From Figure 7, it is evident that mold temperature and screw rotation speed had the biggest effect on optic replication fidelity. Factors with less significant effects included hold pressure and time, injection speed, and mold position. It is noteworthy that there was agreement on the preferred value for each of the factors. For example, screw rotation had a significant effect on 6 different measurements of 2 different features. The best measurement for each of these features occurred at the same value of screw rotation. The only factor for which this agreement did not occur was the mold temperature. The blaze error was best when mold temperature was high, but the Fresnel astigmatism was best when the mold temperature was low. However, the F test for the blaze error had an incredible value of 1/p>10,000 while the Fresnel astigmatism F test revealed 1/p=42. From this comparison it is clear that the overall replication was much better with a high mold temperature.

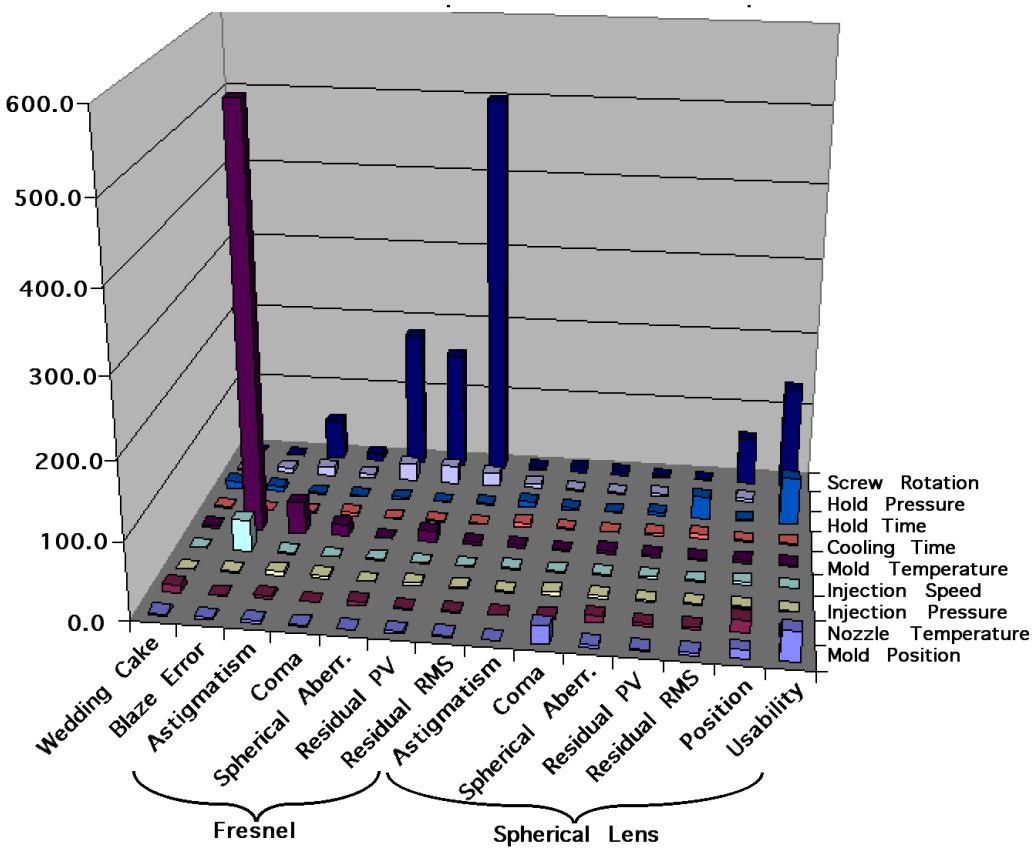

Figure 7 Effect of Factors on Optical Feature Replication

9.3.3 THE BEST REPLICATION ACHIEVEMENTS

The molding experiment showed that injection molding is a viable means of replicating meso and micro-optics in very large production volumes. Table 2 shows the minimum error achieved in the replicated lenses produced in the design of experiment. It is significant to note that these

errors were achieved using the extreme factor values and that the best molding conditions are likely to lie somewhere between the extreme values. Therefore, it can be assumed that the minimum achievable error is better than shown in the table. The table shows that the 1.2μm step height of the blaze grating was replicated within 112nm (7%) and that the smallest step height error of the replicated wedding cake structure was 1.8μm (0.9%). These small errors are especially impressive when combined with the high volume production that would be possible as the longest cycle time was just over 13 seconds. Figure 8 shows replication ability through a scanning electron microscope images of the Fresnel lens feature in the mold and replicated in PMMA. Figure 9 is an SEM image of a replicated wedding cake feature.

Table 2 Minimum Error Achieved in Replicated Lenses During Design of Experiment

Feature	Measurement	Smallest Error Measured (nm)
Spherical Lens	Astigmatism	232.7
	Coma	146.8
	Spherical Aberration	33.5
	PV Sphere Residual	690.7
	RMS Sphere Residual	127.3
Fresnel Lens	Astigmatism	282.7
	Coma	118.1
	Spherical Aberration	728.4
	PV Sphere Residual	448.3
	RMS Sphere Residual	75.7
Blaze Grating	Average Step Height	73.3
Wedding Cake	Average Step Height	668

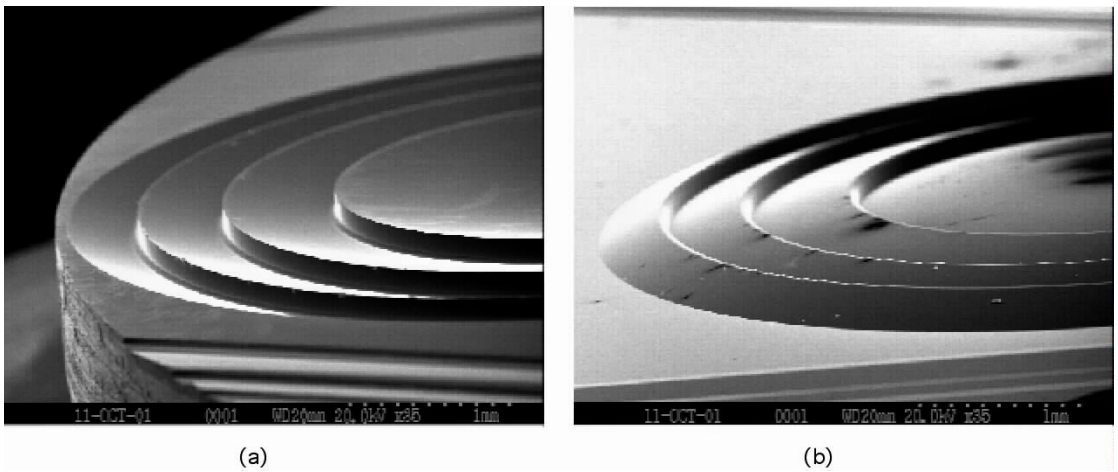

(a) (b)

Figure 8 SEM Image of Fresnel Lens Replication Fidelity in the Mold(a) and PMMA(b) at 35X

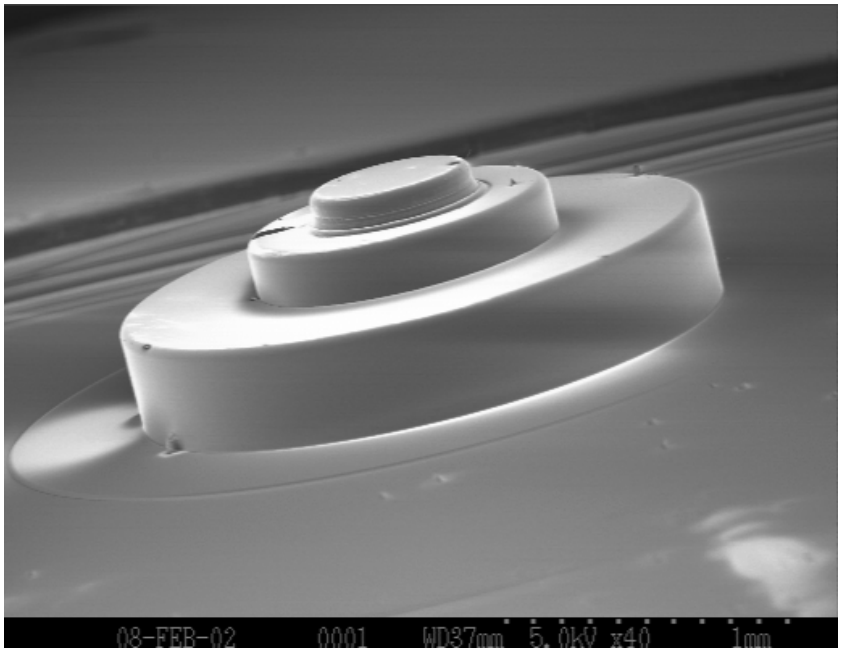

Figure 9 SEM Image of Replicated Wedding Cake Feature at 40X Magnification

9.4 SUBSTRATE CO-MOLDING

A factor that has limited the use of polymer optics in the past has been the high coefficient of thermal expansion of polymer. Many of the optics that are used in current applications must be able to withstand relatively large temperature changes while not allowing the optical properties of the lens to be altered. Past research has shown that thin polymer optics on thicker thermally-stable substrates produce a combination that has the thermal stability of the substrate and the moldability of the polymer [3]. This process has been used to apply diffractive optical features to the surface of spherical lenses, thus reducing lens aberrations. The processes used in the past, involving UV photopolymer, have had long cycle times. It was necessary to create a high volume process for the production of co-molded lenses. The successes of replicating complex precision optics through injection molding prompted the application of injection molding to substrate co-molding.

9.4.1 ADHESION AND SILANE CHEMISTRY

The first challenge of co-molding is the adhesion of the polymer to the substrate. In perfectly dry conditions (relative humidity < 0.1%) the polymer would adhere to the glass. However, at humidity levels above 0.1%, a monolayer of water forms on the surface of the glass, changing the surface free energy such that the polymer no longer adheres. In fact, even if the bond were made at such low humidity, any exposure to higher humidity would risk delamination due to the water travelling through the glass and weakening the bond from the other side.

This problem has been studied for other applications including the coating of photoresist for lithography techniques and the adhesion of epoxy to fiberglass in composite materials. A class of chemicals called silanes has been developed to act as an intermediary layer joining the silicon in the glass to the carbon structure of the polymer. Three silanes provided by United Chemical Technologies and used in this research are shown in Figure 10 with the polymer-reactive end on the left and the substrate reactive end on the right. The silane is combined with water in a hydrolysis reaction and then the silicon end of the molecule bonds with the silicon of the glass through hydrogen bonding as shown in Figure 11. The carbon end of the molecule adheres to the polymer by entanglement, hydrogen bonding, or covalent bonding. The target silane coating thickness is 3-8 monolayers. This thickness is considered to promote adhesion without introducing its own surface properties to the bond.

The key question is how the silane promotes bonding in the presence of water, relieves stress at the interface, and still prevents the polymer from growing and shrinking over temperature changes. One theory [4] is that the ionic bonding at the silane-substrate interface can break and reform bonds with adjacent sites to maintain equilibrium as the concentration of water at the surface changes. The theory suggests that the pressure during injection causes the polymer chain to be deformed. The semi-permanent covalent bond maintains this deformation and prevents the polymer from changing dimension through temperature changes. A pictorial representation of this theory is shown in Figure 11 with the polymer represented by the coil at the top of the picture. The steps from left to right show the process by which the polymer chain is deformed and then bonded to the reactive (R) end of the silane (step C in the Figure). The bottom end of the silane is shown undergoing hydrogen bonding with the substrate surface in a process that produces water.

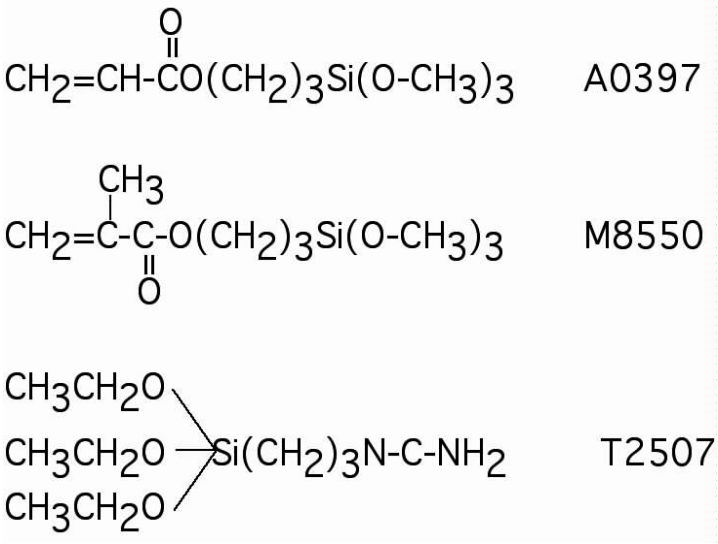

Figure 10 Molecular Structure of 3 Silane Adhesion Promoters

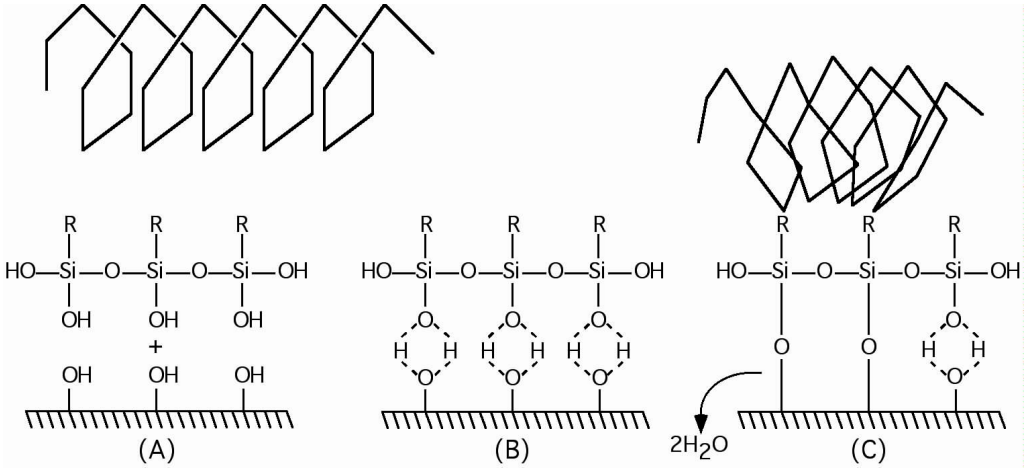

Figure 11 Silane Adhesion Theory for Polymer Coil on a Substrate

The silane solution was applied to the surface of the glass substrate and cured at room temperature for 24 hours or at 100°C for 10 minutes. A mold was created that allows molding with or without a substrate. When inserted in the mold, the substrate was fully supported to assure that the high pressures of the molding environment would not cause the substrate to fracture. The same optical features used in the previous molding correlation experiment were again used for molding on the substrate. The adhesion of the polymer to the substrate is being studied as is the stress introduced in the polymer during cooling while connected with the substrate.

9.4.2 SUBSTRATE MOLDING CHALLENGES

There are other challenges to substrate molding beyond the adhesion issue. The first is the need to mold on the "wrong" side of the mold. This challenge is illustrated in Figure 12. In conventional injection molding, it is desirable that the mold features and most of the cavity volume be positioned on the moving side of the mold. This design helps the polymer part to stay with the moving mold half when the mold opens, which allows the ejector system to eject the part from the mold. However, if this design is used (as is shown as option 2 in the figure), the substrate thickness must be very tightly toleranced. This is due to the requirement that the moving side of the mold seal against both the substrate and the fixed side of the mold to create a closed mold cavity. The substrate most commonly used in this research was microscope slides which do not have tight thickness tolerances.

The alternate substrate molding option is shown as option 1 in Figure 12. In this design, the mold features are on the fixed side of the mold. The cavity is formed by the fixed mold half clamping against the substrate, and the nozzle is able to inject the polymer directly into the mold. Differences in the thickness of one substrate versus another are unimportant as long as each substrate is fairly uniform in thickness from one end to the other. However, there are

disadvantage for this design. The sprue puller is now covered by the slide, so the substrate must be held firmly by the moving side of the mold and the polymer must be firmly attached to the substrate for the lens to be pulled from the sprue, from the mold features, and from the cavity which are all in the fixed side of the mold.

Another challenge is the possibility of thermal shock to the substrate as the 500°F polymer hits the room-temperature substrate. A third challenge is the smoothness of the controls to allow the mold to clamp on the brittle substrate with high force without breaking the substrate. All of these challenges are being studied and addressed in the current research.

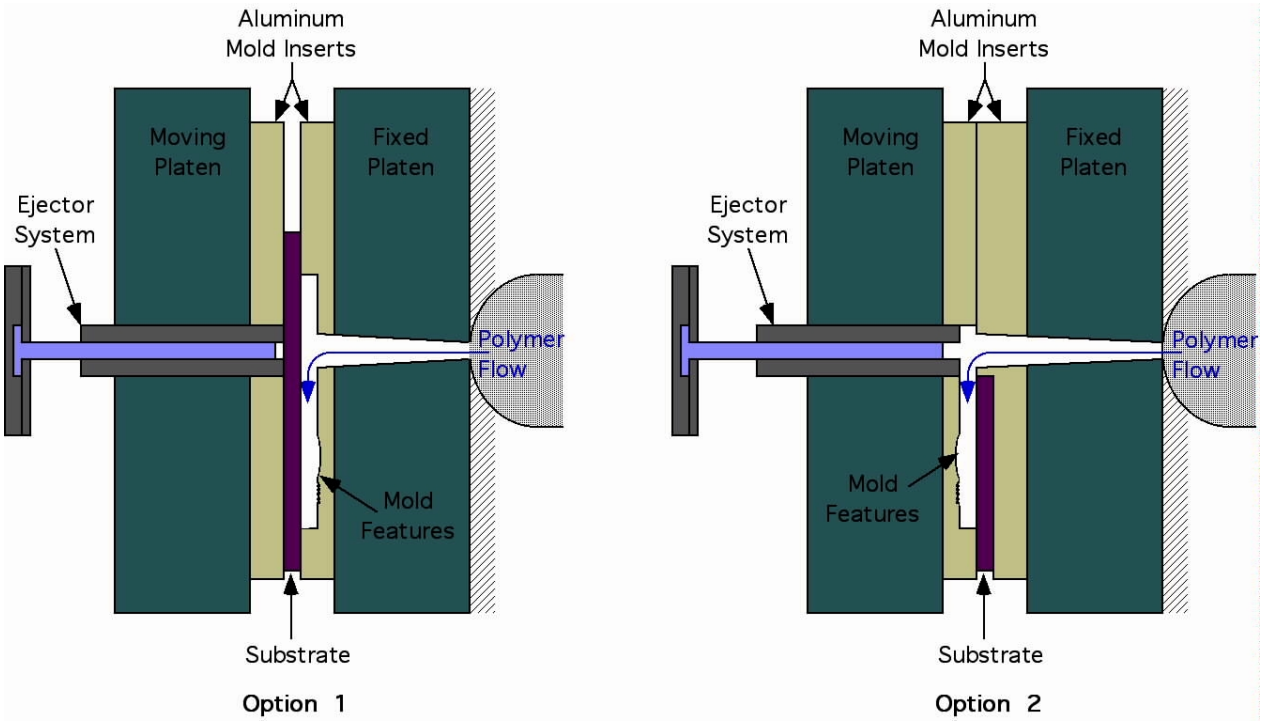

Figure 12 Two Mold Design Options for Co-Molding with a Substrate

9.5 CONCLUSION

The research has shown the viability of replicating micro and meso optics in high volumes through injection molding. A design of experiment showed the molding factors that had significant effects on the replication fidelity of the optics. Mold temperature and screw rotation had the biggest effects on the replication of optics while hold pressure, hold time, injection speed, and mold position were also found to have significant effects, though not as marked. Through the design of experiment optical features were replicated with errors of less than 1 wave and it is expected that these errors could be further reduced with more extensive testing and process development.

The co-molding of optics on thermally-stable substrates has begun with experiments on the adhesion promotion available from silanes. This research is addressing many of the challenges that come from molding on brittle substrates. The methods show promise for creating optically complex polymer features rigidly bonded to thermally-stable substrates.

REFERENCES

1. Bauer et al., "Advanced Micromolding of Optical Components," *SPIE Conference on Miniaturized Systems with Micro-Optics and MEMS*, Sept. 1999, Vol. 3878, pp261-270
2. Blough et al., "Single-Point Diamond Turning and Replication of Visible and Near-Infrared Diffractive Optical Elements," *Applied Optics*, July 10, 1997, vol. 36, n. 20, pp.4648-4654
3. Dannberg et al., "Wafer Scale Integration of Micro-Optic and Optoelectronic Elements by Polymer UV Reaction Moulding," *SPIE proc.*, Jan. 1999, vol. 3631, pp.244-251
4. Plueddemann, E.P., Silane Coupling Agents, Plenum Press, 1982

10 RAPID DIAMOND MILLING

Nobuhiko Negishi
Graduate Student
Thomas A Dow
Professor
Mechanical Engineering Department

Single crystal diamond turning is the standard method of creating optical surfaces in industry. However the geometric and material limitations of diamond turning has led to the search for improved methods of producing optical surfaces. The Ultra-Mill is a tool actuator that allows free form single crystal diamond machining of materials previously thought to be too hard (such as silicon carbide) or chemically incompatible (like steel). The Ultra-Mill uses a technique known as Elliptical Vibration Assisted Machining. Experiments performed at the PEC have reproduced the advantages of EVAM machining in steel and silicon carbide. Reduced tool wear and improved surface finish have been reported. A cutting force model has been created based on the Arcona model for diamond turning. The model has accurately predicted cutting forces for experiments conducted at the PEC. The Ultra-Mill High Speed(UMHS) is the next generation EVAM tool actuator currently being constructed at the Precision Engineering Center. This actuator is designed to have a larger bandwidth then the current Ultra-Mill. This non-resonant research actuator will be used to study the effects of tool velocity and the viability of this method in industrial applications. Efforts to optimize and construct the UMHS have focused on proper piezo stack actuator temperature control and kinematic head design. Piezo stack temperature distributions under specified operating conditions have been modeled, with model assumptions verified by experimental data. Static and dynamic analysis of the kinematic head has been done with finite element analysis package ProMechanica.

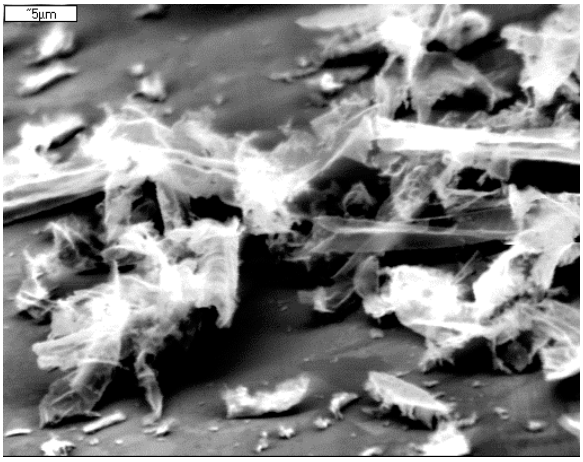

10.1 INTRODUCTION

Diamond turning is an important method for creating optical surfaces. However traditional diamond turning has two limitations: the first is the number of materials that can be satisfactorily machined by a single crystal diamond. The second limitation is the inherent geometrical requirements for a turned work piece.

The material limitations of diamond turned pieces are well known. Nonferrous metals such as aluminum, copper and electroless nickel and some plastics such as acrylic yield excellent surface finish and tool life. Using a diamond to machine hard ferrous materials such as steel or ceramics such as silicon carbide generate excessive tool wear and poor surface finish. The advantage of creating precision optical surfaces from steel or silicon carbide is the enhanced material properties which are useful in certain industrial applications. Some efforts to increase the range of materials that can be turned by diamond tools have focused on changing the machining environment. Flooding the chip forming area with carbon to reduce graphitation of the diamond in steel has been attempted with marginal results.[1] A more promising method of reducing tool wear is Elliptical Vibration Assisted Machining (EVAM). Elliptical Vibration-Assisted Machining is a technique that combines linear tool motion with an oscillatory motion in both the feed and thrust directions.[2] Oscillating a diamond tool at a high rate and small amplitude is one approach that has been proven to increase tool life and surface finish when machining steel.[3] The effectiveness of EVAM on standard materials has already been proven by experiments performed at the PEC. Benefits such as reduced cutting forces and reduced tool wear have been reported.

Innovative designs such as the fast-tool servo, developed at the PEC, have eased the geometric constraints of standard turning, allowing the machining of non-axis symmetric features. However the FTS cannot easily machine bi-conic surfaces and has no true free form capability.

The UltraMill is the next iteration towards progressing to a free form milling capability of diamond machined optical surfaces. The UltraMill can be mounted in a multi-axis machine and used as a free form milling tool. This flexibility combined with the promise of elliptical vibration assisted machining will revolutionize the precision optic industry.

10.2 VAM BASICS

Elliptical Vibration Assisted Machining refers to the superposition of a small (50 μm major axis, 7.5 μm minor axis) elliptical tool path on the standard cutting motion. The result of this superposition is an interrupted machining process with chip thicknesses that range between the tens of nanometers to two micrometers with nominal depths of cut up to 7 μm. The diamond tool contacts the work piece for a small section of the elliptical tool path. The majority of the tool

travel is out of contact. Small chip thicknesses and short cutting intervals are thought to be the mechanisms behind EVAM's advantages. The tool motion of the Ultra Mill causes chip thickness to be a function of feed rate, depth of cut and position along the elliptical tool path. Figure 1 is a simplified example of the chip formation during the EVAM process and illustrates how the chip thickness varies. The maximum chip thickness occurs late in the tool path. This thickness is much less then the depth of cut due to the material removed by the previous cutting cycle.

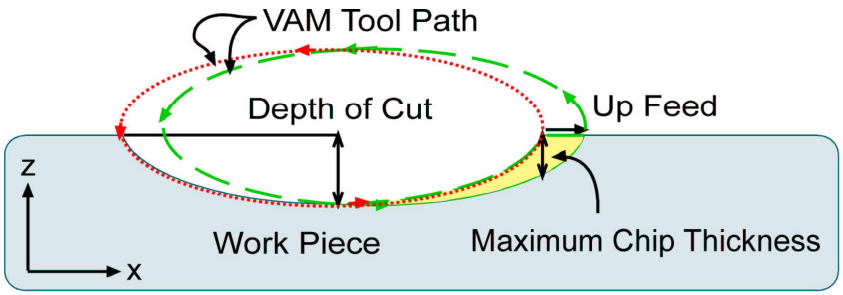

Figure 1. VAM Tool Path

The elliptical oscillating motion of the tool is generated by attaching the diamond tool to a kinematic linkage. This linkage consists of two 44 layer piezo stack actuators connected to a 'T' shaped kinematic head via two 1 mm radius ceramic half rounds and flexure to preload the whole system. A pair of sine waves, 90˚ out of phase, are used to drive the piezo actuators and generate the elliptical tool motion. For a given actuator displacement the dimensions of the 'T' determine the shape and the major axis of the tool path ellipse. The Ultra-Mill High Speed has "arms" of the 'T' that are 5 mm each and a vertical beam that is 26 mm. This geometry results in an ellipse with a major axis of 40 μm and a minor axis of 8 μm for an actuator stroke of 22 μm.

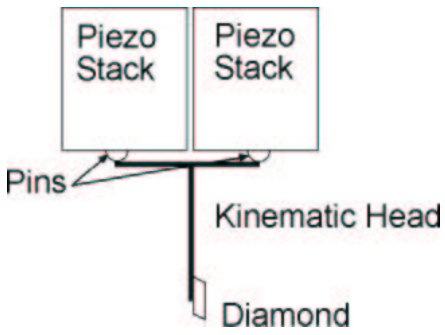

Figure 2. UltraMill Linkage

The piezo stack actuators are driven by two Kinetic Ceramics KC N15-1 1500 watt amplifiers with sinusoidal input from a Hewlett Packard 8904A function generator. This design is a non-resonant approach that allows research into the effects of different actuation frequencies over several octaves, amplitudes, and path tilts. The modular capability of the UMHS also permits alternate kinematic head designs to be mounted for greater performance or different experiments.

10.3 MODELING TWO DIMENSIONAL CUTTING

A program to model groove cutting with EVAM was constructed to study the relationship between of the machine parameters and the cutting conditions. The variable parameters for EVAM cutting include oscillation frequency, horizontal velocity and depth of cut. The cutting conditions are chip thickness, duty cycle, tool sliding and cutting force. Duty cycle is the percentage of the path that the tool is in contact with the work piece during one cycle. Tool sliding distance or Distance Ratio is the total distance that the diamond tip slides along the surface. This parameter is important in understanding the trade off of multiple cuts at small depths leads to longer cutting distances which most directly effect wear on the tool flank. The machine parameters were condensed into the Velocity Ratio, (the ratio of linear velocity of the work piece to the maximum velocity of the oscillating cutting tool) and depth of cut.

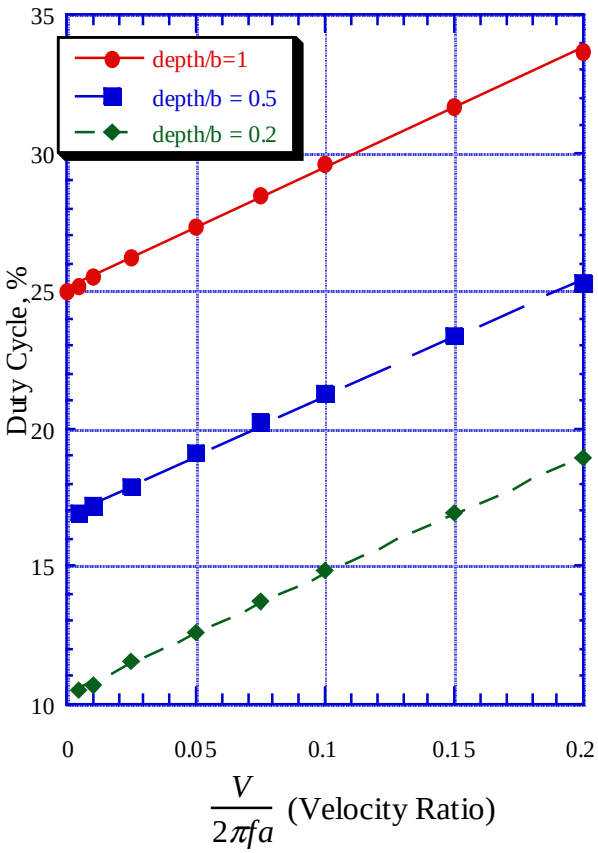

Figure 3. Duty Cycle as a function of velocity ratio and depth of cut

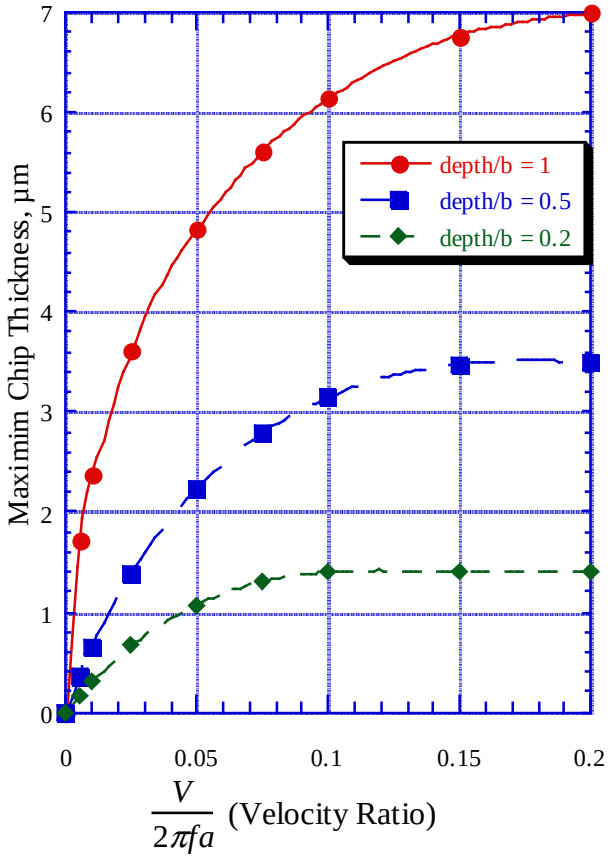

Figure 4. Maximum chip thickness as a function of the velocity ration and depth of cut

(major axis of ellipse = a, minor axis = b, part speed = V, frequency = f)

Figure 3 shows that a constant depth of cut has a minimum duty cycle that increases with increasing velocity ratio. This characteristic minimum shows the limit of duty cycle percentage for a given depth. For increased removal rates at a desired duty cycle it may be advantageous to

decrease depth of cut and increase work piece velocity. As shown in Figure 4, for a given depth of cut, a smaller velocity ratio results in a smaller chip thickness. Increasing the velocity ratio causes the maximum chip thickness to approach the static depth indicating that the lowest point of the tool path ellipse occurs at an uncut section of the work piece.

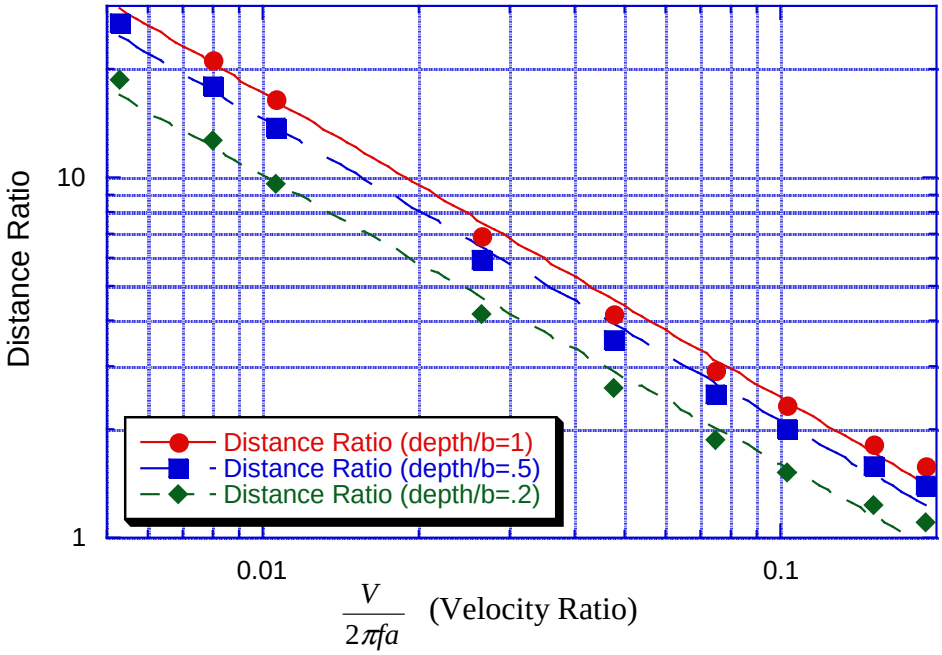

Figure 5. Distance Ratio as a Function of Velocity Ratio

Distance Ratio describes the increased sliding distance that is a result of the EVAM process. It is the ratio of EVAM sliding distance and distance slid with conventional machining. Plotted against the log of the velocity ratio Figure 5 illustrates the decreasing distance ratio with increasing work piece velocities.

The cutting forces were predicted based on the work done by Carroll, Drescher and Arcona to develop a tool force model for diamond turning.[4] The thickness of the EVAM chip varies with tool path position. This results in periodic cutting and thrust forces. The forces for one cutting cycle are shown in Figure 6. The general shape of the force curves can be explained by the instantaneous chip thicknesses and contact lengths. The chip begins at some small finite thickness and continues to increase reaching a maximum and rapidly reducing in magnitude afterwards. The cutting force follows this trend. The thrust force component is dominated by the length of the wearland along the circumference of the tool in contact with the work piece. This force reaches its peak when the tool is at the maximum depth and shows a rapid drop off as the tool begins to pull out of the work piece.

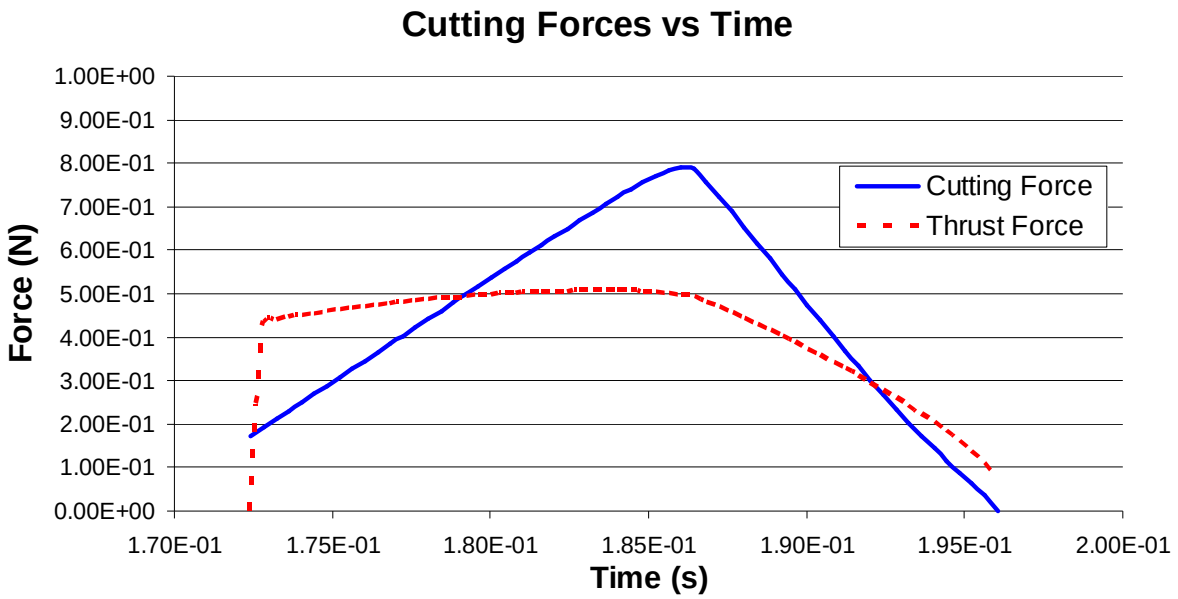

Figure 6. EVAM Cutting and Thrust Force as a Function of Position (EVAM Freq. 10 Hz, Velocity Ratio .01 and Depth of Cut of 7 μm)

10.4 MODELING THREE DIMENSIONAL CUTTING

The three dimensional EVAM chip is a complex non-symmetric shape. Figure 7 shows an idealized computer image of a steady state EVAM chip and the surface from which it was generated. The elliptical tool path is in the x-y plane and the work piece is moving in the negative x direction. The cross feed is in the negative z direction. The surface shows two rows of EVAM cuts that are overlapping and 180˚ out of phase. When the cutting rows are 180˚ of phase the peak of one cut coincides with the trough of the adjacent cut this type of phase shift results in the lowest theoretical surface roughness. The previous cuts are numbered to show the effect on the steady state chip form.

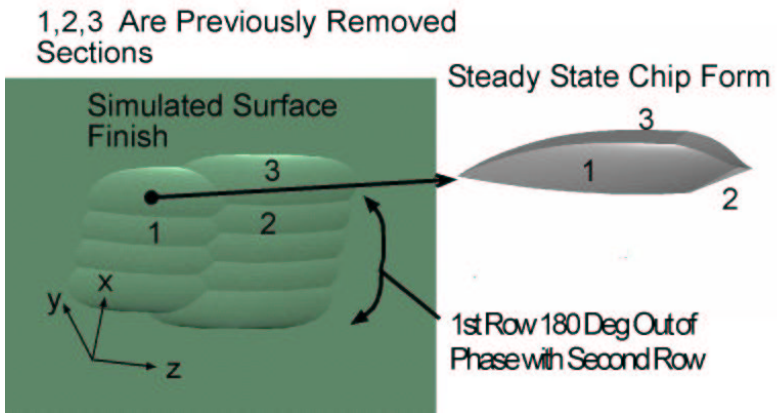

Figure 7. Steady State Chip Shape in 3-D Surface Machining

10.5 CUTTING TESTS OF AISI TYPE 1 STEEL

Reduced tool wear is an important advantage of Elliptical Vibration Assisted Machining. This is especially true when attempting to machine materials such as steel that promotes chemical wear in diamond tools. This chemical reaction results in catastrophic wear of the tool. Identical 0.5 mm radius diamond tools were used to machine twenty meters of tool steel (AISI Type 1 steel, Vickers Hardness 2.152GPa) using EVAM and static turning. Each sample has two 5 mm bands that required twenty meters of machining. A comparison of the Ultra-Mill and standard diamond turning with steel samples highlights the advantages of EVAM. Figure 8 shows the samples with roughness measurements taken with a white light interferometer.

a) Standard PV 0.161 μm, RMS 0.034μm

b) Ultra-Mill PV 0.024 μm, RMS 0.006 μm

Figure 8. Comparison of AISI Type 1 steel turned finishes

The static machined sample, Figure 8(a), has a Peak-to-Valley and RMS roughness that is an order of magnitude lower for the EVAM steel sample, Figure 8(b). Optimizing the EVAM parameters could easily increase this value. An optical quality surface finish is attainable with the UltraMill, visible in Figure 8(b). Conventional diamond turning cannot achieve a high quality finish due to dramatic tool wear. SEM micrographs comparing the cutting edges show fracture and damage on the diamond used in standard turning, Figure 9(a). The EVAM diamond tool has some wear but no damage, Figure 9(b).

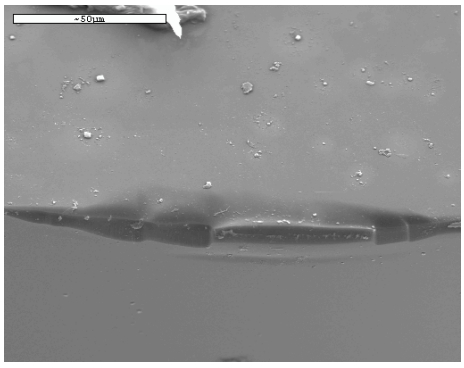

a) Standard Diamond Turning

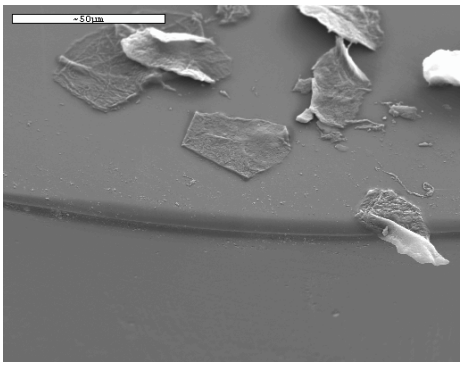

b) Vibration Assisted Machining

Figure 9. Comparison of Diamond Tools 8000x

10.6 CUTTING TESTS OF CVD SILICON CARBIDE

The possibility of diamond machining silicon carbide using VAM was also explored. A single, machined groove was attempted to verify the concept. The maximum chip thickness before fracture from previous grinding experiments with SiC was found to be 10 nm. This value represents the theoretical maximum ductile chip thickness and the target range for optimal cutting conditions. The Ultra-Mill cycle frequency was arbitrarily set at 200 Hz, well below the 700 Hz natural frequency.

10.6.1 EXPERIMENTAL APPARATUS

As shown in Figure 10 tilting the sample with respect to the feed of the tool would gradually introduce the tool into the work piece and minimize chip thickness during this ramp up period. This method produces a continuous feature with varied chip thickness and depths of cut to study the effects of VAM machining on a range of cutting conditions.

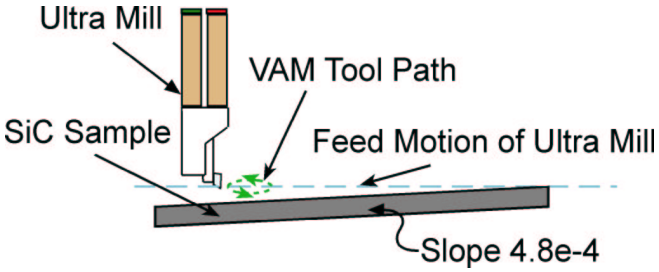

Figure 10. Feed Motion Relative to Sample Surface

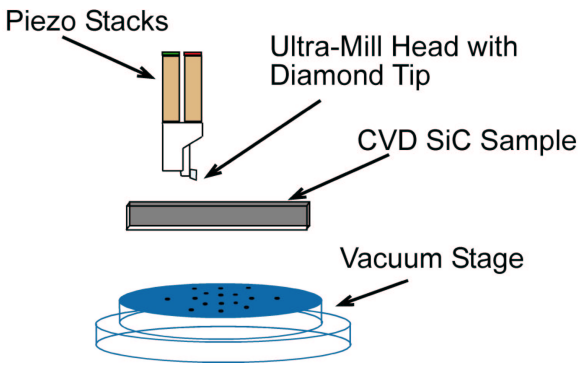

Figure 11. Apparatus For SiC Experiment

The cutting test was conducted using a Rank Pneumo ASG2500 diamond turning machine. The SiC sample was vacuum mounted to an aluminum stage attached to a fixed spindle chuck. The Ultra-Mill was mounted to the cross slide. The sample was machined with a cycle frequency of 200Hz, and up feed of 1 mm/min using a 0.5 mm radius natural diamond tool. A video camera recorded the chip formations during the experiment.

10.6.2 EXPERIMENTAL RESULTS

The Ultra-Mill produced no surface fracture for chip thickness up to 20 nanometers and depths of cut up to 3.5 μm. The chips generated at these depths appear ductile and discontinuous. Cross sectional surface roughness was measured with a Form Talysurf stylus profilometer at distances along the groove. These measurements are paired with the corresponding cutting conditions in the Table 1.

Table 1. Cutting Conditions and Surface Features

Cutting Conditions		Groove Features	
Depth of Cut (measured)	**Chip Thickness (calculated)**	**Surface Roughness (Rq) (measured)**	**Chip Form (observed)**
0-3.5 μm	**0-19nm**	**15-18 nm**	**Ductile**
3.5-8.6 μm	**19nm-2.3 μm**	**18-135nm**	**Brittle**

It is encouraging that at the end of the groove, sections towards the edges of the cut, remained smooth and undamaged. Signifying that machining SiC is possible for chip thickness up to twenty nanometers. Shown in Figure 12, the edges, depths up to 2.1 μm, remained undamaged with sectional roughness Rq of 0.190 μm. As the depth increases up to 4 μm the surface begins to transition with brittle fracture and tool wear effects, this surface has a roughness, Rq, of 0.04 μm. The deepest section of the groove is badly fractured with surface roughness, greater then 0.15 μm .

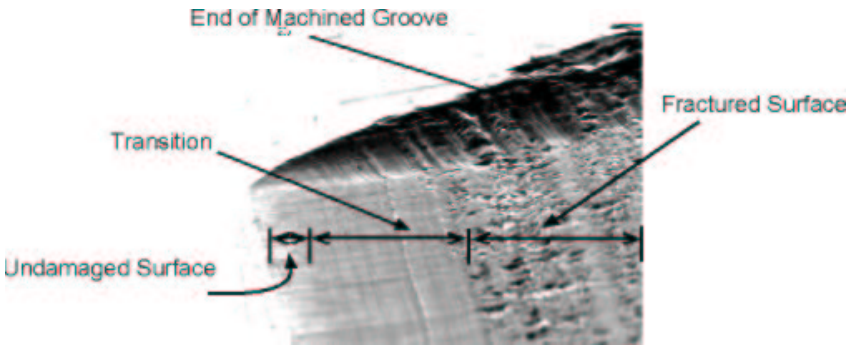

Figure 12. Deep End of Machined Groove (CVD SiC)

10.7 ULTRA-MILL HIGH SPEED

The UMHS was designed to study the effects of tool velocity and the viability of the EVAM technique in an industrial application. The Ultra-Mill High Speed was designed to operate at oscillation frequencies up to 5 KHz or ten times the maximum operational frequency of the current EVAM tool actuator. To achieve this increase in operational bandwidth the main structural and functional components were optimized. The non-resonant piezo stack actuated kinematic head design of the UMHS requires the components to be both rigid and lightweight. The PZT actuators shown in Figure 13 are a custom design built by Kinetic Ceramics that maximizes stiffness and weight. The triangular cross section allows the centroidial axis of the stacks to be placed close together, while still providing a large foot print for contact with the

base. This shape also sheds unnecessary weight while retaining high stiffness. The kinematic head, shown in Figure 14, is constructed out of CoorsTek Alumina AD-995 that has a high stiffness to weight ratio. The elastic modulus of AD-995 is 1.7 times that of steel and the density is less then half. The diamond tool is bonded directly to the ceramic head with structural epoxy to eliminate the conventional fixture and reduce weight. The linkage pins were also constructed out of alumina to reduce weight and increase wear resistance.

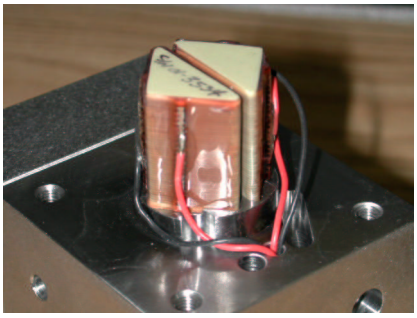

Figure 13. Triangular Stack Actuators

Figure 14. Alumina Kinematic Head

The original UMHS head designed by Matthew Cerniway had a calculated natural frequency of 27.45 KHz, mass of 4.811 grams and was constructed with Alumina AD-995.[5] The shape and wall thickness of this head has been changed to decrease weight while maintaining stiffness. The profile of the design is shown in Figure 15. The overall height of the head is 26 mm. By reducing wall thickness, base diameter and changing the profile of the head to remove any excess material, a 13% reduction in weight was realized. The design was analyzed using ProMechanica, a FEA program produced by Parametric Technologies Corporation. The deflection under a 5 N load was reduced from 0.5 μm to 0.35 μm or a 43% increase in stiffness. The natural frequency natural frequency was increased to 29.9 KHz from 27.5 KHz. The location of the center of mass was shifted 30% closer to the centerline of the head as well. Figure 16 is a ProMechanica screen shot from a deflection simulation.

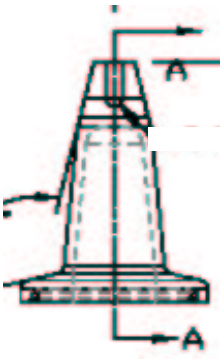

Figure 15. UMHS Head

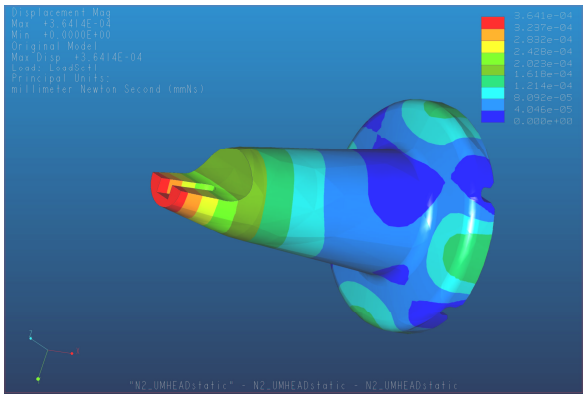

Figure 16. ProMechanica Deflection Simulation

The alumina head was received from CoorsTek and measurements have been made to verify accuracy with the drawings. There are some errors in the machined form which were discovered during this process. The channel located at the tip of the head to accept the diamond tool has a radius where the drawing specified a flat. The radius profile would increase the needed epoxy thickness between the diamond and the ceramic head. The profile also reduces the epoxy contact area on the diamond tool. The changes in bonding thickness would decrease stiffness reducing actuation precision at high frequencies. However modifications to the diamond tool will be made to fit this radius with minimal epoxy thickness. The profile and dimensions of the pin channels were measured using Repro-Rubber (Figure 17). The pin channels were cast in this meterology rubber and then sliced along their cross-section. Each section was placed on a glass slide and examined with a light microscope. Some irregularity was noted both in shape and dimensions. The form and dimensional accuracy of the pin channels relate directly to the stiffness and stability of the kinematic head. Irregular contact length and angle can produce variations in linkage stiffness and localize stresses. Finish grinding at the PEC will be done to clean up these irregularities.

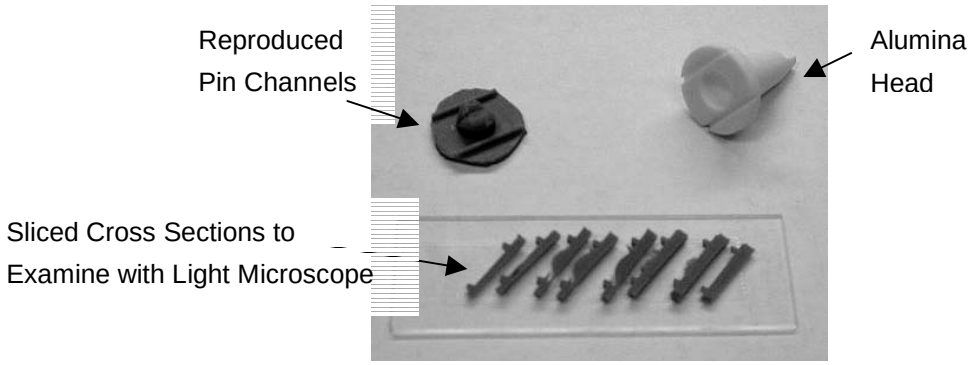

Figure 17. Repro-Rubber Slide

10.8 PIEZO ACTUATOR HEAT ANALYSIS

At high frequencies (5-15 KHz) and large voltages the heat generation of a piezo stack is significant and must be managed so that internal temperatures do not exceed the Curie temperature or the temperature above which irreversible de-poling of the piezo structure will occur. To predict the internal temperature of the stacks during operation a finite difference program was created in Maple. The piezo was modeled the piezo stack attached to a steel base that behaved as a thermal energy reservoir and immersed in a constant temperature fluid. This model neglected the thin (5-20μm) foil electrodes between each layer and assumed a solid PZT core surrounded by an epoxy coating. Using known material properties of the PZT a temperature distribution at steady state conditions was determined. Figure 18 is a plot of piezo stack layer

temperature as a function of position. The program simulated four different operating frequencies ranging from 1 kHz to 15 kHz. Each curve represents a temperature distribution along the length of the PZT stack. Heat generation is predicted to increase linearly with increasing operating frequency.

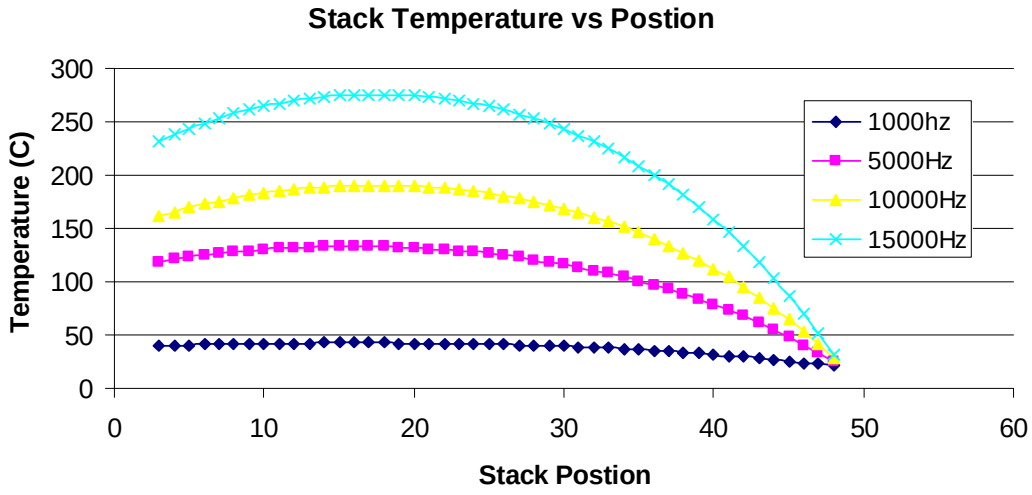

Figure 18. Finite Difference Temperature Distribution

To verify the assumption that the internal structure of the piezo stack can be modeled as a single monolithic unit a heat conduction experiment was performed. This was done by placing the piezo stack in an insulated environment and applying a heat source to one end of the stack and measuring the temperature at both ends. For this experiment a resistor was placed within a copper plate shown in Figure 19 and used as the heat source and method of conduction to the stack. Thin gage J type thermocouples (Figure 20) were placed at the heat source and the opposite end of the stack to measure the temperature difference through the length of the stack.

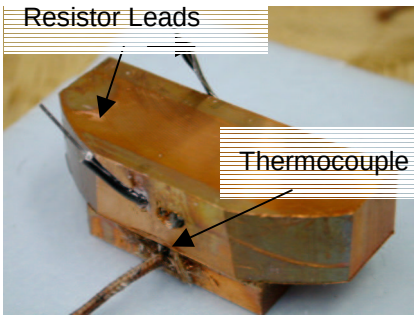

Figure 19. Copper Heat Source

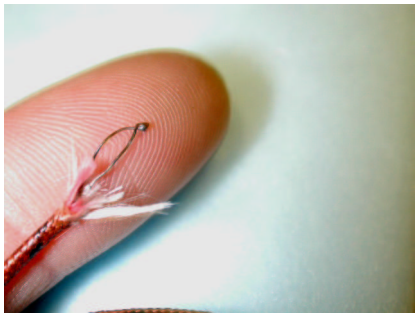

Figure 20. J Type Thermocouple

With the measured temperature difference and the known heat generation of the resistor the conductive heat transfer coefficient k can be determined with the Equation (1).

$$k = \frac{qL}{A \cdot \Delta T} \tag{1}$$

The average experimental *k* was 7.42 w/mK, this is comparable to the specified value of 7 w/mK for PZT100 given by the data provided by Kinetic Ceramics.

There are several different approaches to predicting heat generation in piezo stack actuators. All of the methods varied with frequency, voltage or field strength and capacitance. Each had approach had unique variables that resulted in vastly different predicted values.

An engineering equation given by Kinetic Ceramics predicted that the heat generated was 15% of the total power required to actuate the stack. The calculated heat generation with Equation 2 at an actuation frequency of 5000 Hz and a peak to peak drive voltage of 800 volts was 60 watts. The stack capacitance is 0.25 μF.

$$P_{heat} = \frac{cap \cdot V_{P-P}{}^{2} \cdot f}{2} \cdot 0.15 \tag{2}$$

Where *cap* is the capacitance of the stack in Farads, $V_{P\text{-}P}$ is the peak to peak drive voltage, and *f* is the actuation frequency in Hz. A formula that has been used at the PEC on a previous project to predict heat generation of a piezo stack is Equation (3).

$$P_{heat} = cap \cdot n \cdot V \cdot f \cdot E^{2.86} \tag{3}$$

Where *cap* is the capacitance of the stack in Farads, *n* is the number of piezo layers, *V* is the volume of each layer in mm^3, *f* is the actuation frequency in Hz and *E* is the field strength in V/μm. The calculated heat generation for the same conditions was 20 watts. Equation (4) was provided by Physik Instrumente's website.

$$P_{heat} = lossangle \cdot f \cdot cap \cdot U_{P-P}{}^{2} \tag{4}$$

The loss angle represents energy losses in the piezo and $U_{p\text{-}p}$ is the peak to peak drive voltage. The calculated heat generation was 23 watts. However information provided by Kinetic Ceramics shows that loss angle is not constant through a range of conditions and this value increases with increasing field strength and frequency. Specified values for loss angle are usually given for low frequencies. The disagreement between the first two equations and the unknown value of the loss angle for the operating conditions resulted in values for heat generation that were questionable.

10.9 DYNAMIC HEAT GENERATION

A dynamic thermal rig was constructed to measure the heat generation of the piezo stack under operating conditions up to 5000 Hz. The testing rig sandwiches the piezo stack between two ground steel plates that are held together by two 1.25" 8-32 steel bolts. An alignment channel shown in Figure 21 insures that the centroidal axis of the piezo stack is coplanar to the preload bolts. The complete dynamic test rig is shown in Figure 22.

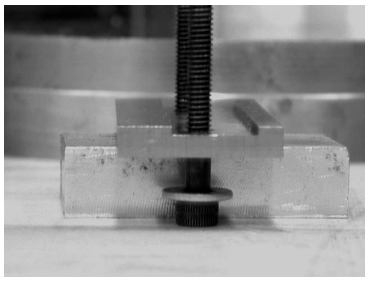

Figure 21. Alignment Groove

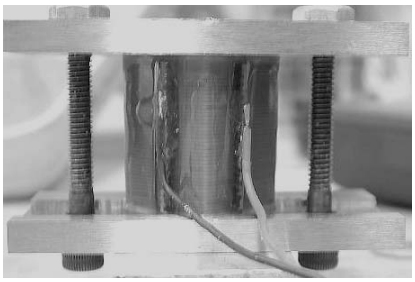

Figure 22. Piezo Stack in Test Rig

This setup provides the necessary preload on the stack and thermal properties that can be calculated. The stack, plates and bolts are wrapped in insulation to create adiabatic conditions. Thermocouples are places on both plates and rate of temperature increase can be measured. Using Equation (5) the heat generated can be calculated.

$$q = m \cdot c_p \cdot \frac{dT}{dt} \tag{5}$$

The calculated natural frequency of the first generation dynamic test rig was 7000 Hz, however the end plates were determined to be deflect excessively under the actuation force of the piezo. To reduce stresses and the possibility of cracking at the corners of the stack the plates were redesigned with a larger area moment of inertia. The added mass from the increase in volume reduced the natural frequency to 5800 Hz but increased the area moment of inertia by an order of magnitude. This trade off is acceptable because the dynamic testing actuation frequencies do not exceed 1000 Hz.

10.10 CONCLUSION

The advantages of VAM have been proven through experiments performed at the PEC. The Ultra-Mill has extended the capabilities of diamond machining by extending tool life in previously difficult to machine and increasing the maximum fracture depth of silicon carbide. The results of the SiC machining experiment prove that for chip thickness up to 20 nm a usable surface finish can be produced with VAM. A cutting force model has been developed and has good agreement with experimental results. Important VAM machining parameters such as

velocity ratio and duty cycle have been identified. However the mechanism for these advantages is still not well understood. VAM is not yet optimized.

The new high-speed Ultra-Mill has been developed and optimized. The kinematic head design has been revised for more weight savings and higher stiffness. The finished alumina head fabricated by CoorsTek has been measured and examined. Temperature distribution through the piezo actuators has been modeled and the conductive coefficient through the stack has been verified by experiment. Dynamic testing for more accurate heat generation predictions is underway. Final construction of the Ultra-Mill high speed has begun with completion scheduled to be at the end of March.

REFERENCES

1. Nakayama, K., Arai, M., Kanda, T., "Machining Characteristics of Hard Materials", Annals of the CIRP, Vol. 37, pp. 89-93, 1988
2. Moriwaki, T., Shamoto, E., "Study on Elliptical Vibration Cutting", Annals of the CIRP, Vol. 43, pp. 35-38, 1994.
3. Moriwaki, T., Shamoto, E., "Ultra-Precision Diamond Cutting of Hardened Steel by Applying Elliptical Vibration Cutting", Annals of the CIRP, Vol. 48, pp. 35-38, 1999.
4. Arcona, C., "Tool Force, Chip Formation and Surface Finish in Diamond Turning", Ph.D. Dissertation, North Carolina State University, 1996.
5. Cerniway, M.,"Elliptical Vibration Machining with Diamond Tools", Masters Thesis, North Carolina State University, 2002.

11 OFF-AXIS BICONIC MIRROR FABRICATION

Ken Garrard
Alex Sohn
PEC Staff Members

Challenges in fabrication and testing have historically limited the choice of surfaces available for the design of reflective optical instruments. Spherical and conic mirrors are common, but more degrees of freedom are necessary to meet challenging performance and packaging requirements. In particular, single-surface astigmatism correction in spectrographs necessitates a toroidal surface, which lacks an axis of rotational symmetry. With support from NASA Goddard Space Flight Center (GSFC), a 94 by 76 mm off-axis, toroidal, biconic mirror has been fabricated using the Variform fast tool servo and the Nanoform 600 diamond turning machine. Issues related to the geometric analysis, decomposition, toolpath generation, controller interfacing, part fixture design, alignment and machining of a pair of these mirrors are discussed.

11.1 INTRODUCTION

The Infrared Multi-Object Spectrograph (IRMOS) is a facility instrument for the Kitt Peak National Observatory's Mayall Telescope (3.8m) and an engineering prototype for a possible design of the Next Generation Space Telescope (NGST) multi-object spectrograph. IRMOS utilizes unconventional optics to reduce package size and improve performance. The most challenging of these optical elements to fabricate is a biconic segment designated as M4. This surface is an off-axis section of an ellipsoidal toroid, meaning that it is not rotationally symmetric about any axis. Two principal methods for fabricating such an optic exist: milling or flycutting with a multiaxis ultraprecision machine or diamond turning using a fast tool servo (FTS). The former method requires large amounts of machining time – sometimes weeks – and must deal with all the complications associated with those longer machining times (e.g., temperature stability, transient noise). The latter, on the other hand, takes no longer than an ordinary turning operation and is therefore cheaper and more reliable than milling. By decomposing M4 into a rotationally symmetric (RS) surface and a residual non-rotationally symmetric (NRS) surface the range requirement of the FTS can be determined. The RS and NRS surfaces are machined simultaneously by a diamond turning machine (DTM) and the FTS, respectively, to produce the desired shape. It does, however, require that the deviation from a rotationally symmetric toolpath be within the available FTS range and that such a toolpath be within the DTM machining envelope. These requirements are met with the Variform FTS and the PEC's Nanoform 600 DTM.

11.2 M4 MIRROR DESCRIPTION

The IRMOS mirror M4 is an off-axis biconic toroidal surface. The surface is a blending of oblate ellipses of different curvature and eccentricity in the XZ and YZ planes. Figure 1 shows a section of the biconic surface as a wire frame and the aperture of the mirror blank as a solid. A general biconic optical surface can be defined in rectangular coordinates as,

$$M4(x,y) = \frac{c_{XZ}\cdot(x-x_0)^2 + c_{YZ}\cdot(y-y_0)^2}{1+\sqrt{1-(1+k_{XZ})\cdot(x-x_0)^2\cdot c_{XZ}^2-(1+k_{YZ})\cdot(y-y_0)^2\cdot c_{YZ}^2}} \tag{1}$$

With the origin at $(x_0, y_0, 0)$, the parameters in Equation (1) that specify the shape of M4 are:

$c_{XZ} = 0.002650$ is the surface curvature in the XZ plane,
$c_{YZ} = 0.002458$ is the surface curvature in the YZ plane,
$k_{XZ} = 0.0778$ is an oblate ellipse in the XZ plane,
and $k_{YZ} = 0.1265$ is an oblate ellipse in the YZ plane.

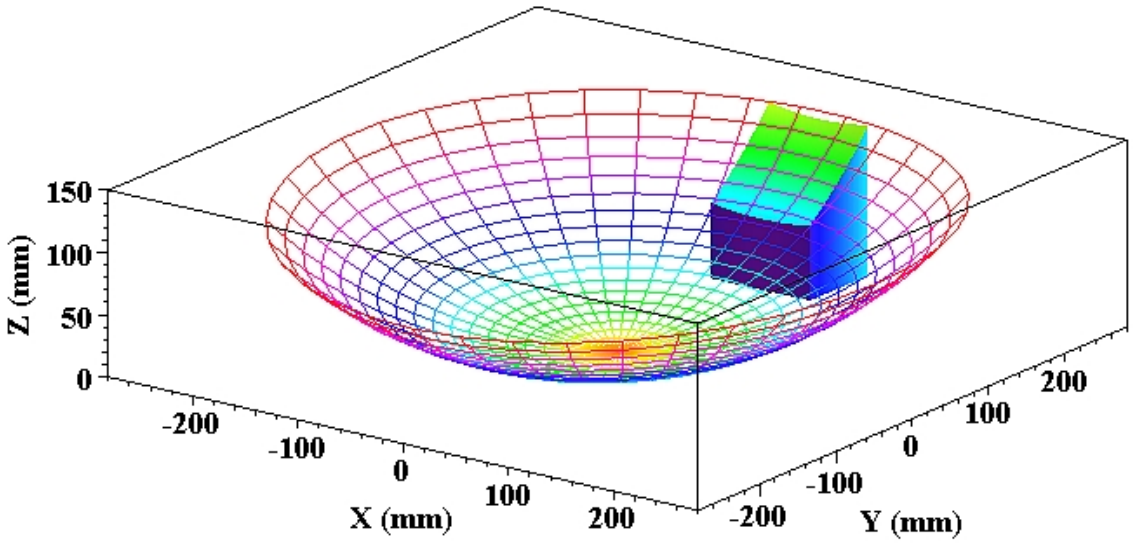

Figure 1. The biconic optic M4.

The aperture of the mirror is 94 mm by 76 mm and its center is located at X = -2.01 mm and Y = 227.41 mm. M4 has 7.549 mm of sag if it is tilted 40.3° in the YZ plane and -0.387° in the XZ plane. If a best-fit, rotationally symmetric asphere is also subtracted from M4, the sag of the resulting surface is 4.582 mm. This is far beyond the 400 μm range of the Variform FTS. Clearly, on-axis machining of the mirror with a Fast Tool Servo is not feasible and another geometric approach is needed to derive a rotationally symmetric asphere which reduces the required FTS travel. The solution must also keep the mirror blanks and mounting fixture within the 600 mm turning capability of the Nanoform.

11.3 GEOMETRIC ANALYSIS

If the optical axis of the M4 mirror is aligned with the spindle centerline on the Nanoform DTM and machined off-axis (i.e., the mirror is machined in its defining coordinate system), then M4 is within the capabilities of the Variform and Nanoform. Removal of a best-fit 4th order asphere results in a residual FTS excursion of 360 μm and the outermost corner of the mirror blank is 280 mm from the spindle center. However, it is possible to do much better than this as will be seen below. Two other issues also must be resolved. First, tool radius compensation must be performed to machine the correct shape. Since the surface slope changes as a function of spindle rotation as well as axial distance, this compensation is three dimensional. Second, if the Variform is aligned with the Nanoform Z axis, an unusually long tool shank must be used to provide clearance from the FTS for the rotating concave mirror blanks. The solution is to rotate the tool axis to an appropriate angle, for example, normal to the center of the workpiece. This has

the benefit of reducing the range of motion required of the FTS, but significantly complicates calculation of its trajectory across an NRS surface.

11.3.1 3D TOOL RADIUS COMPENSATION

To compensate for the tool radius in three dimensions a parallel biconic surface was derived that is offset from M4 by the radius of the tool. Since M4 is concave, this new surface, denominated Q4, has greater curvature than M4, but a smaller aperture. Q4 defines the trajectory of the tool center that generates the surface of M4 at the tool edge as a function of tool radius (d), radial position (R) and spindle angle (θ). The parameters of Q4 can be found by noting that parallel ellipses in a plane separated by a fixed distance, d, simply have A (major axis) and B (minor axis) parameters that differ by d. So, Q4 can be derived by finding A and B for M4, subtracting the tool radius (since Q4 is smaller than M4) and then calculating the conic constant and curvature for the new ellipse. This can be done independently for the XZ and YZ planes of the biconic and the parameters substituted into Equation (1) to generate data points on Q4. The values of A and B for an oblate ellipse as functions of curvature and conic constant are,

$$A = \frac{\sqrt{k+1}}{c \cdot (k+1)} \tag{2}$$

$$B = \frac{1}{c \cdot (k+1)} \tag{3}$$

Solving Equations (2) and (3) simultaneously for c and k gives,

$$c = \frac{B}{A^2} \tag{4}$$

$$k = \frac{B^2}{\left(A^2 - B^2\right)} \tag{5}$$

The shape parameters for M4 and Q4 are summarized in Table 1 for the 2.9646 mm radius tool that was used to machine the M4 mirrors.

Table 1. M4 and Q4 biconic shape parameters.

	Plane	A	B	k	c
M4	XZ	363.518	350.152	0.0778	0.002650
	YZ	383.357	361.192	0.1265	0.002458
Q4	XZ	360.553	347.187	0.07847	0.002670
	YZ	380.393	358.227	0.12757	0.002475

The coordinates of the center points of Q4 when the tool edge is at the corners of M4 can be found by intersecting normal lines from each M4 corner with the surface of Q4. For any

continuous, differentiable surface a normal line is perpendicular to any two tangent lines that intersect at a right angle. In particular, the tangent lines that lie in the XZ and YZ planes define a plane tangent to the surface and can be used to find the normal. Parametric expressions for these two lines tangent to F of length u are,

$$L_{XZ}(u,x,y) = \left[x+u,\ y,\ F(x,y) + u \cdot \left(\frac{\partial F}{\partial x} \right)(x,y) \right] \tag{6}$$

$$L_{YZ}(u,x,y) = \left[x,\ y+u,\ F(x,y) + u \cdot \left(\frac{\partial F}{\partial y} \right)(x,y) \right] \tag{7}$$

The normalized cross product of unit length tangent lines, L_{XZ} and L_{YZ}, evaluated at any (x,y) defines a normal to the surface at (x,y) as shown in Equation (8).

$$NL(x,y) = \left\| \left[L_{XZ}(1,x,y) - L_{XZ}(0,x,y) \right] \times \left[L_{YZ}(1,x,y) - L_{YZ}(0,x,y) \right] \right\| \tag{8}$$

A function that gives the coordinates of the endpoints of a normal line of length u is then defined as,

$$PNL(u,x,y) = \left[x + u \cdot NL(x,y)_1,\ y + u \cdot NL(x,y)_2,\ F(x,y) + u \cdot NL(x,y)_3 \right] \tag{9}$$

Substituting the function *M4* of Equation (1) for F in Equation (9) and evaluating it with u set to the radius of the tool gives the coordinates on Q4 (tool center) for any point (x,y) on M4 (biconic surface). These calculations are easily performed in Maple® for any radius tool. Figure 2 shows M4 (tiled surface) and Q4 (wireframe) along with the normal (red) and tangent (blue) lines at selected (x,y) locations.

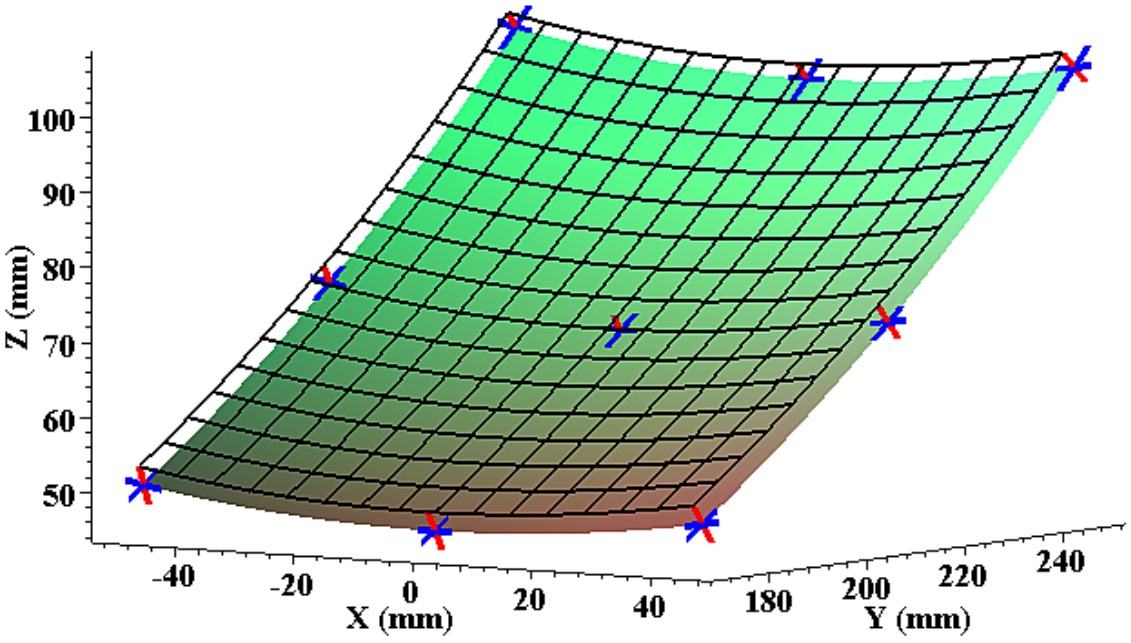

Figure 2. M4 and the parallel surface Q4.

11.3.2 SURFACE DECOMPOSITION INTO NRS AND RS COMPONENTS

By considering off-axis translations and tilt angles other than that of the best fit plane, the range of NRS motion required to machine the surface can be dramatically reduced. Translations were considered first to avoid the complications of shimming the mirror blanks on a vacuum fixture. The procedure was to generate a grid of data points on Q4 using Equation (1), calculate the radius, R, of each point from the optical center, and fit a 4th order polynomial in R to this data. The range of the residuals gives the FTS excursion required to machine the mirror. A Y offset of -17 mm was found to reduce the residual range to 76 μm, 19% of the maximum range of the Variform. Data reduction was initially performed using the **pro Fit** software package and replicated using JMP®. Algebraic and numerical verification were obtained with Maple. The resulting NRS surface that must be created by the Variform is shown in Figure 3. The best-fit 4th order polynomial defining the asphere to be machined by the Nanoform is given in Equation (10). Higher order polynomials yield no significant improvement.

$$P4(R) = 46.126 + \left(-0.896 + \left(8.532 \times 10^{-3} + \left(-2.552 \times 10^{-5} + 3.752 \times 10^{-8} \cdot R\right) \cdot R\right) \cdot R\right) \cdot R \qquad (10)$$

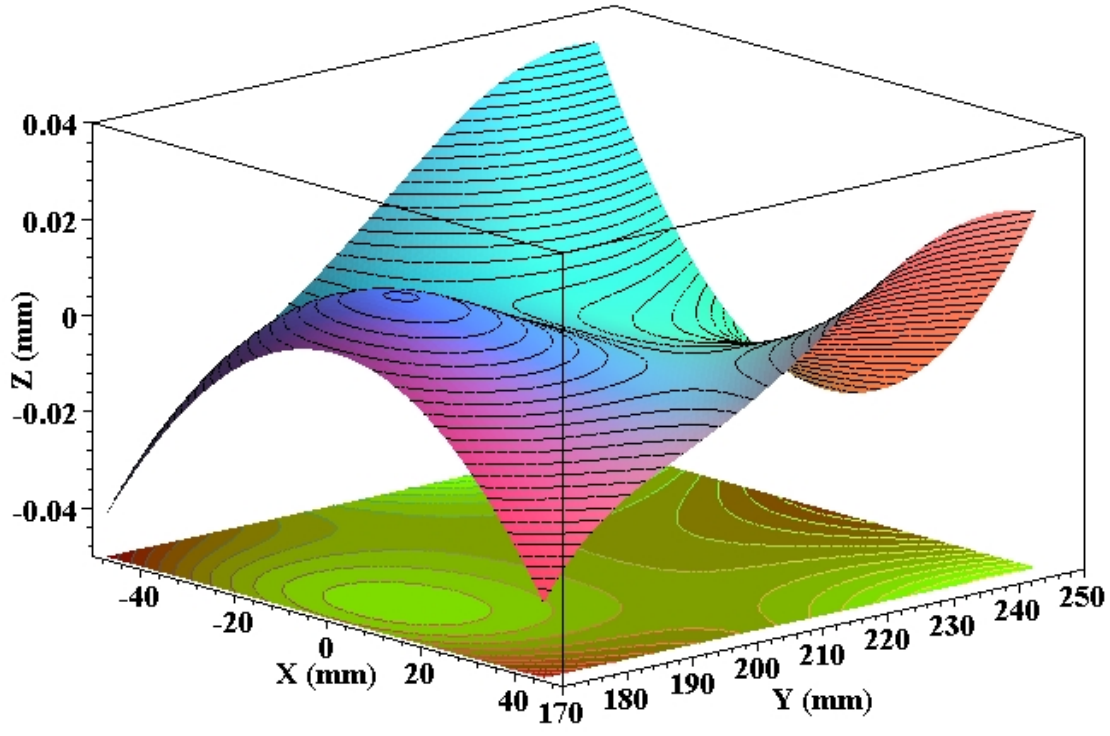

Figure 3. FTS component of toolpath for Q4.

Careful examination of Figure 3 reveals that while the maximum range of FTS travel along any given radius is approximately 65 μm, that excursion must be accomplished within an angular space of about 15°. By transforming the equation defining the NRS motion into 3D polar

coordinates and taking the first derivative with respect to θ, the velocity required of the FTS can be determined for any given spindle speed. A plot of this slope function in Figure 4 shows that a maximum velocity of 4.1 mm/sec per Hz of spindle rotation is needed to machine M4. Since the Variform is capable of a velocity of 20 mm/sec, a spindle speed of 120 rpm (2 Hz) is feasible and will yield reasonable machining times.

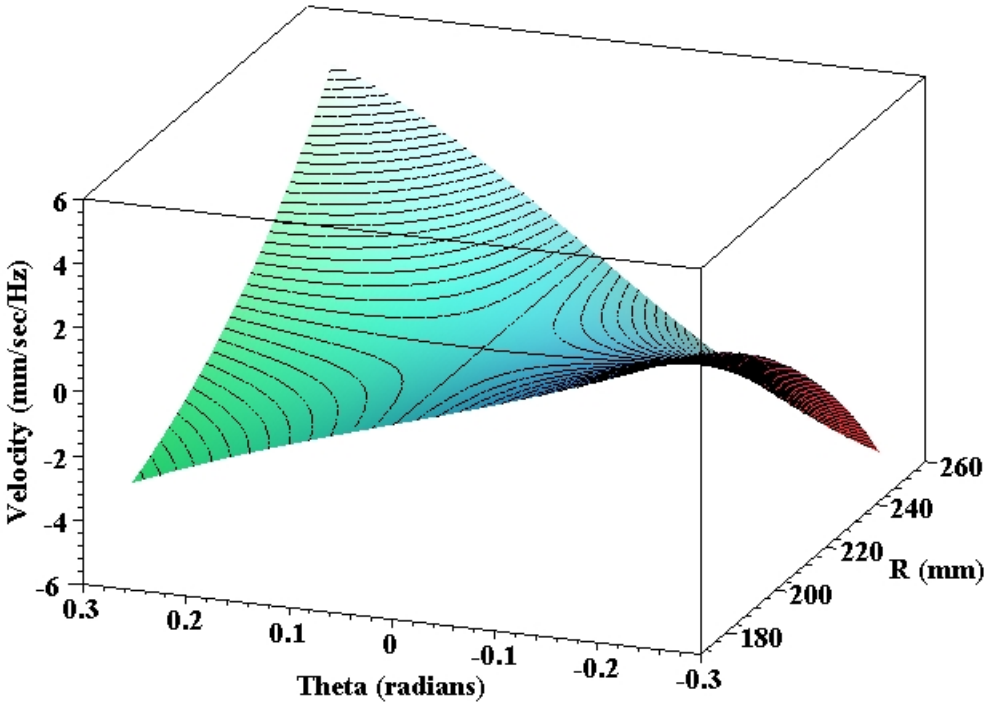

Figure 4. FTS velocity.

11.3.3 TOOL AXIS TILT COMPENSATION

To provide clearance to the mirror blanks as they rotate past the Variform structure, the tool post is mounted at an angle of -35.3° with respect to the Z axis of the DTM. The FTS trajectory calculations described above give tool positions as a function of R and θ that are co-linear with the Z axis. However, as the tilted FTS moves in the Z direction it also moves in the R direction. Since the FTS controller cannot change R by moving the DTM X axis as a function of θ, it must move the FTS such that the center of the tool always lies on Q4 (and hence the cutting edge machines M4). This requires finding the intersection of a line along the tool axis through P4 at R with Q4. This line varies as a function of both R and θ and is given in Equation (11).

$$T(R,r) = \frac{(r-R)}{\tan\varphi} + P4(R) \tag{11}$$

where R is a radius on P4 as defined by the DTM X axis, φ is the tilt angle of the tool axis and r is the radius on Q4 of the desired intersection point. For a given R and θ, tool center locations for the tilted tool may be determined by first solving Equation (12) for r,

$$0 = M4(r \cdot \sin\theta, r \cdot \cos\theta) - T(R,r) \tag{12}$$

and then evaluating Equation (13) to find the required FTS excursion in the tool axis direction.

$$FTS(R,r,\theta) = \frac{\left[M4(r \cdot \sin\theta,\ r \cdot \cos\theta) - P4(R)\right]}{\cos\varphi} \tag{13}$$

Figure 5 shows both the compensated and uncompensated FTS tool center locations that generate the NRS component of the Q4 surface. The contoured surface in the figure is uncompensated and the shaded surface is with tilt compensation. Note that the two surfaces intersect and the compensated surface is flatter, requiring 62 μm of FTS excursion.

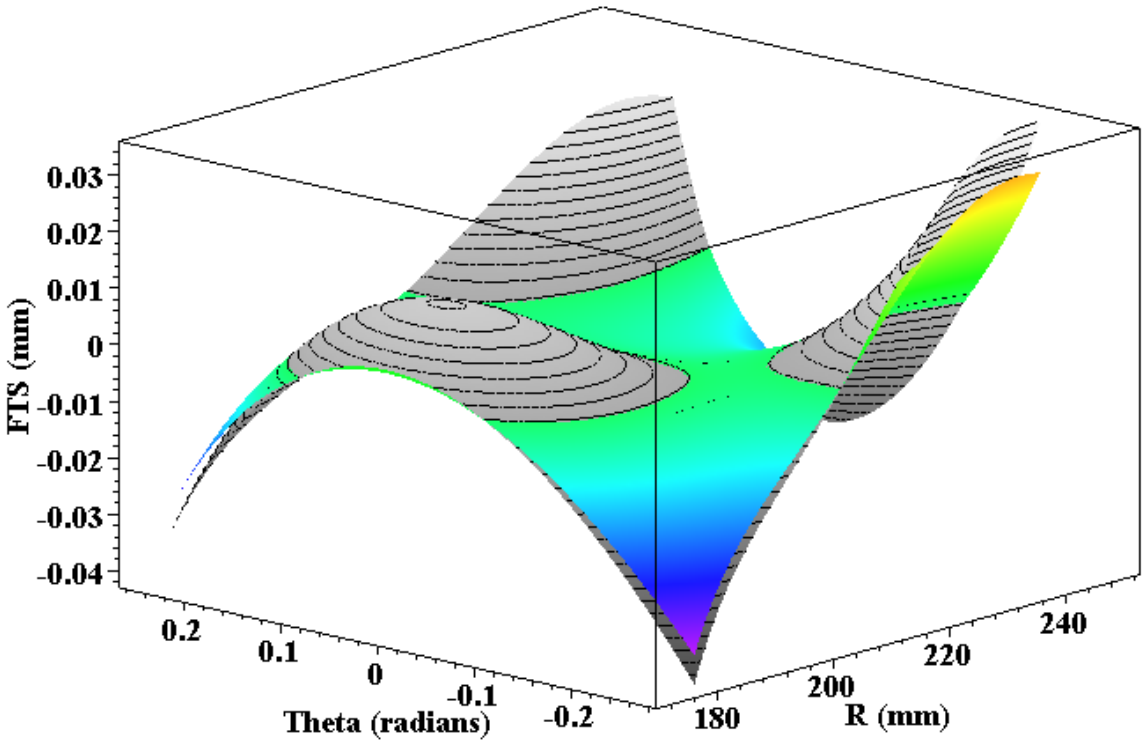

Figure 5. Tool tilt compensation for Q4.

11.4 TOOLPATH GENERATION

Unfortunately there is no closed form algebraic solution for Equation (12). For given values of R and θ the FTS excursion can be found numerically with a root finding algorithm such as

bisection search or Newton-Raphson. This presents a performance problem when calculating FTS tool locations *on-the-fly* as the best-fit asphere is being machined. Three possible options were considered.

1. Purchace a faster controller to solve the equations in real-time.
2. Derive some other, simpler function that approximates the correct answer.
3. Interpolate over a grid of exact tool locations calculated offline.

Option 1 is clearly the best; however sufficient project resources (time and money) were not available. Option 2 was pursued to the extent that a 9^{th} order interpolating polynomial was derived for r as a function of R and θ. This polynomial gives acceptably small residuals, but the time needed to evaluate the interpolating function was deemed excessive for real-time implementation with the available controller.

11.4.1 BILINEAR INTERPOLATION

The approach used to machine M4 follows option 3 with a bilinear interpolation algorithm over a grid of 168 (R) by 68 (θ) machine axis locations. The interpolation is expressed in 3D polar coordinates since the Nanoform cross-feed axis (X) and spindle define a polar space. This size table is easily managed by the control system and yields an FTS toolpath with residual errors smaller than the positioning accuracy of the Variform. The basic idea of multi-dimensional interpolation is to find the neighborhood of an untabulated value in the table and construct a weighted average of the values of the nearest points as an estimate of the unknown value. For a two dimensional table, there are four nearest points to consider. A linear estimator uses the product of the distance ratios from the untabulated point to the grid lines intersecting each neighbor point in each dimension as the weighting factor for that tabulated neighbor point. Higher order estimators that use cubic functions, splines and tabulated derivatives can produce smoother, more accurate interpolators; all at the cost of more computation time and larger tables.

The interpolation grid covers an area somewhat larger than the aperture of the mirror to avoid edge discontinuities that induce vibrations and degrade surface finish. The interpolation grid is also extended in the negative X direction (i.e., the X decenter of M4 is removed) so that the leading and trailing edges of the table in the θ direction contain the same FTS values. Thus when the mirror rotates beyond the θ boundary of the table the FTS will be in the correct position when the mirror re-enters the tabulated range as it completes a revolution. To properly balance the spindle, two mirror blanks are machined at a time. The spindle angle, θ, must be manipulated so that the interpolation table is used twice per revolution (without storing the table twice). It is also convenient for the angle to range from $-\pi/2$ to $+\pi/2$. This is easily accomplished with the conditional function in Equation (14) over input θ values ranging from zero to 2π,

$$\Omega = \left\{ \begin{array}{cc} \theta - 2\pi & \text{for } \theta \geq \frac{3}{2}\pi \\ \theta - \pi & \text{for } \theta \geq \frac{1}{2}\pi \\ \theta & \text{otherwise} \end{array} \right\} \tag{14}$$

Bilinear interpolation for Q4 expressed in polar coordinates means first finding the two rows and columns that bound an input *(R, Ω)* data point. Saturation instead of extrapolation at the table boundaries accomplishes the objective of having the tool position not change as a function of spindle rotation outside the aperture of the two rotating mirrors. For an equally spaced rectangular grid the indices of nearest neighbor tabulated points to *(R, Ω)*, can be found by calculating,

$$ri = \left\lfloor \frac{R - r_{\min}}{r_{delta}} \right\rfloor \quad \text{and} \quad ti = \left\lfloor \frac{\Omega - \theta_{\min}}{\theta_{delta}} \right\rfloor \tag{15}$$

where r_{delta} and θ_{delta} are the radial and angular grid spacings and r_{min} and θ_{min} are the lower boundaries of the interpolation table, respectively. The four nearest points are located at [row, column] positions: *[ri, ti], [ri+1, ti], [ri, ti+1],* and *[ri+1, ti+1]*. Weighting factors for the radial and angular dimensions are,

$$w_r = \frac{\left(R - Vr_{ri}\right)}{r_{delta}} \quad \text{and} \quad w_t = \frac{\left(\Omega - Vt_{ti}\right)}{\theta_{delta}} \tag{16}$$

where *Vr* and *Vt* are vectors of the radius and angle values defining the interpolation grid. The FTS position is estimated as,

$$z_{FTS} = w_r \cdot w_t \cdot Mz_{ri+1,ti+1} + w_r \cdot \left(1 - w_t\right) \cdot Mz_{ri+1,ti} + \left(1 - w_r\right) \cdot w_t \cdot Mz_{ri_i,ti+1} + \left(1 - w_r\right) \cdot \left(1 - w_t\right) \cdot Mz_{ri_i,ti} \tag{17}$$

where *Mz* is the two dimensional interpolation table of exact tool locations.

11.4.2 TOOLPATH VERIFICATION

Prior to machining, a C program was written to simulate the use of bilinear interpolation as a toolpath trajectory generation method for Q4. The program iterates through all possible combinations of R and θ locations at the feedback resolution of the system (approximately 1.5 million data points in the aperture of a single mirror blank). A plot of the resulting surface is shown in Figure 6. A each point, a comparison was made between the interpolation value for the FTS position obtained from Equation (17) and a more accurate value calculated from Equations (11-13) with a bisection search determining the root of Equation (12). The termination criterion for the bisection algorithm was set to 10^{-10} mm. These reference values were also calculated at the 11,424 interpolation table grid points and compared with those found by Maple's numeric equation solver. Examination of the residual error in the z_{FTS} calculation revealed a very small

slope as a function of R. A final step was added to the bilinear interpolator to remove this slope by applying Equation (18) to z_{FTS} values from Equation (17).

$$z'_{FTS} = z_{FTS} + (0.0703787466 - R \cdot 0.0003333488) \cdot 0.001 \tag{18}$$

The residuals errors from the modified interpolator are normally distributed with a mean of -0.3 nm, a standard deviation of 3.45 nm, a minimum of -12.82 nm and a maximum of 13.97 nm. The error distribution is leptokurtic with more than 75% of the data points having an error of less than 2.5 nm.

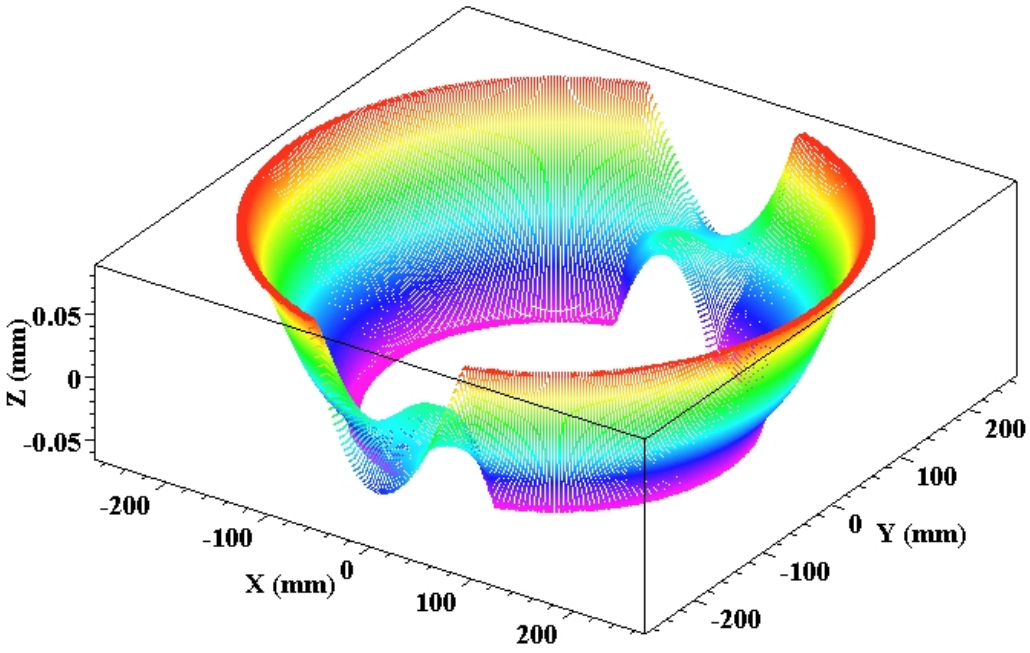

Figure 6. Simulated FTS motion for interpolated Q4 toolpath.

11.5 MACHINE SETUP

Figure 7 shows the aluminum vacuum chuck that was designed and built to hold the M4 mirror blanks and the tool centering fixture. The diamond machined chuck dimensions are 580 mm x 127 mm x 135 mm (to the top of the pedestals) and its mass is approximately 18 kg. Due to the low spindle speeds and large cross section of the chuck, deflection due to centripetal forces is minimal. The figure shows PMMA test parts mounted on the pedestals in place of the heat treated Al 6061 M4 mirror blanks. A pair of mirrors, located 180° apart on the chuck, are machined at the same time. A video camera is placed behind the DTM splash shield to observe fiducial marks on the rear of the mirrors for part alignment in the radial and angular directions. As the parts rotate, the tool is guided by the DTM's X and Z axes to machine the RS portion of

the mirror surface (i.e., the best-fit asphere) while the FTS moves in synchronization with the spindle and X axis to produce the NRS surface. To provide clearance between the rotating parts and the Variform structure, the FTS is shown mounted at a 35.3° angle.

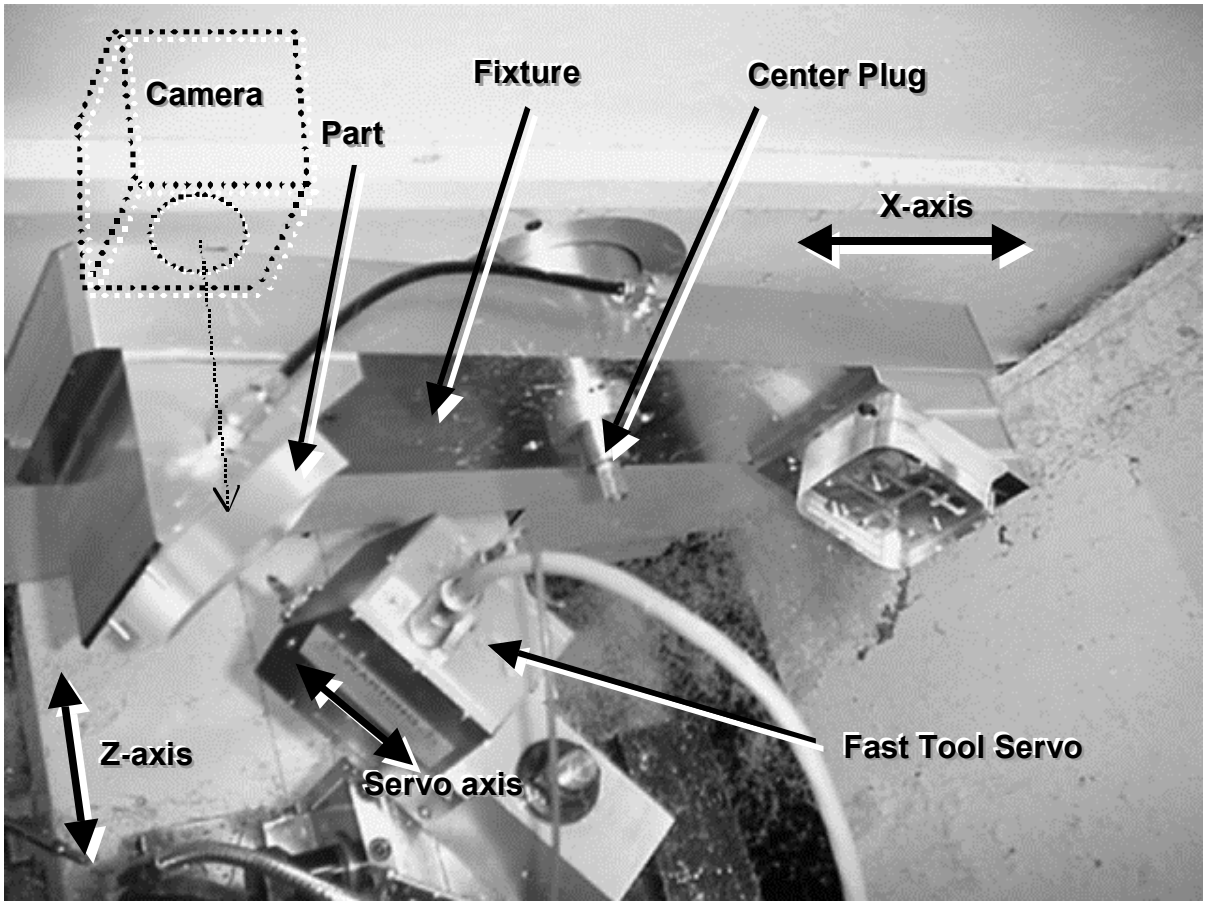

Figure 7. Machine setup. PMMA test blanks are mounted on the vacuum pedestals. The alignment camera is behind the splash shield.

11.5.1 ALIGNMENT

Alignment of both the mirror blanks and the single-crystal diamond tool required several specialized procedures. The freshly lapped diamond tool radius had to be determined over the full 80° window to allow for accurate radius compensation and alignment. This was done using a Zygo NewView 5000 white-light interferometric microscope. The instrument comes equipped with precision X, Y, and Z stages for stitching multiple images to produce a large scale surface map. In this case, the NewView was used as an optical coordinate measurement machine (CMM) by turning the microscope objective into a high resolution alignment tool and collecting position data on the tool edge in X, Y, and Z. A simple least-squares circular curve fit found the tool

radius to be 2.9646 mm. The tool was aligned to the DTM spindle axis using the PMMA centerplug shown in Figure 7.

The pair of M4 mirror blanks had to be aligned with six degrees of freedom to the machine axes. The biconic surface is located with respect to fiducials machined onto the back and sides of each mirror blank. The blanks were constrained to a plane which was diamond flycut at 35.3° onto the pedestals of the chuck. These surfaces mate with the flat flycut surface on the back of each blank. The correct angle was ensured using the DTM axes to probe the surface of the wedge-shaped pedestals with an electronic indicator. The radial position, rotation on the pedestal and angular position with respect to the spindle were aligned using two crosshair marks machined into the rear surface of the parts. A video vision system was positioned behind the X axis splash shield and aligned to the X axis and spindle using a needle. The needle had been previously located with respect to the spindle centerline and was subsequently moved to a known radius given by the X axis positions of the fiducial crosshairs. At this X position a pair of camera crosshairs were aligned with the needle. Through a set of holes in the chuck the camera could then be used to accurately position the parts by aligning the part fiducials with the camera crosshairs. This provided a method for placement of each part to within 25 μm in X and Z and 120 μm in the direction of spindle rotation (i.e., the Y direction).

11.5.2 System Configuration

The machining system, shown schematically in Figure 8, consists primarily of the diamond turning machine, the fast tool servo and two controllers. The DTM is commanded by a Delta Tau PMAC controller using standard lathe G-codes. This controller issues position commands to the machine axes via linear servo amplifiers to produce the aspheric rotationally symmetric portion of the part surface. It also executes a PLC which sends a simulated, pulsed encoder signal of X axis position information to the PC31 digital signal processor (DSP) which runs the FTS trajectory generator. These pulses occur at 50 μm intervals. The DSP calculates the FTS toolpath according to current position information from the spindle (via its own encoder interface) and the simulated X axis position output. A custom counter interface circuit was built to count and buffer both position signals for digital input to the PC31. The FTS toolpath signal is an open-loop analog waveform since the Variform amplifier electronics contain both an analog closed-loop controller and a hysteresis compensator.

11.5.3 Testing

The system was tested by machining a tilted flat. This method consists of commanding the FTS to follow a sine wave with a period of one spindle revolution whose amplitude is a linearly varying function of radial position from the spindle centerline. This allows the range and frequency requirements of the FTS for machining the M4 optics to be exercised while still

allowing the resultant part to be easily measured with an interferometer. The final results of this test produced a surface finish of 8-16 nm rms and a form error of 43 nm rms; both acceptable with respect to the specifications of 10 nm and 63 nm, respectively.

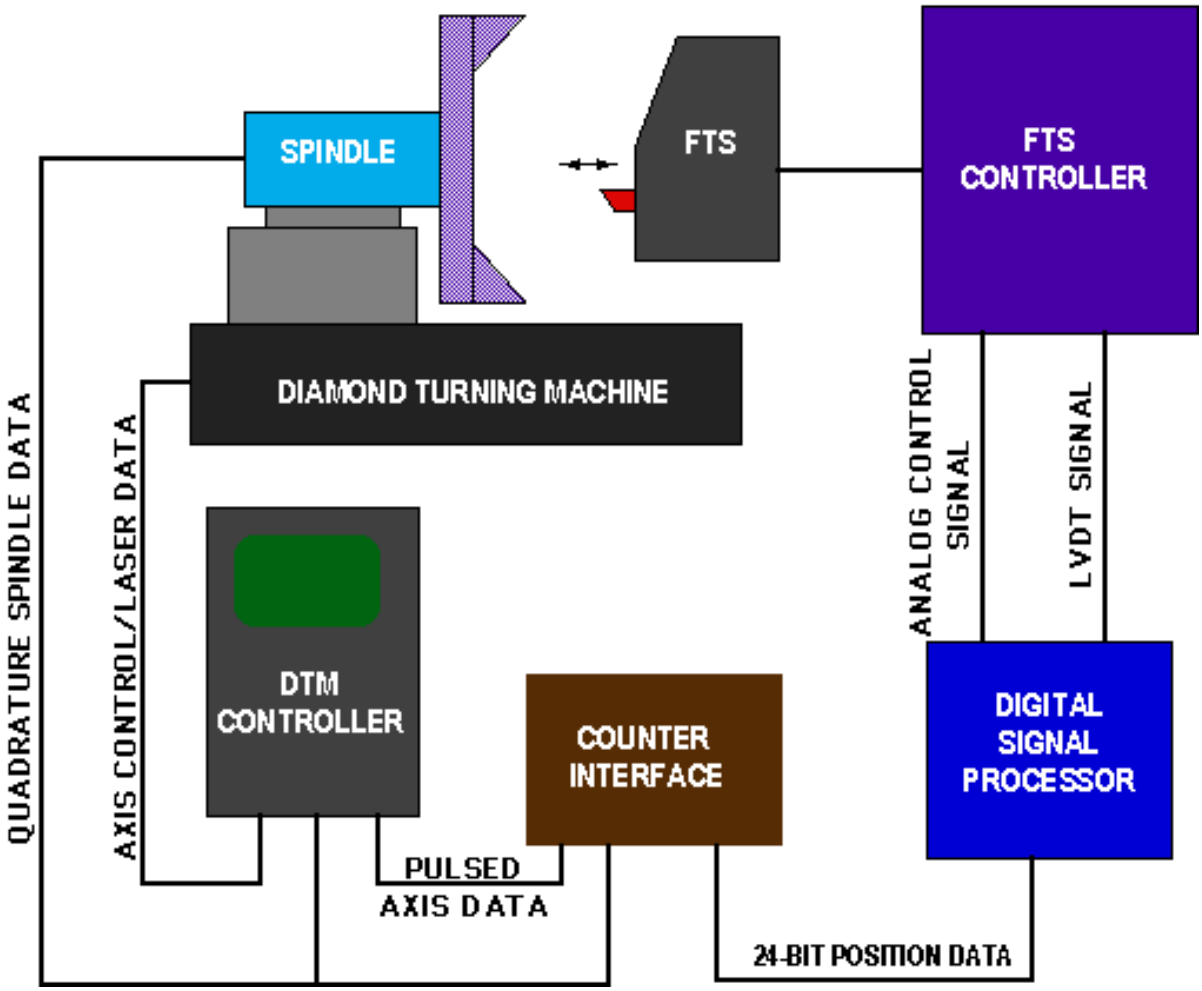

Figure 8. Schematic of the machine layout and control interfaces.

11.6 MACHINING

Before machining the biconic, the part fixture and alignment procedures were tested with PMMA test blanks mounted in place of the 6061 aluminum blanks. The FTS was commanded to follow a sine wave that mimics the Q4 NRS toolpath excursion in amplitude and location on the blanks. There were two reasons for doing this: acrylic is much more forgiving of a large depth of cut if there is an error and the aluminum blanks had significant processing invested in them (e.g., E.D.M. mounting tabs, stress relieving, crosshair fiducials, diamond flycut reference surfaces and a milled biconic front surface). Though the PMMA blanks were not stable enough to allow

accurate form measurements, they did provide a good general test and an evaluation of the surface finish.

Machining of the aluminum blanks occurred in two phases: roughing and finishing. Several roughing passes were performed without FTS excursion. Cuts 10 μm deep were made with the spindle rotating 250 rpm at a feedrate of 25 mm/min. 250 μm of material were removed in this manner until the entire surface of both parts was fully machined. The tool was then replaced with a freshly lapped tool which was centered using an acrylic centerplug. At this point, the servo was activated and another 140 μm was removed in 10 μm intervals. Once the entire surface of the parts was machined, a final finishing cut was made. A 1 μm deep finish pass was made with the spindle rotating 125 rpm at a crossfeed of 0.25 mm/min. The theoretical surface finish of 0.2 nm for this cut was far in excess of what was practically possible to ensure that this would not be a limitation. Chips were removed with a low-volume oil spray during the 8 hours of machine time required for the final cut.

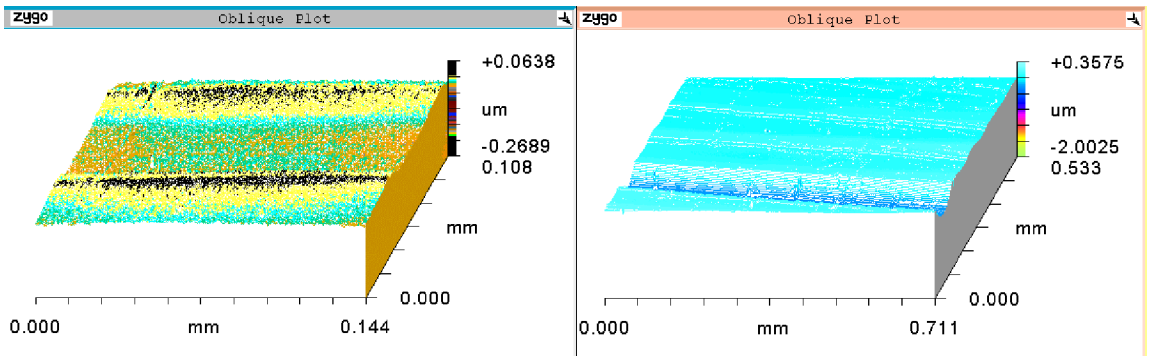

Figure 9. Surface finish is dominated by 16 nm rms regions (left) although frequent occurrence of 400 nm deep cusps causes finish to worsen considerably over larger areas (right).

11.7 RESULTS

The finished mirrors were measured for both form and surface finish. The visual appearance of the surface was poor, with significant scratching in the machining direction. As shown in Figure 9 surface finish measurements made with the Zygo NewView 5000 microscope revealed that most of the surface had a finish of 16-18 nm (rms). However, these relatively flat regions were interspersed with cusps on the order of 400 nm deep, occurring every 0.5 to 1.0 mm in the feed direction. Furthermore, their width (98 μm) is consistent with radius of the tool and the feature depth. This causes the overall finish to worsen considerably, but allows figure measurements to be made on an interferometer. The marks may have been caused by errant motions of the machine axes or, more likely, noise in the Variform LVDT feedback signal or the PC31 analog command signal. Using GSFC's Computer Generated Holographic (CGH) reference mask,

figure measurements, shown in Figure 10, revealed a dominant trefoil error with approximately 8% of the servo amplitude. This residual error has the same shape and orientation as the NRS motion of Figure 3 and shows that the part is "too large" (i.e., the servo amplitude was too great). Factors being investigated as the cause of this error are: a mistake in the servo command signal calculation procedure, an incorrect tool radius value, an error in the tilt angle of either the mounting pedestals or the Variform, a mismatch between the parameters used to manufacture the CGH and those used to machine the mirrors, and an incorrect calibration of the amplitude of the servo command signal. The latter seems most plausible as the PC31 output signal was scaled with a gain of 1.0811 to achieve the correct servo amplitude as measured by the Variform LVDT with an oscilloscope during system setup and testing.

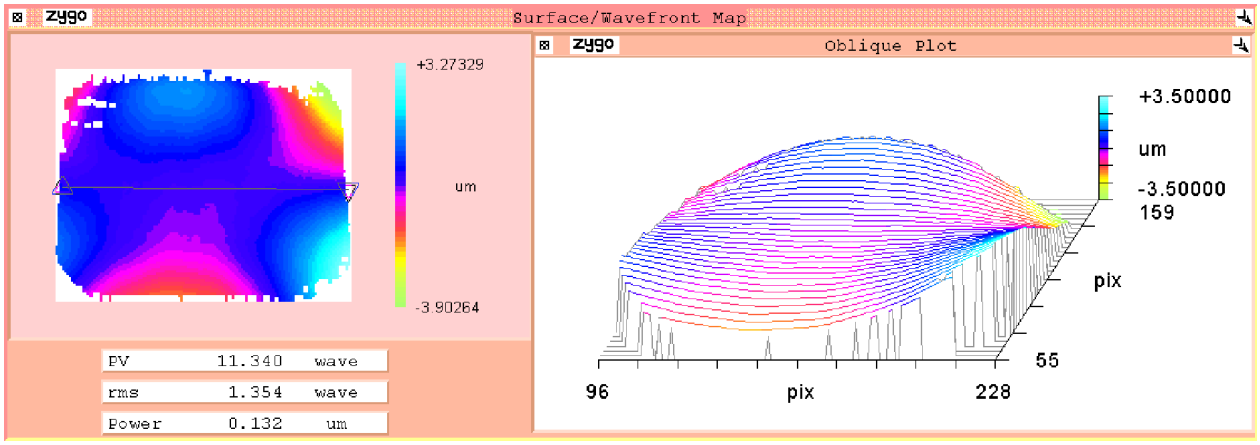

Figure 10. Figure error on M4 is dominated by the shape of the FTS excursion with a magnitude of 8% that of the servo. (Compare with Figure 3).

11.8 CONCLUSIONS

The M4 mirror geometry has been thoroughly analyzed and a procedure developed that allows it to be machined with the Variform FTS and the Nanoform 600. A special vacuum chuck has also been designed and built to mount and align the mirror blanks. A custom hardware interface has been built that provides X axis and spindle position information in real-time to the PC31 DSP. In this way commanded motion of the Variform can be synchronized with the movement of the Nanoform axes to produce non-rotationally symmetric surfaces on the diamond turning machine.

While results have been less than stellar, the aluminum M4 mirrors fabricated have proven that the method for machining these biconic surfaces is sound. With the elimination two anomalies, the specified surface finish of 10 nm (rms) and figure error of 63 nm (rms) should be achievable. Notwithstanding, the machining experiments have produced a pair of engineering prototypes suitable for preliminary testing of the assembly and operation of IRMOS.

12 LASER SCRIBING FOR USE AS A PRECISION SHAPING TECHNIQUE

Bryan M. Love[1]
Graduate Student
Jeffrey W. Eischen
Associate Professor
Department of Mechanical and Aerospace Engineering

Accurately controlling the shape of the read/write heads is critical in the performance of a modern hard disk drive. These heads or "sliders" are typically composed of alumina and titanium carbide (AlTiC) and act as an air bearing when passing over the disks. Controlling the curvature of the slider is of primary importance. A laser scribing system is used in industry to produce curvature by inducing residual stress into the slider. Predicting the curvature created by a pattern of scribes is of great importance to increase the control over the sliders' shape. Using finite element analysis, a force system that produces stresses similar to the laser scribing is applied. The curvatures created by the force system are calibrated to an experimental result with the same scribe geometry. The model was then further verified by predicting the shape of several other experimental scribing geometries with high accuracy. A library of scribing results has been built to allow, through superposition, the shape of sliders with complicated scribing patterns to be predicted. Ultimately, with this library of scribe results, a scribing pattern could be generated to give a desired final shape based on the initial shape of the head.

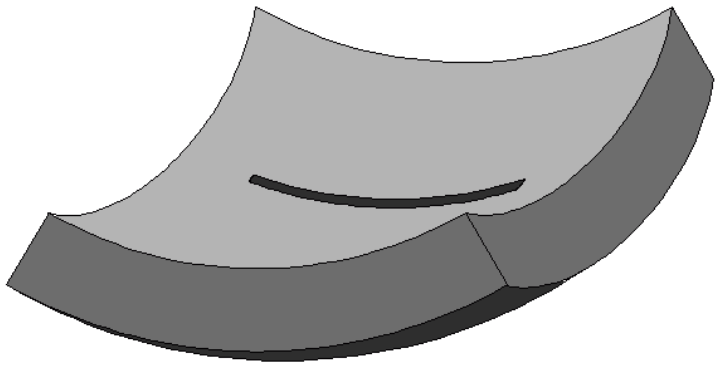

[1] Currently pursuing a PhD at Va Tech.

12.1 INTRODUCTION

In a modern hard disk drive, the flying height of the read/write head is one of the primary influences on data storage density and hard drive speed. The read/write head is contained within a slider that acts as an air bearing—therefore; the shape of the slider directly determines the flying height of the read/write head. The flying height in modern hard drives has dropped below 25 nanometers, thus accurate control of the slider's shape is necessary to increase performance [1]. Controlling this shape is very demanding—the peak-to-valley deflections of the slider are on the order of nanometers while the slider itself is approximately 1.2 mm by 1 mm.

IBM has pioneered a technique using laser scribing that allows controlled adjustment of the curvature of the slider. Known as Laser Curvature Adjust Technique (LCAT), the system relies on a pulsed laser to create localized residual stress, which results in very small deflections of the slider. The LCAT system, while operational and experimentally tested, uses a closed-loop measurement and scribing system (along with experimental history) to determine where scribes are placed [1]. In an effort to speed production, as well as control the curvatures of the slider more accurately, a model is sought which would allow theoretical determination of the curvatures produced by a scribe or a set of scribes. Such a model would allow theoretical determination of a scribing pattern that would produce a desired shape, without resulting to tedious experiments to determine the effects of various scribe geometries. Also, with a well-developed model, the LCAT system could be used to "flatten" sliders that already contained too much deflection or to remove asymmetries in the shape of the slider while producing the final shape desired by the designers.

12.2 LASER SCRIBING

12.2.1 BACKGROUND AND NOMENCLATURE

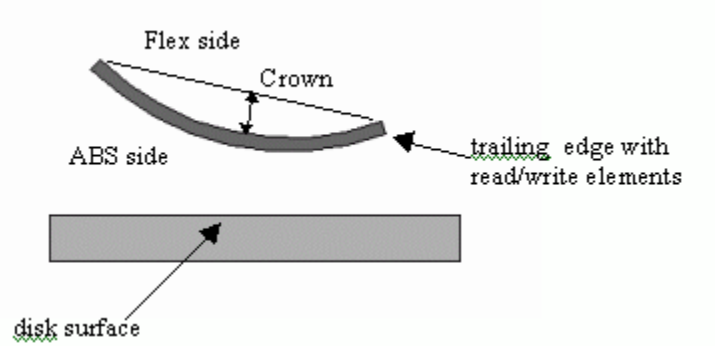

Figure 1. Slider Geometry

The sliders currently used by IBM are fabricated from an alumina-titanium carbide ($A1_2O_3$-TiC) wafer, and when finished, measure 1.2 mm by 1.0mm by 0.3 mm. The two large surfaces of the

slider are known as the ABS (air bearing surface) and the flex side (shown in Figure 1); the curvature that is critical to operation is the curvature of the ABS side. Laser scribes deflect the slider towards the scribe, so all scribing is performed on the flex side (Figure 1 shows a slider with the desirable curvature).

To parameterize the shape of the slider (both before and after scribing), IBM utilizes a bi-quadratic curve fit to give three critical curvature parameters that indicate the shape of the ABS side. These three curvatures, known as crown, camber and twist, are defined as follows

$$\begin{aligned} z &= C_0 + C_1x + C_2y + C_3x^2 + C_4y^2 + C_5xy \\ Crown &= -C_3L^2/4 \\ Camber &= -C_4L^2/4 \\ Twist &= -C_5L^2 \end{aligned} \qquad (1)$$

where L = 1mm, and x, y, and z are defined in Figure 2 below. Note that crown is the curvature in the flying direction (see Figure 1), camber is perpendicular to crown, and twist is an asymmetry in the curvature.

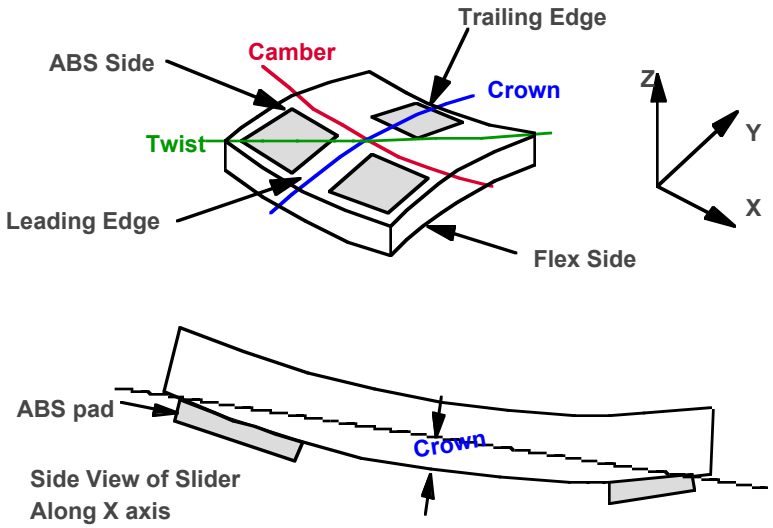

Figure 2. IBM Curvature Notation

The bi-quadratic curve fit assumes a constant curvature in the x (along the 1.25mm dimension) and y (along the 1.0mm dimension) directions, and while this is not strictly true, it addresses some of the metrology issues. The alumina and titanium carbide grains have different optical properties; therefore, the surface roughness of the sliders when measured with an optical instrument is very high compared to the deflections created by scribes. The constant curvature assumption allows nanometer level curvatures to be detected when the surface roughness is on the order of 100 nm.

The laser scribes are formed with a pulsed laser focused on the surface of the slider—the laser melts a small amount of material that, after solidification, forms a localized stress field, resulting in deformation of the slider. When the "dots" created by the laser pulses reach a critical spacing, the amount of deflection created "saturates", and the dots appear as a continuous line approximately 40 μm wide. The amount of deflection generated depends on the dot spacing, the laser power, and the geometry of the scribe—however, IBM has experimentally determined the ideal laser power and dot spacing, so this study will focus exclusively on scribing geometry.

Currently, sliders are scribed with nearly full-length scribes in the x or y direction, without scribes crossing (most sliders have scribes in a single direction). This scribing pattern allows precise control over either crown or camber, but not both. The laser scribing process produces a nearly constant crown/camber ratio so that if one is changed, the other is as well. Also, twist (which represents a major problem) cannot be created (nor compensated) by symmetrical scribing patterns.

12.2.2 THEORETICAL MODELING

To model the deflections created by laser scribing, an adaptation of the line-dipole force model [2] used by Austin and Scattergood was implemented. The line dipole solution modeled a *mechanical* scribe as two sets of forces separated by a small distance. However, for the mechanical scribing case, the scribe produced curvature perpendicular to the scribe, but not parallel curvature. So, to produce this parallel curvature as seen in the laser scribe, a set of forces parallel to the scribe were added. Two different force models were developed for the laser scribe, one with a distributed parallel force (Figure 3a) and another with concentrated forces at the end of the scribe (Figure 3b).

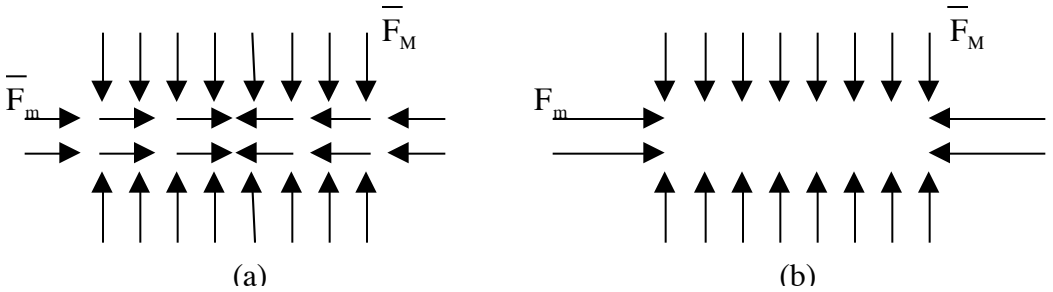

Figure 3. Laser Scribing Force

Since each of these force models has loads in both *x* and *y* directions and the loads have endpoints, the theoretical beam theory solution (as performed by Scattergood and Austin) is not a practical way to solve this problem. Numerical methods such as finite element analysis can be used to solve a problem of this geometry and produce a solution to the force model based on solid mechanics.

As with the mechanical scribing model, the FE model requires calibration with a "control group" of laser scribes. For a symmetrical scribing pattern, there are two desired quantities (camber and

crown) and two variables in the finite element analysis (the ratio F_m/F_M and a linear scaling factor). So, given the curvatures from one laser scribe pattern, the model can be calibrated and then used to predict other scribing patterns.

12.2.3 MEASUREMENTS

The results of a series of measurements on sliders was presented in the 2000 Precision Engineering Center Annual Report [3,4]. These measurements were performed on the laser scribing system at IBM and measurements of the distorted heads were made using a Wyco white-light interferometer. The data best fits the end force model of Figure 3(b). One plausible mechanism that would validate the end force model involves the process by which the scribe is produced. The scribe is actually a collection of "dots" created by the pulsed laser placed close together. If the residual stress induced by the scribe is created by the resolidification of the melted material, the stress from each dot in the scribe direction would be cancelled by the dots on either side. Except for the dots on the end, which would create tensile stresses on the end (similar to the end force model).

The end force model predicts the shape of the scribe sliders quite well. However, for a full calibration, a linear factor was be introduced to establish the actual magnitude of the curvatures. The measured magnitude of the curvatures does not necessarily obey intuition or solid mechanics (if the assumption of the same material is true). For example, in the scribe length study, the longer scribes did not necessarily produce more deflection than the shorter ones (a result that comes from both intuition *and* finite element model). However, the finite element model does produce the correct shape (crown to camber ratio). The influences on this linear factor are the material properties and the strength of the scribe—both of which could be influenced by the change in material. Upon further examination, it was found that all of the sliders that did not match the full calibration within 5% error came from the *same row*—possible indication that material properties are causing the error. A possible remedy for this would be to calibrate each row on one slider with a test pattern. Further investigation will reveal if this is necessary. But overall, the end-force model does show a great deal of promise—it predicts the shape of the sliders with good accuracy and, discounting that single row, produces excellent results for the overall magnitudes of the curvatures.

Several further steps were taken to create a model capable of predicting the effect of a scribe of any length or direction. These included:

- extending the scribing geometry to include scribes in the *x* direction
- dealing with the fact that the heads are scribed while connected together in a row,
- modeling new scribe geometries and verifying their curvatures experimentally
- developing models that generate twist
- construct a library of solutions

Extending the model to include *x*-direction scribes is relatively simple: a new mesh was developed, scribing geometries tested with the calibration found above, and results verified with the experiments conducted.

One source of error in the early model was that it was for a single slider while the actual sliders are scribed and measured as part of a row (which is 44 sliders attached together). While modeling an entire row is impractical, it was found that modeling 3 sliders attached together and taking data from the middle slider created excellent results.

Once the model was verified, the project involved the development of a library of solutions. Since superposition is obeyed, a collection of single scribe results can be summed to give complicated scribe geometries. Of primary interest were scribing arrangements that generate twist—twist is one of the primary problems in slider processing. A final verification of the model was conducted by theoretically modeling a scribe pattern that generates twist, performing the experiment and comparing results. Excellent agreement was obtained.

12.2.4 PREDICTED RESULTS

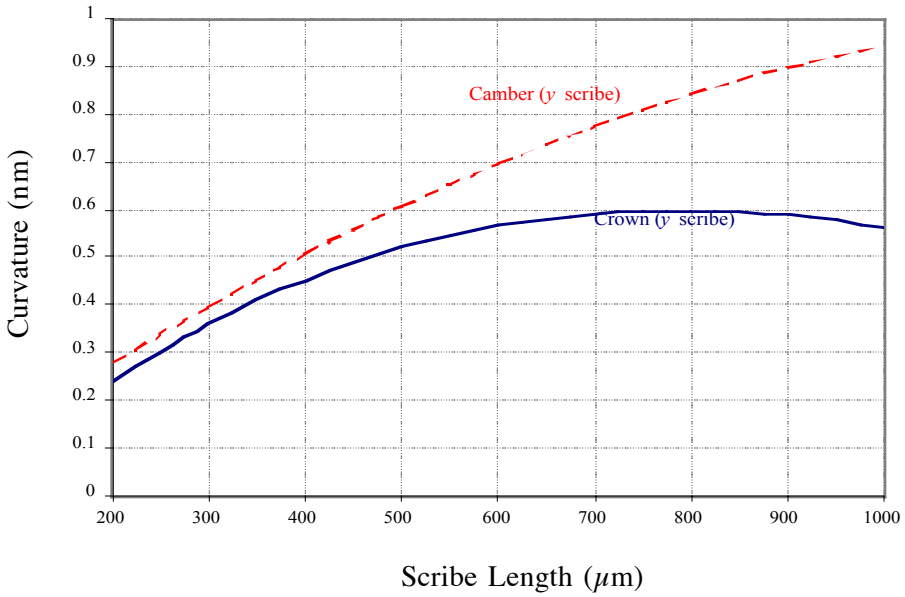

Figure 4. Curvature as a Function of a Centered Scribe Length- y direction

To find the deflections generated by an arbitrary laser scribe, several steps were taken. First, the force system was applied to a finite element idealization of a specific geometry on a slider (or row). Then, the force magnitudes were manipulated to match experimental results of the same geometry. This calibration is then verified by checking different scribing geometries. Finally, the calibrated force system was used to model scribes of different geometries. Figure 4 shows representative

results for the case of a single scribe in the y direction, centered on the slider. The plot shows the effect of scribe length on the curvatures. Since the scribe is symmetrically placed, no twist is induced. Note that the curvature length scale is measured in nanometers, i.e. the displacements induced by a single scribe are extremely small. Similarly, Figure 5 shows representative results for the case of a single scribe in the x direction that is centered on the slider.

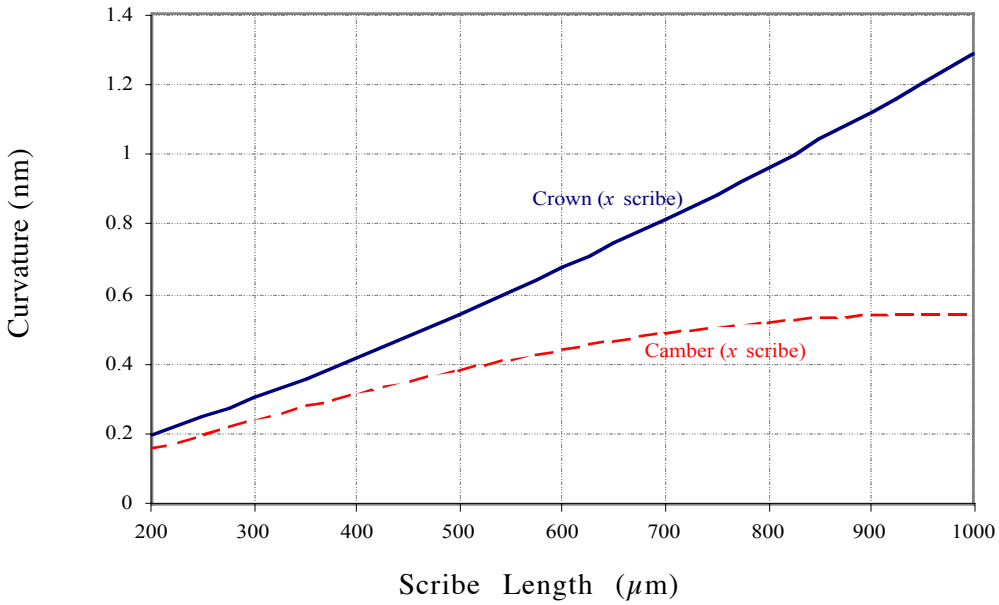

Figure 5. Curvature as a Function of Centered Scribe Length- x direction

12.3 CONCLUSION

Through experimentation and finite element modeling, it was shown that the curvature produced by laser scribing can be predicted theoretically. A finite element mesh with an appropriate force system (in this case, a line dipole with parallel end forces) can be calibrated using experimental results, and then used to predict other scribe geometries. Since superposition is obeyed, single scribe results can be modeled theoretically and then added to construct more complicated geometries.

The preliminary investigation into calibrating the model has shown excellent results. With the fully calibrated model, a library of single scribe solutions was created. This library could be used to construct a scribing pattern based on a desired shape—allowing more sophisticated control over the scribing system and ultimately, better shape control of the sliders.

REFERENCES

1. Tam, A.C., et. al., *Manufacturing: Stress on the Dotted Line*, IBM Corp., Almaden Research Center, December 1999.
2. Austin, B., *Scribing of Brittle Materials*, MS Thesis – Materials Science, NC State University, 2000.
3. Modeling Laser Scribing for use as a Precision Shaping Technique by Bryan Love and Jeffrey Eischen, PEC Annual Report, 2000, pg 35-46.
4. Eischen, J. W., Love, B. M., Dow, T.A., Scattergood, R.O., "Laser Scribing for Use as a Precision Shaping Technique," Proceedings of the Seventh Pan American Congress of Applied Mechanics, Temuco, Chile, January 2-5, 2002.
5. Love, Bryan,

FACULTY, STAFF AND STUDENTS OF THE PRECISION ENGINEERING CENTER

Standing (L to R): W. Panusittikorn, A. Sohn, K. Garrard, T. Dow, R. Scattergood, D. Kametz, S. Clayton and D. Gill

Sitting: P. Morrissey, N. Negishi, T. Wu and L. Underhill

Faculty Not Pictured: J. Eischen, G. Buckner, P. Ro, A. Shih., P. Russell, D. Griffis, K. Falter, D. Youden

Students Not Pictured: D. Hood, J. Qu, G. Mou, M. Cerniway, B. Love, M. Bauer, M. Heinrich

FACULTY

THOMAS A. DOW

Director, Precision Engineering Center
Professor, Department of Mechanical and Aerospace Engineering

BS, Mechanical Engineering, Virginia Polytechnical Institute, 1966
MS, Engineering Design, Case Institute of Technology, 1968
PhD, Mechanical Engineering, Northwestern University, 1972

After receiving his PhD degree from Northwestern University in 1972, Dr. Dow joined the Tribology Section of Battelle Columbus Laboratories and worked there for ten years. His research interests were in the areas of friction and wear and included studies on a wide variety of topics from lubrication of cold-rolling mills using oil-in-water emulsions to wet braking effectiveness of bicycle brakes to elastohydrodynamic lubricant film generation in ball and roller bearings. He developed experimental apparatuses, established analytical models, and corroborated those analyses with experimental measurements. Dr. Dow joined the faculty at North Carolina State University in 1982 and was instrumental in developing the academic and research program in precision engineering. His current research interests include the design of precision machining systems, real-time control, and metrology. He was one of the founders of the American Society for Precision Engineering and currently acts as the Executive Director.

GREGORY D. BUCKNER

Assistant Professor, Department of Mechanical and Aerospace Engineering

BS, Mechanical Engineering, Louisiana State University, 1986
MS, Mechanical Engineering, Virginia Polytechnic Institute, 1987
PhD, Mechanical Engineering, University of Texas at Austin, 1996

After receiving his PhD degree from the University of Texas at Austin in 1996, Dr. Buckner joined the University of Texas Center for Electromechanics (UT-CEM), where he served as a research engineer until 1999. His research at UT-CEM focused on the design and implementation of advanced controllers for electromechanical systems. Applications included self-learning control systems for active vehicle suspensions, magnetic bearings for flywheel systems, and manufacturing processes. Dr. Buckner joined the faculty at North Carolina State University in 1999 as an Assistant Professor of Mechanical and Aerospace Engineering. Dr. Buckner's research and teaching interests focus on the design and control of electromechanical systems, with an emphasis on self-learning algorithms. Current research topics include electromechanical actuators for system identification of milling processes, and magnetic bearings for flywheel and milling applications.

JEFFREY W. EISCHEN

Associate Professor
Department of Mechanical and Aerospace Engineering

BS, Mechanical Engineering, UCLA, 1978
MS, Mechanical Engineering, Stanford University, 1981
PhD, Mechanical Engineering, Stanford University, 1986

Dr. Eischen has been with N.C. State since 1986 and his research areas of interest include computational solid mechanics, elasticity, fracture mechanics and structural dynamics. Dr. Eischen worked with Failure Analysis Associates from June 1978 - June 1986 as a Mechanical Engineer. His primary responsibilities included analysis and prevention of industrial equipment failures.

KARL J. FALTER

Senior Development Engineer, Eastman Kodak Company
Adjunct Assistant Professor, Department of Mechanical and Aerospace Engineering

BS, Mechanical Engineering NC State University, 1988
MS, Mechanical Engineering NC State University, 1990
PhD, Mechanical Engineering NC State University, 1992

Prior to joining Eastman Kodak's Manufacturing Systems Technology Division in 1997, Dr. Falter was a Research Engineer for Rank-Pneumo, a division of Rank-Taylor Hobson. He also assisted the Rank-Taylor fellows in their research at the Precision Engineering Center. Dr. Falter previously worked as a post graduate researcher at the Precision Engineering Center on a variety of projects. These projects ranged from study of the acoustic disturbance of a diamond turning machine to finite element analysis of diamond tools. Dr. Falter's PhD dissertation concerned simplifications of finite element models used in the shock response analysis of electronic assemblies. His MS thesis, which concerned a laboratory technique used to measure power flow in vibrating structures, was completed as a student in the Precision Engineering Center.

PAUL I. RO

Associate Professor
Mechanical and Aerospace Engineering Department

BS, Mechanical Engineering, University of Minnesota, 1982
MS, Mechanical Engineering, Massachusetts Institute of Technology, 1985
PhD, Mechanical Engineering, Massachusetts Institute of Technology, 1989

Dr. Ro joined the faculty of North Carolina State University in January 1989, as an Assistant Professor in the Mechanical & Aerospace Engineering Department. He became an Associate Professor in July 1994. Dr. Ro has developed two graduate courses in the department (multivariable Control and Robotics) and has taught undergraduate Automatic Control and Dynamics courses. His research covers a wide range of controls and various applications of control theories in the following three areas: Precision Engineering, Robotics and Intelligent Vehicle Control.

In precision engineering, Dr. Ro's research concentrates on the characterization and control of microdynamic behaviors of precision slide systems (ball-screw, traction drive, piezo-electric drive, electrostatic drives and magnetic servo levitated drive) to enhance their nano-motion capabilities, development of advanced control schemes and experimental verifications to improve diamond turning process using force and position sensory feedbacks, design of a long-range fast tool servo system using magnetic servo levitated actuators, and active control of precision slide vibration using piezo-electric drives. In robotics, some of the on-going projects include design and implementation of free-floating non-holonomic space robot and a planar passive-joint robot for fuel consumption minimization, neural-fuzzy hybrid scheme for mobile robot path planning, and two-arm coordinated motion control for fixtureless assembly. In intelligent vehicle control, on-going projects include nonlinear tire model identification by Artificial Neural Network, hybrid neural-sliding mode control of 4 Wheel steering for robust handling, semi-active suspension control using energy based Fuzzy Logic scheme, and others.

PHILLIP E. RUSSELL

Professor
Department of Materials Science and Engineering

BS, Physics, Appalachian State University, 1975
MS, Physics, West Virginia University, 1977
PhD, Materials Science and Engineering, University of Florida, 1982

After graduate work at the University of Florida, Dr. Russell joined the Solar Energy Research Institute (a DOE lab) in Golden Co. in 1980. There he developed a photovoltic materials and device characterization laboratory with emphasis on electron and ion beam analytical instrumentation. After three years at SERI, Dr. Russell joined JEOL, Inc. in Boston, Massachusetts, an electron optical instrumentation company where he led the technical and application groups. One of his major projects was the development of an electron beam based integrated circuit metrology system. He was also involved in the development and application of focused ion beam systems and electron beam lithography systems, as well as numerous analytical instrumentation projects.

On joining North Carolina State University, Dr. Russell took on the role of Director of the Analytical Instrumentation Facility and has established graduate level courses in electron optics and electron optical instrumentation techniques. He was awarded the NSF Presidential Young Investigator Award in 1987. His research at NCSU and the Precision Engineering Center are in the areas of Scanned Probe Microscopy, Focused Ion Beam Technology, Scanning Electron Microscopy, Lithography metrology and beam testing of integrated circuits.

RONALD O. SCATTERGOOD

Professor
Materials Science and Engineering Department

BS, Metallurgical Engineering, Lehigh University, 1961
MS, Metallurgy, Massachusetts Institute of Technology, 1963
PhD, Metallurgy, Massachusetts Institute of Technology, 1968

R.O. Scattergood is a Professor in the Department of Materials Science and Engineering. He received BS degrees in Mining Engineering and Metallurgical Engineering from Lehigh University. His MS and PhD degrees were obtained in Metallurgy from M.I.T. In 1968 he became a member of the basic research staff in the Materials Science Division at the Argonne National Laboratory. In 1981, he joined the faculty as a Professor of Materials Engineering at North Carolina State University.

Professor Scattergood's major research interests have been focused on the mechanical behavior of solids. He has worked in the areas of strengthening mechanisms in solids, continuum theory of defects, radiation effects, wear and fracture processes in ceramics, and precision engineering with emphasis on machining processes. He has expertise in both analytical and computer modeling as well as in mechanical testing methods and microscopy. He has published over 140 technical papers, books and reports.

ALBERT J. SHIH

Associate Professor
Mechanical and Aerospace Engineering

BSME, National Cheng Kung University, Taiwan, 1984
MSME, National Cheng Kung University, Taiwan, 1986
PhD, Purdue University, 1991

Before joining N.C. State University in 1998, Dr. Shih worked in the Fuel Systems and Technical Center of Cummins Engine Company for seven years. He developed innovative and cost-effective manufacturing processes for sub-micron precision grinding of ceramic and hardened steel diesel engine components. He also worked in teams to implement the sub-micron precision ceramic plungers for diesel fuel systems. He led a team of three companies, Cummins Engine Co., Milacron, Inc. and Goldcrown (part of the UNOVA) to win a NIST ATP (Advanced Technology Program) grant on "Sub-micron Precision Grinding of Advanced Engineering Materials" in 1997. At Cummins, he continued to conduct basic research and publish results in the broad area of mechanical engineering.

DAVID YOUDEN

Technical Associate, Eastman Kodak Company
Adjunct Lecturer, Department of Mechanical and Aerospace Engineering

ASME, Central New England College, Worcester, MA, 1965

Prior to joining Eastman Kodak's Manufacturing Systems Technology Division in 1997, Mr. Youden was Research and Development Manager at Rank Pneumo, a division of Rank Taylor Hobson Inc. for ten years. Before that, he was Director of Engineering at the Cone Blanchard Machine Company. He has also worked at Ocean Systems, Inc. of Reston, Virginia and the Heald Machine Company, a division of Cincinnati Milacron. During his professional career, Mr. Youden has been granted numerous patents in the field of machine tools, and he has published and presented technical papers on the design and testing of ultra-precision machine tools in the US, Japan, and Germany.

Mr. Youden graduated from Central New England College and attended Worcester Polytechnic Institute and Clark University. He is a charter member of the American Society for Precision Engineering.

STAFF

KENNETH P. GARRARD

Research Assistant
Precision Engineering Center

BS, Computer Science, North Carolina State University, 1979
MS, Computer Studies, North Carolina State University, 1983

As a full-time research assistant, Mr. Garrard is studying the design of systems software that supports the development of high-speed real-time applications for special purpose multiprocessor computer systems. He has several years experience in academia and industry designing and implementing real-time systems. As a Precision Engineering Center staff member, Mr. Garrard's current activities include the design and implementation of software for Diamond Turning Machine and Fast Tool Servo controller projects.

ALEXANDER SOHN

Research Assistant/Lecturer
Precision Engineering Center

B.S., Physics, University of Texas at Arlington, 1992
M.S., Physics, University of Texas at Arlington, 1994

Mr. Sohn joined the Precision Engineering Center in August, 1997 as a member of the technical staff. His current research interests range from machine design and metrology to the design and fabrication of nonimaging optics. Mr. Sohn's varied research activities began in microwave optics and atomic physics as a student at the University of Texas at Arlington and later progressed to precision machine design, design and fabrication of plastic optics as well as automation and machine vision at Fresnel Technologies, Inc. in Fort Worth, Texas.

LAURA UNDERHILL

Administrative Assistant
Precision Engineering Center

BA, Education, University of North Florida, 1994

Ms. Underhill became a member of the PEC Staff in August 2001. Previously she was an administrative assistant at North Florida Shipyards in Jacksonville, FL, and Computer Source in Jacksonville, FL. Ms. Underhill brings to the Center many years of administrative experience. Ms. Underhill provides the overall administrative support for the Center.

GRADUATE STUDENTS DURING 2001

MARKUS BAUER received his MS degree in Mechanical Engineering (Diplom-Ingenieur) in March 1998 at RWTH-Aachen (Technical University of Aachen, Germany). For his Master's thesis he designed a computer-controlled robotic manipulator arm using PZT actuators to control joint impedance and incremental angular encoders for position feedback. He is currently pursing a PhD degree in Mechanical Engineering. His research involves the design and implementation of an ultrasonic piezoelectric motor.

MATTHEW A. CERNIWAY received his BS degree in Mechanical Engineering from NC State University in 1996. Matthew's professional experience covers a wide range of engineering fields. Ranging from facility design and management with Nan Ya Plastics to equipment design with II-VI Inc and most recently as a field advisor to the Polar Ice Coring Office on the NSF's '99 Drilling season in Siple Dome, Antartica. Matthew is currently working towards his MS degree in Mechanical Engineering. His on going research is the "Ultra-Mill", a high speed piezo-actuated mill, sponsored by Kodak.

STUART CLAYTON received his BS degree in Mechanical Engineering from NC State University in May of 2001. After taking a summer off from school, Stuart enrolled in graduate school here at the PEC. Currently, he is pursuing a Master's of Science degree in Mechanical Engineering. His research involves an investigation of deflections of high-speed miniature milling tools and the ability to compensate for tool deflections using magnetic bearing spindles.

DAVID GILL received his BS degree in Mechanical Engineering from Texas Tech University in 1994. He completed a MS degree in Mechanical Engineering from Purdue University in 1997 in the area of Computer Aided Design and Manufacturing. Prior to coming to N. C. State in 1999, he worked in Manufacturing Engineering and Product Engineering at Caterpillar, Inc. Currently he is working towards a Ph.D. in Mechanical Engineering. His specific area of study and research is precision replication of optics.

MATIAS HEINRICH received his BS degree in Mechanical Engineering from NC State University in December of 1998. After working on the development of a third axis for the Nanoform 600 Diamond Turning Machine, he returned full time to pursue his MS degree at the PEC in the Summer of 1999. His research focuses on the development of a Piezoelectric Motor for use in Cryogenic environments of space. Design specifications are based on those for the Next

Generation Space Telescope (NGST) that will utilize such motors for the fine adjustment of a large flexible optical mirror.

DAVID HOOD received his BS degree in mechanical engineering from NC State University in 2001. The next semester he enrolled at NC State and is currently pursuing his MS degree in Mechanical Engineering. His research involves active magnetic bearings and compensation for high-speed miniature milling tools and the ability to compensate for tool deflections.

DAVID KAMETZ received his BS degree in Mechanical Engineering in August of 2000 at Clarkson University in Potsdam, NY. David had a second major in Aeronautical Engineering while at Clarkson, but did not complete the program in order to enroll in graduate school. While at Clarkson he was the team leader of his senior design group in both his mechanical engineering and aeronautical engineering programs. His first semester at NCSU was spent as a teaching assistant in the machine shop, where he taught welding, machining and fabrication. David's research for IBM involves the improvement of both manufacturing lapping plates and the lapping process.

BRYAN LOVE received his BS degree in Mechanical Engineering from NC State University in May of 1999. After working in the product development group at Controls Southeast, Incorporated this past summer, he returned to NC State to work on his MS degree in Mechanical Engineering. His specific area of study and research is stress analysis and finite element modeling.

PATRICK MORRISSEY received his BS degree from NC State University in December of 2000. During his undergraduate studies he worked at Guilford Mills in Greensboro, NC for two summers where he worked on improving the heating system used to dry dyed fabrics. He is currently pursuing his MS in Mechanical Engineering, and has been a member of the PEC since August of 2001. He is now working on a project with Los Alamos National Laboratories that involves the design of thin composite cylinders.

GANG MOU received his BS and MS degree in Mechanical Engineering from Sichuan Institute of Technology, China, in 1992 and 1995 respectively. Prior to come to NC State University in Fall 1999, he worked in an engineering company at Chinese Academy of Sciences. He is currently pursuing a PhD degree in Mechanical Engineering. His specific area of study and research is control technology and its application.

WITOON PANUSITTIKORN received his MIE degree in Industrial Engineering from NC State University in 1998, and MS degree in Mechanical Engineering from NC State University in 2001. For his Master's thesis, he designed a nonlinear controller to manipulate a friction-based object transport system. He is currently pursing a PhD degree in Mechanical Engineering. His research involves the nonlinear controller design to compensate magnetic hysteresis in a magnetostrictive transducer.

JUN QU received his BS and Master's degrees in Precision Instrument Engineering from Tianjin University in People's Republic of China in 1995 and 1998. He received his second Master's degree in Mechanical Engineering from Iowa State University in 1999. Currently he is pursuing a Ph.D. degree in Mechanical Engineering. His specific area of study and research is Precision Engineering.

QUN WAN received his B.S. degree in Thermophysics from University of Science and Technology of China in 1996. After working as manufacturing engineer in Teling (TRANE CHINA) Air-Conditioning Co. Ltd for one year, he came to the National University of Singapore, where he received his M.S. degree in Mechanical and Production Engineering in 2000. Prior to come to NC State University in Fall 2000, Qun had worked as software engineer in Vector Technology Co. Ltd (Singapore). Currently, he is a PhD student under Dr. Andrey Kuznetsov and his research focuses on Numeric Simulation on Cooling Effect of Ultrasonic Acoustic Streaming.

TAO WU received her BS and MS degree in Electrical Engineering from Northwestern Polytechnic University, China in 1993 and 1996. Prior to coming to NCSU in August 2000, She also received her PhD degree in Electrical Engineering in Shanghai Jiaotong University, China in 1999 and studied in University of Virginia for one year. Currently she is a PhD student in Mechanical and Aerospace Engineering and her research focuses on the development of a novel ultrasonic cooling concept for microelectronics.

GRADUATES OF THE PRECISION ENGINEERING CENTER

Student	Degree	Date	Company/Location
Jeffrey Abler	PhD	December 1994	ETEC Systems, Inc. Tucson, AZ
William Allen	PhD	December 1994	North Carolina State Univ. Raleigh, NC
Kelly Allred	MS	June 1988	
Christopher Arcona	PhD	May 1993	Norton Worcester, MA
Bradford Austin	MS	June 2000	IBM Corporation Fishkill, NY
Markus Bauer	PhD	December 2001	SCYNEXIS Chemistry & Automation, Inc. Research Triangle Park, NC
Tom Bifano	PhD	June 1988	Boston University Boston, MA
Scott Blackley	MS	May 1990	Motorola Austin, TX
Peter Blake	PhD	December 1988	NASA Goddard Greenbelt, MD
Mark Cagle	MS	June 1986	NASA-Langley Norfolk, VA
John Carroll	PhD	January 1986	Cummins Engine Co. Columbus, IN
Matthew Cerniway	MS	October 2001	Naval Surface Warfare Ctr West Bethesda, MD
Damon Christenbury	MS	June 1985	Michelin Tire Co. Spartanburg, SC
James Cuttino	PhD	December 1994	UNC – Charlotte Charlotte, NC
Bob Day	PhD	July 1998	Los Alamos National Lab Los Alamos, NM

Joseph Drescher	PhD	May 1992	Pratt & Whitney East Hartford, CT
William Enloe	MS	December 1988	ITT Roanoke, VA
Karl Falter	MS	December 1989	Eastman Kodak Company Raleigh, NC
Peter Falter	PhD	May 1990	Lockheed-Martin Orlando, Florida
John Fasick	MS	May 1998	Burleigh Instruments Fishers, NY
Steven Fawcett	PhD	June 1991	MicroE Natick, MA
Andre Fredette	PhD	May 1993	IBM Research Triangle Park, NC
Jim Gleeson	MS	June 1986	Battelle Columbus Labs Columbus, OH
Mary Smith Golding	MS	May 1990	Harris Corporation Melbourne, FL
David Grigg	PhD	August 1992	Zygo Corporation Middlefield, CT
Hector Gutierrez	PhD	October 1997	Florida Inst. Of Tech. Melbourne, FL.
Christian Haeuber	MS	December 1996	Harris Corporation Melbourne, FL
Matias Heinrich	MS	July 2001	Vistakon Jacksonville, FL
Gary Hiatt	PhD	May 1992	Caterpiller Zebulon, NC
Peter Hubbel	MS	December 1991	Delco Electronics Kokomo, IN
Konrad Jarausch	PhD	December 1999	Intel Corporation San Jose, CA
Bradley Jared	PhD	December 1999	Corning Inc. Corning, NY

Jerry Kannel	PhD	June 1986	Battelle Columbus Labs Columbus, OH
Byron Knight	MS	May 1990	Harris Corporation Melbourne, FL
Mark Landy	MS	June 1986	Battelle Columbus Labs Columbus, OH
Mike Loewenthal	MS	December 1988	Cummins Engine Co. Columbus, IN
Michael Long	PhD	June 2000	Eastman Kodak Rochester, NY
Bryan Love	MS	May 20001	Virginia Tech
Michael Hung-Tai Luh	MS	June 1989	Proctor and Gamble Cincinnati, OH
Dan Luttrell	MS	1987	Corning, Inc. Corning, NY
Edward Marino	MS	September 1999	Pratt Whitney Hartford, CT
Edward Miller	MS	December 2000	General Electric Greenville, SC
Michele Miller	PhD	December 1994	Michigan Tech. University Houghton, MI
Paul Minor	MS	September 1998	Pratt & Whitney Palm Beach, FL
Gary Mitchum	MS	June 1987	Harris Corporation Melbourne, FL
Charles Mooney	MS	December 1994	JEOL Peabody, MA
Larry Mosley	PhD	June 1987	Intel Corporation Chandler, AZ
Patrick Moyer	PhD	May 1993	UNC-Charlotte Charlotte, NC
Ayodele Oyewole	MS	October 1997	Pratt & Whitney East Hartford, CT
Hakan Ozisik	PhD	December 1989	Aerospace Corporation Long Beach, CA

John Pellerin	MS	May 1990	Sematech Austin, TX
Ganesh Rao	MS	December 1994	Oak Ridge National Lab Oak Ridge, TN
John Richards	MS	September 1997	Intel Corporation San Jose, CA
Walter Rosenberger	MS	May 1993	The East Group Kinston, NC
Alex Ruxton	MS	December 1996	Pratt &Whitney Palm Beach, Florida
Anthony Santavy	MS	August 1996	3M Corporation Petaluma, California
Keith Sharp	PhD	May 1998	Morganite Wales, England
Gordon Shedd	PhD	March 1991	Burleigh Instruments Fishers, NY
Wonbo Shim	PhD	May 2000	Seagate Inc. Oklahoma City, OK
Robert Skolnick	MS	September 1997	Chemtronics, Inc. San Diego, CA
Denise Skroch	MS	May 1989	IBM Corporation Raleigh, NC
Elizabeth Smith	MS	April 1989	
Stanley Smith	PhD	May 1993	Komag, Inc. Santa Clara, CA
Ronald Sparks	PhD	May 1991	Alcoa Corporation Pittsburg, PA
Brent Stancil	MS	December 1996	Harris Corporation Melbourne, FL
Gene Storz	MS	May 1994	
Anand Tanikella	PhD	August 1996	Norton Industrial Ceramics Northboro, MA

Donna Thaus	MS	May 1996	Northern Telecom Research Triangle Park, NC
John Thornton	MS	December 1993	Digital Instruments Santa Barbara, CA
Michael Tidwell	MS	December 1991	
John Tyner	MS	June 1995	Naval Depot - Cherry Point

ACADEMIC PROGRAM

Problems and limitations associated with precision manufacturing can originate in the machine, the process, or the material. In fact, most problems will probably be caused by a combination of these factors. Therefore, improvement of current processes and development of new manufacturing methods will require knowledge of a multi-disciplinary array of subjects. The educational goal of the Precision Engineering Center is to develop an academic program which will educate scientists and engineers in metrology, control, materials, and the manufacturing methods of precision engineering.

The graduate students involved in the Precision Engineering Center have an annual stipend as research assistants. They can take up to 3 classes each semester while spending about 20 hours per week on their research projects. These students also work in the Center full-time during the summer months.

The Precision Engineering Center began in 1982 with an emphasis on the mechanical engineering problems associated with precision engineering. As a result, the original academic program proposed was biased toward courses related to mechanical design and analysis. However, as the research program has developed, the need for complementary research in sensors, materials, and computers has become obvious. A graduate student capable of making valuable contributions in the computer area, for example, will require a significantly different academic program than in mechanical engineering. For this reason, the Center faculty have set a core curriculum and each student in the program is required to take at least 3 of these core courses. The remainder of the courses for the MS or the PhD degree are determined by the university or department requirements and the faculty committee of the student.

The required courses are:

- MAE 545 Metrology in Precision Manufacturing
- PY 516 Physical Optics
- MAT 700 Modern Concepts in Materials Science
- CSC (ECE) 714 Real Time Computer Systems

PhD DEGREE PROGRAM

The PhD program in Precision Engineering has been set up as a multi-disciplinary program, drawing upon courses throughout the University to provide background and expertise for the students. It should contain required courses to insure solid grounding in the fundamentals plus electives to prepare the student in his area of specialization. Because Precision Engineering is concerned with an integrated manufacturing process, students interested in computer control, materials, machine structure, and measurement and actuation systems are involved in the program. Student research projects include the wide variety of topics addressed in this report. Each student's thesis should have an experimental component because Precision Engineering is basically a hands-on technology.

MS DEGREE PROGRAM

The Master of Science degree will have a higher percentage of application courses than the PhD degree. The emphasis will be to develop the foundation for involvement in precision engineering research and development. A total of 30 credits including 6 credits for the MS thesis is required. The thesis, while less comprehensive than the PhD dissertation, will be directed at important problems in Precision Engineering. Typically the MS program will take four semesters plus one summer.

UNDERGRADUATE PROGRAM

The undergraduate degree broadly prepares an engineering student for industrial activities ranging from product design and engineering sales to production implementation. Because a large share of engineers only have the BS degree, these will be the people who must implement the new technology developed in research programs like the Precision Engineering Center. Therefore, a way must be found to acquaint engineers at the BS level with the techniques, problems, and potential of precision manufacturing.

In most undergraduate degree programs only limited time is available for technical electives. However, these electives offer the student the opportunity to expand his knowledge in many different directions. Beginning graduate courses (such as metrology) can be used as undergraduate electives.

Undergraduate projects and summer employment have also been utilized to include undergraduate students into the research program of the Center. During the 1998-1999 academic year, four undergraduate students in Mechanical Engineering were involved various projects at the PEC.

STUDY PLANS

Study plans for several example students are given below both for the MS and the PhD degree. Because of the breadth of the field and the wide range of thesis topics, few if any study plans will be exactly the same. The plan will depend upon the student's background, his interests, his thesis topic, the department, and the chairman and members of his committee.

PhD PROGRAM IN MECHANICAL ENGINEERING

Major Courses:

- MAE 740 Advanced Machine Design I
- MAE 741 Advanced Machine Design II
- MAE 706 Heat Transfer Theory & Applications
- MAE 713 Principles of Structural Vibration
- MAE 760 Computational Fluid Mechanics and Heat Transfer
- MAE 545 Metrology in Precision Manufacturing
- MAE 715 Nonlinear Vibrations
- MAE 716 Random Vibration
- MAE 714 Analytical Methods in Structural Vibration
- MAE 742 Mechanical Design for Automated Assembly
- MAE 895 Doctoral Dissertation Research

Minor Courses:

- MA 511 Advanced Calculus I
- MA 775 Mathematical Methods in the Physical Sciences I
- CSC 780 Numerical Analysis II
- PY 516 Physical Optics
- ECE 716 System Control Engineering
- MAT 700 Modern Concepts in Materials Science
- ECE 726 Advanced Feedback Control
- ECE 764 Digital Image Processing

PhD PROGRAM IN MATERIALS ENGINEERING

Major Courses:

- MAT 710 Elements of Crystallography and Diffraction
- MAT 700 Modern Concepts in Materials Science
- MAT 556 Composite Materials
- MAT 715 Transmission Electron Microscopy
- MAT 795 Defect Analysis/Advanced Materials Experiments
- MAT 753 Advanced Mechanical Properties of Materials
- MAT 712 Scanning Electron Microscopy
- MAT 895 Doctoral Dissertation Research

Minor Courses:

- PY 414 Electromagnetism I
- ST 502 Experimental Statistics for Engineers I
- MAE 740 Advanced Machine Design I
- MAE 741 Advanced Machine Design II
- MAE 545 Metrology in Precision Manufacturing
- PY 516 Physical Optics
- MA 401 Applied Differential Equations II

PhD PROGRAM IN ME (FOR STUDENT WITH MS DEGREE)

- ECE 716 System Control Engineering
- ECE 791 Gate Array Design
- MAT 700 Modern Concepts in Materials Science
- PY 516 Physical Optics
- MA 502 Advanced Mathematics for Engineers and Scientists II
- MA 775 Mathematical Methods in the Physical Sciences I
- MA 780 Numerical Analysis II
- MAE 732 Fundamentals of Metal Machining Theory
- MAE 740 Advanced Machine Design I
- MAE 741 Advanced Machine Design II
- MAE 545 Metrology in Precision Manufacturing
- MAE 716 Random Vibration

MS PROGRAM FOR ME STUDENT

- MAE 713 Principles of Structural Vibration
- MAE 740 Advanced Machine Design I
- MAE 545 Metrology in Precision Manufacturing
- MAT 700 Modern Concepts in Materials Science
- PY 516 Physical Optics
- MA 501 Advanced Math for Engineers and Scientists I
- MA 502 Advanced Math for Engineers and Scientists II
- MAE 695 Master's Thesis Research

MS PROGRAM FOR COMPUTER SCIENCE STUDENT

- CSC 501 Operating Systems Principles
- CSC 506 Architecture of Parallel Computers
- CSC 512 Compiler Construction
- ECE 521 Computer Design and Technology
- CSC 715 Concurrent Software Systems
- MAE 545 Metrology for Precision Manufacturing
- MAE 789 Digital Control Systems
- ECE 764 Digital Image Processing

MS PROGRAM FOR MATERIALS SCIENCE STUDENT

- MAT 700 Modern Concepts in Material Science
- MAT 710 Elements of Crystallography and Diffraction
- MAT 715 Transmission Electron Microscopy
- MAT 712 Scanning Electron Microscopy
- MAT 722 Advanced Scanning Electron Microscopy and Surface Analysis
- MAE 545 Metrology for Precision Manufacturing
- PY 516 Physical Optics
- ECE 738 IC Technology and Fabrication
- MAT 695 Master's Thesis Research

MS PROGRAM FOR PHYSICS STUDENT

- PY 516 Physical Optics
- PY 552 Introduction to Structure of Solids I
- PY 753 Introduction to Structure of Solids II
- PY 781 Quantum Mechanics I
- PY 782 Quantum Mechanics II
- PY 783 Advanced Classical Mechanics
- PY 785 Advanced Electricity and Magnetism I
- PY 786 Advanced Electricity and Magnetism II
- MAT 700 Modern Concepts in Material Science
- MAE 545 Metrology for Precision Manufacturing
- PY 695 Master's Thesis Research

SHORT COURSES AND TV COURSES

Six graduate level courses: Scanning Electron Microscopy (MAT 712), Advanced SEM Surface Analysis (MAT 722), Modern Concepts in Material Science (MAT 700), Mechanical Properties of Materials (MAT 705), and Metrology (MAE 545) have been offered as video courses nationwide via National Technological University. In a typical year, approximately 120 students from industry and national laboratories participate in these courses. Future plans call for a MS program in Precision Engineering to be offered via the television network.

TECHNICAL REPORTS

Volume 1 - 1983	December 1983	136 pages
Volume 2 - 1984	January 1985	168 pages
Volume 3 - 1985	January 1986	294 pages
Volume 4 - 1986	January 1987	255 pages
Volume 5 - 1987	December 1987	336 pages
Volume 6 - 1988	December 1988	362 pages
Volume 7 - 1989	March 1990	357 pages
Volume 8 - 1990	March 1991	385 pages
Volume 9 - 1991	March 1992	382 pages
Volume 10 - 1992	March 1993	289 pages
Volume 11 - 1993	March 1994	316 pages
Volume 12 - 1994	March 1995	268 pages
Volume 13 - 1995	January 1996	251 pages
Volume 14 - 1996	January 1997	232 pages
Volume 15 - 1997	January 1998	298 pages

PUBLICATIONS

PAPERS PUBLISHED

1. Bauer, M.G. and T.A. Dow, “Design of a Linear High Precision Ultrasonic Piezoelectric Motor”, *Proceedings from ASPE 2001 Annual Meeting,* pp. 123-126.

2. Buckner, G.D., “Intelligent Bounding of Modeling Uncertainties: Applications to Sliding Mode Control of a Manufacturing Process”, *Proceedings of the IEEE International Conference on Systems, Man, and Cybernetics,* Tuscon, AZ, October 2001.

3. Buckner, G.D., “Intelligent Sliding Mode Control of Cutting Force during Single-Point Turning Operations”, *ASME Journal of Manufacturing Science and Engineering*, Vol. 123, No. 2, pp. 206-213.

4. Buckner, G.D., K.T. Schuetze and J.H. Beno, “Intelligent Feedback Linearization for Active Vehicle Suspension Control”, *ASME Journal of Dynamic Systems, Measurement, and Control*, Vol. 123, No. 4, pp. 727-733.

5. Caprio, M.T. and G.D. Buckner, “Controlling the Torque-Speed Characteristics of a Polyphase Induction Motor using a Switched Rotor Ballast Network”, *Proceedings of the American Controls Conference,* Washington, DC, June 2001.

6. Curry, A.C., A.J. Shih, J. Kong, R.O. Scattergood, S.B. McSpadden and R.B. Dinwiddie, “Grinding Temperature Measurements in MgO-PSZ using Infrared Spectrometry”, *Proceedings from ASPE 2001 Annual Meeting*, pp. 401-404.

7. Dow, T.A., M.A. Cerniway, A. Sohn and N. Negishi, “Vibration Assisted Diamond Turning using Elliptical Tool Motion”, *Proceedings from ASPE 2001 Annual Meeting*, pp. 92-97.

8. Eischen, J. W., B. M. Love, T.A. Dow, and R.O. Scattergood, "Laser Scribing for use as a Precision Shaping Technique," *Proceedings of the Seventh Pan American Congress of Applied Mechanics*, Temuco, Chile, January 2-5, 2002.

9. Gill, D.D., T.A. Dow and A. Sohn, “Replication of Precision Optical Features through Injection Molding”, *Proceedings from ASPE 2001 Annual Meeting*, pp. 66-69.

10. Heinrich, M.D. and T.A. Dow, “Development of Miniature Actuator for Cryogenic Applications”, *Proceedings from ASPE 2001 Annual Meeting,* pp. 224-228.

11. Jared, B.H. and Dow, T.A., "Investigation of the Direction of Chip Motion in Diamond Turning", *Precision Engineering: Journal of the ASPE*, Vol. 25, No. 2, pp 155-164, April 2001.

12. Pichot, M.A., J.P. Kajs, B.R. Murphy, A. Ouroua, B.M. Rech, J.H. Beno, G.D. Buckner and B. Palazzolo, "Active Magnetic Bearings for Energy Storage Systems for Combat Vehicles", *IEEE Transactions on Magnetics*, Vol. 37, No. 1, pp. 318-323.

13. Qu, J., A.J. Shih, R.O. Scattergood and S.B. McSpadden, "Cylindrical Wire Electrical Discharge Machining Process Development", *Proceedings from ASPE 2001 Annual Meeting*, pp. 501-504.

14. Qu, J., A. J. Shih, and R. O. Scattergood, "Development of the Cylindrical Wire EDM Process", Symposium of Nontraditional Manufacturing Research and Applications, *2001 ASME IMECE,* New York, NY.

15. Rhoney, B.K., A.J. Shih and R.O. Scattergood, S.B. McSpadden, R. Ott, J.A. Akemon, D.J. Gust, T.M. Yonushonis and M.B. Grant, "Wire Electrical Discharge Truing of Metal Bond Diamond Grinding Wheels", *Proceedings from ASPE 2001 Annual Meeting*, pp. 429- 432.

16. Sohn, A., K.P. Garrard and T.A. Dow, "The Polar Profilometer *Polaris*", *Proceedings from ASPE 2001 Annual Meeting*, pp. 28-31.

17. Shih, A.J., "A New Regulating Wheel Truing Method for Through-Feed Centerless Grinding", *ASME Journal of Manufacturing Science and Engineering*, Vol. 123, No. 2, pp. 319-324.

18. Shih, A.J. and J.L. Akemon, "Wear of the Blade Diamond Tools in Truing Vitreous Bond Grinding Wheels. Part I – Wear Measurement and Results", *Wear*, Vol. 250, pp. 587-592.

19. Shih, A.J., W.I. Clark and J.L. Akemon , "Wear of the Blade Diamond Tools in Truing Vitreous Bond Grinding Wheels. Part II – Truing and Grinding Forces and Wear Mechanism", *Wear*, Vol. 250, pp. 593-603.

REPORTS PUBLISHED

1. Bauer, M.G. and T.A. Dow, "Design of a Linear High Precision Ultrasonic Piezoelectric Motor", 2001 Precision Engineering Center Interim Report, pp. 17-23, August 2001.

2. Curry, A., R.O. Scattergood and A. Shih, "Grinding Temperature Measurement using Spectrometry", 2001 Precision Engineering Center Interim Report, pp. 75-80, August 2001.

3. Gill, D.D. and T.A. Dow, "Replication of Precision Optical Features through Injection Molding", 2001 Precision Engineering Center Interim Report, pp. 39-43, August 2001.

4. Heinrich, M.D. and T.A. Dow, "Development of Miniature Actuator for Cryogenic Applications", 2001 Precision Engineering Center Interim Report, pp. 25-31, August 2001.

5. Kametz, D., T.A. Dow and R.O. Scattergood, "Lapping Plate Charging", 2001 Precision Engineering Center Interim Report, pp. 7-15, August 2001.

6. Love, B. and J. Eischen, "Laser Scribing for use as a Precision Shaping Technique", 2001 Precision Engineering Center Interim Report, pp. 69-73, August 2001.

7. Negishi, N., M. Cerniway and T.A. Dow, "Vibration Assisted Diamond Machining of Non-Typical Materials", 2001 Precision Engineering Center Interim Report, pp. 45-51, August 2001.

8. Qu, J., A. Shih and R.O. Scattergood, "Cylindrical Wire EDM Process Development", 2001 Precision Engineering Center Interim Report, pp. 53-61, August 2001.

9. Sohn, A. and K.P. Garrard, "Off-Axis Biconic Mirror Fabrication", 2001 Precision Engineering Center Interim Report, pp. 63-67, August 2001.

10. Sohn, A. and K.P. Garrard, "The Polar Profilometer Polaris", 2001 Precision Engineering Center Interim Report, pp. 1-5, August 2001.

11. Wu, T., A. Langley and P.I. Ro, "Piezoelectric Bimorph Resonators for Microelectronic Cooling", 2001 Precision Engineering Center Interim Report, pp. 33-38, August 2001.

PAPERS SUBMITTED OR ACCEPTED FOR PUBLICATION AND PRESENTATIONS

1. Curry, A.C., A.J. Shih, R.O. Scattergood and S. B. McSpadden, "Grinding Temperature Measurements in MgO PSZ using Infrared Spectrometry", accepted, *J. Am. Ceram. Soc.*

2. Dixit, R.K. and G.D. Buckner, "Sliding Mode Observation and Control for Semiactive Vehicle Suspensions", in review, *Journal of Vehicle System Dynamics.*

3. Dow, T.A., E.L. Miller and K. Garrard, "Tool Force and Deflection Compensation for Small Milling Tools", submitted, *Precision Engineering, Journal of the International Societies for Precision Engineering and Nanotechnology.*

4. Esterling, D.M., G.D. Buckner and F.D. Caulfield, "Integrated Chatter Prediction and Avoidance System", accepted, *Metal Cutting and High Speed Machining.*

5. Garrell, M. G., A. J. Shih, B. M. Ma, E. Lara-Curzio and R. O. Scattergood, "Mechanical Properties of Nylon Bonded Nd-Fe-B Permanent Magnets", submitted, *Mat. Science and Engr. (A)*

6. Garrel, M. G., B. M. Ma, E. Lara-Curzio, A. J. Shih, and R. O. Scattergood "Mechanical Properties of Injection Molded Nd-Fe-B Permanent Magnets", submitted, *IEEE Transcation on Magnetics.*

7. Qu, J., A.J. Shih and R.O. Scattergood, "Development of the Cylindrical Wire Electrical Discharge Machining Process: Part I: Concept, Design, and Material Removal Rate", accepted, *ASME Journal of Manufacturing Science and Engineering*.

8. Qu, J. and A.J. Shih, "Analytical Surface Roughness Parameters of an Ideal Profile Consisting of Elliptical or Circular Arcs", submitted, *Precision Engineering*.

9. Qu, J., A.J. Shih and R.O. Scattergood, "Development of the Cylindrical Wire Electrical Discharge Machining Process: Part II: Surface Integrity and Roundness", accepted, *ASME Journal of Manufacturing Science and Engineering*.

10. Qu, J., L. Reister, A.J. Shih, R.O. Scattergood, and E. Lara-Curzio, "Nanoindentation Characterization of Surface Layers of Electrical Discharge Machined WC-Co", submitted, *Materials Science and Engineering: A* .

11. Rhoney, B.K., A.J. Shih, R. O. Scattergood, J. L. Akemon, D. J. Gust and M. B. Grant, "Cylindrical Wire Electrical Discharge Machining of Metal Bond Diamond Wheels for Ceramic Grinding", submitted, *International Journal of Machine Tool and Manufacture*.

12. Rhoney, B.K., A.J. Shih, R. O. Scattergood, R. Ott and S. B. McSpadden, "Wear Mechanism of Metal Bond Diamond Wheels Trued by Wire Electrical Discharge Machining", accepted, *Wear* .

13. Shih, A.J., A.C. Curry, R.O. Scattergood, T. M. Yonushonis, D. J. Gust, M. B. Grant and S. B. McSpadden, "Grinding of Zirconia using the Dense Vitreous Bond Silicon Carbide Wheel", submitted, *J. Am. Ceram. Soc.*

14. Zhang, X., H. Wang, R. O. Scattergood, J. Narayan and C. C. Koch, "Modulated Cyclic Hardening and Dynamic Recrystallization in Cryomilled Nanocrystaline Zn", submitted, *Acta Mater.*

15. Zhang, X., H. Wang, R. O. Scattergood, J. Narayan and C. C. Koch, "Mechanical Properties of In Situ Consolidated Bulk Ultrafine Grained and Nanocrystalline Zn Studied by Miniaturized Disk Bend Tests and Tests", submitted, *Mat. Science and Engr, (A).*

PENDING PATENTS

1. Bauer, M. and T.A. Dow, "Ultrasonic Piezoelectric Standing Wave Motor"

2. Long, M. and T.A. Dow, "Force Sensor Based on the Magnetoelastic Effect"

THESES AND DISSERTATIONS

1. Bauer, Markus, *Design of a Linear High Precision Ultrasonic Piezoelectric Motor*, Ph.D. Dissertation, North Carolina State University, December 2001.

2. Cerniway, Matthew, *Elliptical Diamond Milling: Kinematics, Force and Tool Wear*, MS Dissertation, North Carolina State University, October 2001.

3. Heinrich, Matias, *Development of a Piezoelectric Actuator for Cryogenic Environments,* MS Thesis, North Carolina State University, July 2001.

4. Love, Bryan, *Mechanical and Laser Scribing for use As Precision Shaping Techniques,* MS Thesis, North Carolina State University, May, 2001.